RESONANT OSCILLATIONS IN THE HAWAIʻIAN ARCHIPELAGO
AND
TROPICAL INSTABILITY VORTICES AND THEIR FRONTS, FRONTAL INSTABILITIES, AND CROSS-FRONTAL DIFFERENCES

A DISSERTATION SUBMITTED TO THE GRADUATE DIVISION
OF THE UNIVERSITY OF HAWAIʻI AT MĀNOA IN PARTIAL FULFILLMENT OF
THE REQUIREMENTS FOR THE DEGREE OF

DOCTOR OF PHILOSOPHY

IN

OCEANOGRAPHY

5 August 2022

By:

Lindsey Ryan Benjamin

Dissertation committee:

Pierre Flament, Chairperson
Glenn Carter
Eric Firing
James Potemra
Oceana Francis

Acknowledgements

This dissertation is the result of much hard work, and without the support of a significant number of people, it would not have been possible. While I could not possibly name everyone who provided everything from assistance to companionship, I would like to thank several in particular.

I would like to thank the Department of Homeland Security, the Office of Naval Research grant N00014-09-1-0807, the National Science Foundation grant OCE-1736709, the National Oceanic and Atmospheric Administration grant NA11NOS0120039, and the Office of the Vice President for Reseach and Innovation at UH Mānoa via STEM Pre-Academy for funding me through graduate assistantships.

My heartfelt thanks goes to Pierre Flament for being my advisor, for offering patience and guidance to me when I was faced with setbacks in my projects, for intriguing scientific discussions, and for tickling my interest in other avenues of research and exploration. I would also like to thank the other members of my Ph.D. committee, Glenn Carter, Eric Firing, Oceana Francis, and Jim Potemra, for their insightful feedback and enduring patience.

I have received significant assistance in obtaining and preparing data: I would like to thank Paul Lethaby and Ken Constantine for their work on and assistance with the high-frequency Doppler radio data; Michael Sawyer for his preparatory work on the SIR-C/X-SAR synthetic aperture radar data; Jefrey Snyder for his assistance with ADCP software and for answering my numerous questions about the instruments; Alexis Mouche for introducing me to his Datavore Xswell catalog of Sentinel-1 images; and Fabrice Collard for showing me Ocean Data Lab's Ocean Virtual Laboratory.

I would like to express my appreciation to Louis Marié, Fabrice Collard, Bertrand Chapron, and Alexis Mouche for meetings, discussions, and emails about synthetic aperture radar.

I have been fortunate enough to be involved in several fieldwork opportunities; while data from absolutely none of these has been incorporated in this dissertation, I would still like to thank Anthony Kirincich, Ian Fernandez, Charina Repollo, Cesar Villanoy, and numerous others who arranged, participated in, or were otherwise involved in these opportunities.

Thank you Kristin Momohara, Lance Samura, Kellie Terada, Catalpa Kong, and other Department of Oceanography support staff for the administrative assistance you have provided me over the years.

This journey would have been much more difficult and lonely without my fellow students in the department, particularly Alma, Angeles, Gabi, Sherry, and Victoria: thank you for listening, speaking, giving feedback, and offering support.

Special thanks to Bénédicte Dousset for all the encouragement offered, stories told, meals shared, and everything else she has given me.

Finally, I would like to thank my family for having faith that I would eventually finish, even if their wit flowed long about it.

Abstract

This dissertation consists of two unrelated parts: an analysis of resonance modes from tsunamis and potential meteotsunamis, and an analysis of tropical instability vortices (TIVs) and fronts.

In the first part, the resonant response of tsunamis and possible meteotsunamis is examined. The 2011 Tōhoku tsunami described from surface currents in high-frequency Doppler radio (HFDR) data and model simulations has two modes over Penguin Bank: a stronger mode with one larger and stronger antinode on the southern part of the bank and a weaker, smaller antinode of opposite polarity on the northern part with 43-min oscillations, and a weaker mode with two relatively equal antinodes of opposite polarity situated in a north-south fashion on the bank with oscillations with periods between 15 and 30 min. Resonance modes depend on local features of bathymetry and coastlines, not the excitation force; other seismic tsunamis as well as meteotsunamis, or long-period waves caused by atmospheric pressure anomalies interacting resonantly with the ocean surface, would be expected to excite the same modes. A search in 29-mo of data using the 2011 Tōhoku tsunami modes as a spatial filter not only did not detect any likely meteotsunami events, but it failed to detect two other, weaker, seismic tsunamis that occurred. The HFDR used was not optimally positioned to detect currents on Penguin Bank, and the inverse relationship between time step width and velocity resolution in all HFDRs means this instrument could only detect stronger currents in the resonance modes. In response, it is recommended that Penguin Bank be instrumented with five moorings, each with an upward-looking ADCP and a bottom pressure sensor, at locations chosen based on modeled resonance modes that would allow *in-situ* detection of resonance mode oscillations; also, another HFDR could be placed in a more optimal position to detect currents on Penguin Bank. Additionally, changes to the currently-installed HFDR and modeling of meteotsunamis in the Hawaiʻian Islands is recommended.

In the second part, the fronts, frontal instabilities, and cross-frontal differences in TIVs are examined. TIVs are 500-km diameter anticyclones with Rossby number ~ -1 on the North Equatorial Front that swirl colder, upwelled equatorial waters northward on their western flanks and advect warmer surface water of ITCZ-origin to the south on their eastern flanks. This swirling creates a cusp of colder water that extends northward of the mean meridional position of the North Equatorial Front with two roughly north-south fronts separating water of different temperatures, salinities, and densities: the leading front on the western side of the cusp separates warm, fresh, less-dense water to the west from the cold, salty, more-dense water in the cusp to the east, while the trailing front on the eastern side of the cusp separates cold cusp water to the west from warmer water to the east. The fronts are rotated and deformed by the swirling currents and simultaneously develop waves, cusps, and breaks due to shear current instabilities. The orientation of TIV fronts, which changes by advection of swirling large-scale currents, means that winds generally support frontogenesis on the trailing front, but either oppose frontogenesis or have little impact on leading fronts. Temperature effects on the wind, including changes in wind speed and drag coefficient, typically explain surface roughness differences across leading fronts, but some of the trailing fronts have large enough differences in currents that can overpower that effect. Currents around sub-mesoscale fronts within TIVs evolve as the fronts are advected. TIV fronts and frontal instabilities should be modeled to determine specifically which shear current instability is present and the amount of energy and heat involved. Wind estimates derived from SAR can be significantly altered by a difference in the currents across the front. SAR can be used to observe sub-mesoscale fronts and frontal instabilities.

Contents

List of Tables

List of Figures

List of Abbreviations

ADCP - acoustic Doppler current profiler

CISK - conditional instability of the second kind

DART - deep-ocean assessment and reporting of tsunamis

ELW - Equatorial long waves

ENSO - El Nño - Southern Oscillation

EOF - empirical orthogonal function

ESA - European Space Agency

EUC - Equatorial Undercurrent

HFDR - high-frequency Doppler radio

ITCZ - intertropical convergence zone

KOK - Koko Head

NEC - North Equatorial Current

NECC - North Equatorial Countercurrent

NEF - North Equatorial Front

PV - potential vorticity

SAR - synthetic aperture radar

SEC - South Equatorial Current

SIR-C - shuttle imaging radar C

SSH - sea surface height

SSHA - sea surface height anomaly

SST - sea surface temperature

TIV - tropical instability vortex

TIW - tropical instabiilty wave

TIWE - tropical instability wave experiment

UTC - universal coordinated time

X-SAR - X-band synthetic aperture radar

Chapter 1

Introduction

This dissertation consists of two unrelated parts: an analysis of resonance modes from tsunamis and potential meteotsunamis, and an analysis of tropical instability vortices (TIVs) and fronts.

In the first part, I will examine the resonant response of surface currents in the Hawaiʻian Islands to seismic tsunamis and possible meteotsunamis. Chapter 2 contains a full introduction, but in summary, seismic tsunamis cause a resonant response when the waves arrive in the Hawaiʻian Islands, exciting a suite of modes all around the archipelago but especially on Penguin Bank, a 50-m deep submerged bank extending westward from the island of Molokaʻi that acts as a probe to island chain resonance modes. These modes are dependent on local features such as bathymetry and coastlines, not on the excitation force; thus other events can cause these same resonance modes to excite, and an examination of mode excitation can isolate both seismic and meteorological tsunamis.

The resonant response of the 2011 Tōhoku tsunami described in Chapter 3 (a modified version of *Benjamin et al.* [2016]) from surface currents from high-frequency Doppler radio (HFDR) and model simulations has two modes over Penguin Bank: a stronger mode with one larger and stronger antinode on the southern part of the bank and a weaker, smaller antinode of opposite polarity on the northern part with 43-min period oscillations, and a weaker mode with two relatively equal antinodes of opposite polarity situated in a north-south fashion on the bank with oscillations with several periods between 15 and 30 min. The first of these modes is also present in tide gauge and deep-ocean assessment and reporting of tsunamis (DART) buoy sea level records which both have the highest spectral amplitudes at 43 min. Near the shore, in the west there are strong oscillations with a period of 43 min with agreement between the model and the observations, while in the east the HFDR currents have much longer periods than the model currents and show little agreement.

Because other excitation forces would activate the same resonance modes as the 2011 Tōhoku tsunami, a 29-mo record of surface currents from the same HFDR that recorded that tsunami was spatially filtered using the resonance modes from the tsunami to look for further excitation events in Chapter 4. While filtering the data based on spectral amplitudes at the periods of the tsunami modes identified 76 possible excitation events, further examination of those events showed that none were actual resonance mode activations with clear oscillations at specific, well-defined periods with a well-defined spatial structure over Penguin Bank, despite two other seismic tsunamis having occurred during the study time frame. The fact that no meteotsunami events were found in the HFDR data does not necessarily indicate that none occurred; during reprocessing to obtain the required temporal resolution, the velocity resolution of the HFDR surface currents more than doubles from approximately 3 cm/s to 7 cm/s, preventing weak oscillation events from being detected. Additionally, even in the eastern Adriatic Sea where meteotsunamis are relatively common, only 17 strong events occurred in a 90 year span. In response to this lack of detected events, it is suggested that five moorings with acoustic Doppler current profilers (ADCPs) and pressure sensors on Penguin Bank and an additional HFDR on Molokaʻi would have a better combination of velocity and time resolution to detect the resonance modes, and observations could then include sea level. The second HFDR would be oriented optimally to view Penguin Bank and would allow reconstruction of full two-dimensional vector currents when combined with radial currents from the existing HFDR instrument. This part ends with conclusions and final thoughts in Chapter 5.

In the second part, I will examine the fronts, frontal instabilities, and cross-front differences in TIVs in the Equatorial Pacific Ocean. An extensive introduction is in Chapter 6, but briefly, TIVs are 500-km diameter anticyclones with Rossby number ~ -1 on the North Equatorial Front that swirl colder, upwelled equatorial waters northward on their western flanks and advect warmer surface water of ITCZ-origin to the south on their eastern flanks. This swirling creates a cusp of colder water that extends northward of the mean meridional position of the North Equatorial Front with two roughly north-south fronts separating water of different temperatures, salinities, and densities: the leading front on the western side of the cusp separates warm, fresh, less-dense water to the west from the cold, salty, more-dense water in the cusp to the east, while the trailing front on the eastern side of the cusp separates cold cusp water to the west from warmer water to the east.

A mesoscale picture of a TIV from satellite sea surface temperature (SST) and sea surface height anomaly (SSHA) data in a frame of reference moving with the vortex in Chapter 7 shows that, while the SSHA field composites nicely into a static image, high variability in the SST fields due to swirling currents as well as missing data due to cloud cover results in significant smearing; individual snapshots represent the temperature field much more accurately and expose the high variability in a single TIV over time and between different TIVs. The evolution of a trailing front shown in three sequential synthetic aperture radar (SAR) images in Chapter 8 shows that the fronts are advected with the TIV while being rotated and deformed by the swirling currents. Additionally, the front in the last of the three images has developed cusps and waves on sub-mesoscales, signs of instability; many other SAR images of both leading and trailing fronts show evidence of instabilities as well. Possible instability mechanisms are explained and examined using ADCP and conductivity-temperature-depth (CTD) data from cruise crossings of TIV fronts and sub-mesoscale model results.

SAR can not only detect fronts themselves due to increased roughness from more frequent wave breaking due to frontal convergence, but different processes and forcings on the two sides of the front may create visible signatures in the images. Differences in back-scatter intensity across a front in SAR images are attributed in Chapter 9 to winds affected by the SST front for the leading front but not necessarily on the trailing front, where back-scatter differences are sometimes opposite from what is anticipated based on SST; in these situations, currents with different magnitudes and directions are capable of producing the observed back-scatter intensity differences. The currents are also shown to be different on the two sides of the front when the surface wave fields are inverted to retrieve surface currents. Conclusions and final thoughts are in Chapter 10.

Part I

Resonance modes of tsunamis and potential meteotsunamis

Chapter 2

Part 1 introduction

Harbors, enclosed inlets, coastal shelves, and other areas defined by bathymetry and coastlines can trap wave energy in patterns of standing waves called resonance modes. The spatial structure and oscillatory periods of these modes are determined by the spatial dimensions and boundaries of the oscillating area; when incoming waves have periods very near the characteristic periods of the resonance modes, the energy is trapped and amplified, where it may linger for hours or days. Resonance modes can be excited by a variety of processes, including tsunamis.

Tsunamis are shallow water waves with very long wavelengths (typically > 200 km) and periods (5 min to 2 h) that are triggered by earthquakes, landslides, and other processes that cause sudden displacement of water in the entire water column; the response to this displacement is to radiate waves in all directions. Tsunamis are shallow water waves even in full ocean depth due to their long wavelengths, and they refract towards the perpendicular of large-scale isobaths, refracting around islands, dispersing or focusing tsunami energy depending on seafloor characteristics, and even diffracting between the islands in an archipelago. All of this makes the resulting wave landscape extremely complex. When tsunami waves shoal, they slow, and wave heights increase dramatically; that, plus the fact that the first wave is not necessarily the largest and that the trough may arrive first can make tsunamis very dangerous to coastal populations.

Tsunamis are not frequent, but they have been studied extensively using sea level observations with tide gauges [e.g., *Allan et al.*, 2012], and satellite altimetry [e.g., *Hamlington et al.*, 2012], sea level modeling [e.g., *Munger and Cheung*, 2008], ocean current observations with acoustic Doppler current profilers (ADCPs) [e.g., *Borrero et al.*, 2013], modeled surface currents [e.g., *Cheung et al.*, 2013], and high-frequency Doppler radio (HFDR) surface currents [e.g., *Dzvonkovskaya et al.*, 2011]. HFDR-derived surface currents were used to observe the 40 to 46 min periodic resonant response of the Kii Channel in Japan [*Hinata et al.*, 2011] following the 2011 Tōhoku tsunami.

The resonant response of the Hawai‘ian Islands following the 2011 Tōhoku tsunami is investigated in Chapter 3 [also published as *Benjamin et al.*, 2016]. HFDR data from an instrument on O‘ahu's south shore were used to map the surface currents from the 2011 Tōhoku tsunami over the 50-m deep submerged Penguin Bank. Past modeling studies had shown that several modes are expressed throughout the island chain but have the strongest expression on Penguin Bank [*Cheung et al.*, 2013; *Munger and Cheung*, 2008], which is thus a probe into tsunami activity in Hawai‘i; however, there had been limited observational data available for validating the model results, particularly the spatial structure of the modes. The first tsunami waves created by a moment-magnitude 9.0 earthquake off the east coast of Japan arrived in Hawai‘i just after 1300 UTC on day 70 of 2011. At that time, strong oscillations with a primary period of ∼43 min appeared on Penguin Bank, most notably on the southern part of the bank's crest. The tsunami-excited resonance modes of Penguin Bank were obtained through empirical orthogonal function (EOF) analysis [Appendix B], and the first two EOFs representing a total of 74% of the variance in the data and 69% in the model agree very well with model simulations in the spatial structure, frequency content, and timeseries data. The first EOF has north-south asymmetry in spatial antinode size and intensity, with a larger, more intense antinode on the south part of the crest oscillating with a clear 43-min period; this is also present in tide gauge and deep-ocean assessment and reporting of tsunamis (DART) buoy sea level records which both have the highest spectral amplitudes at 43 min. The second EOF has two antinodes of equal size and intensity on the north and south parts of the bank with a complex mix of periods between 15 and 30 min. The frequencies of both modes place them as island chain modes rather than local Penguin Bank resonance modes, meaning they could have been excited when tsunami waves encountered other parts of the island chain.

As noted earlier, resonance modes are dependent on local bathymetry and coastlines; one consequence of their dependence on physical features of the location rather than the exciting force is that other processes such as meteotsunamis and infragravity waves can also excite the coastal and shelf resonance modes.

Meteotsunamis are long-period, long-wavelength shallow water ocean waves that are generated by atmospheric pressure anomalies resonantly exciting the ocean surface. Four specific conditions are needed for meteotsunamis to form [Figure 2.1]: 1) a traveling atmospheric pressure disturbance; 2) resonance between the atmospheric pressure disturbance and the ocean surface; 3) shelf amplification; and 4) harbor resonance [*Monserrat et al.*, 2008]. The atmospheric pressure disturbance can be either a single anomaly, such as a front or storm, or a wave, such as a ducted gravity wave or a self-amplifying wave (i.e., wave-CISK, Conditional Instability of the Second Kind, where uplift of moist air by a gravity wave causes amplification). If the atmospheric pressure disturbance moves with the same velocity as shallow water gravity waves, Proudman resonance can transfer energy resonantly to shallow water gravity waves and may amplify the wave amplitude by up to a factor of five [*Šepić et al.*, 2012]; Greenspan resonance can also occur, where the atmospheric pressure disturbance has a velocity close to that of one of the edge wave modes [*Pattiaratchi and Wijeratne*, 2015]. Through these mechanisms, weaker atmospheric pressure disturbances can excite meteotsunamis: a pressure anomaly of 5 hPa moving over the ocean for 10 min can be sufficient [*Pattiaratchi and Wijeratne*, 2015]. As the newly-formed ocean waves move onto a shelf, shoaling and/or shelf resonance may cause amplification. Finally, as the amplified waves reach harbors, resonance may again occur; amplification due to harbor resonance may be extreme, especially for long, narrow harbors that trap energy. For example, a meteotsunami that reached 4.8 m in the back of Nagasaki Bay started as a 3 cm disturbance on the ocean surface [*Monserrat et al.*, 2008].

Meteotsunamis have been observed in numerous seas, lakes, channels, and harbors around the world [*Monserrat et al.*, 2008], mostly with tide gauges. Meteotsunamis on the west coast of Japan have been caused by a combination of gravity waves and wave-CISK [*Tanaka*, 2010]; harbor resonance in this area, particularly in Nagasaki Bay (such as in Figure 2.1), can create extremely high waves. Meteotsunamis have been formed by squall lines [New Jersey 2013, Florida 1992, and Louisiana 2008 by *Lipa et al.*, 2013; *Sallenger et al.*, 1995; *Sheremet et al.*, 2016, respectively], but also by tropical storms [Newfoundland 1999 and 2000, *Mercer et al.*, 2002]. Interestingly, one event in North America was also a reflection event [*Lipa et al.*, 2013], where the atmospheric pressure disturbance moved away from the coast, and the shore-detected event was a reflection from the continental shelf edge. In the Great Lakes, meteotsunamis can be forced by atmospheric pressure disturbances, wind disturbances, or a combination of the two [*Linares et al.*, 2016] and are primarily associated with convective storm systems [*Bechle et al.*, 2016]. Meteotsunamis are less rare in the Adriatic Sea, particularly in the islands off Croatia where there have been 17 strong events between 1926 and 2016 [*Šepić et al.*, 2016]. This is because traveling atmospheric pressure disturbances are frequent over the Adriatic, but also because shallow seas allow Proudman resonance to amplify the resultant ocean disturbances [*Šepić et al.*, 2012]. Meteotsunamis occur in the wider Mediterranean Sea, such as in the Balearic Islands where atmospheric pressure disturbances can create coastal trapped waves that then trigger harbor oscillations [e.g., *Tintoré et al.*, 1988], or in Sicily where atmospheric systems excite resonance between the Sicilian and Tunisian coasts [*Candela et al.*, 1999]. Meteotsunamis in the mouth of a harbor on New Zealand's North Island are linked to the passage of large-scale low pressure systems [*Goring*, 2009]. Meteotsunamis have also been recorded in other areas including the Aegean Sea, the Black Sea, the English Channel, the Baltic Sea, the Yellow Sea, the Pacific Northwest, and on the Argentine Coast [*Monserrat et al.*, 2008]. Most recently, the Hunga Tonga-Hunga Haʻapai volcanic eruption of 15 January 2022 produced meteotsunamis; the shock wave in the atmosphere resulting from the explosion caused sea level oscillations when it reached the Pacific coast of Mexico before the seismically-generated tsunami [*Ortiz-Huerta and Ortiz*, 2022], and it produced multiple pressure wave peaks visible in sea level in the Gulf of Mexico and Caribbean, where the seismic tsunami did not reach [*Ramírez-Herrera et al.*, 2022]

Infragravity waves [Figure 2.2] are surface waves with frequencies between 0.004 Hz and 0.04 Hz, below the frequencies of wind-generated waves [*Bertin et al.*, 2018]. Coastal reflection of infragravity waves can lead to edge waves, and they can excite resonance in harbors [*Okihiro et al.*, 1993]. The likely mechanisms of formation are different for shallow and steeper bottom slopes. For steep slopes, larger waves within a wave group break sooner, so there is a shift in the location of the breakpoint within a wave group that produces a standing wave with longer periods onshore of the breakpoint and a traveling wave offshore of the breakpoint [*de Bakker et al.*, 2016]. For shallow slopes, the larger waves in a wave group move more water, creating a dip in sea level; the opposite is true for the smaller waves. This long-period wave propagates with the group as a bound wave until shoaling, when wave speeds change and the phase shift between the bound wave and wave group changes. This allows energy to be transferred from the wave group to the long-period wave, which is released and follows normal surface gravity wave dispersion [*Bertin et al.*, 2018]. Additionally, the short waves remaining after breaking reorganize themselves into bores, and, because larger bores travel faster, they catch up to smaller, slower bores and merge with them, resulting in increased wave periods and contributing to energy transfer to longer periods [*Bertin et al.*, 2018].

The excitation of resonance modes in the Hawai'ian Islands by processes other than the 2011 Tōhoku tsunami is explored in Chapter 4. Specifically, we seek to determine the frequency and strength of resonance mode excitation, the distribution of triggering processes, and the spatial and time scales involved. The local resonance modes over Penguin Bank are known through data analysis and modeling (Chapter 3), so an examination of the activity of the modes might lead to the detection of possible tsunami, meteotsunami, or infragravity wave events. Surface currents over Penguin Bank during a 29-mo period from the same HFDR used to define the resonance modes were decomposed using the known modes as a basis. An examination of the spectral content of the resulting time series of mode activity identified 76 possible mode excitation events. More detailed analyses of the full spectrum, the raw timeseries of currents, and EOFs for each possible event were inconclusive. None of the 76 possible events consisted of the full suite of expected features (except the 2011 Tōhoku tsunami itself), and two other seismic tsunamis that occurred during the study period passed unnoticed. These two tsunamis were significantly weaker than the 2011 Tōhoku tsunami but were present in DART buoy and tide gauge data, indicating that they were likely below the threshold of detection for the HFDR. In order to obtain the required temporal resolution through data reprocessing, the velocity resolution of the HFDR surface currents more than doubles, preventing weak oscillation events from being detected. This is also a possible explanation for the lack of meteotsunami events detected. To counter this limitation, the placement of five moorings with ADCPs and pressure sensors on Penguin Bank and an additional HFDR on Molokaʻi is suggested as the *in-situ* instruments have a better combination of velocity and time resolution and would allow detection of modes in sea level as well as velocity. The second HFDR would be oriented optimally to view Penguin Bank and would allow reconstruction of full two-dimensional vector currents when combined with radial currents from the existing HFDR instrument. One other possible factor in the lack of meteotsunami events is their infrequency: while they are relatively common in the eastern Adriatic Sea, in terms of actual occurrences there were 17 strong events in a 90 year period [*Šepić et al.*, 2016]. There is no guarantee that any meteotsunamis occurred in the 29-mo study period.

Chapter 5, the last of Part I, contains conclusions and a discussion of the possible implications.

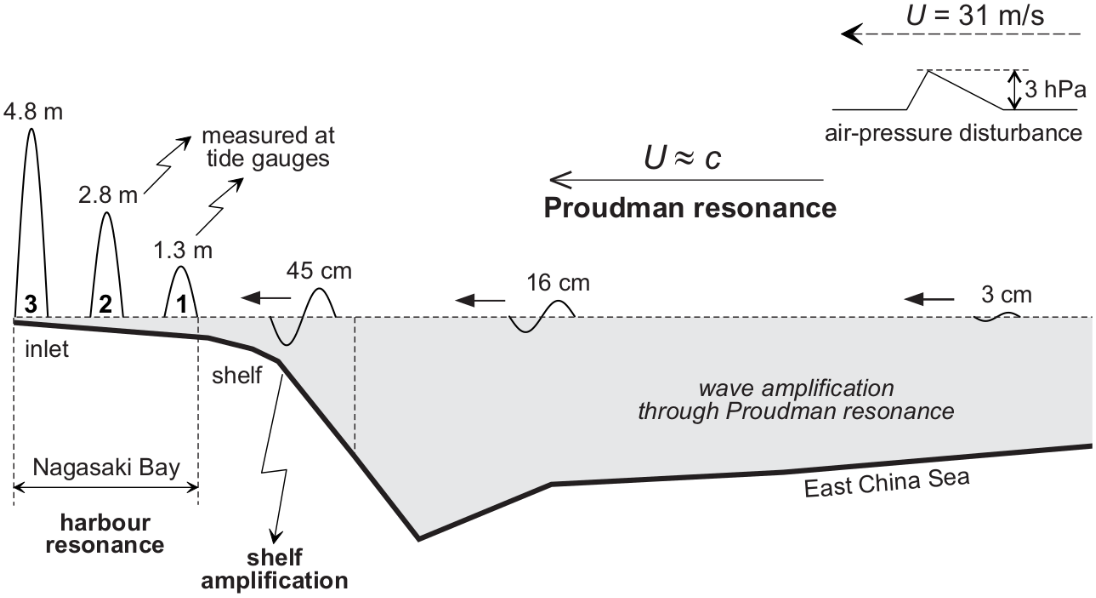

Figure 2.1: Reproduced from *Monserrat et al.* [2008], their figure 4. The process of meteotsunami formation from a 3 hPa air pressure disturbance in the East China Sea to 4.8 m oscillations in Nagasaki Bay, Japan.

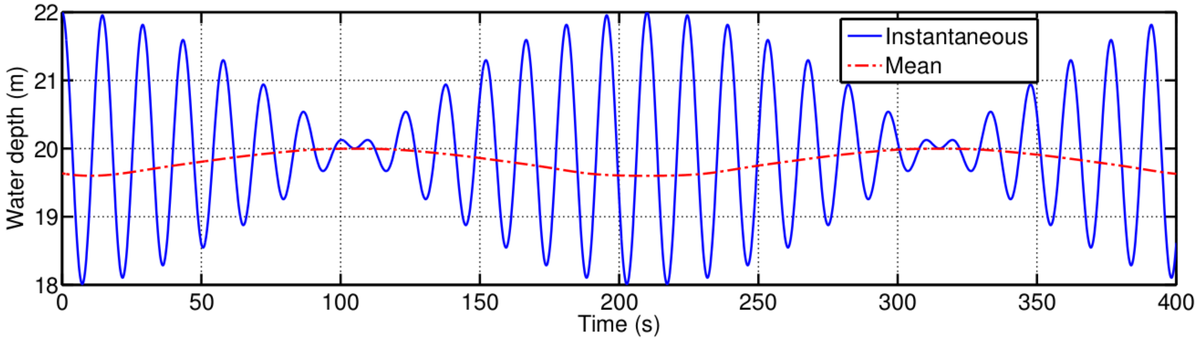

Figure 2.2: Reproduced from *Bertin et al.* [2018], their figure 2b. Infragravity wave formation showing the instantaneous water depth resulting from two wave trains with slightly different frequencies (blue), and the mean water depth resulting from the superposition of the two waves (red).

Chapter 3

The 2011 Tōhoku tsunami south of O‘ahu: High-frequency Doppler radio observations and model simulations of currents

Where it is shown that on a shallow submerged bank linked through bathymetry to the coastlines of an island archipelago, a strong far-field tsunami excites resonance modes in surface currents that are dependent on the local bathymetric and coastal features, which are observed by high-frequency Doppler radio and accurately predicted by a non-hydrostatic wave model.

A modified version of this chapter was published as *Benjamin et al.* [2016].

3.1 Introduction

On day 70 of 2011 at 05:46 UTC, a moment-magnitude 9.0 earthquake struck off the coast of Japan, with an epicenter 140 km east of Sendai and 373 km northeast of Tokyo. The earthquake involved a 200-km long section of the Eurasian plate sliding 60 m along a 10° incline over the subducting Pacific Plate and generated a large tsunami [*Yamazaki et al.*, 2011a]. The sea level measurement nearest to the epicenter, the Deep-ocean Assessment and Reporting of Tsunamis (DART) buoy 21418, recorded a 1.75 m high tsunami wave in 4000 m of water. The near-field tsunami devastated the northeast coast of the island of Honshu, with maximum run-up of 39.7 m near Miyako and inundation greater than 5 km on the Sendai Plain [*Mori et al.*, 2008]. Nearly 16,000 people were killed, and almost 3,000 are still missing [*National Police Agency of Japan*, 2011]. The total damage in Japan is estimated at \$156–\$244 billion [*Mimura et al.*, 2011].

Though not as devastating as the near-field tsunami, the far-field tsunami caused damage around the Pacific, including in Hawai‘i [*Fiedler et al.*, 2014]. In the Kuril Islands, a building was flooded and ice deposited on the beaches [*Kaistrenko et al.*, 2013]. In New Zealand, several harbors and vessels suffered minor damage [*Borrero et al.*, 2013]. In the Galapagos Islands, several buildings and coastal properties were flooded [*Lynett et al.*, 2013]. There was some damage along the West Coast of the United States, particularly to harbors and vessels as even small wave amplitudes can cause swift currents [*Allan et al.*, 2012]. In Hawai‘i, strong currents damaged over 200 small vessels in Keehi Lagoon and some dock facilities; total damage was estimated at \$30 million [*Dunbar et al.*, 2011]. Additionally, King Kamehameha Hotel in Kailua-Kona, Hawai‘i Island, was flooded [*Stanton*, 2011].

Strong currents caused most of the damage in Hawai‘i. Despite the dangers posed by tsunami currents, they have not been studied until recently because the unpredictable generation of tsunamis precludes the timely deployment of current meters. Fortuitous detection of tsunami currents with acoustic Doppler current profilers (ADCPs) allowed point comparison to modeled currents [*Cheung et al.*, 2013; *Yamazaki et al.*, 2012; *Zhou et al.*, 2014], but observations were fairly sparse; 25 point-measurement instruments were used to validate one tsunami model for the whole $\sim$70,000 km^2 area surrounding the main Hawai‘ian Islands [*Cheung et al.*, 2013]. There has been no two-dimensional spatial comparisons of currents near the coast needed to validate model results, important for maritime hazard mapping.

High-frequency Doppler radios (HFDRs) can map surface currents over an area, measuring the surface current radial to the instrument. Theoretical studies of the HFDR backscatter [*Grilli* *et al.*, 2015; *Gurgel et al.*, 2011] and particle velocities [*Lipa et al.*, 2006] have shown its potential for mapping tsunami currents, a concept first proposed by *Barrick* [1979]. The HFDR measurement volumes are small (∼1 km in range, ∼10° in azimuth, ∼1 m in depth) relative to the wavelength of tsunamis so the currents within the volumes are relatively homogeneous.

Wave shoaling increases particle velocity, enabling detection of tsunami currents by HFDRs in shallow areas, which may further exhibit signs of resonance if energy is trapped. The 2011 Tōhoku tsunami was detected by HFDR in Chile [*Dzvonkovskaya et al.*, 2011], multiple locations along the U.S. West Coast and Japan [*Lipa et al.*, 2011, 2012], and in the Kii Channel in Japan [*Hinata et al.*, 2011]. These datasets were either insufficient to study resonance, or no such study was performed despite model evidence for resonance [e.g. *Yamazaki and Cheung*, 2011; *Yamazaki et al.*, 2013].

During the Tōhoku tsunami, an HFDR was operational on O‘ahu’s southeastern shore. Its coverage extended beyond the shallow (50 m) Penguin Bank 20–40 km to the southeast. These observations provided an opportunity to detect currents excited by the tsunami, analyze the patterns of resonance, and compare them with a model hindcast. Uniform incoming wave fronts are not expected because waves are scattered by the Northwest Hawai‘ian Islands [*Yamazaki et al.*, 2012]. Instead, the resonant response and subsequent trapping of tsunami energy are expected to dominate in the Hawai‘ian Islands. Previous models of tsunami responses have shown strong, prolonged, and complex resonant oscillations that depended less on the characteristics of individual tsunamis and more on the natural resonant modes of the region [e.g. *Munger and Cheung*, 2008; *Roeber et al.*, 2010; *Yamazaki and Cheung*, 2011]. Several of the modes described have strong antinodes over Penguin Bank or along O‘ahu’s south shore [*Munger and Cheung*, 2008, Figures 2 and 4]. Because the maximum of spectral amplitude lies over Penguin Bank, it is a place to probe for resonant activity in the islands.

In this paper we provide an inter-comparison of the recorded HFDR currents of the Tōhoku tsunami with the model results of *Cheung et al.* [2013]. The model results, which have been validated by point measurements of surface elevation and current around the Hawai‘ian Islands, exhibit strong resonance oscillations over Penguin Bank. Section 2 describes the data and methodology. Section 3 contains the results and the discussion. Section 4 concludes and makes recommendations for future work.

3.2 Data and methods

The WERA HFDR [*Gurgel et al.*, 1999a,b] at Koko Head (KOK) detected radial currents south of O‘ahu during the 2011 Tōhoku tsunami [Figure 3.1] through the Bragg frequency. The Doppler shift of electromagnetic waves Bragg-scattered by surface waves has two parts: one from the phase speed of the scattering ocean waves, and a second from the surface currents. The 12-element receive array operated at 16.13 MHz with a range of about 100 km and boresight at 221°. Four times hourly, 11.2 min of data with 2048 chirps were gathered. The data was processed by breaking the 2048 chirps into half-overlapping 4.2 min periods of 768 chirps. Radial velocity is the difference between theoretical waves-only and observed waves-plus-currents Bragg frequencies, Δf, times the ocean Bragg wavelength, L (half the radio wavelength). As Δf is limited by the spectral resolution $1/T$ for record length T, the theoretical velocity resolution is L/T, or 0.07 m/s for this HFDR. Radial velocity v_b was actually computed as the weighted mean inferred directly from the backscatter spectra over an interval centered on the maximum amplitude of the Bragg scatter, $v_b =< vP(v) > / < P(v) >$. The velocity therefore appears as a continuous variable, having finer resolution than the theoretical resolution based on record length. The spatial range-resolution was 1.5 km and the beam width was 11°. KOK has 121 angular cells and 54 range cells, with 96% of the data available between 13:00 UTC on day 70 and 01:00 UTC on day 71. Missing data points in space or time were interpolated. A low-pass Hamming finite impulse response (FIR) filter with a 3 dB cutoff at 8 min was applied forward and backward to all HFDR data to reduce noise, while a high-pass Hamming FIR filter with a 3 dB cutoff at 200 min was applied to remove the tides and other lower frequency motions (e.g., near-inertial motions, Kelvin waves).

The Non-hydrostatic Evolution of Ocean Wave (NEOWAVE) model, developed by *Yamazaki et al.* [2009, 2011b], describes the Tōhoku tsunami from its generation at the earthquake source to the coastlines of Hawai‘i. Because the model includes a non-hydrostatic pressure term and a shock-capturing scheme, it can model weakly dispersive waves and flow discontinuities associated with steep slopes, tsunami bores, and hydraulic jumps. The NEOWAVE model results have been validated at basin and coastal scales using DART buoys, tide gauges, bottom-mounted pressure sensors, and ADCPs [*Bai et al.*, 2015; *Cheung et al.*, 2013; *Yamazaki et al.*, 2011a, 2012, 2013]. Modeled, depth-integrated currents for the HFDR coverage areas were taken from *Cheung et al.* [2013]. The model's arrival time as measured by the initial peak was about 6 min early relative to the HFDR, which may be due to variations in water density and the elasticity of the Earth that are not taken into account [*Tsai et al.*, 2013; *Watada*, 2013]. The model data set was shifted 6 min to correct this difference. The modeled data at 1-min, 24-arc second resolution was regridded to match the spatial and temporal sampling of the KOK HFDR, and the velocity vectors from the model were projected onto the radial directions of the HFDR. The same high-pass and low-pass FIR filters were applied to the model currents for consistence in the comparison.

Sea level sampled at 1 min from the Honolulu harbor tide gauge and from the DART buoy 51407, ~225 km southeast of Honolulu [Figure 3.1], were used to identify the tsunami's arrival time and benchmark the NEOWAVE results for comparison. Sea level data were subject to the same FIR filtering schemes.

Fourier transforms were performed using half-overlapping blocks of 200 points (200 minutes) for sea level data and 112 points (230 min) for current data. Blocks were windowed with a tapered cosine function and zero-padded. Power spectral densities (PSDs) were computed as the energy per frequency band over each block time, and then averaged over all blocks. The spectral variances are χ^2-distributed with two degrees of freedom. The blocking and windowing alter the degrees of freedom to ~12 for sea level data and ~10 for current data. The 1-σ error on the power spectra is found from the inverse χ^2 cumulative distribution. Spectral phases were determined by the argument of the original Fourier transform.

Empirical orthogonal function (EOF) analysis was performed over subset areas of the HFDR coverage during the first ~12 hours of the tsunami to find the dominant spatial modes and their temporal series over the entire domain; this procedure and the various motives are defined in Appendix B. Correlations between the time series of EOF modes and raw data were examined for leakage between modes.

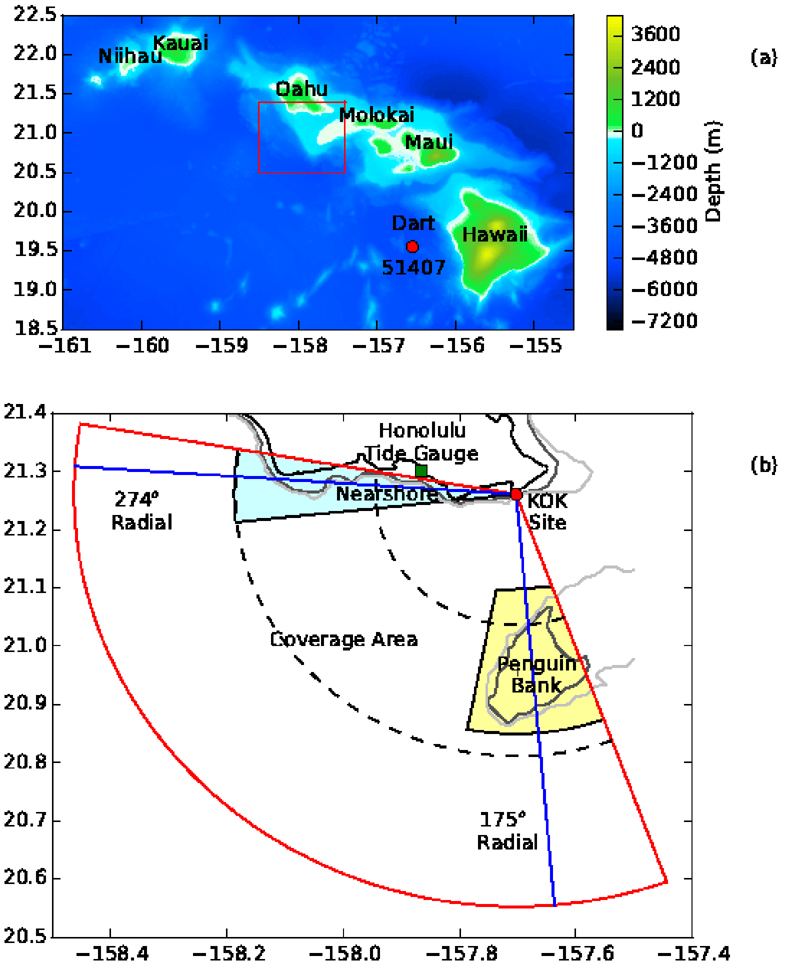

Figure 3.1: Map of the (a) Hawai‘ian Islands showing the location of DART 51407. The area within the red box, inlayed in Figure (1b), is the main study area. Also shown are the areas over which EOFs were computed. Range rings indicate 25, 50, and 75 km.

3.3 Results and discussion

The peak of the initial tsunami wave reached south of Oʻahu at 13:17 UTC on day 70, with near-simultaneous arrivals at the Honolulu tide gauge and the DART [Figure 3.2]. Energetic oscillations are observed in both data sets, although the amplitude at Honolulu is nearly three times that of the DART. The observations and model match well in amplitude, phase, and periods of spectral peaks. The long-period oscillations at Honolulu continue with little damping until 18:00. The smaller, short-period oscillations dampen more quickly. There are few short-period oscillations present in DART data, and the long-period oscillations begin to attenuate around the same time as those at Honolulu. The peak period of the oscillations for both the DART and the tide gauge is 43 min. *Munger and Cheung* [2008] found a strong 43-min mode of oscillation covering the entire archipelago. *Cheung et al.* [2013] numerically showed that the eigenmodes for Honolulu Harbor, a semi-enclosed harbor and the location of the Honolulu tide gauge, are 10.5 and 15 min, similar to the ∼10 and 16 min waves in the tide gauge data. The 27-min mode around Molokai, Lanai, and Maui and their common shelves [*Cheung et al.*, 2013] may also have leaked into Honolulu Harbor, based on the spectral peak at 27 min in the tide gauge data.

The tsunami arrival is marked by energetic oscillations over Penguin Bank [Figure 3.3a, b], where particle velocities are amplified over shallow bathymetry. The HFDR data shows north-south asymmetry of magnitude and duration of the oscillations over the bank: stronger and lasting longer south of the bank than north (-0.16 to 0.15 m/s for 6+ h versus -0.08 to 0.09 m/s lasting ∼2 h). The regularity in the timing of the oscillations in the HFDR data on the southern part of the bank suggests standing waves. Typical filtered currents away from the bank are -0.02 to 0.02 m/s. In the model, the northern and southern flanks of the bank are not separated from one another, the asymmetry in strength being less prominent (-0.22 to 0.26 m/s south, -0.21 to 0.20 m/s north).

The arrival of the tsunami near-shore is marked in the HFDR data by a weak long-period current and in the model by stronger currents in two shallow regions: one near the HFDR site to the east, and one near the western point of the south shore [Figure 3.3c, d]. These anomalous near-shore currents originate in the west and move eastward, with their direction reversing periodically, suggesting excitation of edge waves [*Bricker et al.*, 2007], that are not resolved by the HFDR. At ∼14:00 UTC, interference patterns emerge from the regular progression of edge waves, implying the presence of waves propagating in the opposite direction. The current strength drops at ∼15:30 UTC and vanishes at ∼18:00 UTC in the east, 21:00 UTC in the west.

The radial currents spatially averaged in the north along the 175° HFDR azimuth do not display good agreement [Figure 3.4a]. The modeled currents oscillate until ∼16:15 UTC before decaying. The largest peak in the modeled currents is at 27 min. For the currents averaged in the south [Figure 3.4b], there is good agreement in period and amplitude for the entire interval shown. The peak at 43 min agrees well, but smaller peaks in the model spectrum between 10 and 20 min are absent in the HFDR.

In the 274° near-shore direction, the currents averaged in the west [Figure 3.4d] show some agreement between HFDR observations and model results, but this is a spatial average over traveling features. In the east [Figure 3.4c], there are very different current patterns and no agreement. The spectra for the currents in the west agree only at the dominant 43-min period, while there is no agreement in the east.

Spectral amplitude maps show that Penguin Bank is a location of enhanced activity of periodic currents [Figure 3.5, columns 1, 2]. HFDR spectral amplitudes in the north are weaker than in the south but in the model they have comparable strength. HFDR currents have a nodal line across the bank that is not as distinct as in the model. HFDR spectral phases [Figure 3.5, column 3] are much less coherent than those of the model [Figure 3.5, column 4] and, while the phases are different across the bank, they do not have the same sharp transition across Penguin Bank visible at 17-min and 43-min in the model.

The EOF maps over Penguin Bank for HFDR and model are similar [Figures 3.6a, b and 3.7a, b, c]. The first mode contains 65% and 53% of the HFDR and model variance, respectively, and shows opposing radial currents over Penguin Bank. Their time series show good phase and amplitude agreement, and the peaks at 43-min agree well. The second modes contain 9% and 16% of the HFDR and model variance, respectively, and, while also having opposing currents over the bank, the locations of the maxima are displaced relative to the first modes. The amplitudes and phases of the EOF time series do not agree, nor do the spectral peaks. The third modes contain 5% and 11% of the HFDR and model variance, respectively, and have strong currents over north and south of the bank in the same direction, with a region of opposing current between. The amplitudes and phases in the EOF time series do not match for this mode, nor do the periods of oscillation. The presence of two or more areas of opposing currents over Penguin Bank with distinct periods of oscillation suggests that these EOFs represent standing waves in surface elevation, with nodes and anti-nodes where the EOF maps are extreme and zero, respectively.

The model EOF maps near the shore have small features located along the coast, while the features in the HFDR are larger and extend farther (up to 10 km more) from the coast [Figure 3.6a, b]. There are only weak similarities between HFDR and NEOWAVE modes 3. None of the EOF time series or their spectra show any agreement between model and HFDR [Figure 3.7d, e, f].

Correlation coefficients between the HFDR EOF time series and HFDR observations (or model EOF time series and hindcast) show linkages between near-shore oscillations and Penguin Bank [Figure 3.8]. The first HFDR modes both over Penguin Bank and in the near-shore [top of Figure 3.8a, c] are closely linked and expressed in deep waters, but the higher HFDR EOF modes are not. For the model, the Penguin Bank modes are strongly expressed over the entire coverage area, while the near-shore modes show weaker ties to Penguin Bank [Figure 3.8b, d]. The high correlations for model modes over the whole domain that are not found in the HFDR modes are likely due to the absence of noise in the model. Instrument noise adds a component to the observations that is uncorrelated with the modes, while the absence of noise in the model allows the small oscillations in deep water to have a strong correlation with the EOF modes. The PSD [Figure 3.5] for deeper waters is 2 orders of magnitude smaller than that of Penguin Bank or near shore due to weaker currents there, and the smoothness of the PSD and phase maps of the model relative to the HFDR highlight the absence of noise in the model. A plot of the cumulative percent variance explained versus the number of EOF modes included [Figure 3.9] shows that the initial three EOFs for both model and HFDR explain roughly 80% of the variance, but the model needs ten modes to explain 99.5% of the variance while more than 40 are needed for the HFDR, possibly due to random measurement noise in the HFDR and the low resolution of the HFDR instrument.

Both Penguin Bank and the near-shore region are at the edges of the coverage area for the HFDR, where the azimuthal resolution is the worst. This degradation in resolution is visible in the HFDR near-shore EOF maps [Figure 3.6a], spectral amplitude maps [Figure 3.5, column 1], and regression coefficient maps [Figure 3.8a, c] as angular smearing of currents. The arcing of the maximum of spectral amplitude at 43 min over Penguin Bank towards the near-shore region may be enhanced by azimuthal side lobe contamination or mapping of currents into an angle other than where they occur because of strong side-lobes.

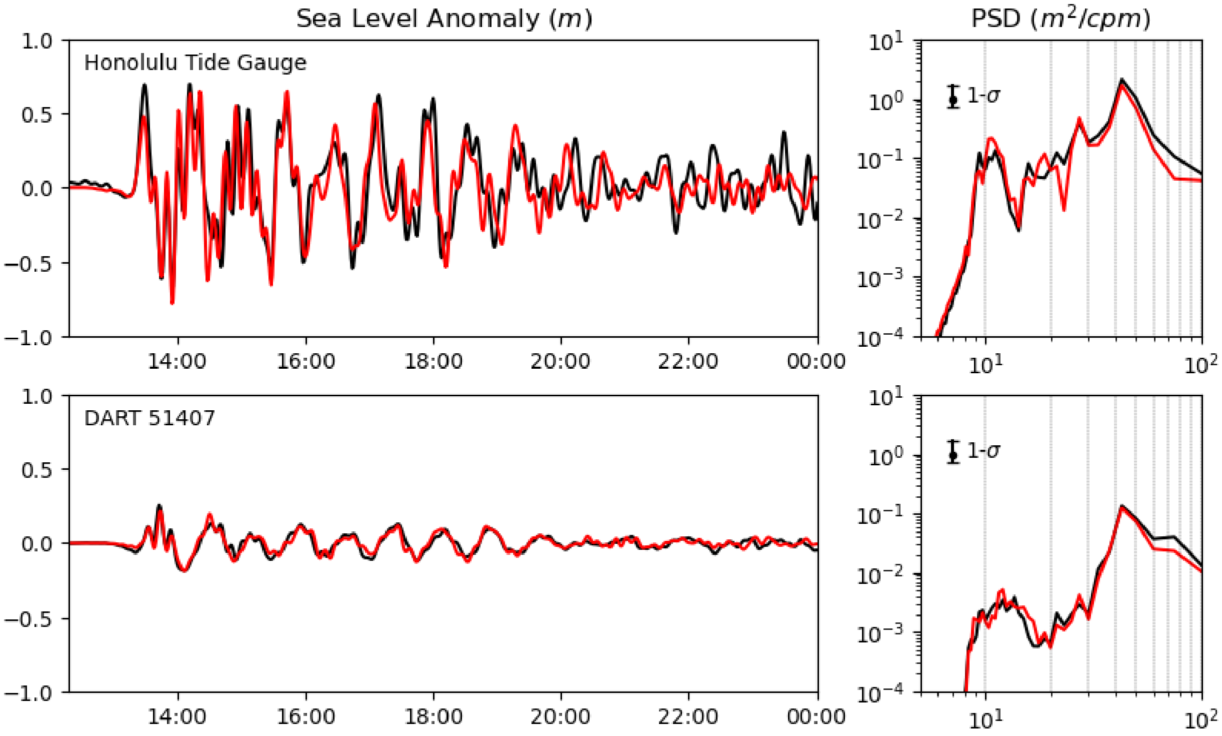

Figure 3.2: (left) Sea level anomalies and (right) PSDs from the (a) Honolulu tide gauge station 1612340 in Honolulu Harbor on O‘ahu, Hawai‘i and (b) DART 51407 west of Hawai‘i Island. The red lines are from the model, and the black lines are from observations.

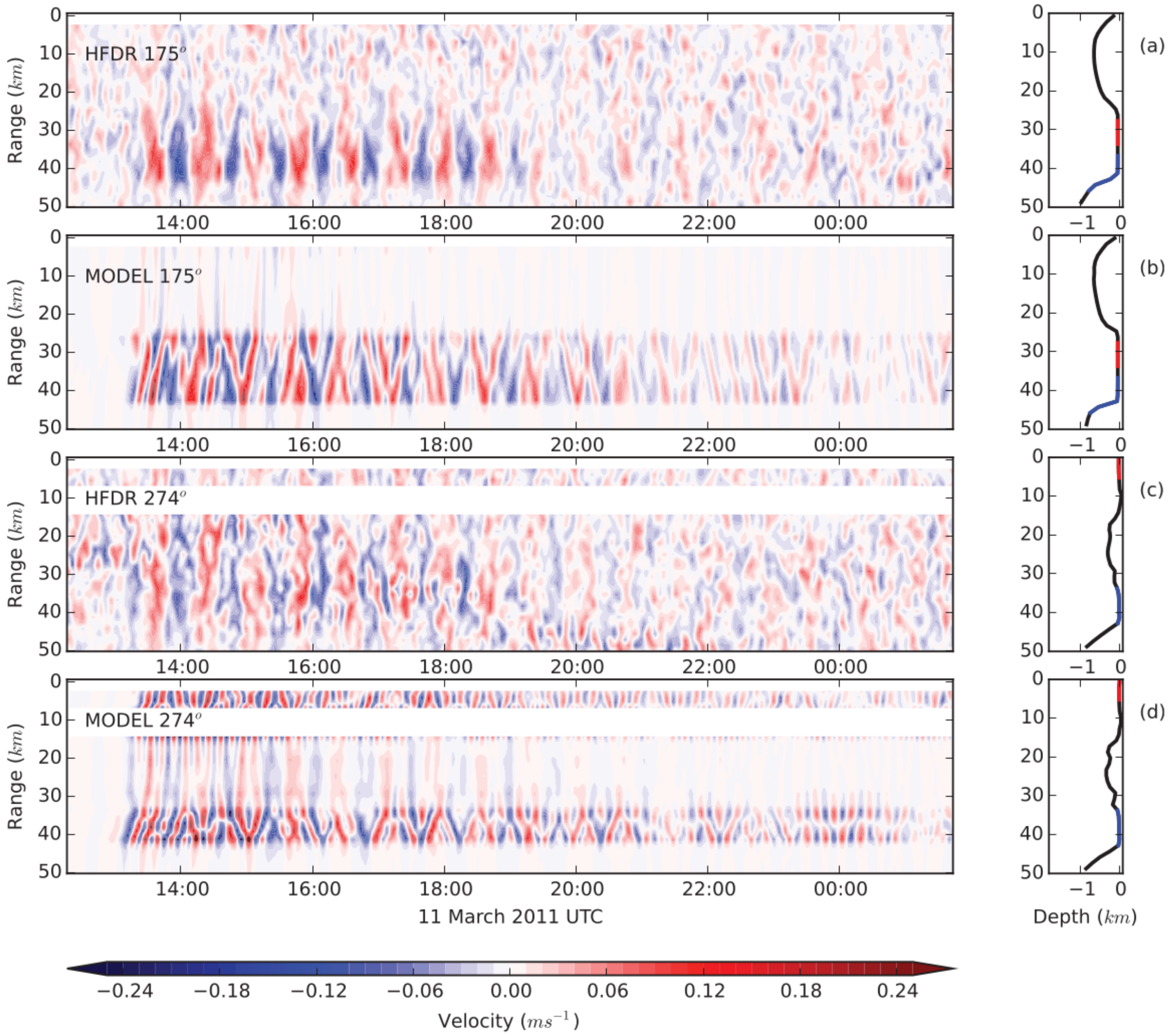

Figure 3.3: Filtered radial current velocity with distance from site as ordinate and time as abscissa: (a, b) for the 175° azimuth, which crosses Penguin Bank, south of Oʻahu and west of Molokaʻi in Hawaiʻi; (c, d) for the 274° azimuth, near the south shore of Oʻahu, Hawaiʻi. The corresponding bathymetry is shown in the right. The boundary between the north and south Penguin Bank areas (red and blue in the bathymetry, respectively) is about 30 km from the HFDR. East nearshore and west nearshore are shown in red and blue in the bathymetry.

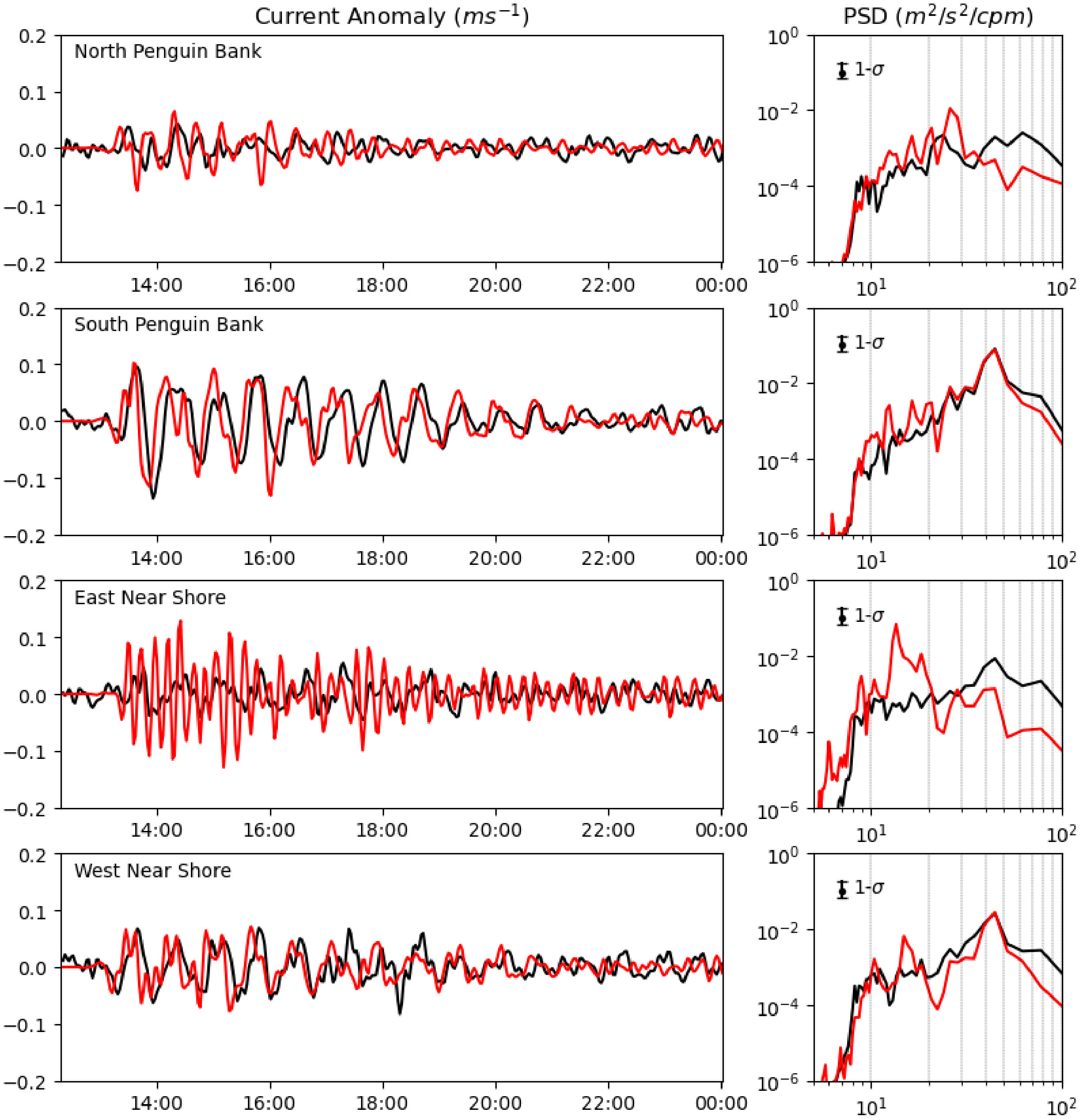

Figure 3.4: Radial velocity averaged along 175° azimuth relative to the KOK HFDR on the south shore of Oʻahu, Hawaiʻi, over the (a) north Penguin Bank and (b) south Penguin Bank areas, both south of Oʻahu and west of Molokaiʻi islands, as well as along the 274° azimuth over the (c) east near-shore and the (d) west near-shore areas of Oʻahu. KOK HFDR data is in black and NEOWAVE model data are in red. PSDs are shown to the right.

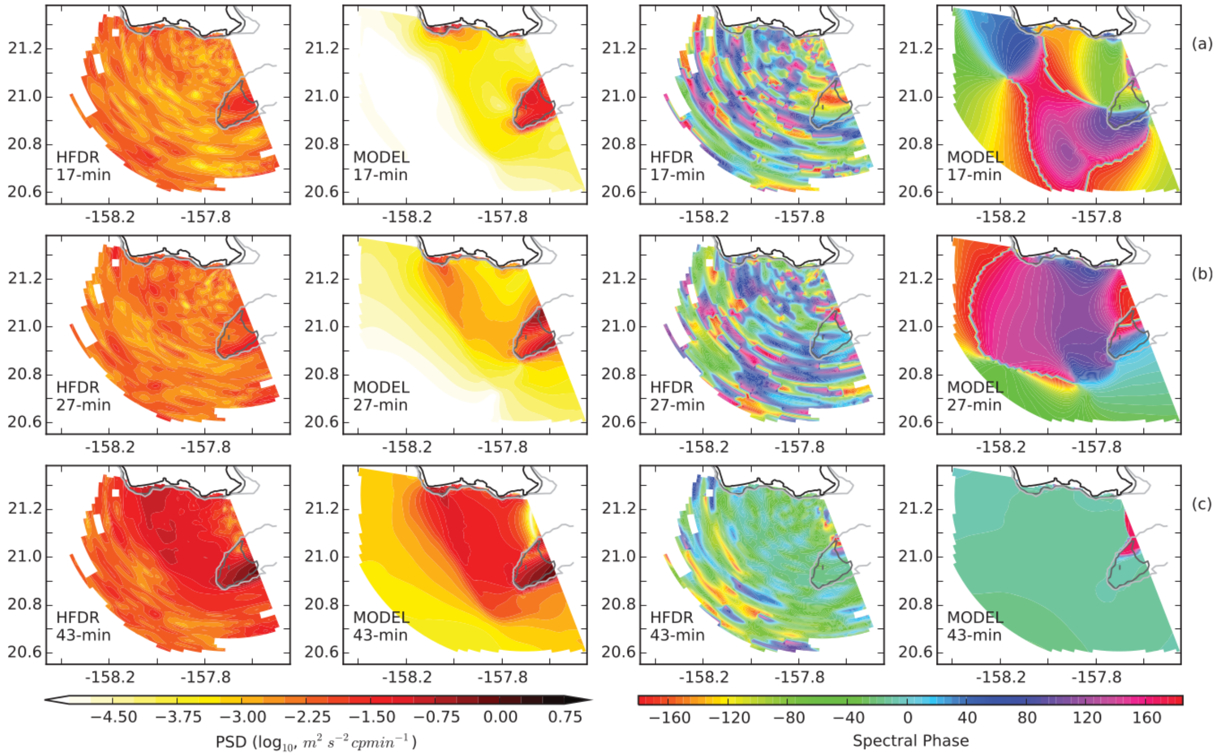

Figure 3.5: (first and second column) Power spectral density and (third and fourth column) phase for HFDR and model at (a) 17, (b) 27, and (c) 43 min periods south of Oʻahu, Hawaiʻi. PSDs are scaled logarithmically and spectral phases are referenced to the first tsunami wave.

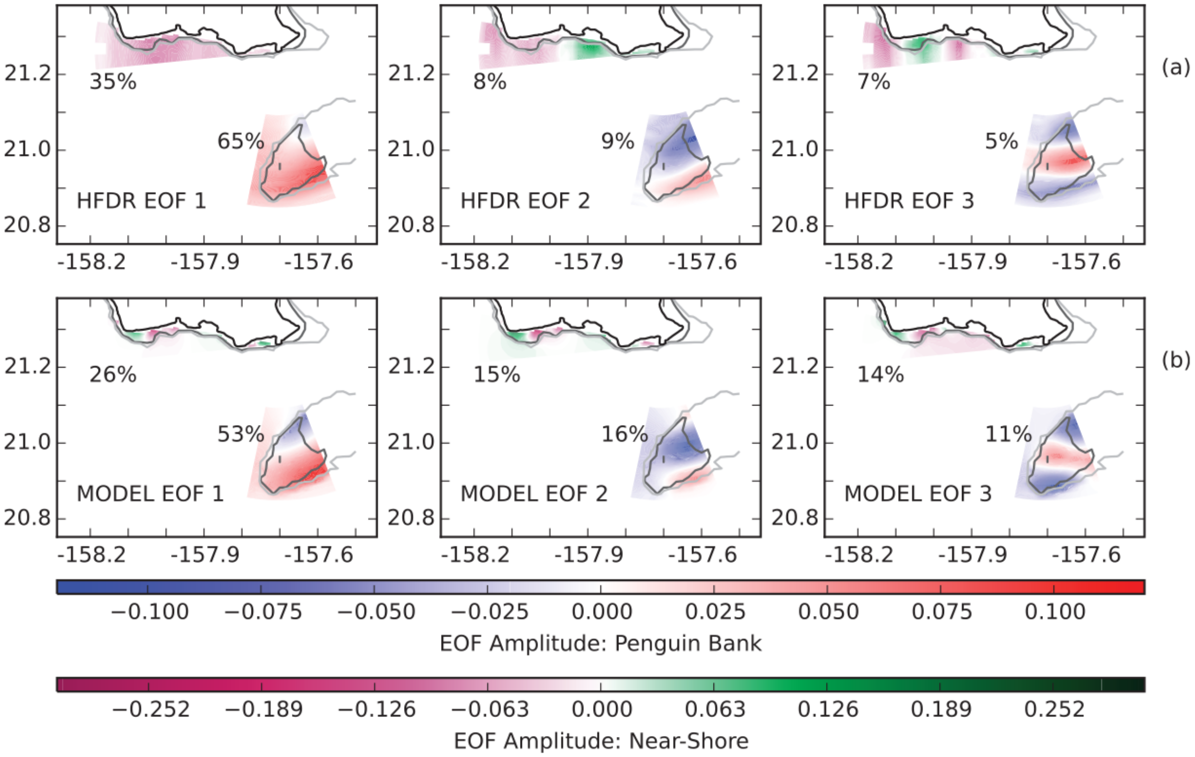

Figure 3.6: The first three EOF maps for (a) HFDR and (b) model data for the Penguin Bank area (608 grid points) south of O‘ahu, Hawai‘i, and the nearshore area (595 grid points) on the south shore of O‘ahu, with the percent variance for each mode. The EOFs are orthonormal and have not been scaled to reflect the number of grid points.

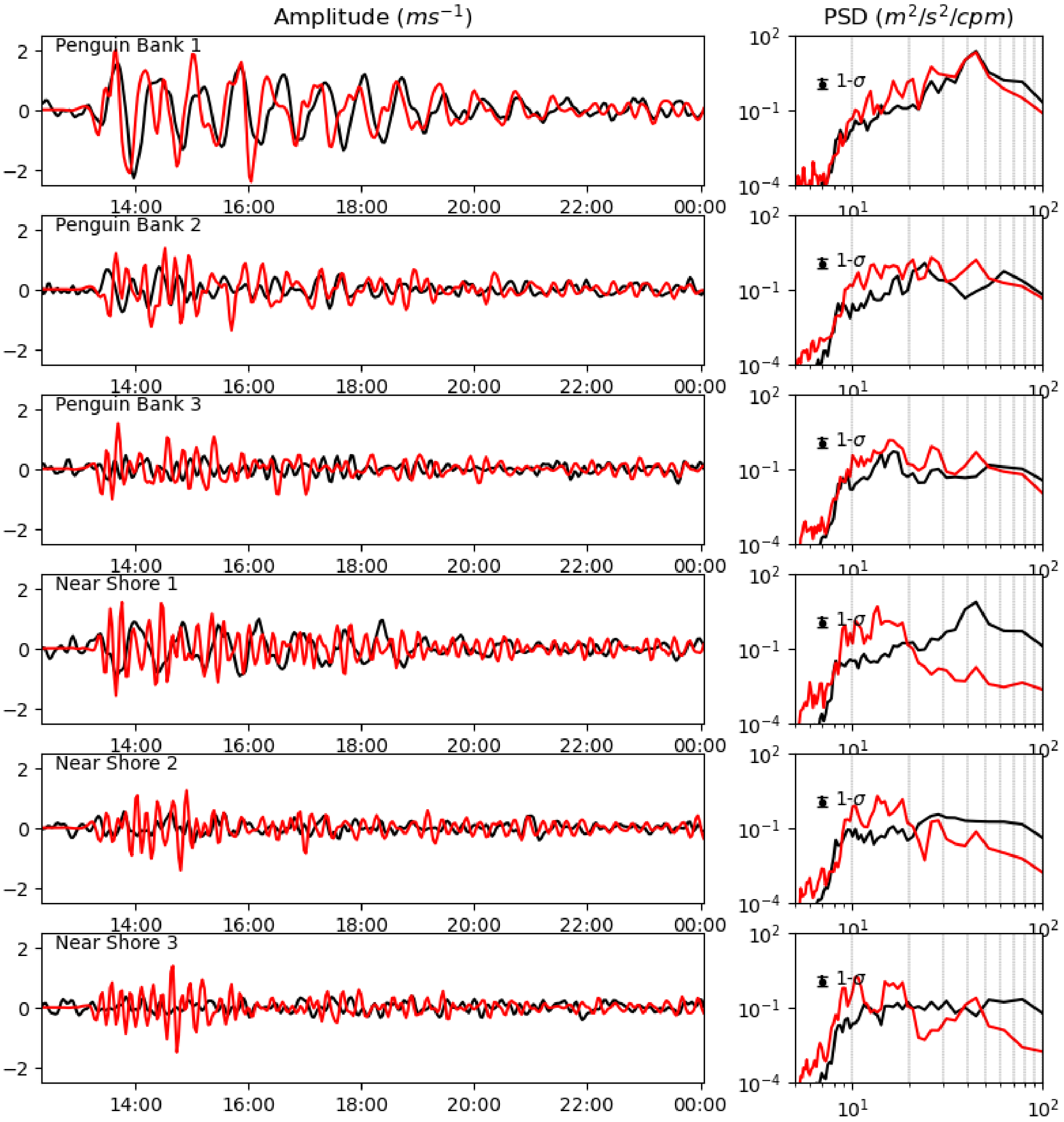

Figure 3.7: Time series (matrix $F = V^TD$, see Appendix B) for the first three EOF modes for (a–c) Penguin Bank, south of Oʻahu, Hawaiʻi, and (d–f) nearshore, on the south shore of Oʻahu. HFDR is denoted in black and the model is in red. Spectra are at right.

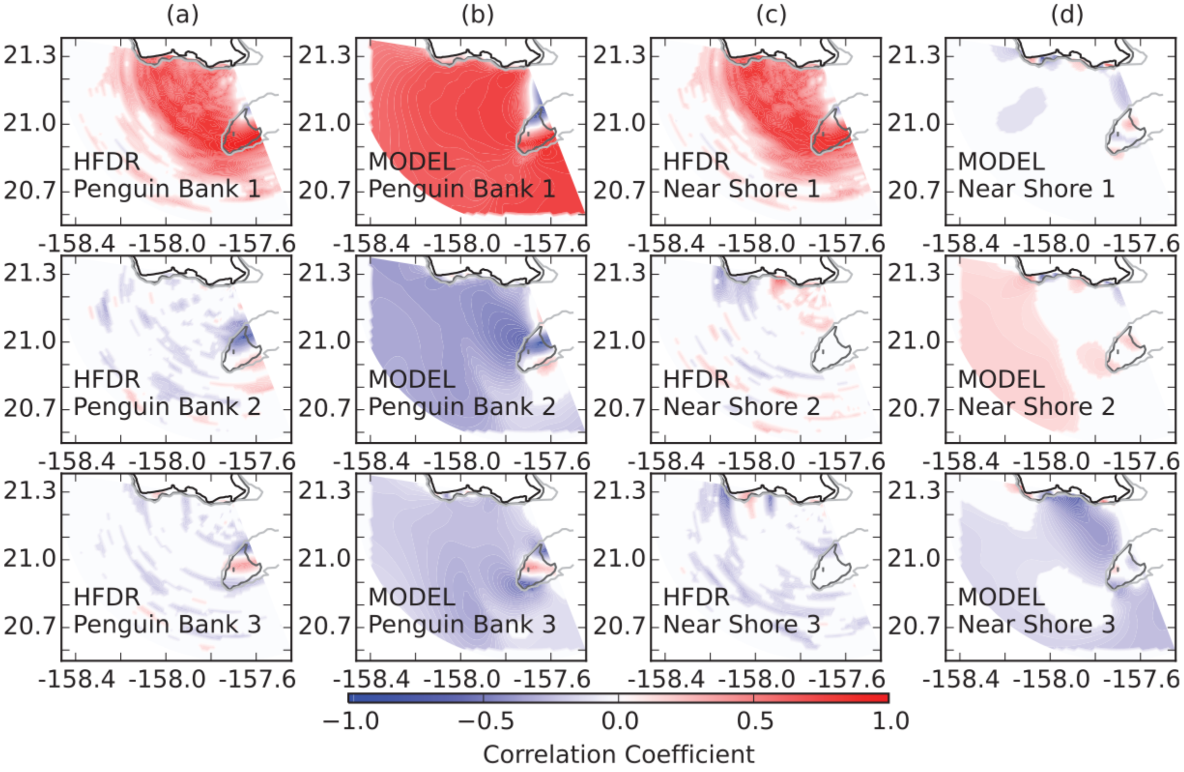

Figure 3.8: (a, b) (a, b) Correlation between the time series of EOFs (matrix $F = V^T D$, see Appendix B) computed over the Penguin Bank subset area, south of O‘ahu, Hawai‘i, and the data over the entire domain; (c, d) same, for EOFs computed over the nearshore subset area, on the south shore of O‘ahu, Hawai‘i.

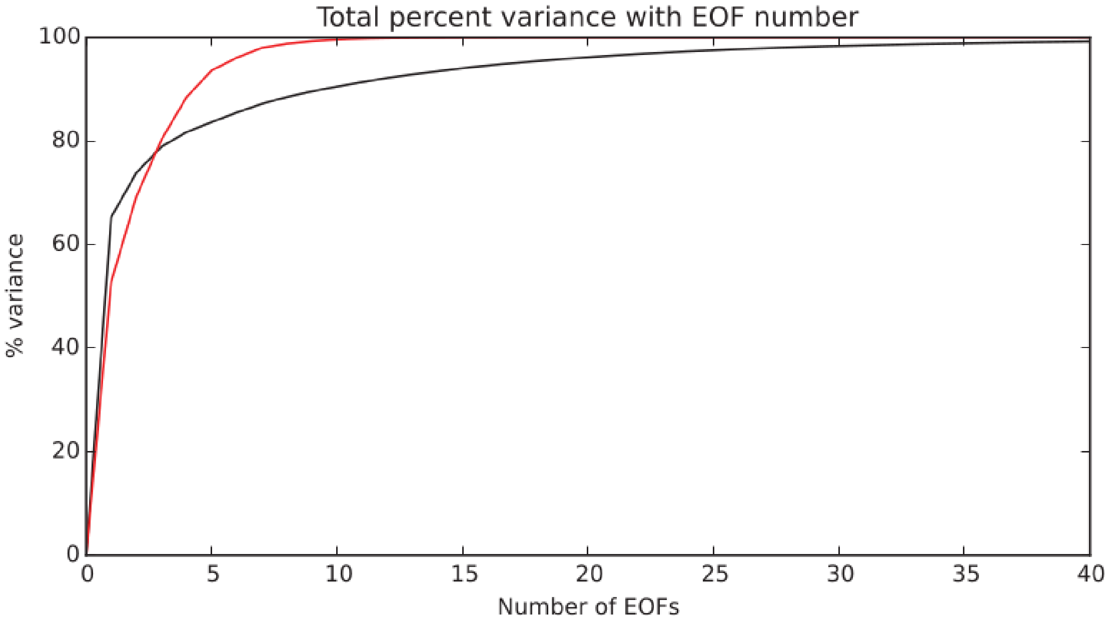

Figure 3.9: Total percent variance with number of EOFs. Model is denoted in red, and HFDR is denoted in black.

3.4 Conclusions and recommendations

The HFDR currents over Penguin Bank indicated that standing waves formed, including 43-min oscillations coincident with those in the near-shore HFDR data, the Honolulu tide gauge data, and DART 51407 data. The strongest component of currents in the HFDR and model matched well over Penguin Bank, and the major spectral and EOF modes showed good spatial agreement. Near shore, a long-period, widespread oscillation was seen in both HFDR and model, but evidence for edge waves in the model was lacking in the HFDR. Disagreements between HFDR and the model primarily occurred where there was high spatial uncertainty due to either decreased angular resolution at high HFDR beam steering angles or azimuthal side lobe contamination, or when the current magnitudes were too weak at small scales combined with the low resolution of the HFDR.

The EOF modal decomposition over Penguin Bank, which acts as a "probe" for resonance around the Hawai'ian Islands, suggests a new method for now-casting the resonance amplitude of tsunamis. By projecting the high-passed real-time data from two or more HFDRs, preferably placed to minimize the dilution of precision over Penguin Bank (i.e., on the SE shore of Oahu and on the west shore of Molokai), into the predetermined EOF eigenvector base, a real-time index of tsunami current amplitude could be implemented. This index would not only yield a better monitoring of the risks of tsunami currents around the islands, but also allow the possible detection of resonance excited by processes other than earthquake waves, such as "meteo-tsunamis" excited by rapid meteorological phenomena [see *Lipa et al.*, 2013].

Chapter 4

Can high-frequency Doppler radio detect resonance excitation in Hawai‘i?

Where it is shown that on a shallow submerged bank linked through bathymetry to the coastline of an island archipelago, weaker far-field tsunamis and meteotsunamis do not necessarily excite resonance modes in surface currents that can be observed by high-frequency Doppler radio.

4.1 Introduction

Local coastlines and bathymetry determine the spatial structure and resonant periods of modes of oscillation. The modes around the Hawai‘ian Islands are known from observations and modeling [Chapter 3, *Benjamin et al.*, 2016], and there is a 29-mo period when data from the same instrument used to make those initial observations is available. The modes and additional data are used to determine if other processes may have excited the modes, specifically:

1. Tsunamis, which are long-period, long-wavelength shallow water waves most often triggered by seismic activity;
2. Meteotsunamis, which are long-period, long-wavelength waves caused by atmosphere-ocean resonance and amplified by oceanic resonance mechanisms; and

3. Infragravity waves, which are surface waves with periods between about 25 s and 5 min.

We seek to determine the frequency and strength of resonance mode excitation, the distribution of triggering processes, and the spatial and time scales involved.

We start with the assumption that tsunamis, meteotsunamis, and high-energy infragravity wave events all occur in Hawaiʻi, which is reasonable. There is a long history of tsunamis in the Hawaiʻian Islands. All elements required for meteotsunami formation occur in Hawaiʻi; there are atmospheric waves, fronts, and disturbances that pass over. While Proudman resonance is unlikely to occur because the islands have relatively small shelves that quickly plunge to depths of more than 1000 m, Greenspan resonance may occur in Hawaiʻi. Approximate coastal slopes vary both per island and per coast of each island, but, with the exception of the very steep south shore of Hawaiʻi and west coast of Lānaʻi, the shelf slopes in the islands range between 0.01 and 0.045 [Table 4.1]. Edge wave dispersion is given by

$$\omega^2 = gk \sin{(2n+1)\beta} \tag{4.1}$$

where ω is the angular frequency, g is the gravitational constant, k is the wavenumber, n is the mode number, and β is the shelf slope. From this, the edge wave phase velocity is

$$c = gT \sin{(2n+1)\beta/2\pi} \tag{4.2}$$

where c is the phase speed and T is the wave period in seconds. For the first three modes,

$$0.016T \leq c \leq 0.35T \tag{4.3}$$

so that for the range of periods expected over Penguin Bank (16 min to 45 min), the phase speed of edge waves would range from 15 m/s to 940 m/s. Obviously the larger phase speeds calculated with large mode number and longer periods would not occur, but even for the zero-mode Stokes edge wave, $c = 42$ m/s, which can be large for a coastal shelf as it is equivalent to the shallow water wave speed at 180 m depth. We would only expect the gravest mode of edge waves for larger periods, while perhaps only the first two modes for the smaller period waves. Atmospheric pressure disturbances like gravity waves or pressure jumps can have wave speeds in this range, and could thus excite these edge waves. Additionally, tsunamis are linked to edge waves in Hawaiʻi as at least one past tsunami excited them [*Bricker et al.*, 2007], plus coastal trapped waves and especially island trapped waves are a feature of the local coastal waters. Finally, amplification and resonance have been shown to occur on a variety of time and space scales [e.g., *Benjamin et al.*, 2016; *Cheung et al.*, 2013]. Regarding infragravity waves, harbor resonance in Haleʻiwa Harbor has been triggered by infragravity waves before [*Okihiro et al.*, 1993], and multi-scale resonance, where resonance modes include a variety of scales, are common in the Hawaiʻian Islands [*Cheung et al.*, 2013].

In section 2, the data and analysis methods are detailed. Section 3 presents results from the analysis, followed by a discussion in section 4. Section 5 contains a summary and conclusions.

Table 4.1: Shelf slopes for different coasts of the Hawai‘ian Islands.

Island	North	East	South	West
O‘ahu	0.028	0.030	0.018	0.042
Kaua‘i	0.028	0.032	0.034	0.013
Moloka‘i	0.037	0.036	0.015	0.020
Lāna‘i	0.018	0.018	0.045	0.096
Maui	0.034	0.041	0.037	0.014
Hawai‘i	0.020	0.024	0.300	0.016

4.2 Data and methods

The Koko Head (KOK) high-frequency Doppler radio (HFDR) mapped surface currents south of Oʻahu [Figure 4.1] with an operating frequency of 16.03 MHz, a range resolution of 1.5 km, and a beamwidth of 11°; it collected data every 15 min from July 2009 to December 2011. Data were reprocessed from the original 11.2 min temporal resolution to 4.2 min resolution, causing velocity resolution to change from 3 cm/s to about 7 cm/s. Penguin Bank, a 50-m deep submerged bank extending west from Molokaʻi that features particularly strong oscillations with the island chain resonance modes excited by tsunamis [*Benjamin et al.*, 2016; *Cheung et al.*, 2013; *Munger and Cheung*, 2008], protrudes into the coverage area between 20 and 40 km from the instrument at the far east end of the azimuthal range.

The KOK HFDR was used to detect the 2011 Tōhoku tsunami in Chapter 3 and *Benjamin et al.* [2016], and the data here were reprocessed in an identical manner. By using the same instrument and processing scheme, we hope to capitalize on that previous work to move forward without needing to reinterpret the Penguin Bank modes with the model as the modes have already been identified. However, because the temporal resolution of the HFDR data is now only 4.2 min and infragravity waves have periods between about 25 s and 5 min, they would not directly excite resonance modes visible in this data. While it is possible that infragravity wave energy can contribute to the excitation of resonance modes with periods long enough to be detected by HFDR, the amount of energy involved would be small and will thus not be considered further. Now that we have the data prepared and know the resonance mode structure, how do we filter the data spatially?

The data must be filtered spatially to isolate the known resonance mode structure in the data. Empirical orthogonal function (EOF) analysis is an excellent tool for looking at standing patterns of oscillations as well as for reducing the noise in a data set by reconstructing the data using only a few modes, so we utilize them here. EOF analysis empirically derives orthonormal modes containing the most variance in the fewest modes. They are dependent on the data used to form them, making the selection of input data important. However, modes formed in one space and time can be expanded to other spaces and times: decomposing data using EOF spatial modes from the same space but different times will yield a time series showing the activity of that mode, while correlating the time series of an EOF mode with the time series of data at the same time but different locations can yield a map showing activity associated with that same mode.

EOF analysis was chosen to investigate the questions posed here because the currents of interest have standing spatial patterns of resonance over defined areas at times defined by the forcings; the dependency of the modes of EOF analysis on the choice of space and time domains is actually used as a method of isolating a process or response. While we are using the fact that EOFs are sensitive to time and space domains of choice to assist in filtering for the resonance mode structure we wish to study, we still must ensure that the decomposition method is not so sensitive that a small change in mode structure would produce completely different results. Several tests were run by altering the 2011 Tōhoku modes, computing the new mode indices and their spectra, and comparing those with the originals during the 2011 Tōhoku tsunami [Appendix C for details]. Overall, the sensitivity tests show that the modes are fairly stable for small amplitude and location shifts, though M2 does have a tendency to show larger 42-min spectral peaks in several types of alterations. However, as the 42-min peak is not a period of interest for M2, this does not affect the results.

Previous tsunami modeling studies [*Munger and Cheung*, 2008; *Roeber et al.*, 2010] have shown that the resonance modes excited by a tsunami depend on the location and not on the source tsunami, so decomposing HFDR data using EOF modes obtained from a tsunami should act as a filter to isolate similar motions. The EOF modes over Penguin Bank during the 2011 Tōhoku tsunami [*Benjamin et al.*, 2016] were used as an orthonormal basis for decomposing the 29 mo of KOK data. The first mode, hereafter M1, which explained 60% of the variance during the tsunami, exhibited strong, regular oscillatory behavior [*Benjamin et al.*, 2016], while the second mode (M2) was weaker [Figure 4.2]. The decomposition produced a timeseries of amplitudes similar to an EOF timeseries, with a data point every 4.2 min over 29 mo. This timeseries must then be analyzed to isolate possible resonance mode excitation, and doing so in spectral space was appropriate because the resonance periods of M1 and M2 are known: 40 to 45 min for M1 and 16 to 17 min, 21 to 23 min, and 26 to 27 min for M2.

The timeseries of mode activity was converted to spectral space with half-overlapping segments of approximately 12 h in length [Figure 4.3], and times where one or both mode indices peaked (above 0.5 m^2/s^2/cpm for M1 and 0.15 m^2/s^2/cpm for M2) were selected as possible times of interest; for comparison, the mode indices for the 2011 Tōhoku tsunami had amplitudes of about 30 m^2/s^2/cpm and 1 m^2/s^2/cpm for modes one and two, respectively. Examination of mode indices and spectral amplitudes at selected frequencies yielded 76 times of interest: six solely from M1, 12 solely from M2, and 58 from both modes together [Figure 4.3]. Other spectral analysis methods such as wavelet analysis are essentially short Fourier Transforms with Gaussian windows; resonance mode excitations are sinusoidal oscillations, but because the oscillations sought would cover several hours at least, there would be higher amplitudes in spectrograms regardless of whether those oscillations cover the entire 12 h of the sample time. In order to examine this many events in a consistent manner to determine whether they might be genuine resonance mode excitations, each event underwent three examinations: one of the spectra for the mode indices, one of the velocity timeseries, and one of the EOFs made with the raw velocity data. Characteristics of each event were determined by these examinations explained below and compared to the 2011 Tōhoku tsunami.

While events were selected based on spectral amplitude at specific frequencies or the band spectral amplitudes, this was done looking at a timeseries of the amplitude at those frequencies rather than by examining the spectrum at all frequencies for each time. Because of this, the event selection methodology allowed the inclusion of times when spectral amplitudes were high at all frequencies, not just those linked with resonance mode excitation. M1 and M2 line spectrograms (plots where at each timestep the spectral amplitudes of the spectrogram are plotted on the same plot) [Figure 4.4] for each event can thus be divided broadly into those with peaks at frequencies of interest (type S1) and those with high amplitude at many frequencies (type S4). We also consider those with peaks at only some of the frequencies of interest (type S2) as well as those with peaks at frequencies other than those of interest (rather than just high amplitude at many frequencies; type S3). Types S1 and S2 are of primary interest, while the 31 events of either types S3 and S4 will not be considered further.

When examining the timeseries of each event we use the radial velocity timeseries of the original data rather than the mode index timeseries, which is the projection of the event onto the modes. Range-time (at 162°) and angle-time (at 38 km range) plots [Figure 4.5] are used to sort events into three categories: those with strong oscillations within an envelope (type T1); those with one or more spikes (type T2), and those that cannot be distinguished from the background (type T3). Events of type T1 are the most tsunami-like, but type T2 events can also be related to tsunamis; the four events with type T3 timeseries will not be considered further.

The third examination was done on the EOFs of the original velocity data. While mode indices can show the projection of the data onto the tsunami modes, the EOF of an event would show the modes that best describe that event, which may be very different from the projection onto the tsunami modes. There were six categories of EOF maps found [Figure 4.6]: one that is strongest in the east and spreads organically to the west while weakening and has north-south oscillations (type E1); one that has a north-south spread of amplitude and east-west oscillations (type E2); one that has coherent antinodes but lacks the orientation of either types E1 or E2 (type E3); one that has east-west oscillations similar to type E2 but whose expression is crowded on the eastern edge of the mode (type E4); one that has coherent but artificial arcs of amplitude with constant range (type E5); and one that has coherent, small-scale, artificial random patches of amplitude (type E6). Types E5 and E6 are due to noise and interference. Type E4 may be due to beamforming issues, but it can also be real. Types E1 to E4 will be considered further, while two E5 and eight E6 events will not.

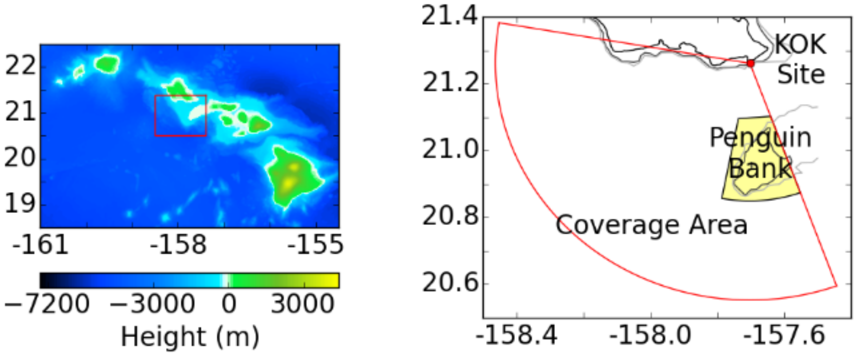

Figure 4.1: Hawai‘ian Islands and bathymetry (left), and study side (right) showing Penguin Bank area (yellow), Koko Head radar site (red dot), and coverage area (red wedge).

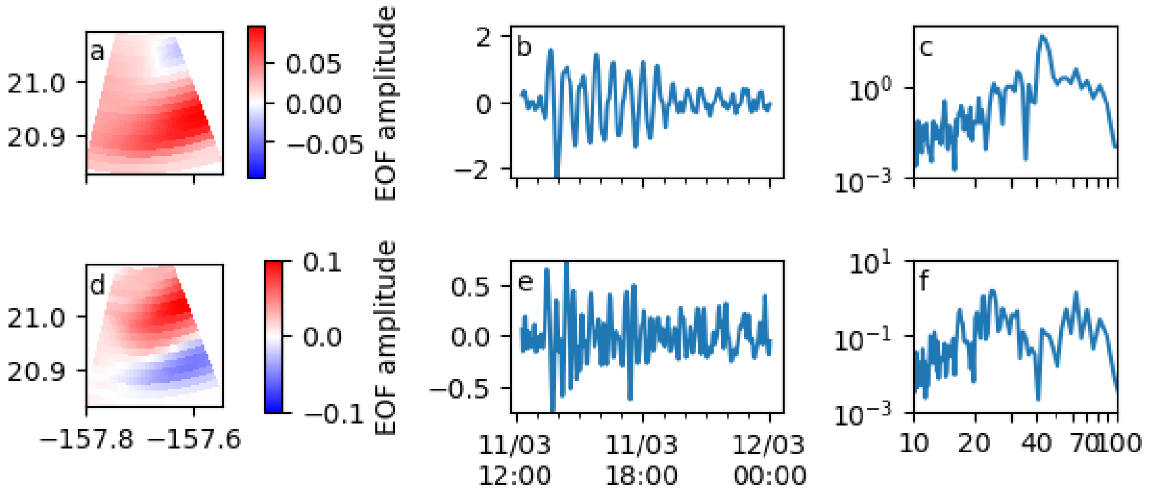

Figure 4.2: Mode 1 (top) and mode 2 (bottom) of 2011 Tōhoku tsunami with Koko Head HFDR over Penguin Bank, south of Oʻahu and west of Molokaʻi in the Hawaiʻian Islands, showing EOF modes (left), associated timeseries (middle), and spectra of the modes (right) with periods in minutes. Multiplying EOF modes by their associated timeseries gives currents in m/s, and the spectra are in $\mathrm{m}^2/\mathrm{s}^2/\mathrm{cpm}$.

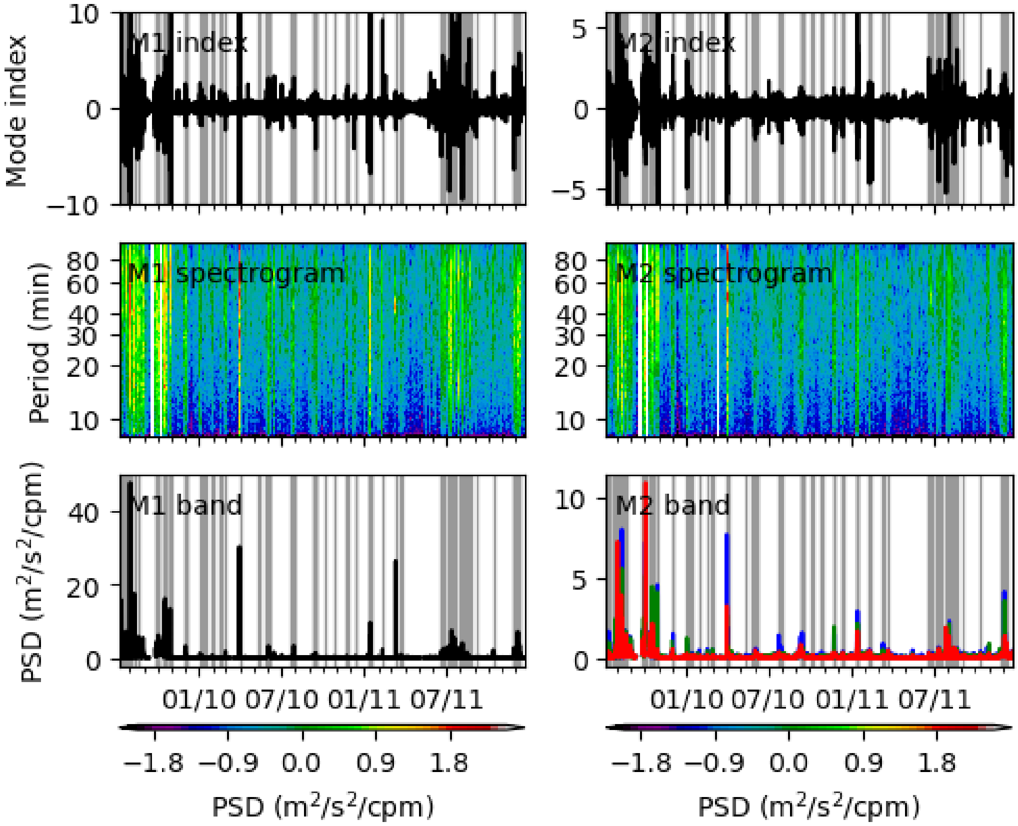

Figure 4.3: (left) Mode one and (right) mode 2 (top row) index, (second row) log10 spectrogram, and (bottom row) spectral amplitude for 43 min for mode 1 and 24 to 26 min, 21 to 22 min, and 16 to 17 min (blue, green, and red, respectively) for mode 2 from decomposition of HFDR data over Penguin Bank, south of O‘ahu, Hawai‘i, using the first two EOF maps generated using the same instrument during the 2011 Tōhoku tsunami. Possible events are highlighted in dark shading in the top and bottom panels.

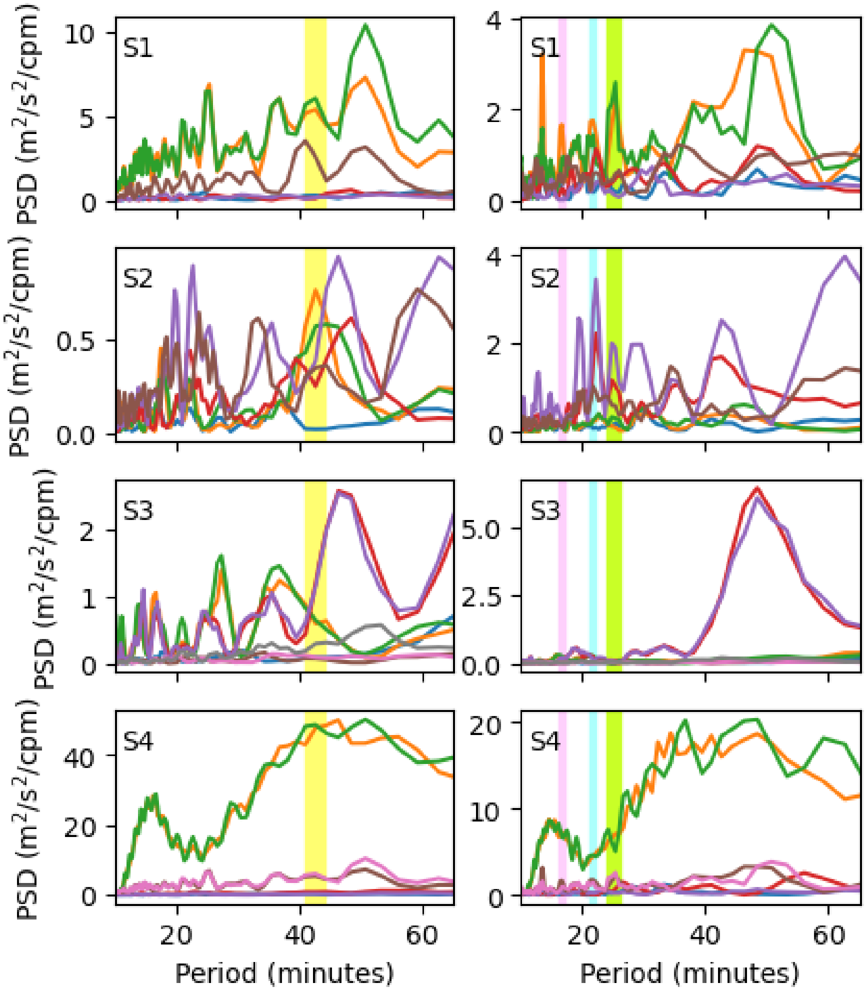

Figure 4.4: (left) M1 and (right) M2 line spectrograms for time periods around and during events showing the four types of spectra from events 7, 44, 58, and 6. These types are: (S1) with peaks at frequencies of interest; (S2) with peaks at only some of the frequencies of interest; (S3) with peaks at frequencies other than those of interest; and (S4) high amplitudes at many frequencies.

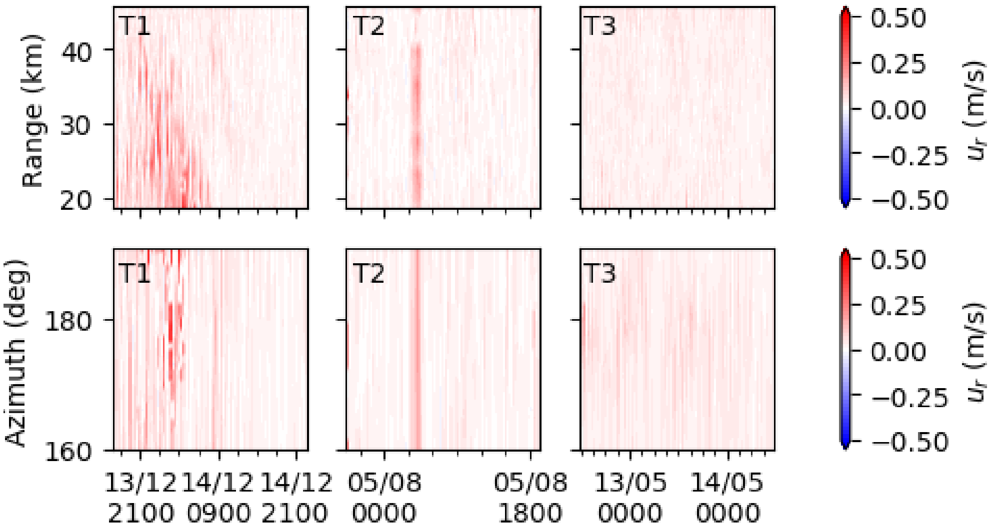

Figure 4.5: Radial velocity timeseries plots in (top) range and (bottom) azimuth for different types T1, T2, and T3 from events (from left) 47, 64, and 29. These types are: (T1) those with strong oscillations within an envelope; (T2) those with one or more spikes; and (T3) those that cannot be distinguished from the background.

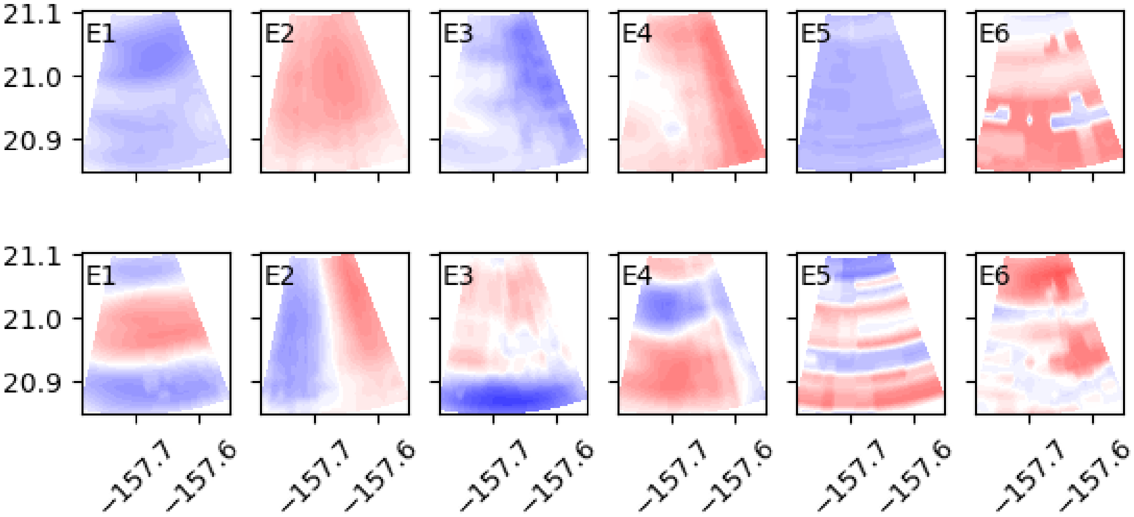

Figure 4.6: (top) EOF 1 and (bottom) EOF 2 maps over Penguin Bank showing the six different types from events (from left) 42, 8, 38, 37, 6, and 2. These types are: (E1) is strongest in the east and spreads organically to the west while weakening and has north-south oscillations; (E2) has a north-south spread of amplitude and east-west oscillations; (E3) has coherent antinodes but lacks the orientation of either types E1 or E2; (E4) one that has east-west oscillations similar to type E2 but whose expression is crowded on the eastern edge of the mode; (E5) one that has coherent but artificial arcs of amplitude with constant range; and (E6) has coherent, small-scale, artificial random patches of amplitude.

4.3 Possible resonance events

The event classification is summarized in Table 4.2 (see Appendix D for the full list of events and their classifications); events classified as S3, S4, T3, E5, or E6 were not included in further analysis because these are strong indicators of interference in the instrument, so there are only 32 events to consider. There were six events with the desired classification, one of which (event 52) was the 2011 Tōhoku tsunami. The other five events (events 10, 34, 36, 39, and 40) were examined further to determine whether they may be resonance mode excitations. Events 34 and 40 are representative of the others and are described below; others are in Appendix D, along with brief descriptions of events matching two criteria.

Event 34 started at ∼0700 UTC on day 156 of 2010 and ended on the next day at ∼2200 UTC [Figure 4.7]. The M1 index only peaks above the threshold at 1600 UTC on day 156 and at 1100 UTC on day 157 has three packets of peaks: one from 1200 UTC to 1600 UTC on day 156; one from 0000 UTC to 0600 UTC on day 157; and one from 1300 UTC to 1800 UTC on day 157. The M2 index also shows stronger amplitudes at those times, but starting slightly earlier and ending slightly later. Peaks in the M2 band spectral amplitudes occur at different times for different periods, indicating that the oscillations are likely not linked as they were for the 2011 Tōhoku tsunami. The line spectrograms show peaks at all periods of interest, but there are strong peaks at several other periods as well which were absent in the seismic tsunami data. The radial velocity timeseries in range and azimuth show the three packets mentioned before. All three packets are concentrated on the southern 2/3 of the bank and on the eastern margin. The EOF 1 map has an antinode on the southeast part of the bank. The EOF 1 timeseries has all three packets of oscillations, with spectral peaks at only one of the periods of interest, 24-26 min. The EOF 2 and EOF 3 maps have two and three antinodes on the bank, respectively, with north-south oscillations between the antinodes. The three packets are less visible in these timeseries. The EOF 2 spectrum has peaks at 16-17 min, 22-24 min, 27 min, and 40 min while the EOF 3 spectrum has a peak only at 22 min. Event 34 does not have the periods and EOFs linked in a way to indicate tsunami mode resonance.

Event 40 started at ∼2000 UTC on day 256 in 2010 and ended at 1600 on the following day [Figure 4.8]. The event was mostly from M2, with the index amplitude higher from 0000 UTC to 1300 UTC on day 257. The band spectral amplitude peaks occurred between 2000 UTC and 0400 UTC, with the 24-26 min period peak being the largest. The line spectrograms of the event show peaks at the expected frequencies as well as some longer periods. The radial velocity timeseries shows two times of increased current amplitudes: one from 2300 UTC to 0300 UTC over the full bank and another between 0400 UTC and 1300 UTC that does not extend to the southern reaches of the bank. The EOF 1 map has an antinode over the northeastern edge of the bank; the timeseries shows two packets: one from 2200 UTC to 0300 UTC and another from 0330 UTC to 1300 UTC. The EOF 1 spectrum has peaks at 25 min and 41 min in addition to some periods not of interest. The EOF 2 map has an antinode in a similar place is M1 but also a second one at the southeast edge of the bank. The EOF 2 timeseries also has two packets, but with periods of 26-27 min and others not of interest. The EOF 3 map has 3 antinodes along eastern Penguin Bank, and the timeseries has no packets. Like the other event discussed here, event 40 does not show convincingly that it represents an excitation of the tsunami resonance modes.

Table 4.2: Summary of the types of events kept and those eliminated; note that those counted in the eliminated categories are not mutually exclusive, so an event with, for example, both S3 and E5 would be counted under each type.

Type Kept	Number	Type eliminated	Number
S1/T1/E1	6	S3	16
S1/T1	5	S4	15
S1/E1	2	T3	4
T1/E1	5	E5	8
S1	0	E6	26
T1	10		
E1	1		
Other	3		

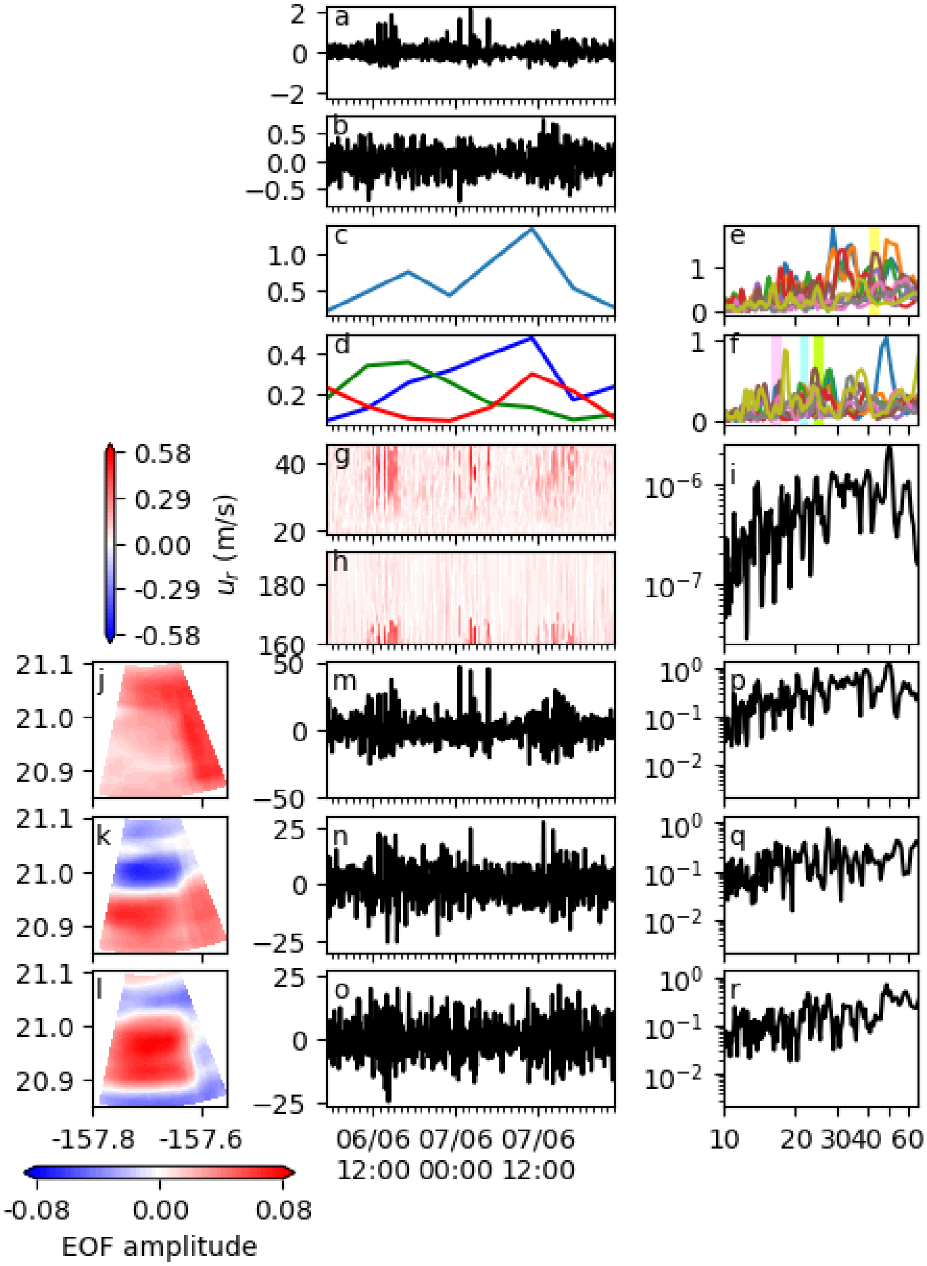

Figure 4.7: Event 34: (a and b) the M1 and M2 indices; (c and d) band spectral amplitudes for M1 and M2;, (e and f) line spectrograms for M1 and M2; (g and h) radial velocity timeseries in range and azimuth; (i) spectrum of radial velocity averaged over Penguin Bank south of Oʻahu, Hawaiʻi; (j, k, and l) EOF 1, EOF 2, and EOF 3 maps; (m, n, and o) EOF 1, EOF 2, and EOF 3 timeseries; and (p, q, and r) EOF 1, EOF 2, and EOF 3 spectra.

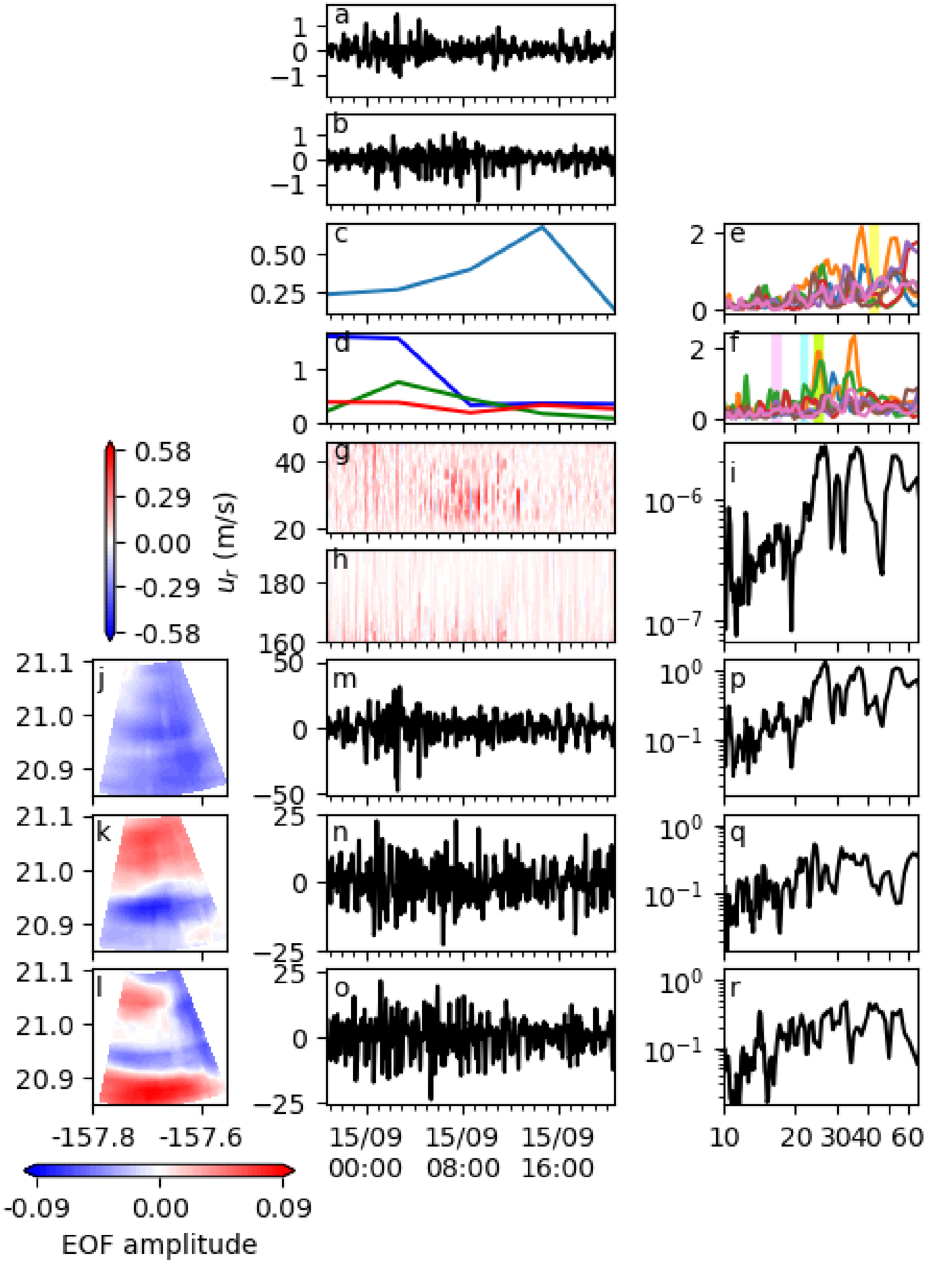

Figure 4.8: Event 40: (a and b) the M1 and M2 indices; (c and d) band spectral amplitudes for M1 and M2;, (e and f) line spectrograms for M1 and M2; (g and h) radial velocity timeseries in range and azimuth; (i) spectrum of radial velocity averaged over Penguin Bank south of O‘ahu, Hawai‘i; (j, k, and l) EOF 1, EOF 2, and EOF 3 maps; (m, n, and o) EOF 1, EOF 2, and EOF 3 timeseries; and (p, q, and r) EOF 1, EOF 2, and EOF 3 spectra.

4.4 Known events

Neither the full S1-T1-E1 match events nor the partial match events (described in the Appendix D) indicated resonance mode excitation with the single exception of the 2011 Tōhoku tsunami. However, there were two other seismic tsunamis during the study period. What do these two tsunamis look like, and why were these tsunamis not among the events identified?

The first tsunami was caused by an 8.1 magnitude earthquake that occurred on day 272 of 2009 at 1748 UTC just south of American Samoa. The tsunami arrived on Hawaiʻi's shores at about 2311 UTC on that same day, causing sea level oscillations of about 0.16 m in Honolulu Harbor. Figure 4.9 shows the time around and following the arrival. Stronger oscillations occur in the M1 index after 0200 UTC the next day, with two very strong peaks around 0500 UTC. The M2 index also increases at around 0200 UTC, but those die around 0800 UTC. Peaks in the band spectral amplitudes occur at between 1000 UTC and 0200 UTC. Line spectrograms for both mode indices do show peaks at all frequencies of interest, but there are several peaks at other frequencies that are just as strong if not stronger than those at frequencies of interest. The radial velocity timeseries in range shows the spreading of currents northward on the bank from the southern end starting after 0200 UTC on day 273, but those currents do not appear to strengthen following the tsunami arrival. The radial velocity timeseries in azimuth shows the appearance of strong currents on the far eastern edge that line up with the spreading described above, but there does not appear to be anything resembling an arrival. The EOF 1 map has an antinode on the southeast part of the bank that spreads out and weakens, as expected; the associated time series only shows stronger and more regular oscillations (with periods of ~32 min and ~40 min) occurring after 0500 UTC on day 273, nearly 6 h after the tsunami arrived. The EOF 2 map has two antinodes along the eastern part of the bank, and the timeseries shows a spike at around 0600 UTC on day 273; the spectrum shows many peaks of similar magnitude between 12 min and 29 min. The EOF 3 map has three antinodes crowded on the southern end of the east side of the bank; the timeseries shows some stronger oscillations between 0500 UTC and 0900 UTC, mainly with 25 min periods. While there are indications of a strong set of oscillations on Penguin Bank after the tsunami arrival, those oscillations do not appear to be the tsunami resonance modes, nor are the oscillations conclusively linked to the tsunami given their start six h after the tsunami arrival time.

The second tsunami was triggered by an 8.8 magnitude earthquake at 0634 UTC on day 58 in 2010 at the shore midway between Concepcion and Santiago. It arrived in Hawaiʻi at 2119 UTC and caused 0.5 m oscillations in Honolulu Harbor. There are two strong peaks in the M1 index just after the tsunami arrival, but there is no indication of a resonance mode activating [Figure 4.10]. The M2 index does have a few strong peaks after 0000 UTC on day 59, but they do not occur regularly. The band spectral amplitudes for both modes do not show a strong and sudden event as expected. The M1 line spectrogram shows weak and broad peaks around 41-45 min while there are sharper and larger peaks between 30 min and 40 min. There are peaks at the three M2 frequencies of interest as well as one shorter period in the M2 line spectrogram, and there is high spectral amplitude at longer periods. The radial velocity timeseries shows a few strong current spikes after the arrival, but the oscillations present had started prior to the arrival time; these oscillations are confined to the southeast parts of the bank, and they only persist until 0000 UTC. The EOF 1 map has an antinode on the southeast corner of the bank; the associated timeseries has a spike that occurs at about the arrival time of the tsunami in Hawaiʻi and has some weaker oscillations that begin a short time after. The EOF 1 spectrum shows a double peak at 36 min and 43 min. The EOF 2 map has two antinodes on the eastern part of the bank, with the northern one being very crowded against the edge of the coverage area. The EOF 2 timeseries shows weak oscillations throughout with a single strong spike at around 1200 UTC on day 59, and the spectrum has strong peaks at 26 min and 35 min. The EOF 3 map has a patchy look due to interference, while the timeseries is just a single spike immediately prior to the tsunami's arrival. There are some spikes that may or may not be related to the tsunami's arrival, and there are some weaker oscillations that occur on the bank; these oscillations do not occur immediately following the arrival of the tsunami, nor are they strong enough with the correct periods to be considered a possible tsunami response.

While three seismic tsunamis occurred during the study period, only the one already studied was found. There was no evidence for the 2009 Samoa tsunami as any strengthened oscillations did not start until six h after the tsunami's arrival. While the first tsunami wave is not necessarily the largest (nor is the first oscillation in a resonance situation always the strongest) for the stronger oscillations to occur six h after the arrival of a relatively weak tsunami is unlikely. As for the 2010 Chile tsunami, there are a couple of spikes that could be related to the tsunami's arrival as they occur at the correct time, but there are no indications of the island chain resonance modes being active.

If resonance mode excitations were fairly weak, they might not excite the island chain modes enough for detection by HFDR. This possibility is supported by the lack of detection of the two seismic tsunamis. As mentioned in Section 2, the trade-off between temporal sampling and velocity resolution means that getting data with the necessary time step to resolve the tsunami resonance modes forces a loss of velocity resolution such that weaker currents are not captured. Both of the seismic tsunamis not captured by the data were significantly weaker than the 2011 Tōhoku tsunami: sea level records from Honolulu Harbor indicate that the Samoan and Chilean tsunamis were only 12% and 38%, respectively, of the strength of the Japanese tsunami. Currents on Penguin Bank during the 2011 Tōhoku tsunami were a maximum of 0.15 m/s, which is not particularly strong when the velocity resolution is 0.07 m/s, so those of the Samoa and Chile tsunamis would be even weaker.

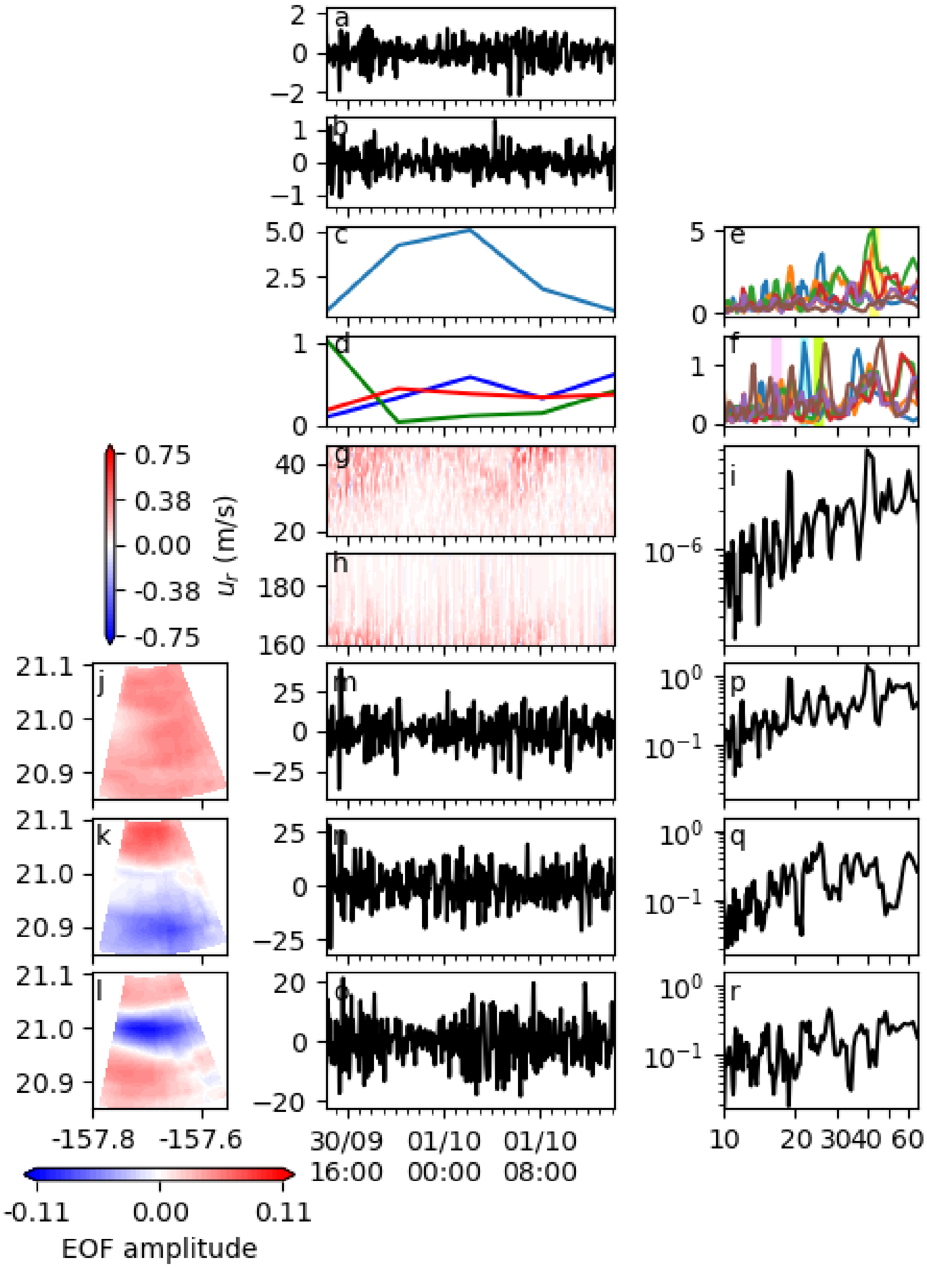

Figure 4.9: Samoa tsunami: (a and b) the M1 and M2 indices; (c and d) band spectral amplitudes for M1 and M2;, (e and f) line spectrograms for M1 and M2; (g and h) radial velocity timeseries in range and azimuth; (i) spectrum of radial velocity averaged over Penguin Bank south of Oʻahu, Hawaiʻi; (j, k, and l) EOF 1, EOF 2, and EOF 3 maps; (m, n, and o) EOF 1, EOF 2, and EOF 3 timeseries; and (p, q, and r) EOF 1, EOF 2, and EOF 3 spectra.

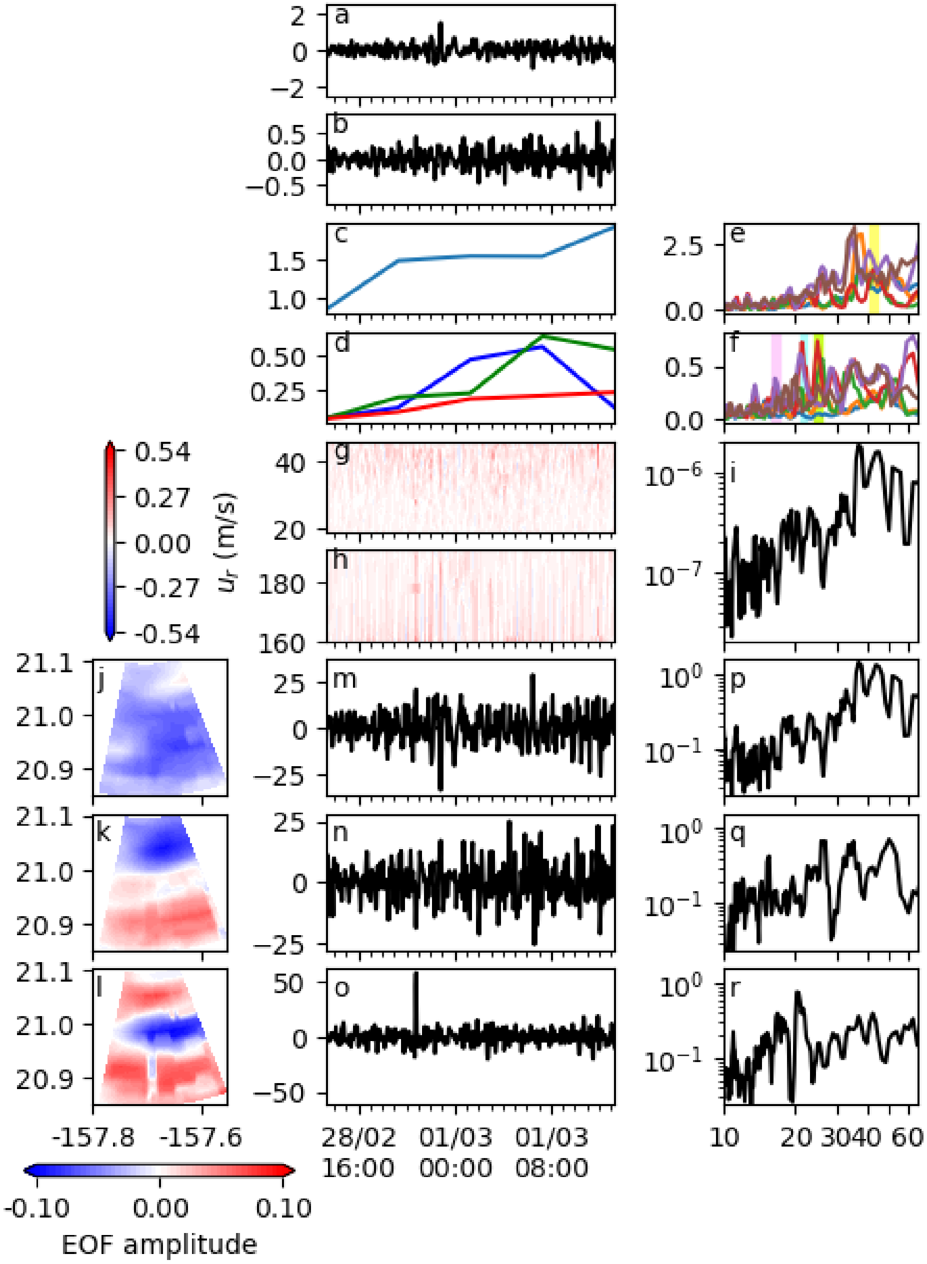

Figure 4.10: Chile tsunami: (a and b) the M1 and M2 indices; (c and d) band spectral amplitudes for M1 and M2;, (e and f) line spectrograms for M1 and M2; (g and h) radial velocity timeseries in range and azimuth; (i) spectrum of radial velocity averaged over Penguin Bank south of Oʻahu, Hawaiʻi; (j, k, and l) EOF 1, EOF 2, and EOF 3 maps; (m, n, and o) EOF 1, EOF 2, and EOF 3 timeseries; and (p, q, and r) EOF 1, EOF 2, and EOF 3 spectra.

4.5 Conclusions

The search for resonance mode excitation in Hawai‘i uncovered five events that shared important spectral, temporal, and spatial characteristics with the 2011 Tōhoku tsunami as well as a further 12 that shared 2/3 of those; however, none of them combined those characteristics into the resonance modes excited over Penguin Bank by a strong seismic tsunami. This complete lack of detection leads to three possible explanations, two relating to the study area and one relating to the methodology: 1. The initial assumption that meteotsunamis occur in Hawai‘i was incorrect; 2. Meteotsunamis do occur in Hawai‘i, but none occurred during the study period; and 3. Meteotsunamis do occur in Hawai‘i, but they were too weak to be detected by the HFDR.

Regarding the first two possibilities which both deal with the study location, there has been no previous research on meteotsunamis in Hawai‘i, so the work of others cannot be used to shed light on whether meteotsunamis do in fact occur in Hawai‘i or how frequently they might happen. Our calculations for edge waves suggest Greenspan resonance is possible here, and previous work has shown that edge waves are associated with tsunamis in Hawai‘i [*Bricker et al.*, 2007]. There are large gaps between confirmed meteotsunami events in the islands off Croatia where these events occur relatively frequently [e.g., *Šepić et al.*, 2016], so it is certainly possible that no meteotsunamis occurred during the 29-mo study period. Infragravity waves were not considered even though they may excite resonance modes because the temporal resolution of the HFDR data almost ensures that they would have little if any visible contribution to mode excitation.

Finally, the two other tsunamis that occurred during the study period that were significantly weaker than the 2011 Tōhoku tsunami were not detected, which supports the idea that any excitations that occurred were below the limit of detection of HFDR. This leads to a recommendation that *in-situ* instruments be deployed on Penguin Bank with specific locations for moorings with pressure sensors and acoustic Doppler current profilers (ADCPs) determined by the mode structure.

Chapter 5

Part 1 conclusions

When tsunami waves arrive in coastal regions, they can excite the local resonance modes if the periods of the incoming waves match the intrinsic periods of these local modes. Modeling studies have documented these modes [*Munger and Cheung*, 2008] and have been validated at point locations with sea level observations [*Yamazaki and Cheung*, 2011] and acoustic Doppler current profiler (ADCP) currents [*Cheung et al.*, 2013]. Our surface current fields expand the catalog of available observations of tsunami resonance modes and allow for two-dimensional validation of modeled output. The ideal location for observing tsunami resonance is Penguin Bank because of the increased amplitudes over the bank for a whole suite of modes that have expressions not only on the bank itself but on the coastlines of Maui Nui or the entire archipelago. These modes are excited by the tsunami but are determined by the local bathymetric and coastal features, so all tsunamis should excite the same modes. High-frequency Doppler radio (HFDR) currents during the 2011 Tōhoku tsunami do agree very well with modes determined by modeling of several tsunamis. The first two modes show clear oscillations on Penguin Bank that are indicative of island chain resonance.

Similarly, other processes that introduce wave energy at the proper matching periods, such as meteotsunamis, would also excite these modes. An extensive analysis over 29-mo using the 2011 Tōhoku tsunami modes as a spatial filter initially identified 76 possible events, but further analysis failed to conclusively show that any were resonance mode excitation events. Meteotsunamis are infrequent even in locations where they occur relatively frequently: only 17 strong events occurred over 90 years in the eastern Adriatic Sea, for example, so this could be a reason for the lack of detection. The two other tsunamis that occurred during the study period that were significantly weaker than the 2011 Tōhoku tsunami were not detected, which may support the idea that any excitations that occurred were below the limit of detection of HFDR. Such a possibility leads to the recommendation that *in-situ* instruments be deployed on Penguin Bank. The spatial structure of the modes of surface currents over Penguin Bank are known from both the earlier HFDR study as well as from modeling; also, the sea level of the modes is known from modeling, and the sea level can be derived from the HFDR modes using the relationship between currents and sea level in waves. Both pressure sensors and upward-looking ADCPs would not have the same limitations as the HFDR. While the ADCPs do have specific averaging times, higher frequency instruments have shorter averaging times, so there is not the same issue. Perhaps five moorings each consisting of a bottom pressure sensor and a bottom-mounted, upward-looking ADCP would yield currents and sea level indications at five locations that would allow determining which modes are active at which times.

What are the implications of the lack of detection of any resonance mode excitation events? The 2011 Tōhoku tsunami created strong oscillations in sea level of more than 0.5 m in Honolulu Harbor, and detected currents on Penguin Bank were up to 0.15 m/s; yet this tsunami was close to the limits of detection for the HFDR. Penguin Bank is on the azimuthal limit of the beamforming array where beamwidths are wider and the determination of direction is less precise; additionally, achieving finer time steps in order to properly sample the resonance modes reduces the resolution of the resulting surface current velocities from 0.03 m/s to 0.07 m/s, about half of the largest velocity magnitudes. The 2011 Tōhoku tsunami was considerably stronger than two other seismic tsunamis that occurred during the study period, and neither was detected in currents on Penguin Bank. HFDRs can create surface maps that show the spatial structure of resonance modes, but they are not the best instruments available for detecting weaker current events, particularly when shorter-period oscillations are the dominant response or when the area of interest is not near the receive array's boresight.

One other important point is that, while there is no evidence that meteotsunamis occurred during the study period, if they do occur they can pose extra hazards to Hawai'i beyond a normal tsunami. The tsunami warning system relies on sea level records at DART buoys for far-field events, but may also result in a warning if there is local seismic activity; for the latter case, a warning may be issued even if no tsunami is initially detected because of the short time between generation and landfall. However, meteotsunamis are not far-field tsunamis and are also not linked to local seismic activity.

This leaves several unanswered questions about the resonance modes in Hawai'i. Do meteotsunamis occur in Hawaii? Are these resonance modes excited by other processes? Do infragravity waves excite the higher-frequency modes? There are three ways of furthering the study of resonance modes in Hawai'i. First, the HFDR on O'ahu could be changed slightly to provide better data over Penguin Bank. While it is currently a beamforming array situated to provide overlapping coverage with two other instruments further west on O'ahu's south shore to form two-dimensional vector currents south of the island, the receive array could be supplemented with two additional antennas that form a square with two existing antennas that would provide better coverage of Penguin Bank through direction-finding. This need not interfere with the current operation of the instrument as the processing allows for selection of specific antenna channels; indeed, one HFDR on the island of Hawai'i currently operates in both beamforming and direction-finding modes simultaneously. Secondly, the recommendation to instrument Penguin Bank with pressure sensors and ADCPs to observe modes in sea level and currents could be implemented. Thirdly, meteotsunami formation processes and infragravity wave impingement could be modeled in Hawai'i. Because supplementing the existing HFDR does nothing to change the limitations on time steps and velocity resolution and *in-situ* instrument deployment can be costly with no guarantee that any events will occur in a given study period, modeling is perhaps the best way of answering some of these questions. This presents some challenges relative to some other meteotsunami modeling studies [e.g., *Šepić et al.*, 2016]: frequently, locations where this is undertaken have uniformly shallow bathymetry that allows for some simplifications that would not be possible in the Hawaiʻian Islands, where shallow shelves of $\sim$50 m quickly drop off to depths of 2000 m or greater.

Part II

Tropical instability vortices and associated fronts

Chapter 6

Part 2 introduction

In the eastern and central equatorial Pacific Ocean, southeasterly trade winds from the Southern Hemisphere and northeasterly trade winds from the Northern Hemisphere converge along the Intertropical Convergence Zone (ITCZ), normally centered at 8°N to 10°N [Figure 6.1]. The change of sign of the Coriolis force at the equator combined with westward trade winds produce Ekman divergence, driving upwelling of cold subsurface water along the equator. Sverdrup balance resulting from the associated wind stress curl drives zonal surface currents: the westward South Equatorial Current (SEC) extending from the center of the South Pacific gyre at 20°S, across the equator, to ∼3°N; the westward North Equatorial Current (NEC) extending from ∼10°N to the center of the North Pacific gyre at 20°N; and the narrow North Equatorial Countercurrent (NECC) flowing eastward typically between 7°N and 10°N. In addition, the subsurface Equatorial Undercurrent (EUC) flows eastward along the equator between 50 m and 150 m depths at speeds up to 1.5 m/s. The boundary between cold, upwelled water and warm, surface waters to the north is the North Equatorial Front (NEF). This current system is subject to seasonal and interannual variations. Trade winds are weakest in boreal spring and reach their peak in boreal fall; consequently surface currents in the gyres are weakest in spring and accelerate in summer and fall. The El Niño-Southern Oscillation (ENSO) also has a strong effect on the equatorial Pacific: during the positive El Niño phase, low latitude winds weaken or reverse, and so do surface currents and upwelling. During the negative La Niña phase, stronger than usual easterly winds drive stronger surface currents and vigorous upwelling. A similar equatorial current structure is found in the Atlantic Ocean.

This meridionally sheared zonal equatorial current system is subject to hydrodynamic instabilities that are strongest in late summer and fall; indeed, a typical meridional shear of 1 m/s between 3°N and 7°N scales as large as $\sim f/4$. Long wavelength oscillations of the NEF seen in sea surface temperature images led to the name equatorial long waves (ELW) [*Legeckis*, 1977], while stability analyses of the mean currents prompted the name tropical instability waves (TIWs) [*Philander*, 1976, 1978]. Studies of ELW energetics suggested different forms of instabilities, powered either by barotropic instability at the equator [*Weisberg*, 1984] or by both barotropic and baroclinic instability over a range of latitudes [*Hansen and Paul*, 1984]. Three separate regimes of instability in space and time were identified [*Luther and Johnson*, 1990]: in fall and winter, the strong horizontal shear between the SEC and the upper EUC around the equator is subject to barotropic instability; in the winter when the EUC is weak, density differences at the surface front between the SEC and NECC produce baroclinic instability; and in spring and summer when the SEC is weak, the NECC thermocline from 5°N to 8°N may be baroclinically unstable.

Moorings and intensive mesoscale surveys as part of the 1990 Tropical Instability Wave Experiment (TIWE) suggested that tropical instabilities manifest themselves in two forms.

1. In the vicinity of the equator, ELWs/TIWs have a typical wavelength of 1000 km, period of 21 d, and phase speed of ~0.5 m/s. They appear as periodic changes in sea level, velocity, and salinity during a well-defined season from August to December. The elliptical near-surface velocity hodographs lean into the SEC-EUC shear, extracting energy from the mean flow [*Qiao and Weisberg*, 1995]. ELWs are weaker during El Niño when the SEC weakens and the SEC-EUC shear decreases [*Halpern et al.*, 1988; *Qiao and Weisberg*, 1998].

2. Along the NEF at ~5°N, tropical instability vortices (TIVs) are anticyclones with a ~30 m thermocline depression and average diameter of 500 km that propagate westward at a translation speed of ~0.3 m/s [*Kennan and Flament*, 2000]. A TIV swirls cold equatorial water northward and a pool of warmer water from the ITCZ southward, and to first order appears as a westward-propagating perturbation of the NEF, visible in sea-surface temperature im-

> ages as a sharp western leading cold front and weaker eastern trailing warm front [*Flament et al.*, 1996]. These cusp-like perturbations in the NEF, observed from July to April, may remain as fossil thermal signatures towards the end of the upwelling season when TIVs are no longer dynamically active. TIVs are absent during El Niño events when winds, Ekman divergence, and equatorial upwelling are all weak, resulting in a weak NEF; they may be present year round during La Niña events when the NEF is very sharp [*Contreras*, 2002]. These TIVs are also seen in the Atlantic Ocean [*Dutrieux et al.*, 2008; *Menkes et al.*, 2002]. We will focus on TIVs in this dissertation.

In Chapter 7, a description of the mesoscale flow around a specific TIV proceeds from *in-situ* and satellite data near 140°W including from the Topex altimeter, the Pathfinder sea surface temperature (SST) product, and the TAO mooring array from September and October 1994. A translating frame of reference removes smearing of the vortex associated with its own westward motion. Geostrophic currents derived from sea surface height anomaly (SSHA) show anticyclonic rotation on the North Equatorial Front that swirls cold, salty, upwelled equatorial water to the north on the western flank while simultaneously bringing warmer, fresher, tropical surface water to the south on the eastern side visible in SST. Examination of the SST and chlorophyll-a from MODIS in multiple TIVs across the Pacific between 2016 and 2019 shows variation in the details such as strengths of gradients, background values, and frontal lines; this is especially true at smaller scales.

Since the 1990 TIWE, various theoretical and numerical modeling authors have studied submesoscale structures potentially associated with TIVs and the NEF. The findings of three particularly relevant studies are summarized below.

Marchesiello et al. [2011] examined TIVs in a numerical model and explored the spectral characteristics of kinetic energy. They found that the leading edge of TIVs is subject to vigorous frontogenesis, including positive surface vorticity and downwelling on the cold side of the front, and negative vorticity and upwelling on the warm side; this is characteristic of ageostrophic secondary circulation across the front to restore the geostrophic balance destroyed by straining. This is consistent with the observations of *Chavanne et al.* [2010], who found positive vorticity and convergence on the cold side of a front and negative vorticity and divergence on the warm side as evidence of such a secondary circulation. *Marchesiello et al.* [2011] also used kinetic energy spectra to show that TIVs release available potential energy that then helps restratify the mixed layer.

Holmes et al. [2014] examined the total potential vorticity (PV) of a TIV at sub-mesoscales in a numerical model, including the horizontal component of PV from horizontal buoyancy gradients. EUC water that is the source for TIV core water has significant horizontal and vertical PV that balance one another for near-zero total PV; following TIV core formation, the water has near-zero PV components as well. The strong vertical shear in EUC water has been subjected to an ageostrophic overturning circulation across a front within the TIV that both reduces horizontal buoyancy gradients and causes vortex tilting; the former reduces horizontal PV to near zero, while the latter, in combination with northward advection of planetary vorticity from EUC latitudes to TIV latitudes, reduces the vertical PV to near zero.

Ubelmann and Fu [2011a] identified smaller ($\leq$ 150 km diameter) cyclonic and anticyclonic vortices embedded in TIVs at the NEF in both observations and a numerical model; these vortices had large diameters more consistent with mid-latitude mesoscale eddies but limited vertical extent more typical of sub-mesoscale eddies. These smaller eddies form where the NEF folds over and occludes to produce a characteristic lambda-like shape. The asymmetry in the maximum vorticities ($2f$ for cyclones and $-f$ for anticyclones) suggests that centrifugal instability prevents anticyclones from further strengthening.

One sub-mesoscale structure of interest is fronts, which can develop with cross-frontal length scales of only a few kilometers [*McWilliams*, 2016, Figure 6.2]. Sub-mesoscale fronts have a cross-frontal buoyancy gradient that induces thermal wind shear in the down-front direction, accelerating the already-present down-front geostrophic current. In response to the buoyancy gradient, an ageostrophic secondary circulation develops that works to flatten the isopycnals and restratify the mixed layer; the direction of the vorticity of this circulation is up-front [Figure 6.2]. However, this restratification can be modified by either large-scale deformation flows that feed frontogenesis by sharpening the buoyancy gradient and thinning the front, or by down-front surface winds that cause cross-front Ekman flow that opposes the surface branch of the ageostrophic secondary circulation, slowing or halting the restratification [*Mahadevan et al.*, 2010]. The development of sub-mesoscale fronts thus depends on several competing processes.

In Chapter 8, we place multi-frequency synthetic aperture radar (SAR) data from the Shuttle Imaging Radar Experiment (SIR-C) [*Evans et al.*, 1993; *Flament*, 1995] and recent SAR observations from the European Space Agency Sentinel-1 satellites [*Copernicus; European Space Agency*, 2011] into the framework provided by the mesoscale analysis of Chapter 7. SAR images capillary waves and any processes that alter the waves (e.g., wind stress, internal waves, currents, bathymetry, surfactant) with very fine spatial resolution, and is thus ideal for examining sub-mesoscale fronts in TIVs. SAR fronts are also SST and chlorophyll-a fronts. SIR-C fronts are shown to be advected by swirling currents, with the same front rotating and deforming over four days within one vortex, and also developing cusps and other indicators of frontal instabilities. Many of the fronts in the Sentinel-1 SAR images also show instabilities. Examination of currents and shear from TIWE-1 and TIWE-2 cruises, plus modeled PV from *Holmes et al.* [2014], indicates that there is strong shear at the interface and a necessary potential vorticity inflection to allow barotropic or baroclinic mixed-layer instabilities, but the positive potential vorticity at the fronts makes gravitational, inertial, and symmetric instabilities unlikely at frontal scales. While low Richardson numbers superficially indicate the possibility of Kelvin-Helmholtz instability also occurring, the mechanics make it unlikely to cause the kind of surface cusps seen at the front and are more likely an indication of mixing.

Interpretation of SAR images can be complex: SAR back-scatter intensity is a function of surface roughness, so any processes that impact capillary waves and thus surface roughness can affect the back-scatter. Fronts are, by definition, dividing lines in properties, and TIVs have obvious fronts in temperature, salinity, density, and chlorophyll-a, but other properties such as winds and currents may also change across fronts. These changes, specifically in temperature, winds, and currents, can be seen in SAR images.

In Chapter 9, we examine synthetic aperture radar images for differences across the front to determine how SST, winds, and currents impact SAR images, and what information about these sub-mesoscale ocean properties can be determined. First, differences in back-scatter, and thus surface roughness, are examined. On the leading front where there is higher back-scatter over warmer water, the influence of temperature on the wind both by the change in wind speed and the change in drag coefficient are sufficient to explain the observations. On the trailing front, higher back-scatter can be associated with either warmer or colder water; the former case is identical to that on the leading front, while the latter has a temperature impact in the opposite direction of the observations. The surface currents alter the total stress, which is the true stress rather than solely the wind stress, such that currents with different magnitudes and/or directions across the front can be responsible for the observations. A closer look is then given to the surface currents, which refract swell and alter the capillary wave field; differences in the wavenumber vector can be used to determine the surface currents. There are two ways of deriving currents, one that finds only the component in the direction of the wavenumber vectors, and another that uses two wavenumber vectors and the least-squares method. Currents derived by the first method are incomplete and tend to be unrealistically large, while those from the second method are fully two-dimensional and constrained in both dimensions, though they may also be too large. A statistical analysis of the difference in wavenumber vectors across the front showed that the difference in the stronger, shorter-wave swell across the front was nearly always statistically significant.

The last chapter of Part II, Chapter 10, contains conclusions and implications.

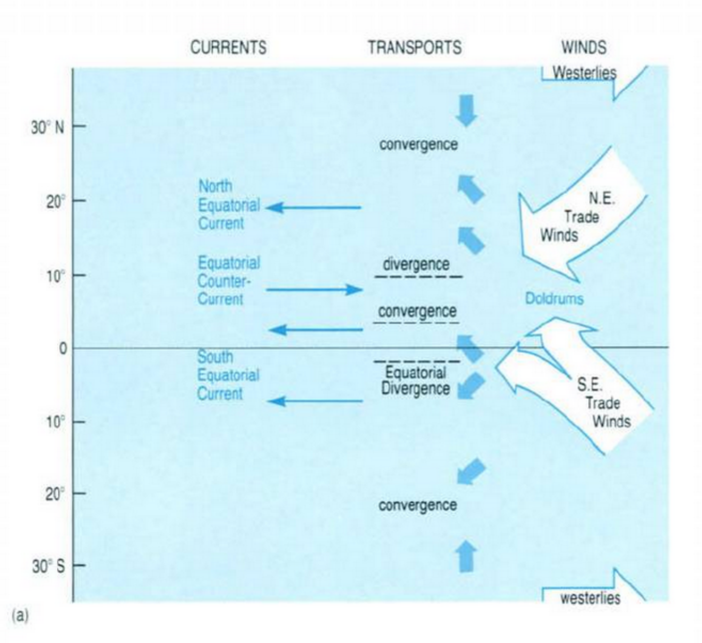

Figure 6.1: Reproduced from *The Open University* [2001], their figure 5.1a. Diagram of conditions in the equatorial Pacific including winds, Ekman transports, and surface currents.

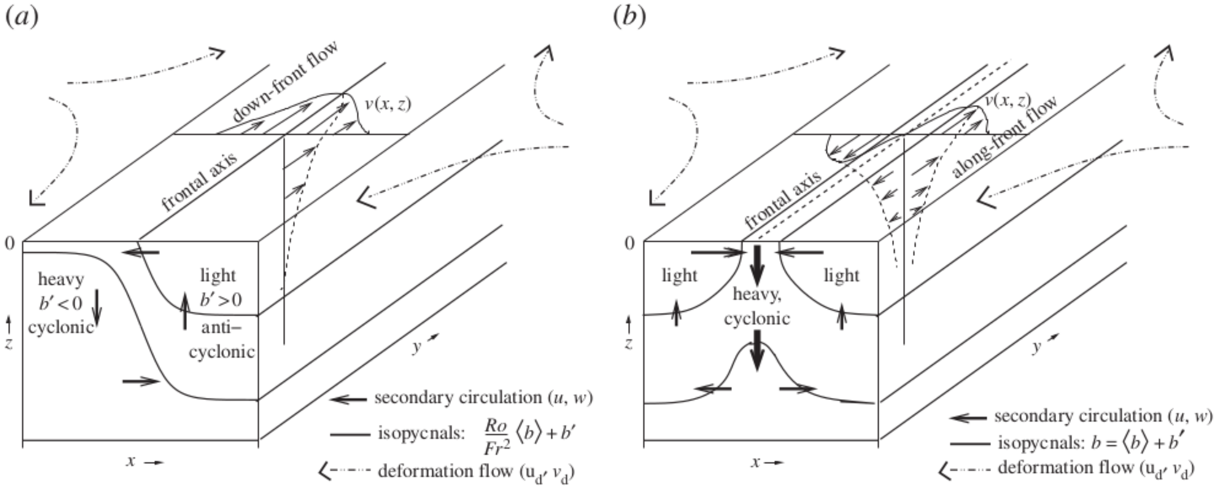

Figure 6.2: Reproduced from *McWilliams* [2016], their figure 5. A diagram of sub-mesoscale (a) frontal development and (b) filament development. Buoyancy is b with its perturbation as b'; Rossby number is Ro; Froude number is Fr; the zonal and vertical components of the ageostrophic secondary circulation are u and w, respectively; the down-front geostrophic and thermal wind combined current is $v(x,z)$; and zonal and meridional components of the large-scale deformation flow are u_d and v_d, respectively.

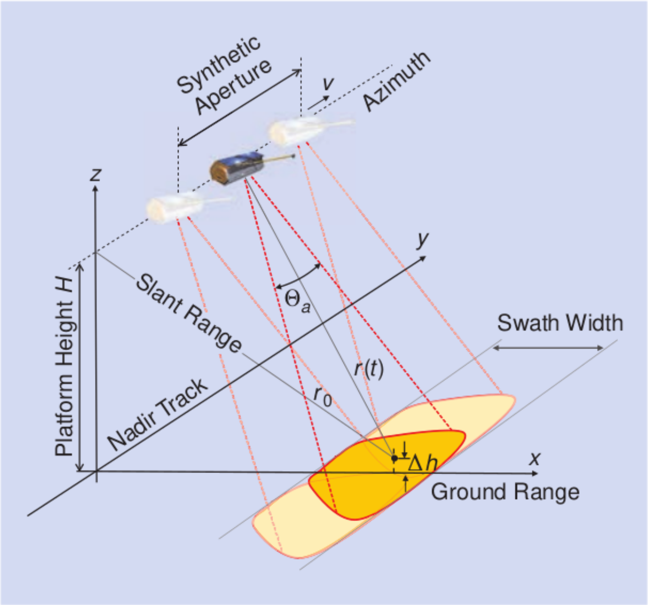

Figure 6.3: Reproduced from *Moreira et al.* [2013], their figure 2. The geometry of SAR imaging, where r_0 is the shortest approach distance, Θ_a is the azimuth beamwidth, and v is the sensor velocity.

Chapter 7

Mesoscale variations of TIVs and associated SST fronts

Where it is shown that in a Rossby number = −1 anticyclonic vortex on the North Equatorial Front, sea surface temperature is advected by the swirling currents, and significant variability exists between vortices.

7.1 Introduction

Previous studies of tropical instability vortices (TIVs) have shed light on the mesoscale structure of these vortices. Convergence along the leading front in TIVs causes aggregation of buoyant diatoms [*Yoder et al.*, 1994], while equally strong $\sim f$ divergence appears in the vortex's core; the center of this convergence/divergence dipole is where energy is extracted from the mean shear through barotropic instability, though baroclinic instability plays a minor role in the northward flow of cold water in the NEF cusp [*Kennan and Flament*, 2000]. Surface drifters follow almost closed-loop trajectories in a frame of reference moving with the vortices, and the strong anticyclonic relative vorticity in the vortex core reaches ~ -1, equivalent to Rossby number $Ro \sim -1$, suggesting a vortex close to the centrifugally-unstable limit [*Kennan*, 1997].

Such $Ro \sim -1$ vortices have been observed previously at high- and mid-latitudes. Sub-mesoscale anticyclones form with near-zero potential vorticity (PV) and $-f$ relative vorticity as water flows from Chukchi Sea into the Beaufort sea; *D'Asaro* [1988] found that frictional boundary torques through Barrow Canyon can produce the necessary relative vorticity. *Flament et al.* [2001] tracked eddies in the lee of the Hawaiian Islands; anticyclones had cores in solid-body rotation with initial orbital periods nearly one pendulum day ($-f$ relative vorticity). Solid-body rotation of the cores indicates that anticyclones have restabilized after centrifugal instability [*Kloosterziel et al.*, 2000]. The destruction and reformation of eddies, redistributing angular momentum to a stable configuration, may take up to several days; *Chavanne et al.* [2010] observed that anticyclones with relative vorticity less than $-f$ were not stabilized while they experienced centrifugal instability for several days. Anticyclones shed from Gran Canaria also initially have cores in solid body rotation [*Sangrà et al.*, 2005, 2007] but merge with other anticyclones or cyclones, increasing their radii and reducing their periods of rotation; anticyclones were near the centrifugally-unstable limit only early in their life. Anticyclonic eddies in the North Brazil Current retroflection are frequently near the centrifugally-unstable limit [*Castelão and Johns*, 2011] and must have already restabilized, since their structure was similar to the one described by *Flament et al.* [2001] and proposed by *Kloosterziel et al.* [2000] as evidence of restabilization.

In this chapter, the aim is to create an accurate description of a TIV on mesoscales that can be used as a framework in which to place the results of later chapters. Sea surface temperature (SST) and sea surface height anomaly (SSHA) data of TIVs will be examined on mesoscales; section 2 describes the data, section 3 explains the translating frame of reference and describes a TIV in such a frame of reference, section 4 describes the variability observed between TIVs, and section 5 contains a brief summary and conclusions.

7.2 Data

Data for this analysis comes from two distinct time periods with specific times and locations chosen to match the available synthetic aperture radar (SAR) images used in later chapters.

For the first time period, centered about ∼5°N, 142°W in early October 1994, *in-situ* temperature and salinity data along with satellite SST and SSHA were used.

Daily in-situ temperatures from the surface to 500 m depth were taken from the TAO moorings located at 2°N, 140°W and 5°N, 140°W from day 185 to day 365 [Figure 7.1b,c]. These temperatures were used in raw form to examine traces of SST changes and shifting thermocline depths, as well as in an inversion to estimate SSH variation. The SSHA was inferred from the mooring temperatures, assuming that the equatorial thermocline is approximated by a surface layer over a motionless deep layer (1.5-layer model, i.e. thermocline depth variations mirror SSHA variations, scaled by the relative density difference between upper and deep layers). The depth of the 20-C isotherm was linearly interpolated from the temperatures at the instrumented depths.

CTD casts from the R/V Cromwell at 5°N, 155°W one month before in August 1994 during a cruise were used to determine the density near the surface and at depth used in the SSHA inversion from mooring temperatures.

Along-track SSHA from the Integrated Multi-Mission Altimeter Data version 4.2 [*Beckley et al.*, 2017] between 5°S and 15°N, 170°W and 100°W during yeardays 250 to 280 in 1994 was used in the translating frame of reference [Figure 7.1d]. A complication when mapping SSHA from satellite altimeters stems from the significant anisotropy of the sampling: while samples are collected along-track at ∼7-km resolution, the longitudinal spacing of the tracks is determined by the orbit repeat cycle, which is 144 orbits over 10 d for Topex, yielding a longitudinal resolution of 2.5° or 278 km near the equator.

Satellite SST was taken from two sources: the Pathfinder version 5.3 level-3 collated SST product [*Saha et al.*, 2018], with 1/24° resolution and twice-daily maps, and high-resolution AVHRR images from NOAA-12 with 1.1 km resolution collected directly by the University of Hawaii HRPT receiving station [Figure 7.1d]. The Pathfinder product was taken for yeardays 267 to 281 in 1994 over the area from 2°S to 12°N and 170°W to 110°W and used in the moving frame of reference. The individual images were taken on days 266, 267, 274, and 276 of 1994; these were processed using the standard NOAA multi-channel SST algorithm but were recalibrated against the better-validated Pathfinder product maps before being composited with them to give clearer, higher resolution snapshots of TIV impacts.

For the second study period between 2016 and 2019 and covering the entire eastern and central equatorial Pacific, both SST and chlorophyll-a were taken from MODIS level 3 standard mapped images from both Aqua and Terra satellites, processed by the Ocean Biology Processing Group at NASA [*NASA Goddard SFC, OEL OBPG*, 2018a,b, 2020a,b]. The variables SST, SST4 (from 4 μm radiance), and chlorophyll-a derived from a standard algorithm using reflectance in the blue-to-green spectral range were taken at 1/24° resolution twice daily for regular SST and chlorophyll-a, but only once daily for SST4. This data was used to examine variability between TIVs.

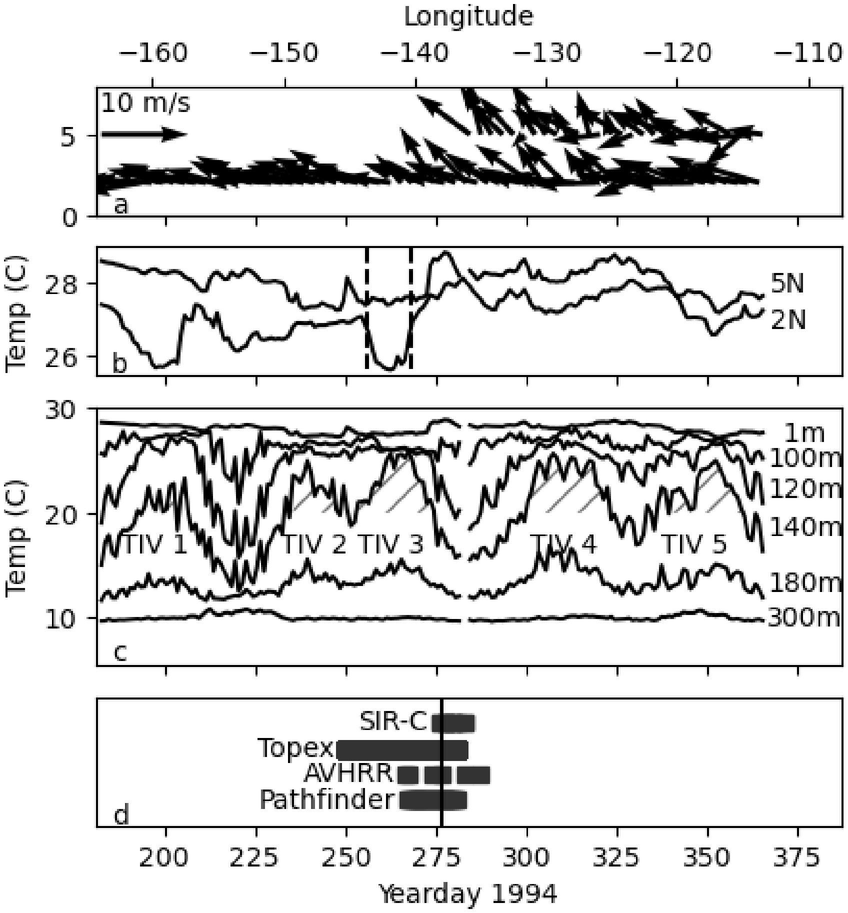

Figure 7.1: (a) Surface winds at the 2°N, 140°W and 5°N, 140°W TAO moorings; (b) 1-m depth temperatures, with the passage of the leading and trailing fronts of TIV #3 are marked by dashed lines; (c) temperatures at the 5°N, 140°W mooring at depths of 1, 100, 120, 140, 180 and 300 m where hatching highlights times when the temperature at 140 m was greater than 20 C and successive TIVs are numbered 1 to 5; (d) times of the individual HRPT AVHRR images, SIR-C SAR images and periods during which TOPEX and global AVHRR products were processed to estimate translation speed are marked above the time axis; the time of the HRPT AVHRR image on day 276 closest to the times of the SIR-C images is marked by a vertical line. The longitude and time x-axis labels are related by the translating frame of reference, with the longitude reference being correct at 0000 UTC on day 274 of 1994.

7.3 TIVs in a translating frame of reference

At 5°N, close to the latitude of the centers of the TIVs, the TAO mooring temperature changed sharply at 140-m depth with the rise and fall of the thermocline, reflecting the geostrophic signature of the anticyclonic TIVs passing that location [Figure 7.1c]. At the time of interest, the well-defined TIV #3 and its deepened thermocline had just passed by the mooring at 5°N. At 2°N (not shown), variations of the thermocline depth respond principally to processes in the equatorial wave-guide, and not to the passage of TIVs. Temperature at 1-m depth is shown with an enlarged scale in Figure 7.1b. At 2°N, the leading front (from warm to cold water) associated with TIV #3 passed 140°W on day 257, while the trailing front (from the northward protrusion of cold water to the warm water pool) passed on day 268; at 5°N, the surface signatures of the passing TIVs and NEF cusps are similar but weaker.

Because TIVs move rapidly westward, mapping such features on a stationary grid smears them out [Figure 7.2]. A commonly used technique for improving the focus on translating eddies consists of mapping the data in a frame of reference moving with eddy centers [*Pingree and Cann*, 1992]. The westward translation will be defined as $y\prime = y$, and $x\prime = x - ct$, where x is longitude, y is latitude, c is the translation speed, $x\prime$ and $y\prime$ are coordinates in the translating frame of reference, and t is the time since 00:00 UTC on day 274 in 1994, chosen as the origin. When gridding non-synoptic data, an optimum translation speed can be estimated as the speed at which the gridding error is minimized [*Kennan and Flament*, 2000; *Menkes et al.*, 2002]. Here, we are limited to satellite data (SSHA and SST) to estimate the translation speed. There were no other moorings within a TIV wavelength, and there were no SVP drifting buoys looping in this TIV to aid in estimating the translation speed.

In the fixed frame of reference, objective mapping algorithms are generally used to produce standard gridded SSHA field for each repeat cycle [LeTraon et al., 1998]. However, in the present case, the rapid westward motion of TIVs within a repeat cycle precludes using these off-the-shelf gridded fields.

To circumvent this sampling limitation and optimally separate signal from noise, we proceeded as follows: (i) the along-track SSHA data were smoothed by a running mean to match the actual 35-km spectral resolution of the TOPEX altimeter [*Tchilibou et al.*, 2018] and interpolated onto a fixed latitude grid; (ii) empirical orthogonal functions (EOFs) of SSHA as functions of latitude were computed by lumping together tracks from the 100°-170° longitude interval and over the July to December season, where and when TIVs are most commonly observed; (iii) the four largest EOFs [Figure 7.3], which accounted for 79.6% of the variance, were retained to construct noise-filtered SSHA data; (iv) the noise-filtered SSHA data were translated using speeds of 0 to 1 m/s westward with 0.02 m/s steps; (v) gridding was then performed as the mean within a 1.5° search radius, following *Kennan and Flament* [2000, their Fig. 12]. Figure 7.4a shows the gridding error as a function of translation speed and latitude, longitudinally averaged over 140°W to 145°W, the region of interest that contains TIV #3 seen in the mooring time series. Figure 7.4b shows the error further averaged meridionally over 4°N 6°N. The error is minimum at a translation speed of -0.34 m/s [Figure 7.4b]. The variance of the SSHA differences at all translated orbit crossings is an alternative parameter to assess the optimum translation speed [Figure 7.4c]; it is minimum at a translation speed of -0.30 m/s.

The gridded SSHA from the altimeter can be compared with the SSHA inferred from the mooring temperatures [Figure 7.4d]. The altimeter SSHA and the depth of the 20-C isotherm correlate best also for a -0.34 m/s westward translation speed. From the slope of the regression a relative density difference of 1/464 can be inferred (for reference, the Levitus climatology at 5°N, 140°W gives a relative density difference of 1/190 between the surface and 300m depth, while CTD casts taken from the R/V Cromwell at 5°N, 155°W one month before the shuttle flight yield a relative density difference of 1/186 for the same depth range). This smaller relative density is a result of the smoothing done to the Topex SSHA during gridding; when the relative density difference from the R/V Cromwell CTD data is used to calculate the expected SSHA, values are between 0 m and 0.26 m, larger than those found in the gridded Topex but much closer to the along-track Topex data (-0.03 m to 0.25 m), which accounts for the discrepancy.

Similarly, the SST was gridded in the moving frame of reference; the median of overlapping pixels in the translated images was computed using speeds corresponding to whole-pixel shifting (i.e., speeds were chosen so that pixel longitudes were shifted by an integer number of locations, simplifying the re-gridding of large data sets). Because SST is uniformly cold along the equator and uniformly warm north of the NEF, and because there are fewer usable cloud-free pixels away from the equator towards the ITCZ, the SST gridding error is a weak constraint to assess the translation speed, even in the 4°N to 6°N latitude band which experiences most of the SST variations corresponding to the passage of TIVs and NEF cusps. Additionally, the temporal variations of temperature at 1-m depth are small compared to those in the thermocline [Figure 7.1b and c]. Figure 7.4e shows the SST gridding error as a function of translation speed, averaged longitudinally over 140°W to 145°W and meridionally over 4°N to 6°N. There is a modest albeit significant minimum at a translation speed of -0.32 m/s.

These three separate assessments point to an optimum translation speed of between -0.30 m/s and -0.34 m/s to bring TIV #3 into focus, i.e., to define a frame of reference in which TIV #3 appears as a stationary or static feature. While this estimated translation speed is subject to uncertainty, note that over the ±3-d temporal span of the SIR-C SAR images, an error of 0.05 m/s in the translation speed converts into a longitude error of only 13 km, or 3 pixels of the global Pathfinder product.

The gridded SST and SSHA fields, assuming translation speeds of -0.32 m/s and -0.34 m/s, respectively, are shown in Figure 7.5 using the longitude scale corresponding to chosen time origin of 00:00 UTC on yearday 274 in 1994, hereafter sub-scripted as $\mathrm{W_T}$. The slightly different translation speeds for the two data sets produce negligible differences while saving significant computational time for the SST field calculations.

The upwelling along the equator is visible, with cold surface water cusps protruding northward to ~6°N at 143°$\mathrm{W_T}$ (corresponding to TIV #3) and also at 136°$\mathrm{W_T}$ (corresponding to TIV #4). The signature of the TIV #3 appears as a 0.15-m high in the SSHA field, which was centered at 6°N, 142°$\mathrm{W_T}$. The signature of the approaching TIV #4 is also seen further east as a 0.17-m high at 136°$\mathrm{W_T}$. The SSHA field reflects the velocity field through geostrophy; this inferred velocity field resolves well the anticyclonic circulation of a TIV, with the western side of the anticyclone bringing cold upwelled water northward and the eastern side bringing a pool of warm surface water of ITCZ origin southward.

The TIV centered at 143°$\mathrm{W_T}$ displays therefore all the dynamical characteristics of the archetypal TIV described by *Flament et al.* [1996] and *Menkes et al.* [2002]: a 500-km diameter anticyclone in cyclo-geostrophic balance, with a maximum peripheral velocity of 0.70 m/s and core vorticity $\sim -0.2f$.

While the dynamical structure of TIVs can be approximated to first order as steady in the translating coordinates, the temperature field may be subject to significant evolution during an orbital period, advected by the swirling velocity field and subject to air-sea interactions and diurnal warming of fresher water in the warm sector. Because the temperature fronts are not stationary, they remain considerably smeared in the gridded global 1/24° JPL-Pathfinder SST product, even after translation [Figure 7.5a]. The evolution of the fronts must therefore be traced in individual SST images.

Individual high-resolution AVHRR images composited with Pathfinder SST product are shown in Figure 7.6. The fronts, traced in each of those images, are shown in Figure 7.7. The leading front (west of the cold northward protrusion) has a westward translation consistent with −0.32 m/s, but only at 4.4°N; it experiences considerable strain/rotation, its orientation evolving from NE-SW to N-S in just 8 days. The trailing front (east of the cold northward protrusion) reflects the more complex southward and clockwise swirling of the warm pool. A section through the SST image on day 274 is shows the main leading and trailing fronts correspond both to transitions of ∼1 C over scales of 3 to 4 km in the SST images, about the same order as the resolution of the AVHRR sensor [Figure 7.8]. Occasionally, multiple temperature steps are observed.

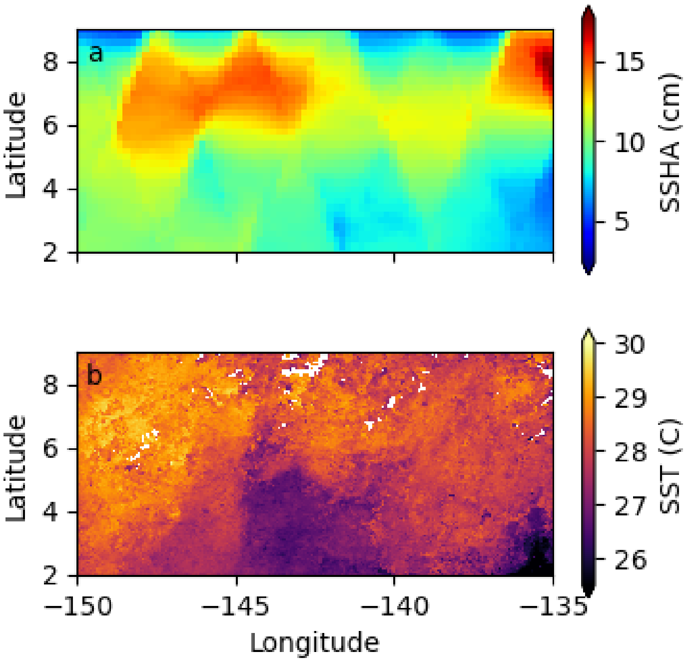

Figure 7.2: (a) Topex SSHA and (b) Pathfinder SST in the area of interest in the equatorial Pacific with no translation. A search radius of 1.5° is used in mapping SSHA, while SST is the mean of co-located pixels.

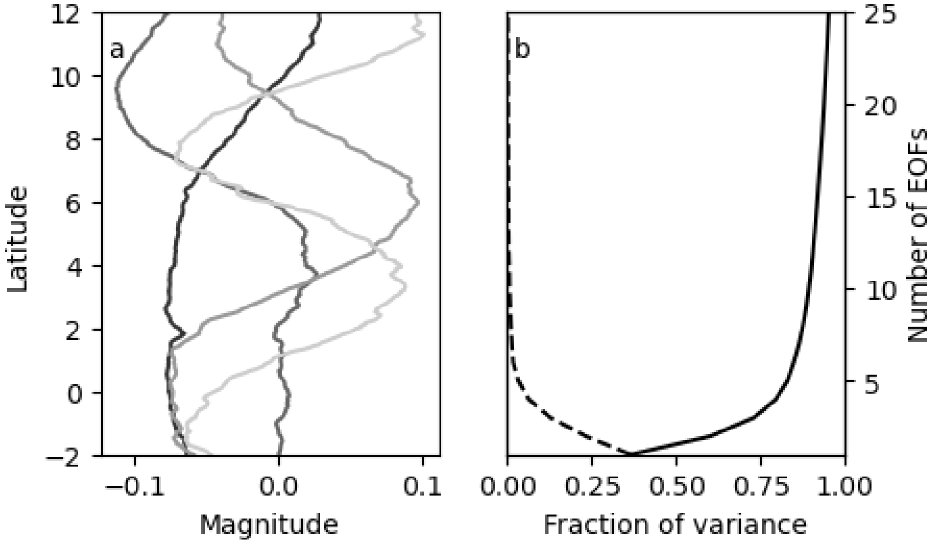

Figure 7.3: (a) Magnitude of the first 4 TOPEX EOFs formed over the equatorial Pacific in the area of interest between -2°N and 12°N, 150°W and 135°W, with higher EOFs being in lighter grey, with (b) the magnitude of the variance explained by a given number of EOFs (solid line) and the magnitude of the variance explained by each EOFs (dashed).

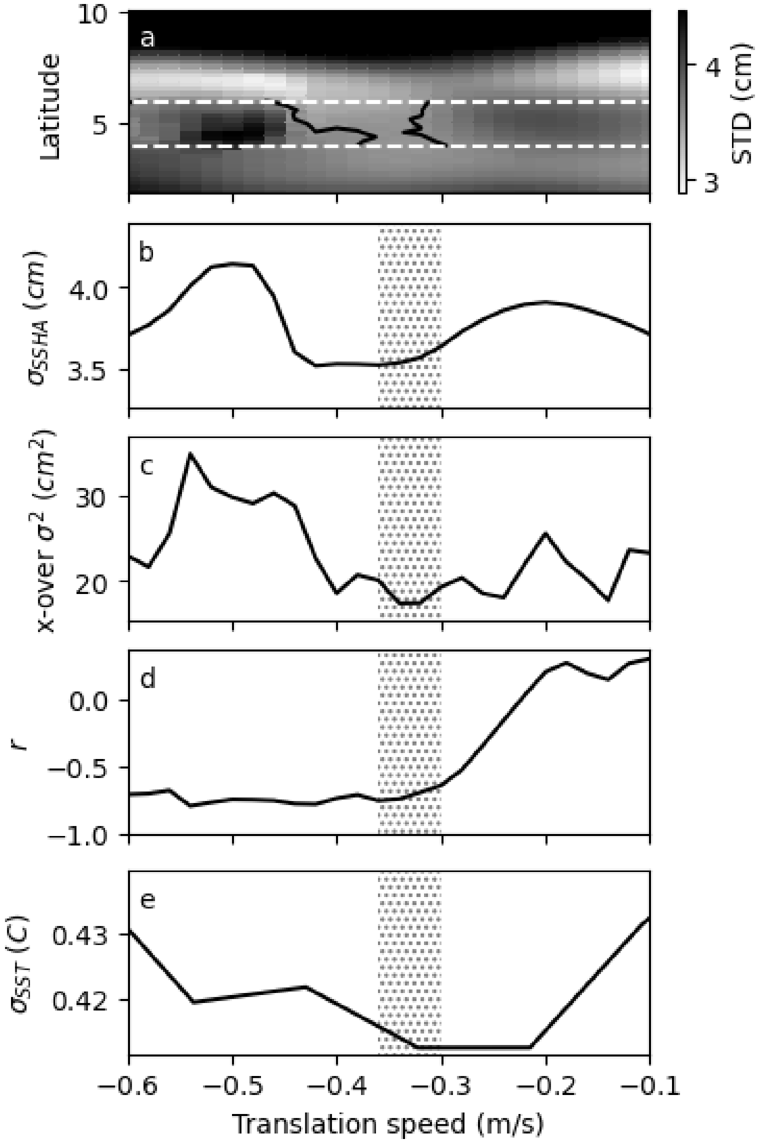

Figure 7.4: (a) The zonal average of the standard deviation of Topex SSHA gridding over 140°W to 145°W; (b) the meridional average of (a) over 4°N to 6°N; (c) the variance at cross-over points in the translated Topex tracks; (d) the correlation coefficient between translated Topex SSHA at 5°N, 140°W with the depth of the 20-C isotherm at a colocated buoy; and (e) the average of variance of Pathfinder SST gridding over 4°N to 6°N and 140°W to 145°W, all for translation speeds between 0.10 and 0.60 m/s westward. Shading in (b) through (e) highlights coincident low errors and high correlation. In (a), the black contours are at 3.58 cm to highlight the minimum between the white dashed contours bounding 4°N to 6°N.

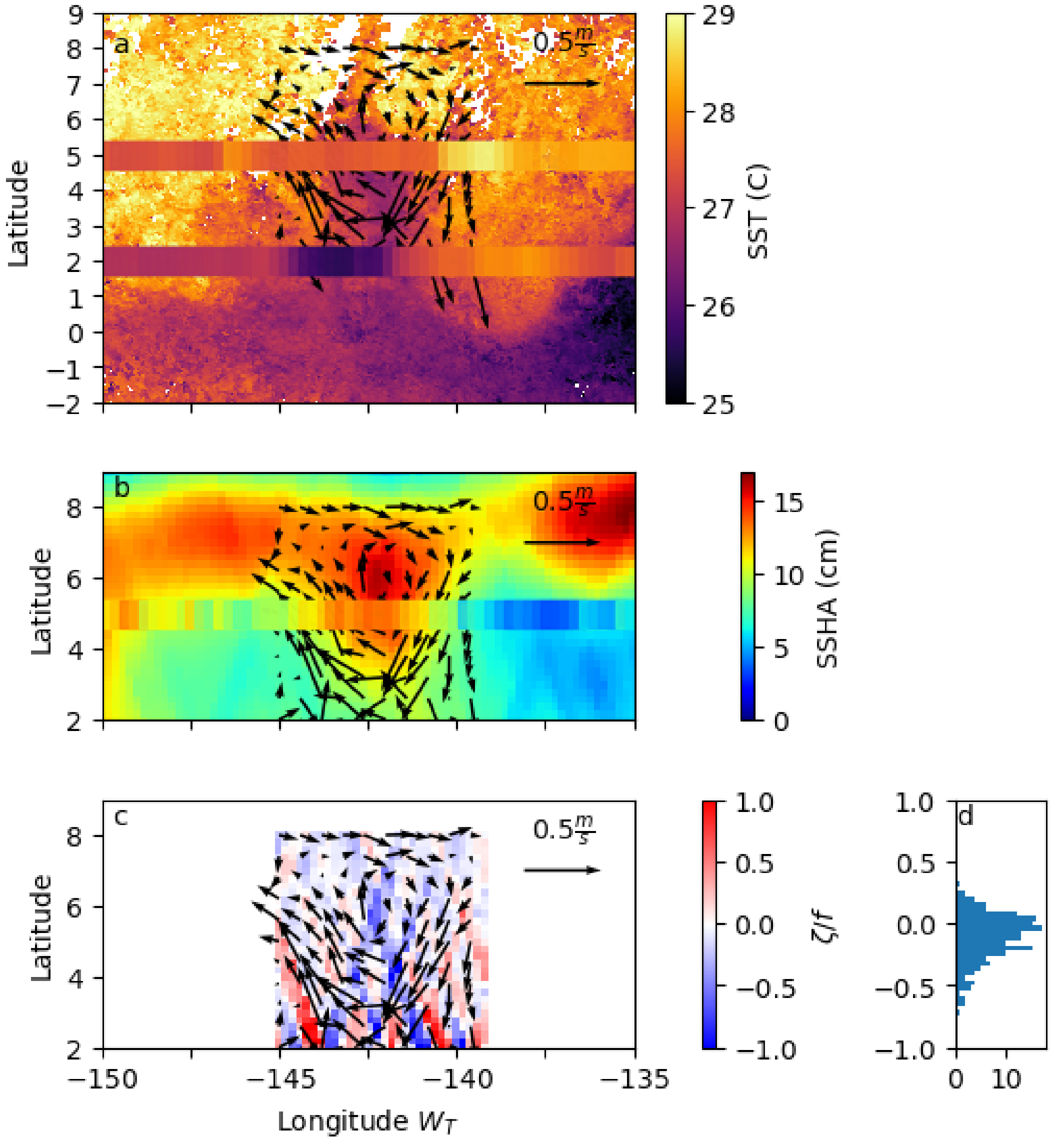

Figure 7.5: (a) Gridded SST field in the area of interest from 2°S to 9°N, 150°W to 135°W, using NASA Pathfinder data for the period overlapping the SIR-C SAR images; (b) gridded SSHA field in the area of interest from 2°N to 9°N, 150°W to 135°W; (c) vorticity, assuming the optimum translation speed of -0.34 m/s. The SST (actually 1-m depth temperatures) from the moorings at 2°N, 140°W and at 5°N, 140°W are overlaid on (a) and the inferred SSHA from the mooring at 5°N is overlaid on (b), as similarly color-coded bands. The geostrophic surface velocity vectors inferred in the vicinity of TIV #3 from the gridded SSHA field are overlaid on (b) and (c). The distribution of vorticity within 1.5° of the center of TIV #3 scaled by f at 5°N is shown to the right of the plots.

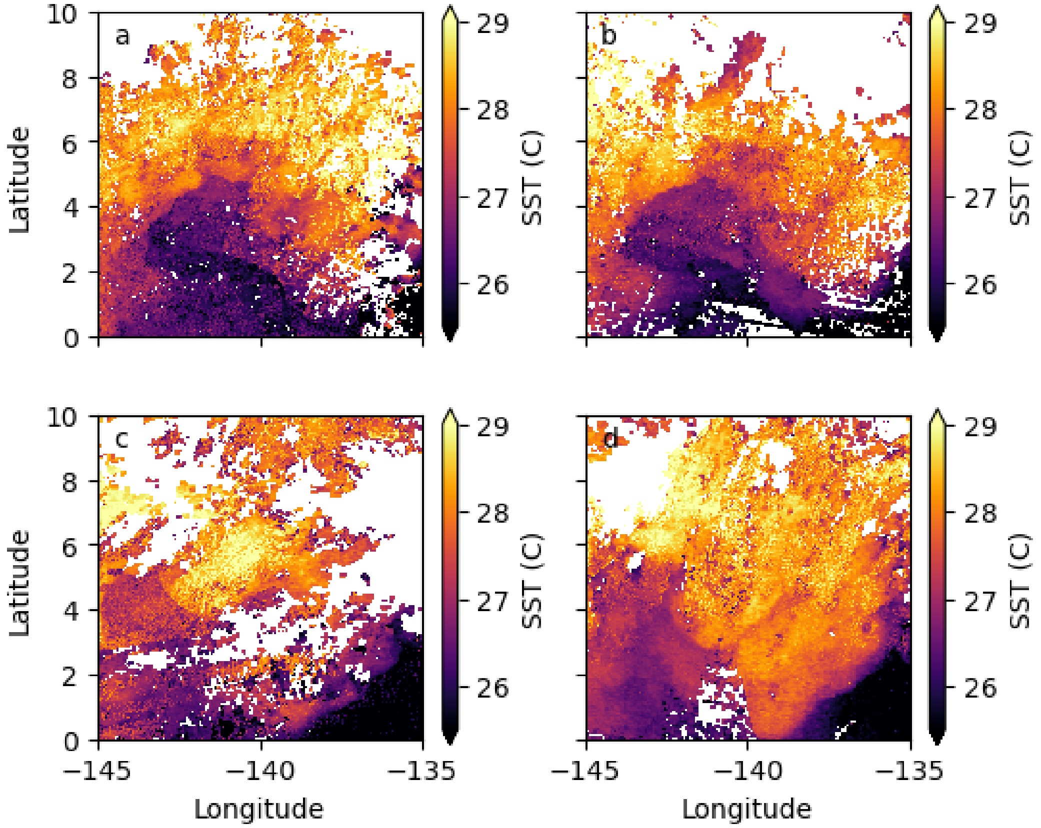

Figure 7.6: Composite of AVHRR and Pathfinder SST in area of interest from 0°N to 10°N, 145°W to 135°W, for yeardays (a) 266, (b) 267, (c) 274, and (d) 276 in 1994.

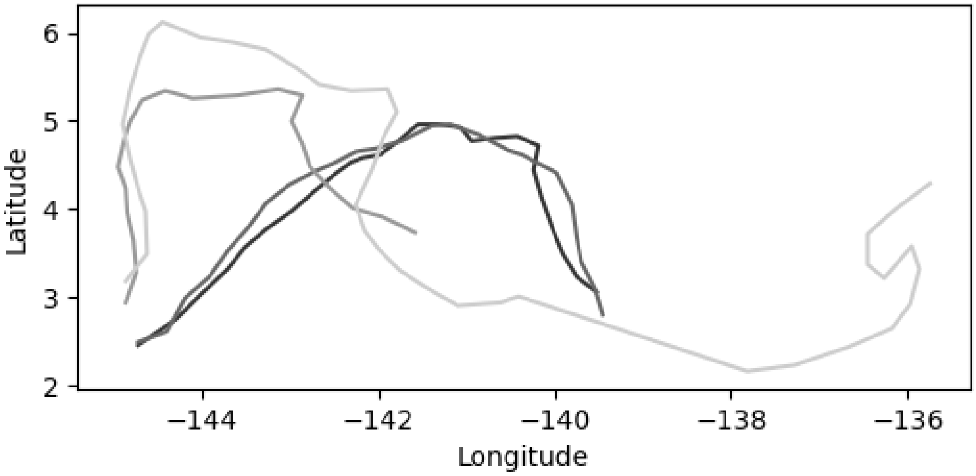

Figure 7.7: Fronts traced in AVHRR/Pathfinder composites in the area of interest from 0°N to 10°N, 145°W to 135°W, on days (from dark to light lines) 266, 267, 274, and 276 in 1994.

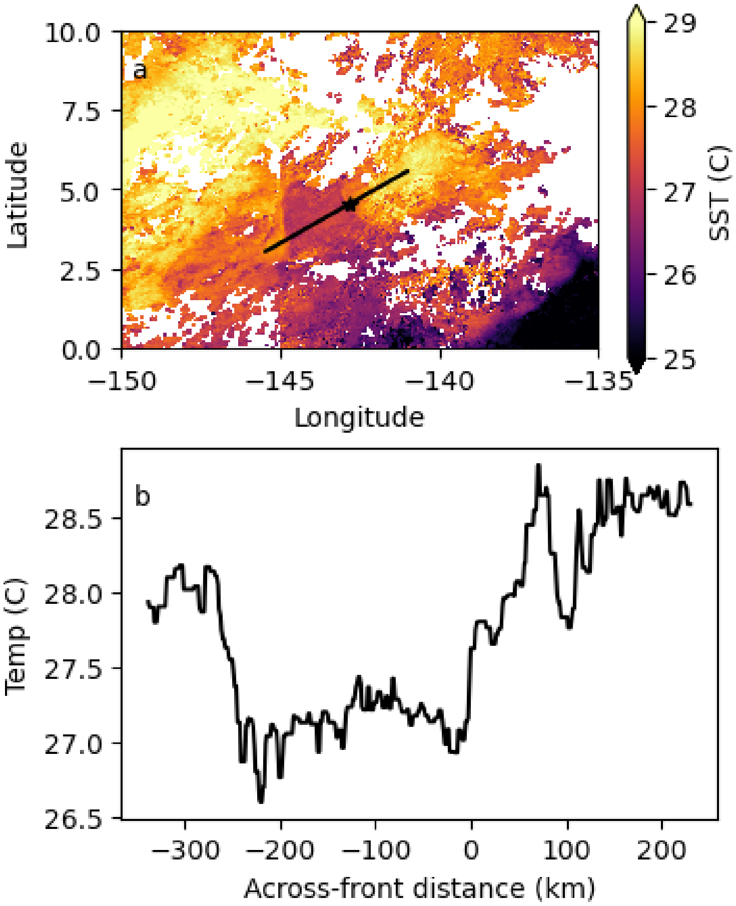

Figure 7.8: (a) AVHRR/Pathfinder SST composite in the area of interest from 0°N to 10°N, 150°W to 135°W, on day 274 with transect across the front (black line) and location of front crossing of transect (black star); and (b) the temperature along the transect in (a) with along-front distance.

7.4 Variability in TIVs

All TIVs are dynamically similar and occur in similar conditions, so there are many similarities between different TIVs but also many differences. Figure 7.9 shows SST and chlorophyll-a concentrations of four different TIVs, all at different locations and times. Chlorophyll-a is higher in colder upwelled water that is enriched in nutrients, so the swirling motion of the TIV is also discernible. The cusps in the NEF created by the swirling of the TIVs are visible in all four sets of panels, though they differ in the details. The time of the year as well as the ENSO state impact the strength of the equatorial Pacific winds, and thus the upwelling and currents. The first two sets of images, on yeardays 149 and 196 in 2016, occur very late in the TIV season, when winds are normally weaker, upwelling is less intense, TIVs are less dynamically active if present at all, and fossil SST signals remain. However, ENSO had switched from a positive phase to a negative phase a few months prior to the first image, so the winds had been abnormally strong in the spring, starting the TIV season earlier than normal. The last two image sets, on yeardays 233 in 2018 and 240 in 2019, occur within the normal TIV season, and the Ocean Niño Index is neutral, indicating neither an El Niño or a La Niña. The winds, upwelling, and currents would be stronger in the last two panels than in the first two panels.

For the TIV on yearday 149 in 2016, colder, chlorophyll-a rich water is advected upward into a blunt cusp while the warmer water swirled southward and formed a smooth front to the south. The TIV two months later differs in that the NEF cusp extends further northward while the warmer water swirled southwards dips into and mixes with the colder water south of the NEF, creating a “dent” in the southern section of the front. The TIV on yearday 233 in 2018 is even more different, with cold water from the NEF cusp being advected eastward across the northern part of the TIV, and the TIV core is colder than the two earlier ones. The leading front on the western edge of the TIV is more diffuse, whereas in the previous two TIVs, this front is well-defined in both SST and chlorophyll-a. The final TIV in Figure 7.9, from yearday 240 in 2019, has a better-defined leading front than the TIV from a year earlier, and the cold water was not advected as far across the northern flank of the TIV as it was then, though still much farther than the two earliest examples. The very center of the core is warmer than the 2018 TIV, and this warm water extends out the eastern side of the TIV.

The resolution of the SST and chlorophyll-a images is not small enough to accurately resolve the features of the TIVs on sub-mesoscales. However, we know that sub-mesoscales are full of filaments, fronts, currents, and eddies that vary widely over small distances and on short timescales. Because of this, TIVs likely vary even more over small scales than visible here, and each TIV likely varies widely over its lifetime.

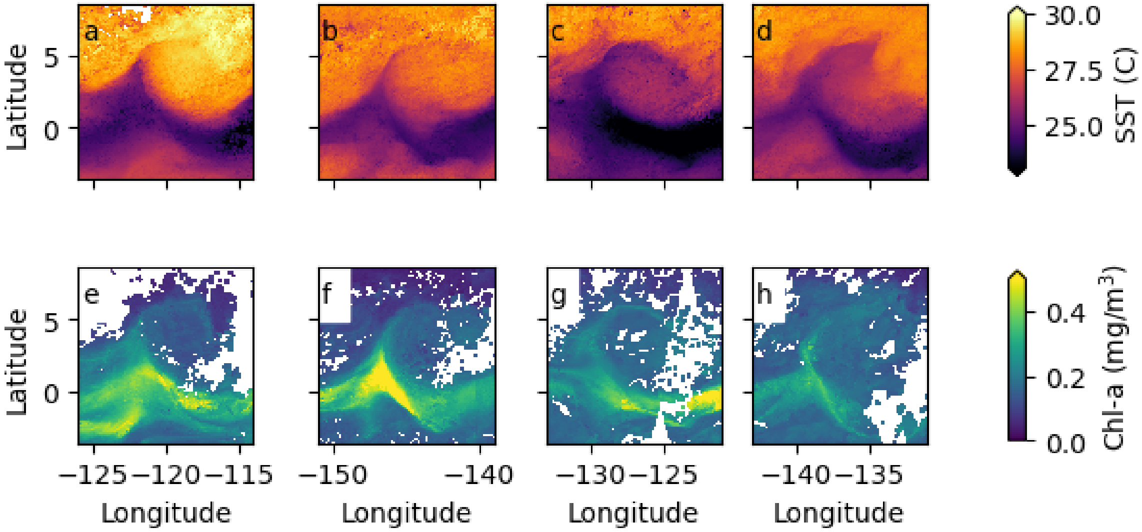

Figure 7.9: MODIS (top row) SST and (bottom row) chlorophyll-a in the equatorial Pacific for (a & e) day 149 in 2016, (b & f) day 196 in 2016, (c & g) day 233 in 2018, and (d & h) day 240 in 2019.

7.5 Summary and conclusions

Winds in the equatorial Pacific create conditions that spin up anticyclonic TIVs that deform the strong temperature front they travel along into cusps. A TIV centered around 6°N, 142°W in early October 1994 had a diameter of about 350 km with maximum swirl velocity of 0.7 m/s and average core vorticity of $-0.2f$. This TIV was seen in a frame of reference translating at 0.32 m/s westward in Pathfinder SST as a cusp of water about 3 C colder than the surrounding surface water protruding northward on the western flank of the vortex. Additionally, the passage of warm and cold water associated with the frontal cusp is seen in SST at two moorings at 2°N and 5°N, 140°W; at the lower-latitude mooring, the SST difference between the cold cusp and warmer water that followed was about 2.2 C, while for the more northerly mooring, that difference was about the same, but the actual temperatures were 1.5 C warmer. In AVHRR snapshots, this temperature difference was only 1.5 C, but there are multiple jumps in temperature when crossing the front indicating several closely-spaced but weaker fronts. AVHRR snapshots show that the fronts around the cold cusp shifted westward in time; the western part of the front at the cusp rotates counterclockwise, while the eastern part of the front at the cusp rotates counterclockwise at first, and then deforms because of the swirling on the currents. The TIV was also in Topex SSHA (in a frame of reference translating at -0.34 m/s westward) as a 0.15 m high point. The SSHA at the 5°N, 140°W mooring derived from the depth of the 20-C isotherm assuming a 1.5-layer model using the inferred density difference between the layers found a 0.13-m high coincident with the TIV followed by a 0.10-m drop following the passage of the vortex. While there are some differences in the details between these observations and inferred quantities, they agree generally with the presence of a TIV.

SST and chlorophyll-a data from MODIS shows the swirling of water with different temperatures and chlorophyl-a concentrations in four different TIVs that also show seasonality and the effects of the ENSO cycle on TIV dynamics. These four TIVs have many similarities at larger scales, though they differ in some of the smaller scale details and are expected to differ even more on sub-mesoscales, though MODIS data does not have the resolution to confirm this.

Chapter 8

TIV fronts, frontal evolution, and frontal instabilities

Where it is shown that in a Rossby number $= -1$ *anticyclonic vortex on the North Equatorial Front, fronts inside the vortex are advected by the swirling and may develop waves, cusps, or even breaks in the line of the front, evidence of shear current instabilities which do not require that total potential vorticity is negative.*

8.1 Introduction

While satellite-derived sea surface temperature (SST) and sea surface height anomaly (SSHA) are suitable for examining mesoscale structures in tropical instability vortices (TIVs), this is not the case for sub-mesoscale structures as data with very fine spatial resolution is necessary. Synthetic aperture radar (SAR), with spatial resolution as fine as 25 m by 25 m, is ideal. Satellite-borne SARs transmit signals with frequencies of 1 GHz to 12 GHz (wavelengths 2 cm to 30 cm; 24 cm for L-band, 6 cm for C-band, and 3 cm for X-band) in the direction orthogonal to flight, the slant range direction [Figure 6.3]. Slant ranges R to the targets are inferred from the travel times, with the bandwidth B of the signal determining the slant range resolution $dR = c/2B$. The azimuths of the targets (in the flight direction) are inferred by processing the Doppler history of the received signals over a certain time interval dt, resulting in a synthesized antenna aperture D_s in the direction of flight $D_s = dt \cdot v$, where v ~7 km/s is the orbital velocity. The azimuthal resolution scales as $dA \sim Rl/2D_s$ for radio wavelength l. With synthetic aperture processing, the azimuthal resolution is much finer than would be obtained using the real physical aperture of the radar antenna, the real beam-width nevertheless limiting the usable integration time dt. For example, at 1.2 GHz L-band ($\lambda = 0.25$ m), from a slant range $R = 275$ km, a 10-m azimuthal ground resolution can be reached with a synthetic aperture $D_s = 3.5$ km, or dt =~0.5 s flight time, using a physical antenna a mere $d = 12$ m long having a physical beam-width of 1.2° or an equivalent real aperture ground resolution of 5.5 km [*Moreira et al.*, 2013]. A critical parameter of space-borne SAR is the ratio R/v, which governs the importance of the so-called azimuthal modulation, i.e. the different imaging response of surface waves whether they travel in the range or azimuth directions. SARs at the typical shuttle altitude of ~225 km provide better imaging of waves traveling in the azimuth direction than SARs at the typical polar orbiter altitude of ~800 km. Vertical polarization yields the strongest back-scatter signal. Processes that modulate the amplitude of the matching capillary waves result in variations of the back-scattered intensity that are visible in the SAR images. Specific to the synthetic aperture processing, processes that Doppler-shift the back-scattered electromagnetic waves will also display signatures in the processed SAR images. Wind stress changes, wave-current interactions, surfactant-induced damping, and heavy rain are the primary processes that modify capillary waves and thus are visible in SAR imagery.

The sheer size of data streamed by SARs until recently restricted coverage to when the satellites were in view of high bandwidth down-link earth stations, of which only a few existed. Recording by on-board tape recorders was also very limited. For a long time, this precluded SAR coverage of the equatorial Pacific and the NEF area. The Shuttle Imaging Radar SIR-C/X-SAR missions [*Evans et al.*, 1993] launched in April and October 1994 were truly the first opportunity to image the equatorial Pacific NEF with SARs. SIR-C was equipped with three SARs operated simultaneously: two dual-polarization SARs at L-band and C-band built by the Jet Propulsion Laboratory, and a vertically polarized SAR at X-band built by the German Space Agency.

The images were processed with typical spatial resolutions of 25 m and 12.5 m, respectively. The Shuttle Imaging Radar SIR-C/X-SAR missions were the first opportunity to image the NEF region with SAR, but the missions consisted of only two 11-d flights, and support for post-mission data processing, calibration, and correction was limited, reducing the utility of the images. Additionally, the missions occurred during a gap in satellite ocean color missions and at a time when storage and transfer of high-resolution data was both difficult and costly, limiting supporting observations.

The European Space Agency's Sentinel-1 mission addresses these issues with two satellites launched April 2014 and 2016 carrying C-band SAR instruments, each with a 12-d repeat cycle but together, an effective six-d repeat cycle. Imagettes, or 20 km by 20 km sections of the ocean imaged every 100 km with alternating look angles (∼24° and ∼37°), produce a sparsely sampled view of the open ocean. Combined with the recent flourishing of satellite-based ocean observation, with multiple satellites measuring SST, ocean color, surface winds, etc., this mission provides an opportunity to observe a variety of fronts in different TIVs.

In this chapter, the aim is to place multi-frequency SAR data from the SIR-C experiment [*Evans et al.*, 1993; *Flament*, 1995] and recent SAR observations from European Space Agency Sentinel-1 satellites into the framework provided by the analysis in Chapter 7, with a focus on the fronts within TIVs, the variety of their features, their spatial evolution, and their instabilities. The data is described in section 2, and the TIV fronts and their imaging are in section 3. Section 4 covers the temporal evolution of the fronts in one TIV, while section 5 describes frontal instabilities and what can be inferred about those in TIVs. The final section contains a brief summary and conclusions.

8.2 Data

During the second shuttle mission lasting from day 274 to day 284 in 1994, SIR-C acquired an extensive set of SAR images over the equatorial Pacific at the peak of the instability wave season. Images taken on days 279, 280, and 282 in 1994 in the trailing front area of a TIV centered at 6°N 142°W are the best for revealing the NEF [Figure 8.1]. All 3 bands were used.

In-situ data from the two TIWE cruises was also used [Figure 8.2]. TIWE-1 took place in August and September 1990, while TIWE-2 took place in November and December 1990. For both cruises, towed CTD on a seasoar platform [*Sawyer et al.*, 1995] and shipboard acoustic Doppler current profiler (ADCP) [*Firing et al.*, 1994] were used. These two data sets were processed for days 214 to 252 in 1990 for TIWE-1 and days 314 to 348 in 1990 for TIWE-2 at ∼5 min resolution along the cruise track with 2-m depth resolution covering from the surface down to 300 m; however, the vertical resolution for the ADCP was 8 m.

All Sentinel 1 imagettes [*Copernicus; European Space Agency*, 2011] before January 2020 between 0°N and 10°N, 115°N and 160°W, were examined to produce a record of fronts associated with TIVs; eight-hundred imagettes with fronts were selected from ∼90,000 imagettes in the selected region during TIW seasons, identified based on the condition of the NEF in SST images [*IFREMER/CERSAT*, 2007]. These 800 were compared with SST and chlorophyll-a observations, and 75 were chosen for further analysis with attention to selecting images with fronts displaying a variety of features. The surface roughness, the ratio between observed and modeled back-scatter [*Quilfen et al.*, 1998], is independent of the SAR viewing angle and was selected over raw back-scatter.

Gridded observations of SST and chlorophyll concentration with 4-km resolution from MODIS Aqua and Terra satellite passes [see Chapter 7 for details; *NASA Goddard SFC, OEL OBPG*, 2018a,b, 2020a,b] over a three-day window centered on each SAR imagette were compared to SAR fronts. The MODIS observations were used in 100-km-by-100-km sections to help identify surrounding features.

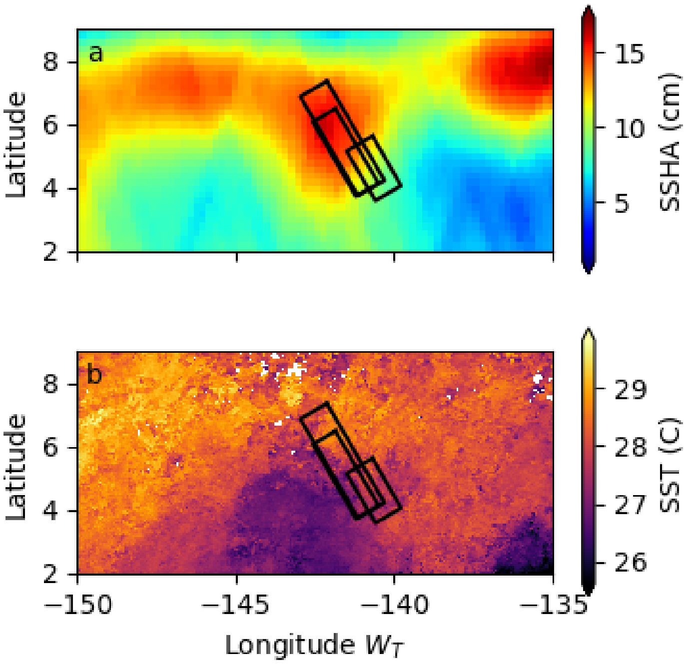

Figure 8.1: Footprints of SIR-C images taken on days 279, 280, and 282 of 1994 overlaid onto (a) SSHA and (b) SST in moving frames of reference (details in Chapter 7.3) in the area of interest from 2°N to 9°N, 150°W to 135°W.

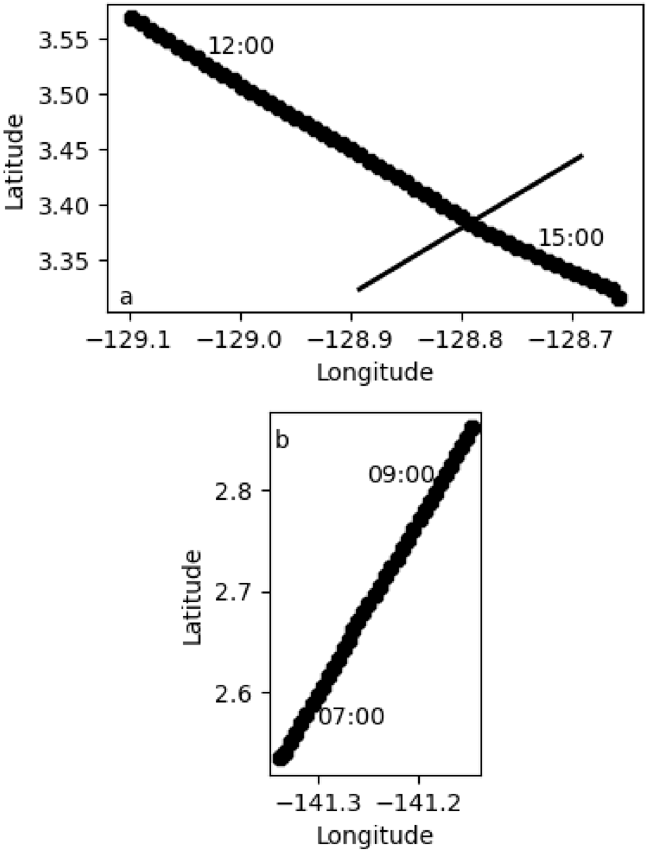

Figure 8.2: (a) Partial cruise track for TIWE-1 with front marked in black and times on day 232 in 1990; and (b) partial cruise track for TIWE-2 with times on day 330 in 1990. The front location is not known exactly in (b) as it is in (a). For both (a) and (b), only the section of track corresponding to data in Figure 8.9 and 8.11, respectively, are shown.

8.3 TIV fronts in SAR images

Fronts in SAR images [Figure 8.3] are really fronts in back-scatter intensity and are caused by physical processes in the ocean and atmospheric boundary layer. Fronts themselves are visible as bright lines because of the increased surface roughness due to increased wave breaking because of convergence at fronts. There are other changes at fronts that make them visible in other data. TIVs lie on the NEF and swirl cold, salty, dense, upwelled water enriched in chlorophyll-a northward on the western flank and warm, fresher, lighter, surface water depleted in chlorophyll-a southward on the eastern flank; SAR fronts are thus frequently coincident with SST and chlorophyll fronts [*Kuang et al.*, 2012, Figure 8.3]. The SAR image on day 154 in 2016 is on the trailing front, and there is a strong gradient of SST and chlorophyll-a across the front. The front in the SAR image on day 218 in 2016 lies on a gently curved section of the leading front, which has a clear gradient of SST across it though not a clear gradient of chlorophyll-a. For the SAR image on day 365 in 2017, the trailing front at the same location has a strong gradient in SST but is not collocated with a front in chlorophyll-a. The conditions of the SAR images on days 3 of 2018 and 254 in 2019 are similar in that both occur on fairly straight sections of leading fronts that have clear SST differences, but clouds in the chlorophyll-a images prevent determining whether there is a collocated chlorophyll-a front. The last SAR image, from day 273 in 2019, is from the upper section of the trailing front on a cold cusp that has cross-frontal differences in both SST and chlorophyll-a.

Across-front sections of SIR-C X-SAR back-scatter intensity provide information on the processes occurring near the trailing front. The intensity averaged along the front [Figure 8.4] peaks at the front, but there is a distinct asymmetry: on the eastern side of the front, intensity increases significantly over the background level over less than 250 m, while on the western side of the front, intensity decreases exponentially to the background level over ∼6 km. This suggests that surface roughness at 1- to 10-cm scales suddenly increases from east to west but decays progressively after crossing the front. Given that SE trade winds produce SE windseas at this location, short wind waves presumably break in concert at the front and continue to do so with decreasing frequency down-wave of the front. This could be indicative of convergence at the front as wave-breaking increases at lines of convergence [*Johannessen et al.*, 1997].

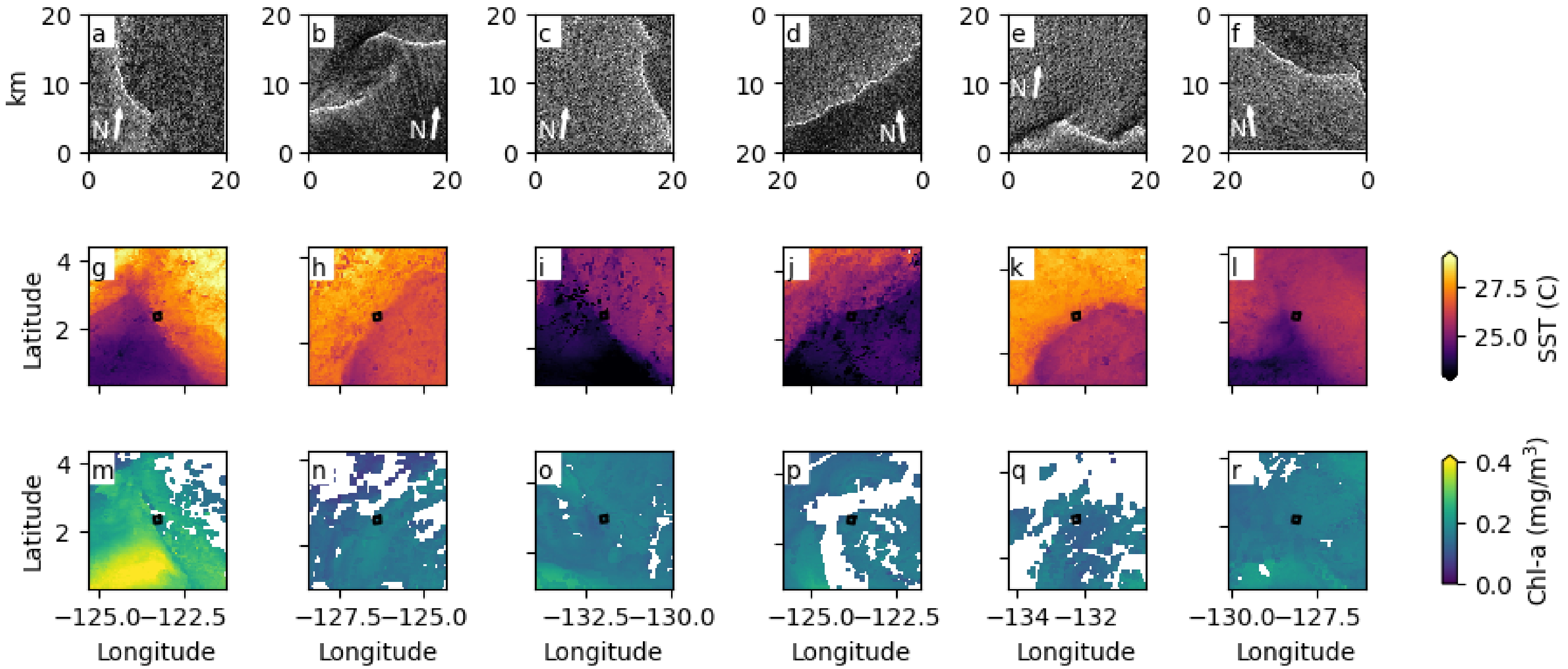

Figure 8.3: Sentinel images, MODIS SST, and MODIS CHL-a levels on days (a,g,m) 154 in 2016, (b,h,n) 218 in 2016, (c,i,o) 365 in 2017, (d,j,p) 3 in 2018, (e,k,q) 254 in 2019, and (f,l,r) 273 in 2019. The direction of north is marked with white arrows in the SAR images, and black squares in the center of each MODIS panel is the outline of the corresponding SAR image.

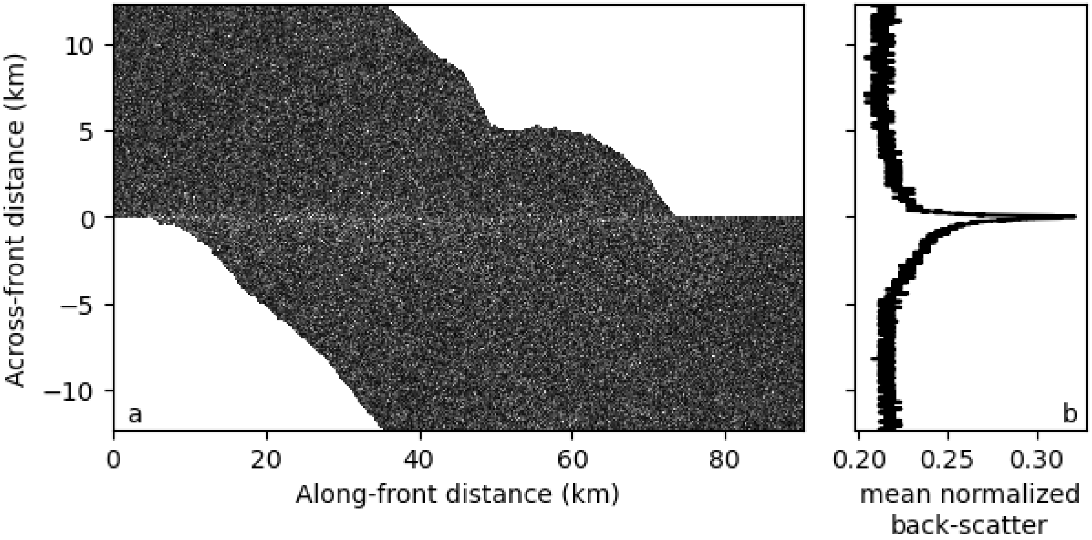

Figure 8.4: X-SAR back-scatter from day 279 in 1994 from the region around 5°N, 141°W in the equatorial Pacific (a) with image shifted to align front, and (b) back-scatter averaged in along-front direction to give mean back-scatter when crossing the front. The top section of the image is east of the front, while the bottom half is west of the front.

8.4 The temporal evolution of a front

Footprints of the SIR-C/X-SAR images overlaid on the SSHA and SST fields viewed from the translating frame of reference [Figure 8.1] show clustering around the trailing front of a TIV at the transition from cold to warm surface water. During the 10-d shuttle mission, the average wind was 7.2 m/s southeasterly at the 2°N mooring (the 5°N mooring did not return meteorological data) and 7 m/s southeasterly from the gridded ERS-1 scatterometer [*Bentamy et al.*, 2002]. The wave conditions from the WAVERYS reanalysis [*E.U. Copernicus Marine Service Information*, 2021a] indicate a dominant southwesterly swell at about 14 s, corresponding to a wavelength of about 300 m, superimposed over weaker swell from the north or northwest at 13 s (260 m), and wind seas from the southeast.

Figure 8.5 shows the quick-look images in range v. azimuth coordinates for three SAR images taken on days 279, 280, and 282 in 1994, whose footprints are in Figure 8.1. These fronts, traced manually on the SAR images, were overlaid on the AVHRR composite images on days 274 and 276 [Figures 8.6]. While these AVHRR images are closest in time to the SAR images, there is inevitably an uncertainty in the translation speed over such short intervals, especially given the rapid evolution of the locations and orientations of the fronts strained by the swirling motion. Rather than adjust the positions based on the monthly-averaged translation speed inferred from the optimum gridding of the altimeter SSHA data, we subjectively used an ad-hoc translation to match the back-scatter intensity and SST signatures. This approach is validated by analysis of a larger data set of SAR images from Sentinel-1 in which the back-scatter fronts are consistently co-located with SST and ocean fronts imaged by other satellite sensors [Chapter 8.3]

This succession of three SAR images shows the evolution of the trailing front, oriented linearly SE to NW at about 5.5°N, 141.5°W. On day 279, the front in the SIR-C and X-SAR images [Figure 8.7a] is fairly straight except for a "kink" at 5.1°N, 141.3°W, that departs from the straight path for ∼10 km. On day 280 [Figure 8.7b], the front is very similar, including the kink (now at 6.0°N, 143.5°W). However, the direction of the front has rotated clockwise by about 8.5°. On day 282 [Figure 8.7c], the front has a stronger curvature, running initially N to S and then bending southeastward with a radius of curvature of ∼150 km at 4.3°N, 140.7°W. As the TIV rotates, cold and warm water are advected. The NEF, and thus the fronts in SAR imagery, are swirled around and deformed. Additionally, in the last SAR image, many small-scale wavy deformations of the front with scales of 1.5 to 6.5 km have appeared [Figure 8.8].

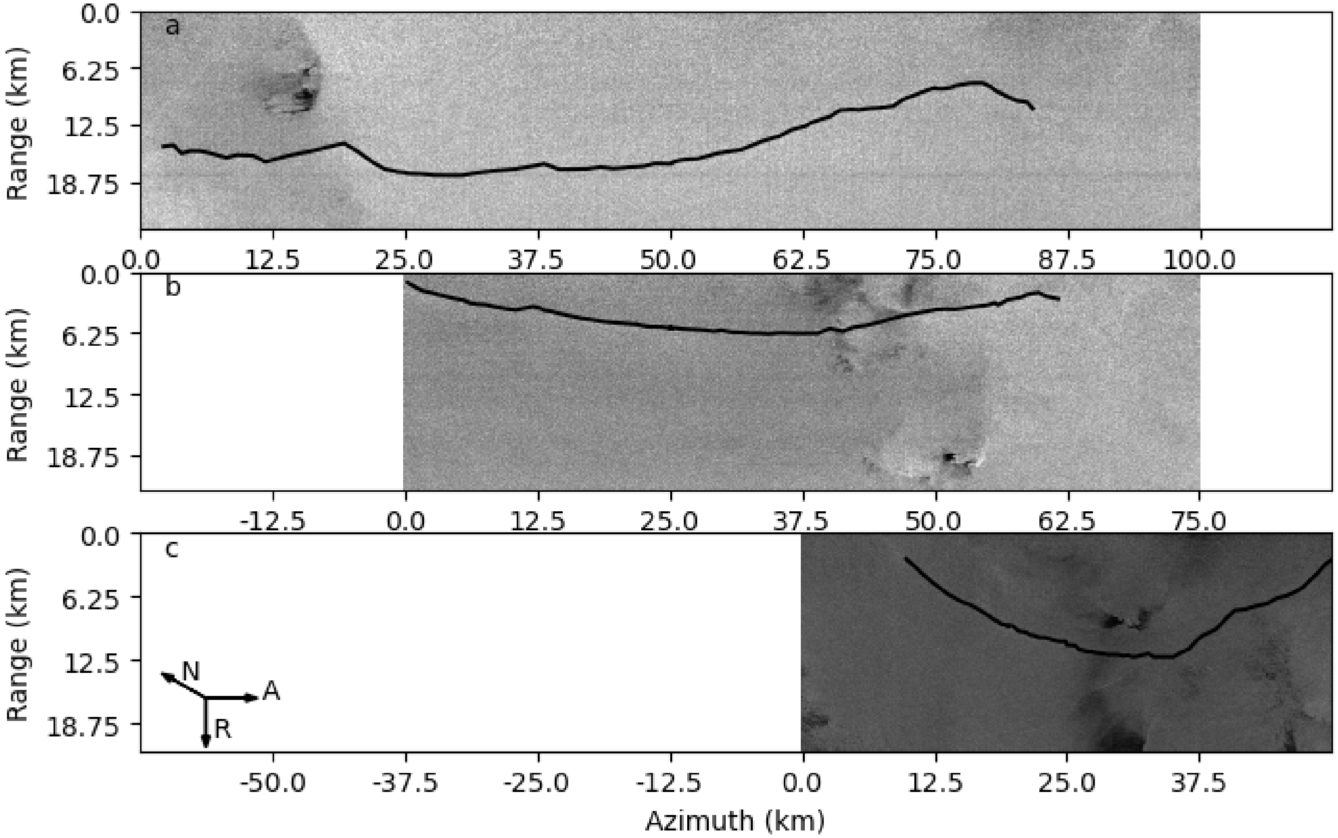

Figure 8.5: SAR back-scatter for quick-look images taken on yeardays (a) 279, (b) 280, and (c) 282 of 1994 in the equatorial Pacific around 5°N, 141°W, with fronts in black. The arrows at the bottom left denote North, Range, and Azimuth directions; the flight direction is in the positive azimuth direction. The azimuth coordinates of each image have been shifted to display the three images correctly in azimuth to one another.

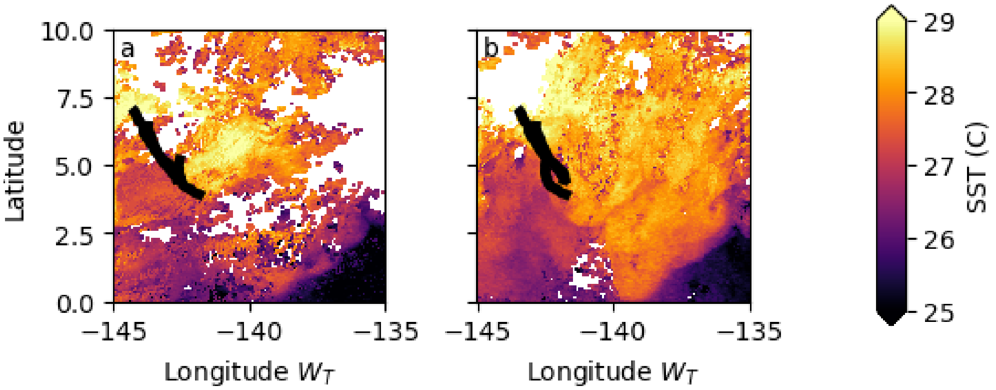

Figure 8.6: SAR fronts (black lines) on AVHRR/Pathfinder SST composite (greyscale) images for days (a) 274 and (b) 276 in 1994 in the equatorial Pacific from 0°N to 10°N, 145°W to 135°W in the translating frame of reference centered on day 274 in 1994.

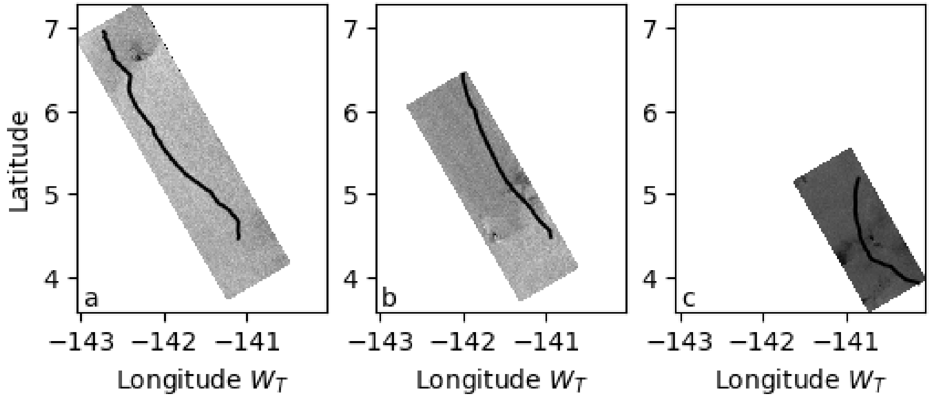

Figure 8.7: SAR back-scatter for quick-look images taken on yeardays (a) 279, (b) 280, and (c) 282 of 1994 in the equatorial Pacific from 0°N to 10°N, 145°W to 135°W in the translating frame of reference centered on day 274 in 1994, with fronts in black.

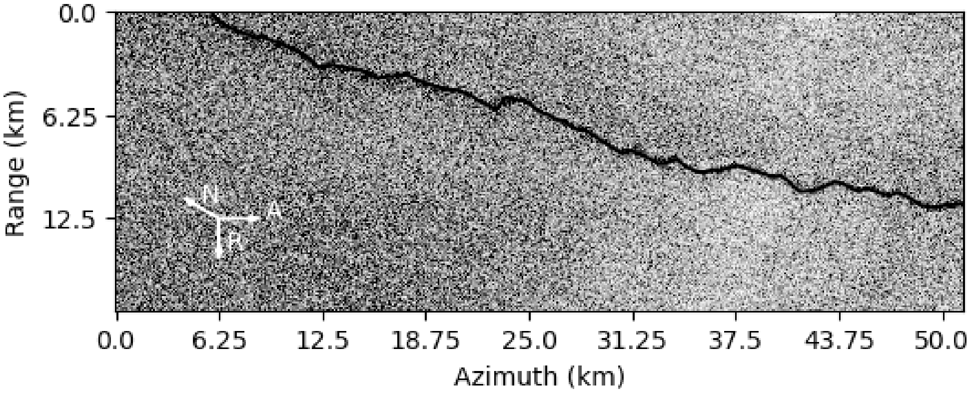

Figure 8.8: SAR back-scatter zoom for X-SAR on day 282 in 1994 in instrument coordinates (range v. azimuth). Front is in black.

8.5 Frontal instabilities

The small-scale deformations of the SAR image on day 282 in 1994 visible in Figure 8.8 are indicative of instabilities developing along the axis of a sub-mesoscale surface density front, which can deform straight or curved fronts into very wavy, cuspy, or even fractured fronts. The front is oriented linearly from north to south with a slight bowing outward to the west, but it has many small scale variations in the line of the front. Winds are down-front, which produces Ekman currents that cross the front from more to less dense water, opposing the ageostrophic secondary circulation and restricting destruction of the cross-front horizontal buoyancy gradient. Other examples of instabilities of the trailing front are in Figure 8.3a, c, and f. The last of these has cyclonic vorticity at the surface from large-scale surface currents. The lambda-shaped occlusion at the density front is very similar to the early stages of the shedding of cyclones in *Ubelmann and Fu* [2011b], where strong downwelling at the surface from strong convergence creates vortex stretching that increases cyclonic vorticity at the front; the front folds cyclonically, and a cyclonic eddy spins off from the front. Winds blow from the southeast, across the front at a shallow angle, so there are some Ekman currents that oppose frontolysis.

One example of a leading front with instabilities is in Figure 8.3d. The front is oriented southwest to northeast with a linear shape marred by cusps with scales between 2 and 10 km. Figure 8.3e is also on the leading front; the shape of this instability, with the strong cusps, may be an earlier stage of Figure 8.3b, where the line of the front is broken. The winds for these images are nearly directly across the fronts, so the Ekman currents have little impact on the expected ageostrophic secondary circulations.

Oceanic fronts can appear in SAR images because there can be convergence at the front, which impacts surface waves and thus surface roughness. The SAR fronts can have many shapes including straight lines, curved lines, wavy lines, cuspy lines, lambda-shaped cusps, and combinations of these [Figure 8.3]. While straight lines and even curved lines can result from simple situations with convergence along a line, wavy fronts, cuspy fronts, and lambda-shaped cusps are due to instabilities. The two main fronts in TIVs have different properties that may impact the type of instability most likely to occur; we discuss these fronts and their instabilities using data from a variety of sources and TIVs despite the significant variability present and thus we limit our conclusions to general statements about “possible” and “likely” processes occurring instead of making concrete statements about the dynamics within a single real TIV instance.

Leading fronts have warm, fresh, less dense water to the west and cold, salty, more dense water to the east. The front forms where the cold water advected northward by the swirling TIV meets the warm equatorial surface waters; the more dense water subducts under the less dense water at the front where there is strong convergence [*Kennan and Flament*, 2000].

The TIWE-1 cruise crossed a leading front from NW to SE, and CTD data [Figure 8.9a] shows that warm, fresher water to the northwest of the front in the shape of a wedge lies above colder, saltier water that extends to the surface southeast of the front. Stratification N^2 is an order of magnitude larger at the interface than elsewhere, and the along-track buoyancy gradient is six times larger at the interface than the background value of 1 x 10^{-7}. ADCP currents show a narrow, southwestward along-front current that occurs in the upper mixed layer just northwest of the front, distinct from the northward current on either side [Figure 8.9c and d]. This is the down-front thermal wind shear produced by the density gradient across the front. There are strong north-northwestward currents southeast of the front and below the narrow along-front current, which pushes the more dense water in the vortex core beneath the less dense water outside [Figure 8.9d].

The current shear in the ADCP data is strong at the front and along the frontal surface between the lighter and denser water, particularly the vertical shear which may be as large as $3800f$. Horizontal shear is much smaller at up to $20f$, but the shear of the meridional current is higher and positive along much of the interface, though not isolated solely to the interface. In a numerical model of a TIV at sub-mesoscales [*Holmes et al.*, 2014], the buoyancy flux is positive [Figure 8.10e], meaning that it is reducing the horizontal buoyancy gradient. The horizontal strain and shearing [Figure 8.10f] is positive at the front at the surface, indicating that the buoyancy gradient is being supported by strain and shear in the horizontal velocity. The modeled vertical potential vorticity (PV) is strongly positive at the front; while there is also strong negative horizontal PV, the total PV is positive [Figure 8.10a,c,d].

The trailing front is a different environment than the leading front, located to the east with cold, salty, dense water on the western side and warmer, fresher, lighter water on the eastern side. The TIWE-2 cruise crossed the trailing front from SW to NE, and CTD data shows more dense water to the west of the front and less dense water to the east [Figure 8.11], with this less dense water again forming a wedge above the more dense water. Stratification N^2 is an order of magnitude larger at the interface than elsewhere, and the along-track buoyancy gradient is also an order of magnitude larger at the interface than the background value of 5 x 10^{-8}. Crossing the front was not associated with a change in current direction, but velocities are stronger in the wedge than outside it. There is also a subsurface region below the wedge between 50 and 100 m with north-northwestward currents. As at the leading front, there is very strong vertical shear at the bottom of the wedge. The horizontal shear rapidly switches direction for both zonal and meridional velocities where the wedge is. In the numerical model of *Holmes et al.* [2014], the horizontal buoyancy gradient is weaker than at the leading front, as is the horizontal strain and shear [Figure 8.10e,f]. As at the leading front in the model, there is strong negative baroclinic PV and strong positive vertical PV at the front, which together these make positive total PV at the front and zero or near-zero PV off the front [Figure 8.10a,c,d].

Several kinds of instabilities can develop in the mixed layer with either negative PV or an inflection in the PV:

$$q = \vec{\omega} \cdot \nabla b = (f + \zeta)N^2 + \vec{\omega}_h \cdot \nabla_h b \tag{8.1}$$

for PV q, vorticity $\vec{\omega}$, buoyancy $b = -g\rho/\rho_0$ with density ρ and reference density ρ_0, Coriolis frequency f, vertical vorticity $\zeta = \partial v/\partial x - \partial u/\partial y$, buoyancy frequency $N^2 = (-g/\rho_0)\partial\rho/\partial z$, horizontal vorticity $\vec{\omega}_h = (\partial w/\partial y - \partial v/\partial z)\hat{\mathbf{\imath}} + (\partial u/\partial z - \partial w/\partial x)\hat{\mathbf{\jmath}}$, and horizontal gradient operator ∇_h. Gravitational, centrifugal, and symmetric instabilities require negative PV to develop, and which of these three occurs depends on what condition or process is responsible for the negative PV. On the other hand, barotropic and baroclinic instabilities are associated with a change in sign of the meridional gradient of vertical PV; which of these two occurs depends on what kind of velocity shear is present.

Gravitational instability occurs when stratification is the reason for negative PV. A simple example where this could occur is in an ocean that is horizontally homogeneous with vertical stratification N^2 [Figure 8.12a]; uniform cooling at the surface creates a dense surface layer with $N^2 < 0$ that is unstable [*Haine and Marshall*, 1998]. When dense water lies over less dense water, energy can be released from the background potential to a perturbation.

Inertial or centrifugal instability occurs when vertical vorticity is the reason for negative PV. This can occur, for example, in a stably-stratified ocean with surface geostrophic current $\vec{u}$ [Figure 8.12b]; if a parcel is perturbed down the gradient of the surface elevation η (i.e., the pressure gradient) and the surface current shear, $\partial u/\partial y$, which is equal to vertical vorticity $-\zeta$ here, is strong enough, or $\partial u/\partial y > f$, the perturbation may grow [*Knox*, 2003]. A region of strong negative vertical vorticity in the Northern Hemisphere may allow kinetic energy from the horizontal shear of the current to be released into a perturbation. Note that the vortex as a mesoscale structure is near the inertial instability limit, but here we discuss instability of the fronts on submesoscales.

Symmetric instability occurs when baroclinicity causes negative PV. A simple example where this could occur is in an ocean with lateral mixed layer density gradients with currents in thermal wind balance and no change along the axis of the currents [Figure 8.12c]. When the baroclinicity $\nabla_h b$, which induces thermal wind currents $\partial u/\partial z = -(\partial b/\partial y)/f$, is large enough that the Richardson number $Ri = N^2/|\partial u/\partial z|^2$ becomes small enough or $Ri < f/(\zeta + f)$, the water column becomes unstable to perturbations along and across isopycnals [*Haine and Marshall*, 1998]. A flow with strong baroclinicity that is symmetric may allow kinetic energy from the shear of the thermal wind current to be released into a perturbation.

Barotropic instability requires that the meridional gradient of PV changes sign [*Vallis*, 2006]. In a barotropic ocean with a zonal jet having horizontal shear [Figure 8.12d], the x-direction current structure can be represented by Rayleigh's equation:

$$(\bar{u} - c)\left[-k^2\tilde{\psi} + \frac{\partial^2\tilde{\psi}}{\partial y^2}\right] + \left[\beta - \frac{\partial^2\bar{u}}{\partial y^2}\right]\tilde{\psi} = 0 \tag{8.2}$$

where $\bar{u}$ is the zonal mean velocity and the streamfunction is represented as $\psi = \tilde{\psi}(y)e^{ik(x-ct)}$. Multiplying the Rayleigh equation by the complex conjugate of the streamfunction and integrating over the meridional region of interest yields:

$$\int_{y_1}^{y_2} \left[\left| \frac{\partial \tilde{\psi}}{\partial y} \right|^2 + k^2 |\tilde{\psi}|^2 \right] dy - \int_{y_1}^{y_2} \left[\frac{\beta - \partial^2 \bar{u}/\partial y^2}{\bar{u} - c} \right] |\tilde{\psi}|^2 = 0 \tag{8.3}$$

The second term contains c, the only complex number in the equation, and the imaginary part must vanish through the vanishing of the integral term if instability is to occur. This can occur if the numerator, $\partial(f + \zeta)/\partial y$, changes sign in the domain. Under these conditions, kinetic energy of the mean horizontal shear current can be released into a perturbation. Barotropic instability is also called horizontal shear instability, and it can occur in layered systems both independent of the layers and in the layers themselves [*Killworth*, 1980].

Baroclinic instability also can occur if the meridional gradient of PV changes sign, but the technical conditions are more complex as there are two terms with imaginary components that must vanish to have instability, one dependent on the meridional gradient of PV and the other on the vertical shear [*Vallis*, 2006]. Baroclinic instability can occur, for example, when lighter parcels at deeper depths are perturbed to shallower regions with denser surroundings in a baroclinic ocean with zonal current that varies in latitude [Figure 8.12e]. The second order PV perturbation can be represented as:

$$(\bar{u} - c) \left[\frac{\partial^2 \tilde{\psi}}{\partial y^2} + \frac{\partial}{\partial z} \left(\frac{f_0^2}{N^2} \frac{\partial \tilde{\psi}}{\partial z} \right) - k\tilde{\psi} \right] + \tilde{\psi} \frac{\partial \bar{q}}{\partial y} = 0 \tag{8.4}$$

while the buoyancy equation can be given as:

$$(\bar{u} - c) \frac{\partial \tilde{\psi}}{\partial z} - \tilde{\psi} \frac{\partial \bar{u}}{\partial z} = 0 \tag{8.5}$$

where again $\bar{u}$ is the zonal mean velocity and the streamfunction is represented as

$$\psi = \tilde{\psi}(y)e^{ik(x-ct)} \tag{8.6}$$

plus f_0 is the Coriolis parameter and N^2 is the stratification. Together, these two equations are similar to the Rayleigh equations for barotropic instability. Following similar methods as for barotropic instability, the integral that must vanish if instability is to occur is:

$$-c_i \int_{y_1}^{y_2} \left(\int_{z_1}^{z_2} \frac{|\tilde{\psi}|^2}{|\bar{u}-c|^2} \frac{\partial \bar{q}}{\partial y} dz + \left[\frac{f_0^2 |\tilde{\psi}|^2}{N^2 |\bar{u}-c|^2} \frac{\partial \bar{u}}{\partial z} \right]_{z_1}^{z_2} \right) dy = 0 \tag{8.7}$$

While this may occur if meridional gradient of PV changes sign, because there are two terms there are now several other ways this can occur:

1. $\frac{\partial \bar{q}}{\partial y}$ changes sign in the domain
2. $\frac{\partial \bar{q}}{\partial y}$ is the opposite sign as $\frac{\partial \bar{u}}{\partial z}$ at z_2
3. $\frac{\partial \bar{q}}{\partial y}$ is the same sign as $\frac{\partial \bar{u}}{\partial z}$ at z_1
4. $\frac{\partial \bar{u}}{\partial z}$ is the same sign at both z_1 and z_2 if $\frac{\partial \bar{q}}{\partial y} = 0$

Potential energy of the mean vertical shear current can be released into a perturbation under these conditions. Baroclinic instability confined specifically to the mixed layer, called baroclinic mixed layer instability, has smaller scales (O 1 km and 1 d) than normal baroclinic instability that put it firmly in the sub-mesoscale regime, but those scales are larger near the equator [*Barth*, 1994; *Boccaletti et al.*, 2007]. Baroclinic instability is a type of vertical shear instability.

Kelvin-Helmholtz instabilities are one last kind of instability considered here. This can occur, for example, when the interface between a lighter surface layer and a heavier deeper layer is perturbed by vorticity produced by strong shear between the layers [Figure 8.12f]. This means that if the shear is significantly larger than the stratification such that the Richardson number $Ri < 1/4$, then kinetic energy from the mean vertical shear current can be released into a perturbation. Kelvin-Helmholtz instabilities are also a type of vertical shear instability.

Numerous studies have diagnosed the instabilities present at fronts, more with modeling than observations because of the logistical challenges involved in acquiring sub-mesoscale observations. Symmetric instability was found in several studies to occur at sub-mesoscale fronts [*Peng et al.*, 2020; *Thomas et al.*, 2013], sometimes in series or simultaneously with baroclinic instabilities [*Mied et al.*, 1999; *Skyllingstad and Samelson*, 2020; *Stamper and Taylor*, 2017]. Baroclinic mixed layer instabilities are the likely culprit in several modeling studies [*Buckingham et al.*, 2017; *Callies and Ferrari*, 2018]. Additionally, ageostrophic baroclinic instabilities allow restratification of the mixed layer to proceed faster by disrupting the thermal wind balance at the front [*Boccaletti et al.*, 2007]. With all of this in mind, what can be determined regarding the frontal instabilities in TIVs visible in SAR imagery?

Examining the PV from *Holmes et al.* [2014] on the leading front, there is strong positive vertical PV at the front; as gravitational and inertial instabilities both have negative vertical PV, they do not likely play a role in the instability of the leading front. There is strong negative horizontal PV, which is required for symmetric instability, but, together with the strong positive vertical PV, there is positive total PV at the front, which eliminates symmetric instability as well. As total PV is higher at the front but lower off the front, there is an inflection point. This means that barotropic instability and baroclinic instability could still play roles. Also, there is strong horizontal and vertical shear, which support these types of instability. While there is very strong vertical shear and there is an isolated patch of low Richardson number ($Ri<1/4$) in the cruise data, this is not true in the model; the vertical resolution of the shipboard ADCP is 8 m, which limits the usefulness of calculated Richardson numbers.

As at the leading front, *Holmes et al.* [2014] shows strong negative baroclinic PV and strong positive vertical PV at the trailing front, which together make positive total PV at the front and zero or near-zero PV off the front, eliminating gravitational, inertial, and symmetric instabilities as likely mechanisms while allowing barotropic and baroclinic instabilities. The strong horizontal and vertical shear to support barotropic instability and baroclinic instability are present. This time, there are regions of low Richardson number in both data and model that would permit Kelvin-Helmholz instability to play a role. However, as noted above, the limits of shipboard ADCP make the Richardson number calculations unreliable for determining whether it is below the threshold value.

Considering Kelvin-Helmholz instability further, it is unclear how the vertical nature of the instability would cause the frontal instabilities observed in the SAR images. It is more likely that, if there are critically low Richardson numbers present at the front, they indicate strong turbulence and mixing at the interface between the lighter wedge and denser surrounding water.

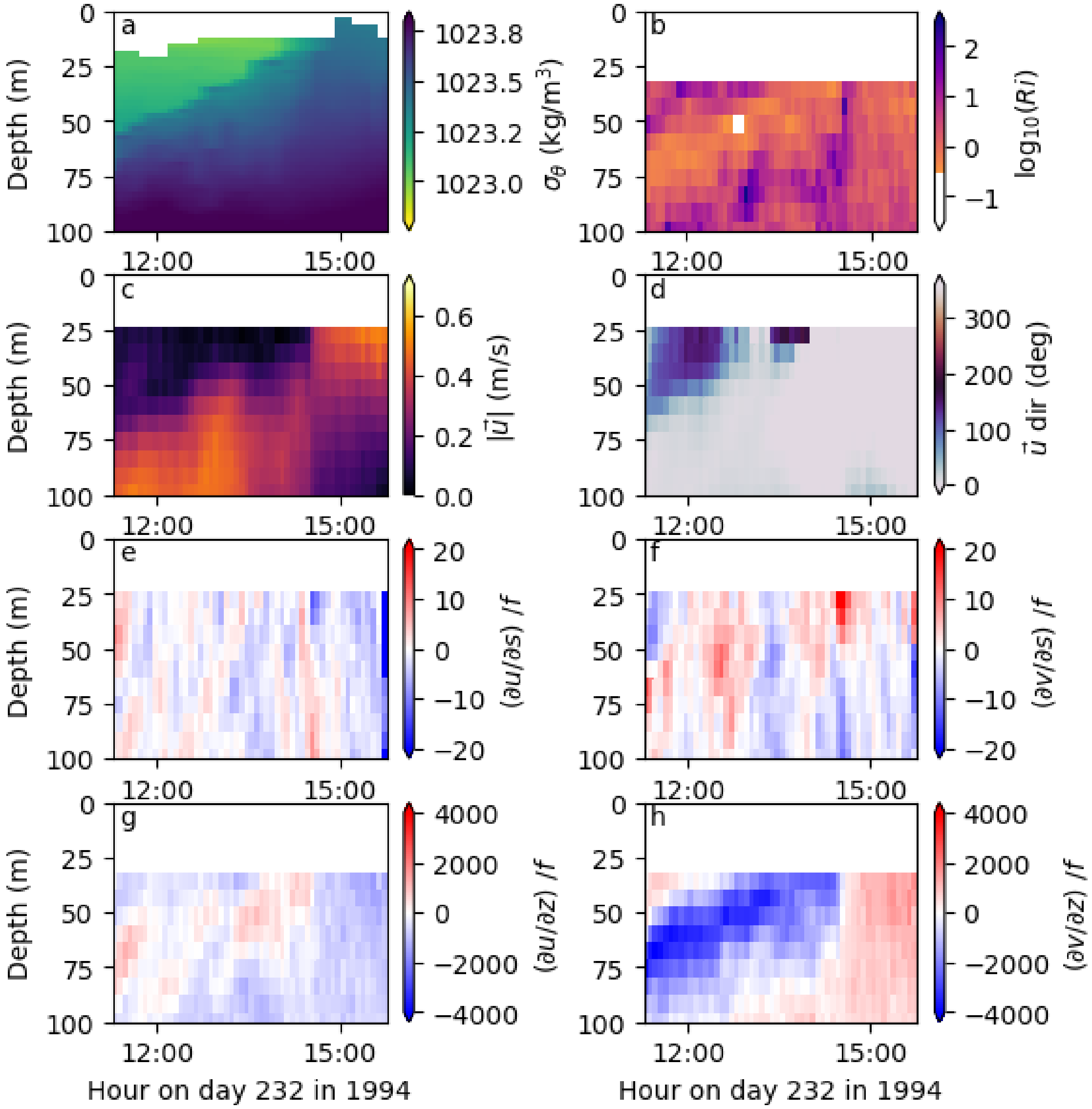

Figure 8.9: (a) potential density (kg/m^3); (b) log10(Ri) for Richardson number Ri, where areas with $Ri < 1/4$ are white; (c) horizontal velocity magnitude in m/s (d) horizontal velocity geographic direction in degrees; (e) shear of zonal velocity in cruise-track direction; (f) shear of meridional velocity in cruise-track direction; (g) shear of zonal velocity in vertical direction; and (h) shear of meridional velocity in vertical direction for TIWE-1 cruise on day 232 in 1994 following a transect from about 3.55°N, 129.1°W to about 3.3°N, 128.65°W, in the equatorial Pacific. Shear values are scaled by f.

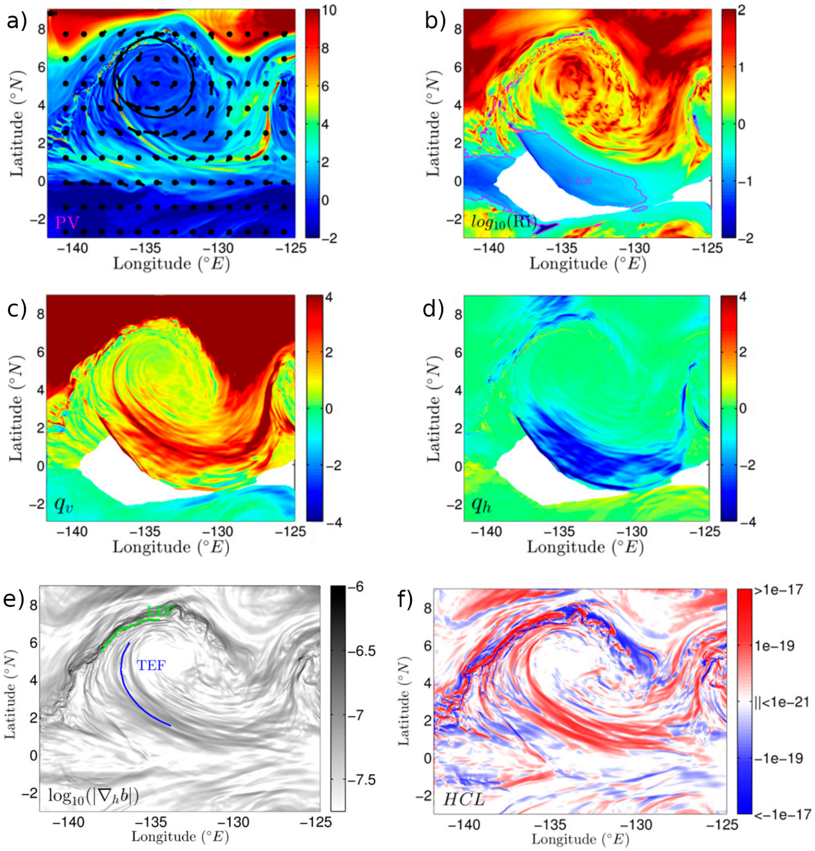

Figure 8.10: Reproduced from *Holmes et al.* [2014]. (a) Map of the total potential vorticity (x 10^{-9} s^{-3}) at 50 m; (b) map of log10(Ri) for Richardson number Ri averaged over an isopycnal layer spanning 1022.8 and 1024.3 kg/m^3; (c) map of the vertical potential vorticity (x 10^{-9} s^{-3}) averaged over an isopycnal layer spanning 1022.8 and 1024.3 kg/m^3; (d) map of the horizontal potential vorticity (x 10^{-9} s^{-3}) averaged over an isopycnal layer spanning 1022.8 and 1024.3 kg/m^3; (e) map of log10 of the horizontal buoyancy gradient (s^{-2}) at 50 m; (f) map of horizontal strain and shearing (s^{-5}) at 50 m, which is positive for frontogenesis and negative for frontolysis; for a TIV modeled in the equatorial Pacific.

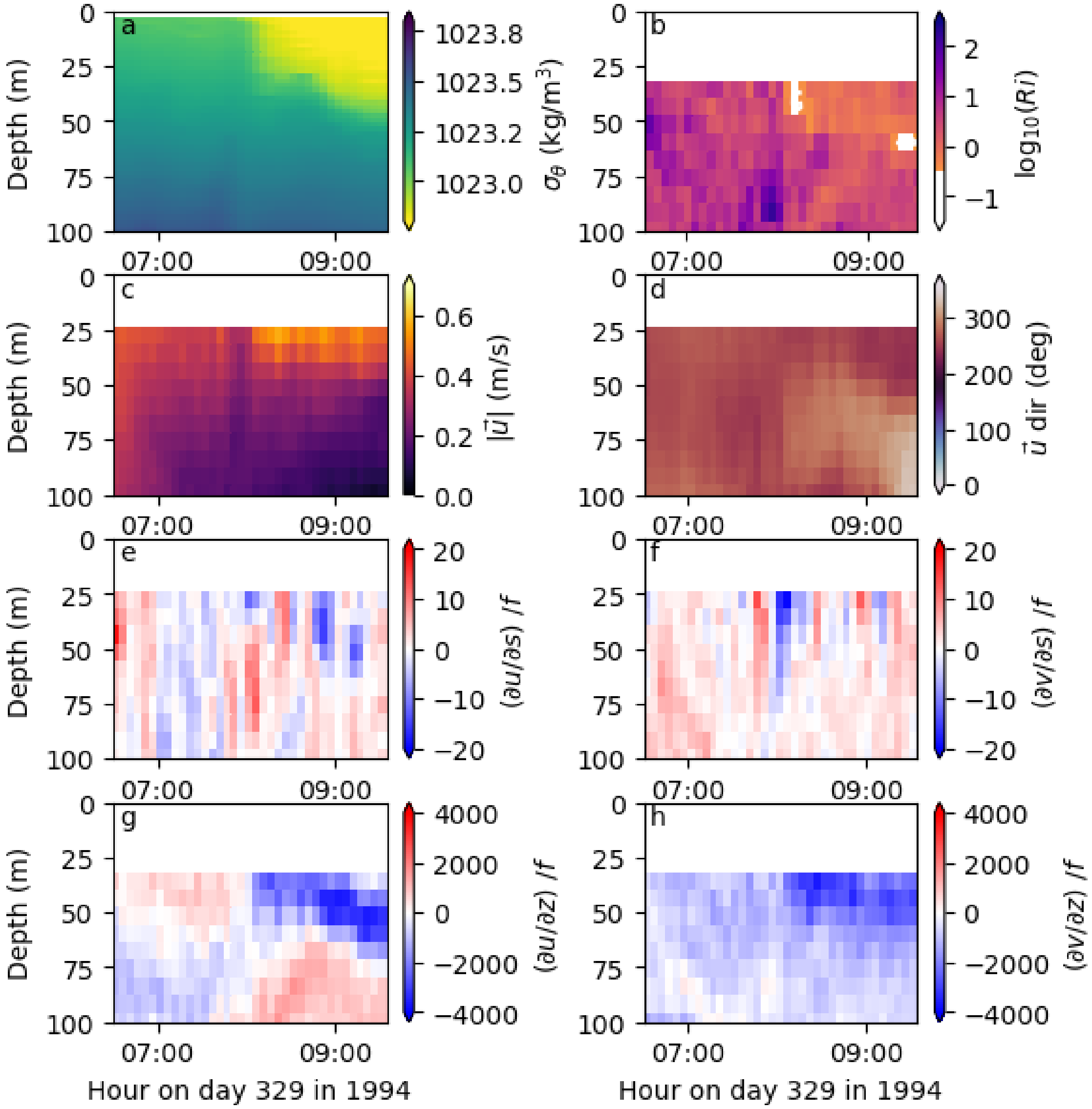

Figure 8.11: (a) potential density (kg/m^3); (b) log10(Ri) for Richardson number Ri, where areas with $Ri < 1/4$ are white; (c) horizontal velocity magnitude in m/s (d) horizontal velocity geographic direction in degrees; (e) shear of zonal velocity in cruise-track direction; (f) shear of meridional velocity in cruise-track direction; (g) shear of zonal velocity in vertical direction; and (h) shear of meridional velocity in vertical direction for the TIWE-2 cruise on day 330 in 1994 along a transect from ∼2.55°N, 143.35°W to ∼2.9°N, 141.1°W, in the equatorial Pacific. Shear values are scaled by f.

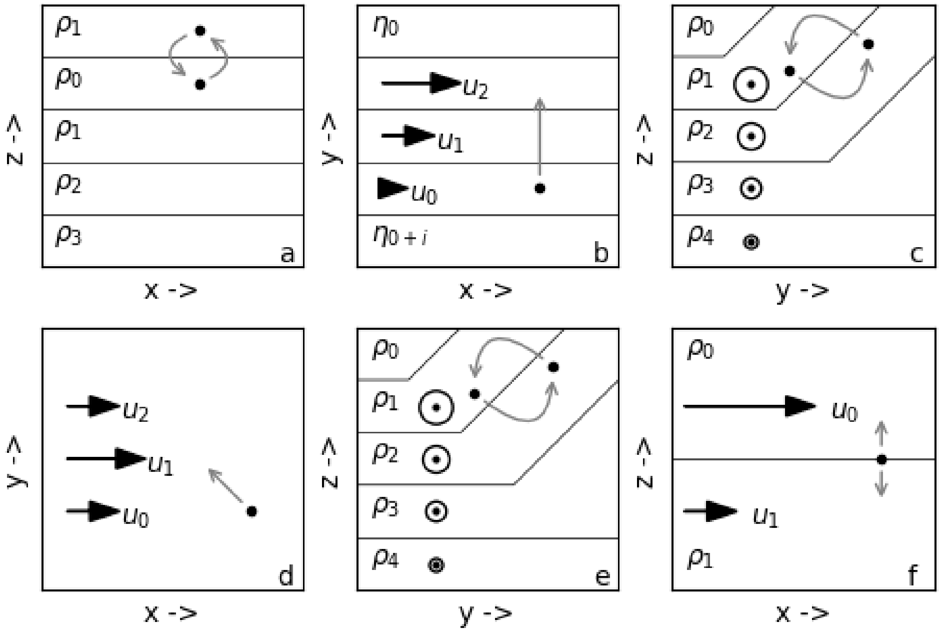

Figure 8.12: Diagram showing simple conditions that may lead to (a) gravitational instability; (b) inertial instability; (c) symmetric instability; (d) barotropic instability; (e) baroclinic instability; and (f) Kelvin-Helmholtz instability. Thin horizontal lines in (a), (c), (e), and (f) are isopycnals, while those in (b) are SSH contours. Black arrows in (b), (d), and (f) along with arrow heads out of the page in (b) and (e) are current vectors. Points and grey arrows show the kind of perturbation that may be unstable.

8.6 Conclusions

TIV fronts separate cold, salty, chlorophyll-rich equatorial upwelled waters and the warm, fresh, chlorophyll-deficient tropical surface waters, with the leading front having less dense waters to the west and the trailing front having more dense waters to the west. The swirling of the TIV translates, rotates, and deforms these fronts. Because of convergence and enhanced wave breaking at fronts, they are visible in SAR images, so we can observe the evolution of the TIV fronts on submesoscales. SIR-C images of the trailing front of a TIV centered at 6°N, 142°W in early October 1994 shows how the front is rotated and a section pushed outward from the center of the TIV to create a sharper curve over the course of four days. The front also develops small-scale deviations in its line indicating the development of frontal instabilities.

Both leading and trailing fronts can develop instabilities consisting of waves, cusps, and breaks. At both fronts, cruise data indicates that less-dense water, which is < 0.8 kg/m^3 lighter, forms a wedge that lies above more dense water. Currents are stronger at the surface in the light wedge on the trailing front, and they are also larger at the leading front at depth below the light wedge and at the surface in the dense water. There is a down-front narrow current on the leading front, but none is visible on the trailing front. There is very strong (up to $3800f$) vertical shear at the base of the lighter wedge at both fronts with positive shear of zonal velocity at the leading front and negative shear of zonal velocity at the trailing front and of meridional velocity at both fronts. The horizontal shear of both current components at both fronts reaches up to $20f$; for the leading front, there is coherent shear of the meridional current along the base of the light wedge, but the shear of the zonal current does not appear related to the density structure. On the trailing front, there is strong horizontal shear in the region of the light wedge in both zonal and meridional velocity components, with the sign of the shear switching rapidly. Richardson numbers for both frontal regions are low just below the less-dense wedge, sometimes reaching below the critical value of 1/4, but low vertical resolution of the shipboard ADCP makes these calculated values of limited usefulness.

Model results from *Holmes et al.* [2014] show that so-called negative PV instabilities (gravitational, inertial, and symmetric instability) are likely not responsible for frontal instability in TIVs because the total PV is positive along both leading and trailing fronts. However, the PV is highest on the fronts and lower off them, which means there is a change in sign of the gradient of PV, so barotropic and baroclinic instability could both play a role here. The low Richardson numbers found in data at both fronts and at the trailing front in the model are likely indications of strong turbulence and/or mixing at the interface.

Scales for baroclinic instabilities are larger at low latitudes, but the instabilities here are quite small. Additionally, the strong vertical shear that could be associated with baroclinic instability is mostly confined to the mixed layer, much shallower than the thermocline. Baroclinic mixed layer instability has smaller horizontal scales than normal baroclinic instability and is confined to the mixed layer, which fits the conditions of TIV fronts better than normal baroclinic instability.

Chapter 9

TIV cross-frontal differences at sub-mesoscales

Where it is shown that in a Rossby number = -1 anticyclonic vortex along the North Equatorial Front, differences across the leading front are likely due to winds that have been affected by sea surface temperature fronts, whereas those across the trailing front are likely due to changes in surface currents, which also affects the surface wave field.

9.1 Introduction

Sea surface temperature (SST), salinity, chlorophyll, winds, currents, and other air and ocean properties can change across a front, sometimes quite dramatically. Are these differences reflected in changes in synthetic aperture radar (SAR) images of tropical instability vortex (TIV) fronts?

Modifications of the marine atmospheric boundary layer change the wind stress and thus the forces working on capillary waves: SST variations produce thermal winds, and air-sea temperature differences change the boundary layer stability and hence the drag coefficient, and may produce convective cells that further modify local surface winds [*Beal et al.*, 1997]. Current divergence and shear alter the medium through which surface waves travel, modifying wave energy density and wave steepness, and modulating capillary waves: steeper capillary waves increase the back-scattered intensity and lead to bright lines in SAR images [e.g., *Johannessen et al.*, 1997], and the breaking of longer waves when they grow steeper scatters radio waves and generates more capillary waves [e.g., *Johannessen et al.*, 2005]. Current convergence and divergence occur at current fronts [e.g., *Kudryavtsev et al.*, 2005], within eddies [e.g., *Kudryavtsev et al.*, 2012], above internal waves [e.g., *Brandt et al.*, 1997], and as flow moves over bathymetry [e.g., *Romeiser and Alpers*, 1997]. Surfactants, such as biological oils, accumulate in convergence zones where their buoyancy prevents downwelling, damping capillary waves and forming dark patches, streaks, and slicks visible in SAR images [e.g., *Johannessen et al.*, 1991, 2005]. Capillary waves are also damped by heavy rain, so that rain cells generally appear as dark areas.

In this chapter, the aim is to examine SAR images for differences across the front to determine how SST, winds, and currents impact SAR images and what sub-mesoscale information about these ocean properties can be determined. In section 2, the data and some calculations are explained; in section 3, winds, temperatures, and currents are explored as explanations for the difference in back-scatter across the front. The currents in SAR images are inferred from wave front via wave-current interactions in section 4. Finally, in section 5, a brief summary and conclusions are given.

9.2 Data and methods

SAR images over the equatorial Pacific were used: the SIR-C images [*Evans et al.*, 1993] for days 279, 280, and 282 in 1994 used in Chapter 8 are part of the current inversion in section 4, and Sentinel SAR images [*Copernicus; European Space Agency*, 2011] for days 197 in 2016; 296, 361, and 365 in 2017; 4 and 265 in 2018, and 272 and 273 in 2019 were used (see Chapter 8 for details).

SST from MODIS level 3 standard mapped images from both Aqua and Terra Satellites were used (see Chapter 7 for details) [*NASA Goddard SFC, OEL OBPG*, 2020a,b].

Daily satellite-derived winds from ASCAT scatterometers on MET-OP satellites at 0.125° spatial resolution were used [*E.U. Copernicus Marine Service Information*, 2021b]. These were estimated for neutral stability at 10-m height, meaning they represent what the wind would be in neutral stability given the wind stress. The winds were interpolated to five points in each SAR imagette: the center and the four corners.

Reprocessed Copernicus-Globcurrent surface currents (0 to 15 m) with sea surface height anomaly- (SSHA-) derived geostrophic component and a modeled Ekman component given on a 1/4° grid every 3 h were used in the back-scatter investigation of section 3 [*E.U. Copernicus Marine Service Information*, 2021c]. Surface currents from the eddy-resolving global ocean reanalysis GLORYS12V1 on a 1/12° grid daily were used for the current inversion of section 4 [*E.U. Copernicus Marine Service Information*, 2021d].

Wave significant heights from WAVERYS reanalysis on a 1/5° grid with 3 h steps were used to estimate the azimuthal cutoff in the current inversion section, and wave periods were tested as possible observed periods in the same section [*E.U. Copernicus Marine Service Information*, 2021a].

In-situ data from the two TIWE cruises, including Seasoar towed CTD and shipboard acoustic Doppler current profiler (ADCP) that were used in Chapter 8, were taken as a general description of the currents at the front in the back-scatter investigation section [*Firing et al.*, 1994; *Sawyer et al.*, 1995].

The CMOD5.N modulation transfer function [*Hersbach*, 2010] in section 3 is an empirically-derived model relating neutral equivalent 10-m wind speeds, wind direction relative to the SAR look direction, and SAR incidence angle to the SAR back-scatter intensity [Figure 9.1]. Using the incidence angle of the image to select the correct CMOD5.N set-up [Figure 9.1 a or b], the back-scatter intensity of the image [Figure 9.1 color] can be used along with estimates of the wind direction [Figure 9.1 x-axis value] from wind streaking in the SAR image or from scatterometry, the wind speed can be estimated [Figure 9.1 y-axis value]. The wind direction is relative to the SAR look angle, which is 80.2° for images on the ascending pass and 279.8° for those on the descending pass.

The drag coefficient needed in Section 3 is

$$C_D = [\kappa/(\ln(z/z_0) - \Psi_m)]^2 \tag{9.1}$$

where $\kappa = 0.4$ is the von Karman constant, $\ln(z/z0)$ is the atmosphere lapse with height z and roughness height z_0, and

$$\Psi_m = 2\ln[(1+x)/2] + \ln[(1+x^2)/2] - 2\tan^{-1}(x) + \pi/2 \tag{9.2}$$

is the atmosphere stability function with $x^4 = 1 - 16(z/L)$. This depends on the Monin-Obukhov stability length:

$$L = \frac{-u_*^3 T_{vs}}{g\kappa C_T U(T_{vs} - \theta_{v10})} \tag{9.3}$$

where $u_* = \tau/\rho$ is a friction velocity, T_{vs} is the virtual temperature of saturated air the same temperature as the sea surface, C_T is the heat flux constant, U is the mean wind speed, and θ_{v10} is the virtual potential temperature at 10 m, or the temperature of dry air with the same density as the measured air temperature brought adiabatically down to 10 m [*Smith*, 1988]. Because drag coefficients depend on C_T, knowledge about heat transfer is necessary, but here is lacking; also of note is that wind stress is needed to calculate drag coefficient as it enters into the friction velocity u_*, but the drag coefficient is needed to calculate the stress. Because of the lack of heat data in the present study and the circular nature of the calculations necessary to compute drag coefficients, the C_D were taken from *Smith* [1988], who used an iterative process to determine C_D over a range of wind speeds and air-sea temperature differences; we have interpolated that data to finer scales for both velocity and air-sea temperature differences using cubic splines [Figure 9.2].

Atmospheric parameters of air temperature, dew point temperature, and sea level pressure from the ECMWF ERA-5 hourly reanalysis on a 1/4° grid [*Hersbach et al.*, 2018] were used in the back-scatter investigation for calculating the virtual potential temperature at 10 m. When air density is not available, the value of 1.17 kg/m^3 is used. The relative humidity is calculated from the air temperature and dew point temperature:

$$RH = \exp\left[\frac{A(T_d - 273.16)}{T_d - B} - \frac{A(T - 273.16)}{T - B}\right] \tag{9.4}$$

where T is air temperature in K, T_d is dew point temperature also in K, and $A = 17.2693882$ and $B = 35.86$ are constants. The saturated vapor pressure is calculated from the air temperature with constant C =610.78 Pa:

$$e_s = C \exp \frac{A(T - 273.16)}{T - B} \tag{9.5}$$

Then the actual vapor pressure can be derived using the relative humidity: $e = RH * e_s/100$. The specific humidity follows:

$$q = \frac{(eM_w/M_a)}{p - (1 - M_w/M_a)e} \tag{9.6}$$

with molar mass of dry air and water vapor M_a and M_w, respectively, and sea level pressure p. The saturated specific humidity q_s is the specific humidity calculated using the saturated vapor pressure e_s rather than the actual vapor pressure e. The virtual potential temperature at height z is then

$$\theta_{vz} = (1 + q(M_a/M_w - 1))T(p_0/p)^{R_d(1-0.23q)/c_{pd}} + \Gamma z \tag{9.7}$$

for specific gas constant for dry air R_d, specific heat capacity for dry air c_{pd}, reference pressure p_0 =100 kPa, and adiabatic vertical rate of temperature change Γ and height z.

The MODIS SST along with the saturation specific humidity from atmospheric parameters were used to calculate the virtual temperature of saturated air at the surface temperature:

$$T_{vs} = T_s(1 + q_s(M_a/M_w - 1)) \tag{9.8}$$

for SST T_s.

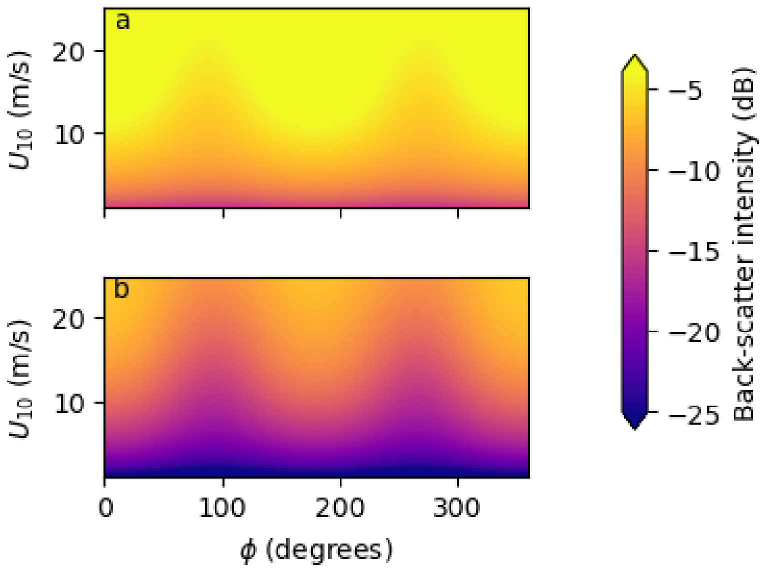

Figure 9.1: CMOD5.N back-scatter intensity (color) plotted on neutral equivalent 10-m wind speed U_{10} and wind direction relative to SAR axes ϕ for SAR incidence angles θ_i of (a) 24° and (b) 37°.

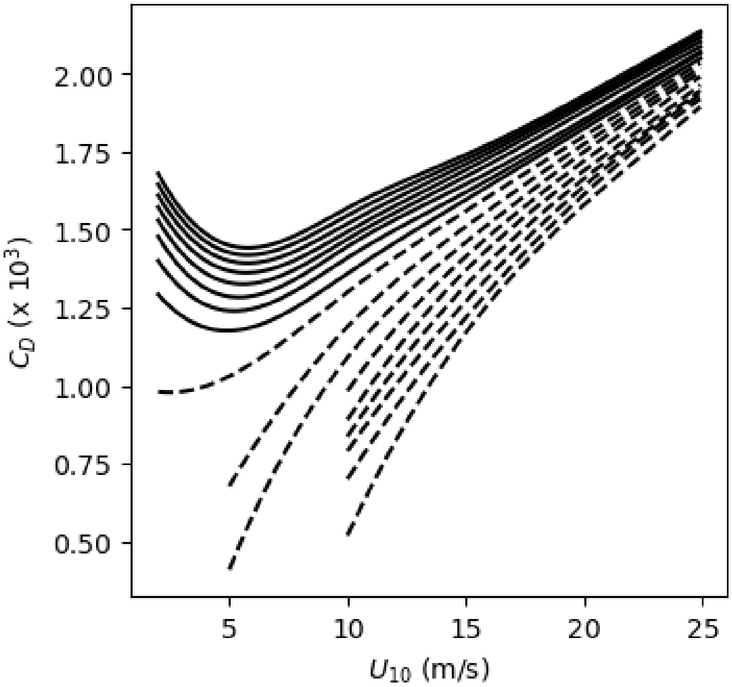

Figure 9.2: Drag coefficients for different U_{10} wind speeds. Plotted lines are for sea - air temperatures differences ($T_{vs} - \theta_{v10}$) of -20° to 20° with a 2.5° step; dashed lines are negative temperature differences. The lines in the plot end where the equations for the drag coefficient break down.

9.3 Backscatter differences

The SAR imagette in Figure 9.3a, taken on day 279 in 2019 and centered at 2.5°N, 142.25°W, has two very noticeable features: 1. An ocean front oriented at 156° is visible as a narrow line of high back-scatter intensity across the image; and 2. The mean back-scatter intensity changes drastically across the front. The SAR front is co-located with an SST front [color of Figure 9.3b] with a sharp temperature change of 1 C over 9 km. The SST data has a much lower spatial resolution than the SAR imagette (5 to 50 m) and so misses much of the smaller scale structure of this front. The SST data has been translated to fit with the SAR imagette, subject to the additional constraint that tracers must translate westward in time in this region. Figure 9.3b also shows the winds and currents as black and white streamlines, respectively. Winds are south-southeasterly trades with magnitudes between 3 and 7 m/s running along the front. Large-scale surface currents are linearly oriented here but swirl clockwise just to the northeast, with currents running mostly along the front at 0.80 m/s. What process or processes are responsible for the difference in back-scatter across the front? What about winds? SST? Or perhaps currents?

Neutral equivalent wind speed can be estimated for both sides of the front using the CMOD5.N modulation transfer function. The SAR image in Figure 9.3a has an incidence angle of 37° and is on an ascending pass; normalized back-scatter (σ_0) on both sides of the front is in Table 9.1, as are wind direction estimates from wind rows (α) and scatterometer (β). Wind rows are a manifestation of Langmuir circulation, where wind stress interacts with Stokes drift to produce shallow, counter-rotating vortices at the ocean surface whose axes are closely aligned with the wind stress [*Thorpe*, 2004]. Because there is only 2° between wind row and scatterometer estimates of wind direction, the wind row direction of 155° is used to calculate wind direction relative to SAR in CMOD5.N (ϕ =255°), which is used to make the wind estimates on either side of the front (U_{10}).

The neutral equivalent winds estimated southeasterly at 155° on the dark side of the front were 8.3 m/s, while those on the bright side of the front were 9.5 m/s. The wind direction is along-front, and along-front winds have been shown to change across a front on mesoscales [e.g., *Kilpatrick et al.*, 2016], and sub-mesoscales, with a 0.65-C change in SST over 500 m causing a 2.5 m/s change in along-front wind speed over less than 2 km [*Wenegrat and Arthur*, 2018], but the warmer side of the front has stronger winds. That is not the case here, where the cold side of the front appears to have winds 1.2 m/s larger than the warm side of the front.

The neutral equivalent winds are the winds that would produce the observed back-scatter if the atmosphere were neutrally stable, but we know that the front is also an SST front, and air-sea temperature differences can affect atmospheric stability. The wind estimates can be adjusted to account for changes in atmospheric stability by adjusting the drag coefficient, which depends on both wind speed and atmospheric stability, with the dependence on stability being a result of vertical density gradients in the air that alter turbulence as well as fluxes of heat and momentum. To quantify the impact of the air-sea temperature differences on the back-scatter, neutral equivalent winds from CMOD5.N are backed out to wind stress using the drag coefficient for neutral stability. All possible wind stresses for $T_{vs} - \theta_{v10}$ between -20 and 20 C and non-neutral winds $|\vec{U}|$ from 0 to 25 m/s were calculated with $|\vec{\tau}| = C_D \rho_0 |\vec{U}|^2$ where drag coefficient C_D varies with air-sea temperature difference and non-neutral wind speed; values for C_D were taken from iteratively-calculated values from *Smith* [1988], where they are given for air-sea temperature difference and wind speed. The line where the difference between the wind stress backed out from CMOD5.N and the field of possible wind stresses is a minimum then gives the relationship between temperature and wind magnitudes. Plotting the relationship for both sides of the front in the manner of the example curves in Figure 9.4 can then show if the influence of the observed temperature difference on the drag coefficient can explain the observed back-scatter difference.

The observed air-sea temperature differences [$T_{vs} - \theta_{v10}$ in Table 9.1] are positive on both sides of the front, indicating that the sea is warmer than the air, and thus the atmosphere is unstable. The temperature difference is larger on the dark side of the front, which is also the cold side of the front; this is unusual as the atmosphere is typically more unstable over warmer water which would lead to higher back-scatter. Figure 9.5 shows the relationship between air-sea temperature difference and non-neutral wind speed for the wind stress on each side of the front. Non-neutral wind speed estimates are 7.9 m/s for the dark side of the front and 9.2 m/s for the bright side of the front for the observed air-sea temperature differences; this is a similar difference as seen in neutral equivalent wind situation above, and the wind speeds are inconsistent with the normal wind response to SST differences. If we assume that the wind estimate on the bright side of the front (9.2 m/s) is correct across the entire image, the air-sea temperature difference on the dark side of the front would need to be -5.0 C or the ocean would need to be 11 C cooler than it is for temperature to explain this (the intersection between the solid vertical line at 9.2 m/s and the solid wind-temperature curve is at $y = -5$ C). That is a very large temperature difference from what is observed, and it is unlikely that such a difference would pass undetected because of the lower spatial resolution of the Modis SST.

While temperature effects cannot explain the back-scatter differences across the front, perhaps surface currents can. Wind stress is a momentum transfer from wind to ocean, but if the ocean surface is moving, that must be accounted for. The relative surface stress $\vec{\tau}_r = \rho_a C_d|\vec{U} - \vec{u}|(\vec{U} - \vec{u})$ is the stress produced by the wind $\vec{U}$ and the ocean current $\vec{u}$ moving relative to one another [*Duhat and Straub*, 2006]. If winds and currents directly oppose one another, the vector made by subtraction is their sum and $\vec{\tau}_r$ is large, while the two moving in the same direction produces a small $\vec{\tau}_r$. For this analysis, we assume that CMOD5.N will give us an estimate of relative motion $(\vec{U} - \vec{u})$ rather than for wind alone.

This vector subtraction of the winds and currents adds a layer of complexity to the analysis because both magnitudes and directions for wind and currents must be estimated. We will assume that the wind row direction from earlier is really the relative motion direction because wind rows depend on wind stress, which has been corrected to relative stress. We can use observations from the TIWE-2 research cruise in November 1990, where the trailing front was crossed, to narrow down the possible current directions and magnitudes. Shipboard ADCP detected currents on the cold side of the front at about 0.4 m/s due west, while those on the warm side of the front were about 0.5 m/s headed 10 degrees south due west. The exact orientation of the front during the cruise was unknown, so the current magnitudes on both sides of the front will be limited to < 4 m/s, and the direction will be limited to within 90° of crossing the front directly for the cold side of the front and with a 10° counterclockwise offset for the warm side of the front.

Back-scatter intensities for both sides of the front are again in Table 9.1 along with wind direction estimates, wind magnitude estimate, and current direction and magnitude estimates. If we assume that the relative motion is along the wind rows, we can calculate possible current magnitudes and directions for different wind magnitudes and the directions [Figure 9.6]. Current magnitudes are very large (>10 m/s) if the wind direction is not to the northwest. Wind magnitudes are frequently larger than current magnitudes, so the wind direction plays a larger role in determining the direction of relative motion, which is to the northwest. There are slight variations between the two sides of the front, with the point of smallest current magnitude being at slightly smaller wind speeds and slightly more clockwise angles of wind direction for the dark side of the front.

If we limit possible current magnitudes and directions based on the ADCP observations from TIWE-2, we find the wind speeds and directions are severely limited [Figure 9.7]. For the bright side of the front, wind speeds can range from ∼6 to 10 m/s with directions ranging from −25° to −50°. On the dark side of the front, wind speeds could be 5 to 10 m/s at −25° to −55°. For both sides, weaker currents converge to more counterclockwise angles of wind direction and a single wind speed (9.5 m/s for the bright side and 8.2 m/s for the dark side), while more clockwise angles of wind direction are associated with large wind speeds.

The currents being at slightly different angles and magnitudes could explain the discrepancy in back-scatter intensity and overcome the expected temperature impact in this image. For example, if the wind magnitudes for the bright and dark sides are 8.0 and 8.25 m/s, respectively, then stronger currents (0.5 m/s greater) oriented more clockwise (80° more) on the bright side than the dark side could explain the difference in back-scatter; as an extreme example, much weaker currents (1.4 m/s less) oriented slightly more clockwise (15°) could also result in the observed back-scatter differences.

This analysis can be expanded with other SAR images [Figure 9.8]: these images are from day 365 in 2017 on the trailing front; day 4 in 2018 on the leading front; day 265 in 2018 on the trailing front; and day 273 in 2019 on the trailing front. Winds are to the northwest in all four new images varying between 5 and 8 m/s in magnitude, while currents are also to the northwest with speeds between 0.4 and 1.2 m/s. SSTs indicate the fronts are also temperature fronts with cross-front temperature gradients of 1 C, 2.7 C, 0.6 C, and 1.6 C, respectively, over about 8 km.

Important values relating to these images are in Table 9.2. The neutral equivalent winds on the bright sides of the fronts are larger than on the dark sides by 1.0 m/s for the image on day 365 of 2017, 1.1 m/s for the image on day 4 of 2018, 1.0 m/s for the image on day 265 of 2018, and 0.4 m/s for the image on day 273 in 2019. The winds were along the front in each of these images except the one on day 4 of 2018, where they were across the front. Also, the bright side of the front is the cold side for each image except the leading front image on day 4 in 2018. This means that, for the other three images, winds are larger on the side of the front where they should be smaller, which is how they were in the first image analyzed. Note that the all of the trailing front images here have higher backscatter over colder water, but that is not always the case. While winds for day 4 in 2018 are in the correct orientation, the effects of the temperature difference across the front should also be considered. All temperature differences are again positive, meaning SST is warmer than air temperatures.

The non-neutral wind speed and temperature relationships for these four images [Figure 9.9] indicate that temperature-affected winds could explain the back-scatter difference if they are (for the dark side and for the bright side) 6.6 m/s and 7.4 m/s, 4.4 m/s and 5.4 m/s, 3.3 m/s and 4.3 m/s, and 4.7 m/s and 5.5 m/s, respectively. However, as noted above, the bright side with larger winds is only the warm side of the front in the image from day 4 in 2018, so the temperature effect is backwards for the other three. As for this leading front image, sub-mesoscale modeling has shown that winds blowing across a front with a 3- to 5-C SST difference over 10 to 15 km from the warm to cold side can result in an O 1 m/s drop in cross-front wind speed [*Redelsperger et al.*, 2019]. While the front here is on the weak end of this scale and winds blow in the opposite direction, this magnitude of change across a front is not unreasonable.

The temperature differences that the dark side of the front would need for temperature alone to explain the back-scatter difference assuming an error due to the lower spatial resolution of MODIS SST are -2.4, -1.75, -1, and -0.7 C for days 365 in 2017, 4 in 2018, 265 in 2018, and 273 in 2019, respectively. These values are 7.4, 8.4, 5.7, and 6.7 C less than the MODIS values, which are again much too large to be considered correct. Temperature definitely does not explain the observed back-scatter difference for the trailing front images.

If we do the same analysis as done before for relative motion to account for currents, relative motion is again to the northwest, and wind speeds are also likely to the northwest, where reasonable current magnitudes are found. We can use cruise observations to limit the current magnitudes and directions considered. The TIWE-2 crossing of the trailing front was described earlier, and the same limits will be applied to the three trailing front images. For the leading front in the SAR image on day 4 of 2018, the TIWE-1 cruise crossed the leading front of a TIV in August 1990; shipboard ADCP showed shallow currents at 20 m on the warm side of the front with a mean speed of 0.05 m/s that crosses the front at a shallow 10° degree angle and on the cold side of the front with a mean speed of 0.45 m/s that cross the front at a 60° degree angle; each of these currents stretches to at least 10 km away from the front, and the front orientation was known for TIWE-1.

Possible wind speeds and directions for restricted current magnitudes and directions are in Figure 9.10. For trailing front images, results are similar to the earlier analysis. For the leading front image, currents converging at the front lead to quite different total motion directions: for the bright side, winds are at $-30°$ to $-65°$, while for the dark side it is just clockwise from $-20°$ to 25°. Smaller current speeds correspond to more clockwise winds on bright side but more counterclockwise winds on the dark side. Current speeds should be very small for the bright side, so the wind speed is high and wind direction is about $-30°$.

Winds and temperature can explain the back-scatter difference in the leading front image, but they actually work to oppose the observations at the trailing front images. Again, differing current magnitudes and directions on the two sides of the front can allow for stronger winds on the warm/dark side of the front but still have larger back-scatter on the cold/bright side.

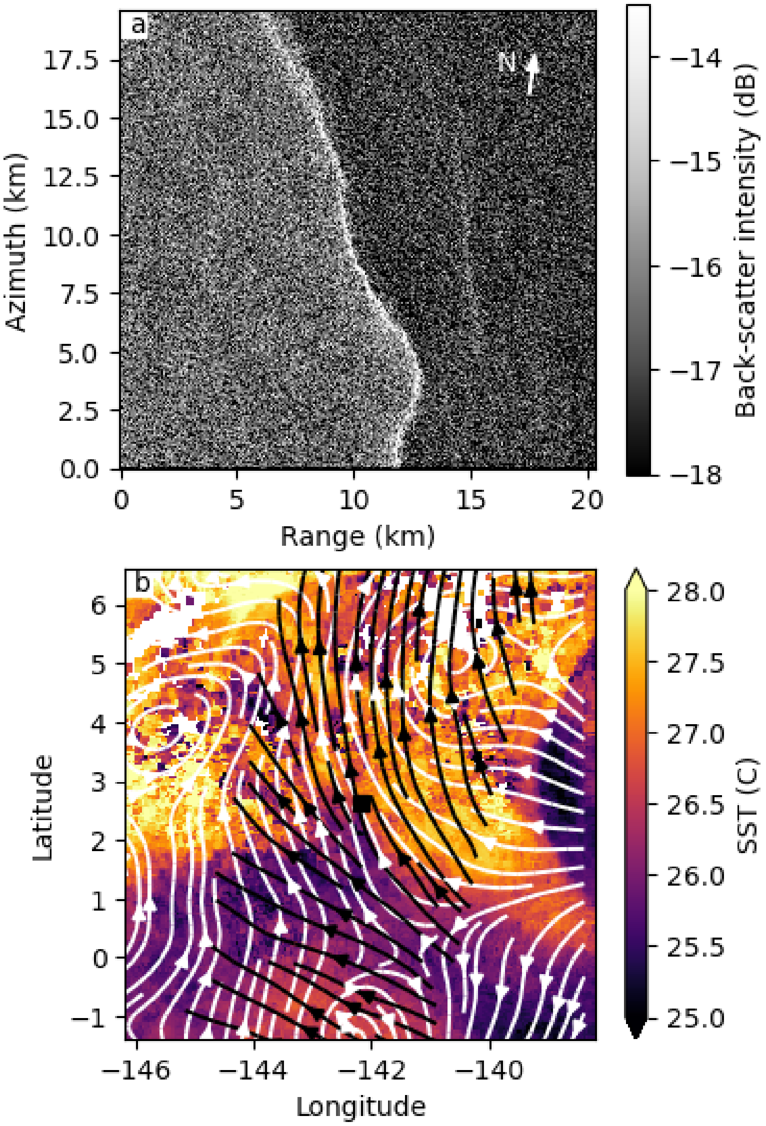

Figure 9.3: (a) Surface roughness from SAR on day 272 of 2019 centered at ∼2.6°N, 142°W, in the equatorial Pacific, with north indicated by the white arrow; and (b) SST (color) from MODIS using both Aqua and Terra satellites for 3 days centered on SAR image date, and surface current streamlines in white and wind streamlines in black. Location of SAR image (a) in panel (b) is black marker in center.

Table 9.1: The front orientation (ϕ_f); SAR incidence angle (θ_i); SAR look angle (ϕ_L); wind direction indicated by wind rows (α); wind direction and magnitude from other data (β and U_β, respectively); current direction and magnitude from other data (γ and u_γ, respectively); backscatter intensities (σ_0); observed air-sea temperature differences ($T_{vs} - \theta_{v10}$); and neutral equivalent wind speed (U_{10}), non-neutral wind speed (U), and stress (τ) in the direction indicated by wind rows for the bright and the dark sides of the SAR image from day 272 of 2019 centered at ~2.6°N, 142°W, in the equatorial Pacific.

Quantity	Bright	Dark
ϕ_f (°)	156	156
θ_i (°)	37	37
ϕ_L (°)	80.2	80.2
α (°)	155	155
β (°)	157	157
U_β (m/s)	6.29	6.29
γ (°)	319	319
u_γ (m/s)	0.80	0.80
σ_0 (dB)	-16.49	-17.21
$T_{vs} - \theta_{v10}$ (C)	5.0	6.0
U_{10} (m/s)	9.5	8.3
U (m/s)	9.2	7.9
τ (N/m^2)	0.134	0.097

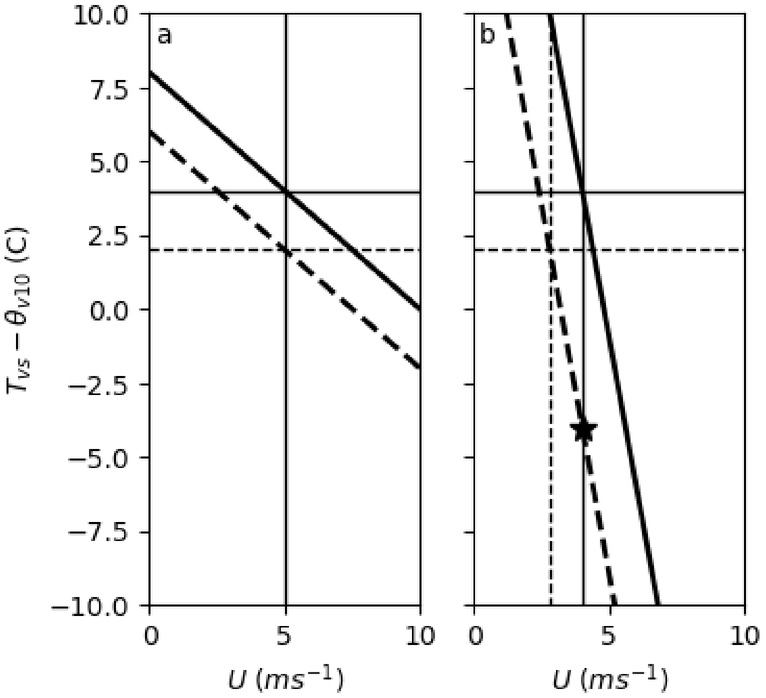

Figure 9.4: Example wind-temperature relationships (thick lines), air-sea temperature differences (horizontal lines), and wind speeds indicated by the relationships and temperature differences (vertical lines) on the bright (solid lines) and dark (dashed lines) sides of the front for two possible scenarios: (a) wind-temperature relationships indicate the same or nearly the same wind speed for the given temperature differences, and (b) the wind-temperature relationships indicate different wind speeds for the given temperature differences. In (a), the temperature effect can explain the back-scatter difference across the front, while in (b) in cannot, although a difference in winds across the front could. The temperature difference indicated in (b) by the black star is the temperature difference the dark side of the front would need to have if the temperature effect were to explain the back-scatter difference: that would require that the ocean on the dark side of the front be nearly 6 C cooler than it is.

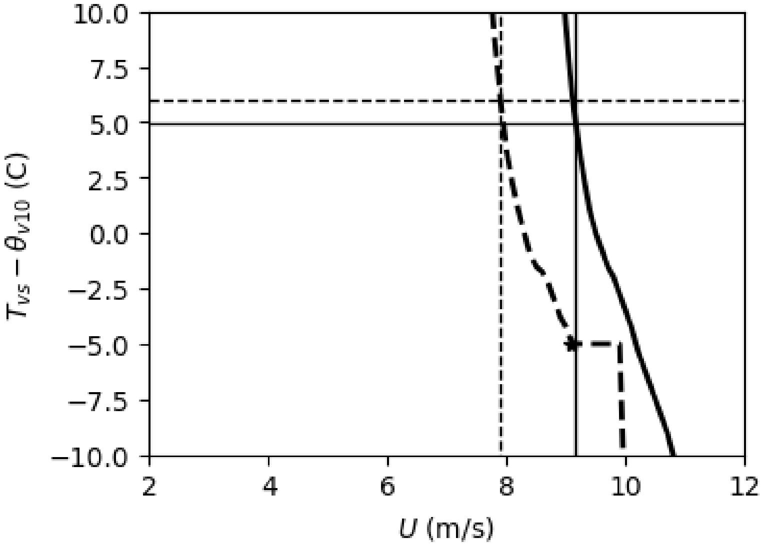

Figure 9.5: Air-sea temperature differences on the bright (solid line) and dark (dashed line) sides of the front necessary to account for the wind stress derived from the SAR image on day 272 of 2019 centered at ∼2.6°N, 142°W, in the equatorial Pacific for different non-neutral winds in the direction indicated by wind rows in the SAR image. Horizontal dashed lines indicate the observed air-sea temperature differences.

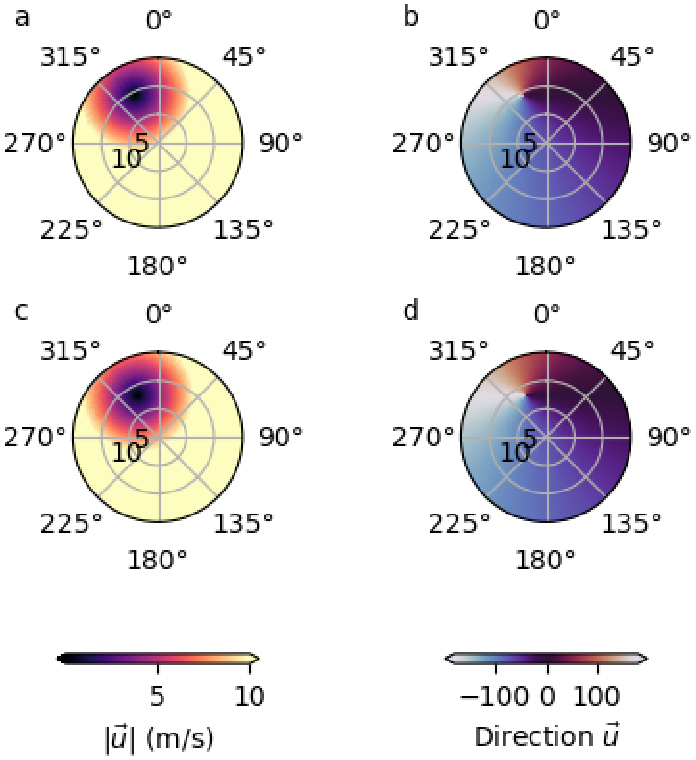

Figure 9.6: Possible current magnitudes (shading, left column) and current directions (color, right column) for bright (top row) and dark (bottom row) sides of the front assuming relative motion direction from wind rows for different wind magnitudes (radial scale) and directions (angle) for the SAR image on day 272 of 2019 centered at ∼2.6°N, 142°W, in the equatorial Pacific.

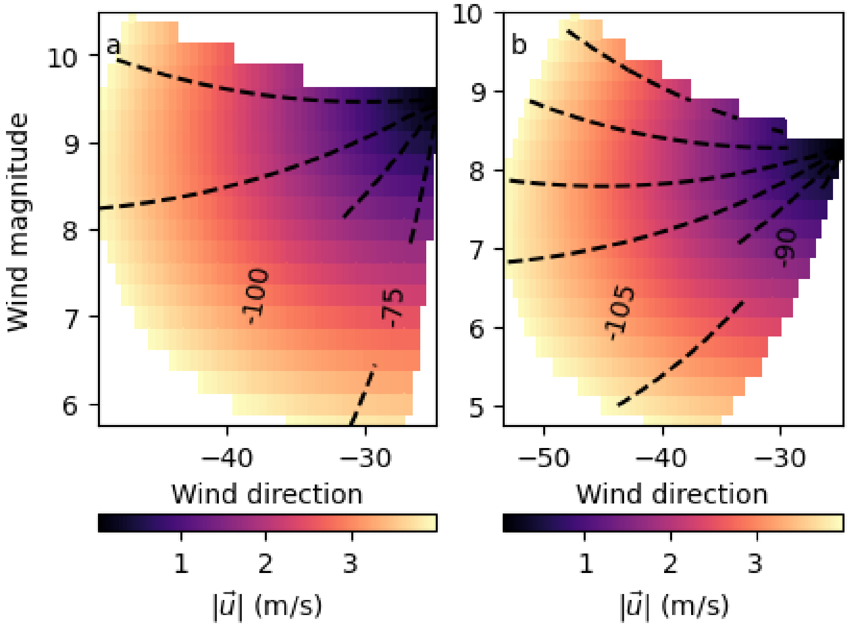

Figure 9.7: Current speed (color) and direction (contours) with possible wind magnitudes (y-axis) and directions (x-axis) for (a) the bright side of the front, and (b) the dark side of the front for the SAR image on day 272 of 2019 centered at ∼2.6°N, 142°W, in the equatorial Pacific. Contours for (a) are from −150° to −75° in increments of 25°; and for (b) are from −165° to −90° in increments of 15°. This is a trim of the data in Figure 9.6.

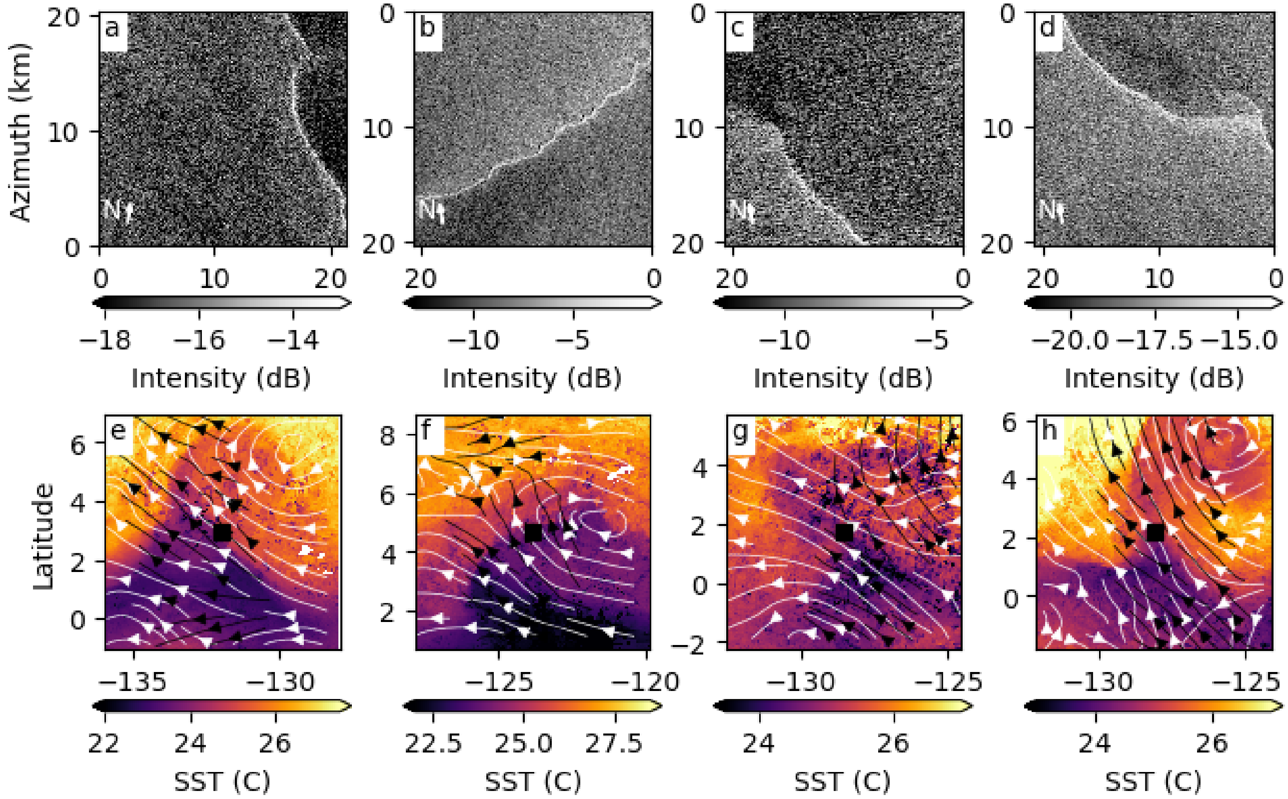

Figure 9.8: Same as Figure 9.3, but for SAR images (from left) taken on day 365 in 2017 centered at ∼3°N, 132.5°W, taken on 4 in 2018 centered at ∼5°N, 124°W, taken on 265 in 2018 centered at ∼2°N, 129°W, and taken on 273 in 2019 centered at ∼2°N, 128°W.

Table 9.2: The front orientation (ϕ_f); SAR incidence angle (θ_i); SAR look angle (ϕ_L); wind direction indicated by wind rows (α); wind direction and magnitude from other data (β and U_β, respectively); current direction and magnitude from other data (γ and u_γ, respectively); backscatter intensities (σ_0); observed air-sea temperature differences ($T_{vs} - \theta_{v10}$); and neutral equivalent wind speed(U_{10}), non-neutral wind speed (U), and stress (τ) in the direction indicated by wind rows for the bright and the dark sides of the images (from top) taken on day 365 in 2017 centered at ~3°N, 132.5°W, taken on 4 in 2018 centered at ~5°N, 124°W, taken on 265 in 2018 centered at ~2°N, 129°W, and taken on 273 in 2019 centered at ~2°N, 128°W.. The wind determinations were made using the direction from the wind rows.

	2017-365		2018-004		2018-265		2019-273	
Quantity	Bright	Dark	Bright	Dark	Bright	Dark	Bright	Dark
ϕ_f (°)	157	157	66	66	145	145	133	133
θ_i (°)	37	37	24	24	24	24	37	37
ϕ_L (°)	80.2	80.2	279.8	279.8	279.8	279.8	279.8	279.8
α (°)	136	136	155	155	143	143	149	149
β (°)	135	135	159	159	134	134	142	142
U_β (m/s)	6.24	6.24	5.28	5.28	6.09	6.09	7.90	7.90
γ (°)	301	301	327	327	302	302	335	335
u_γ (m/s)	1.05	1.05	0.43	0.43	1.19	1.19	0.63	0.63
σ_0 (dB)	−16.82	−17.45	−8.35	−9.26	−8.99	−10.13	−18.11	−18.65
$T_{vs} - \theta_{v10}$ (C)	4.0	5.0	6.6	3.9	4.7	5.3	5.4	7.0
U_{10} (m/s)	7.7	6.7	5.8	4.7	4.7	3.7	5.9	5.3
U (m/s)	7.4	6.6	5.4	4.4	4.3	3.3	5.5	4.7
τ (N/m^2)	0.081	0.062	0.042	0.026	0.026	0.016	0.044	0.034

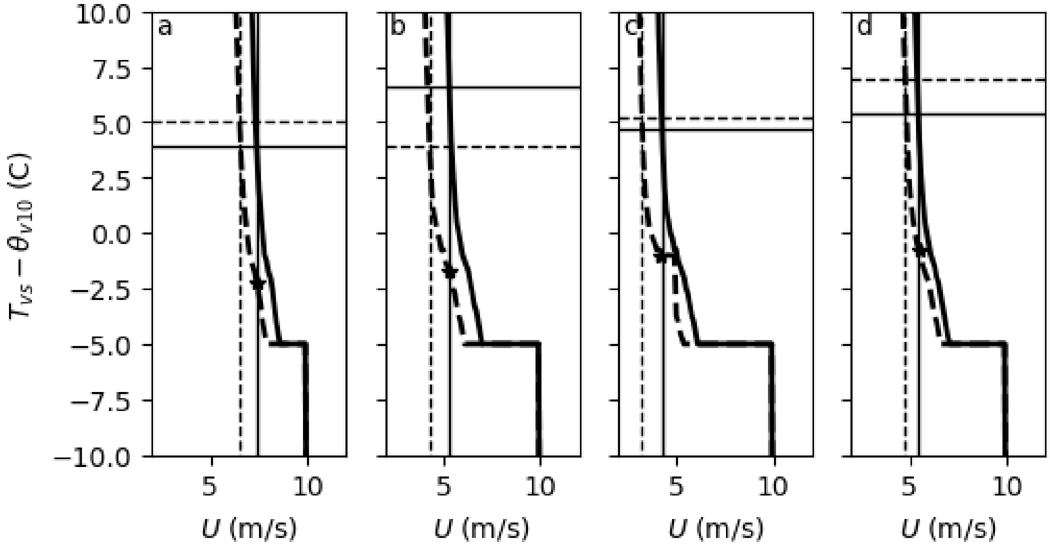

Figure 9.9: Same as Figure 9.5, but for SAR images (from top) taken on day 365 in 2017 centered at ∼3°N, 132.5°W, taken on 4 in 2018 centered at ∼5°N, 124°W, taken on 265 in 2018 centered at ∼2°N, 129°W, and taken on 273 in 2019 centered at ∼2°N, 128°W.

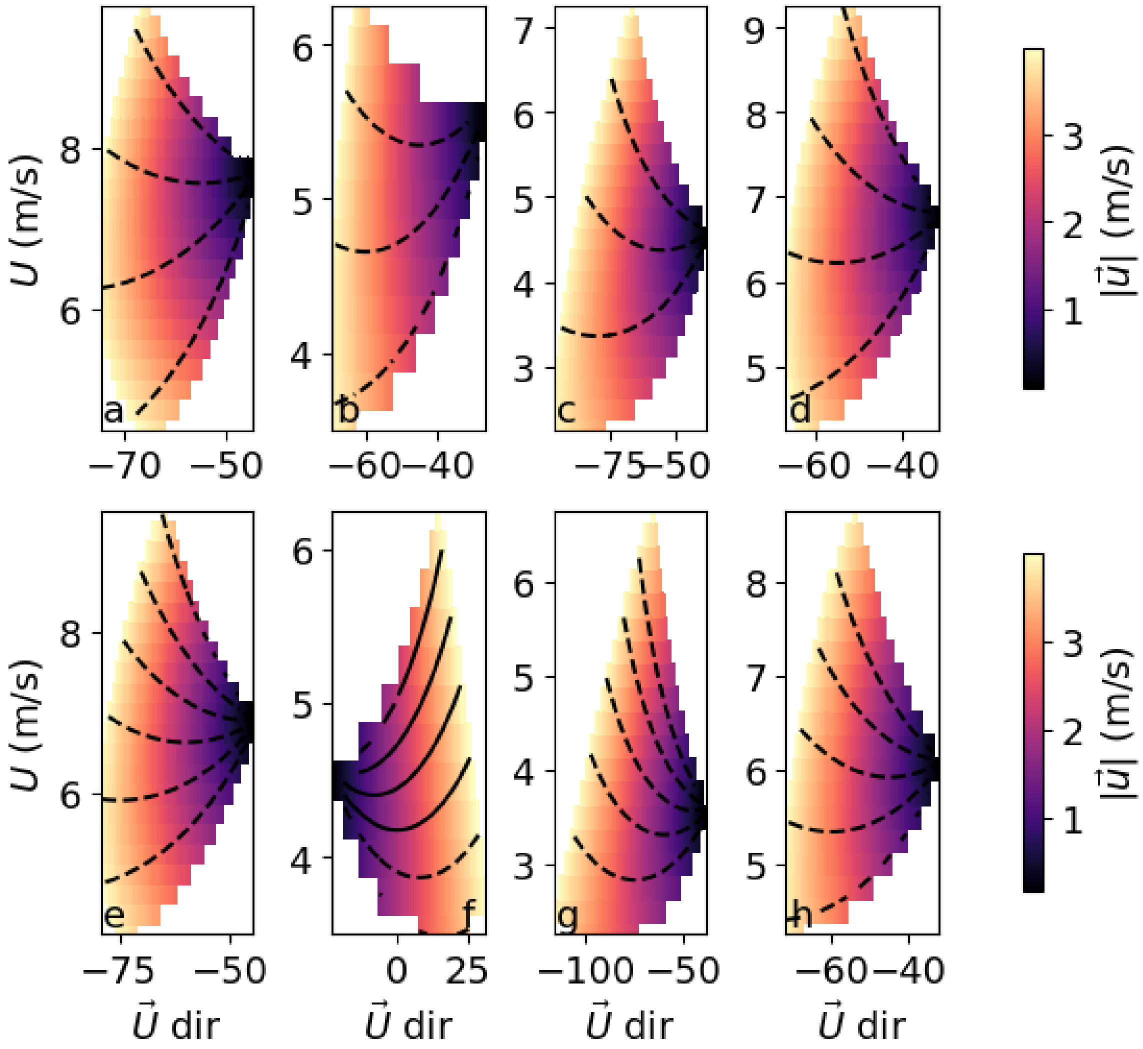

Figure 9.10: Current speed (color) and direction (contours) on with possible wind magnitudes (y-axis) and directions (x-axis) for (top) the bright side of the front, and (bottom) the dark side of the front for images (columns from left) taken on day 365 in 2017 centered at ∼3°N, 132.5°W, taken on 4 in 2018 centered at ∼5°N, 124°W, taken on 265 in 2018 centered at ∼2°N, 129°W, and taken on 273 in 2019 centered at ∼2°N, 128°W.. Contours for top cover (from left) −150° to −75° by 25° increments, −135° to −105° by 15° increments, −150° to −100° by 25° increments, and −175° to −100° by 25° increments; contours for the bottom cover (from left) −165° to −90° by 15 increments, −16° to 24° by 8° increments, −165° to −105° by 15° increments, and −165° to −105° by 15° increments.

9.4 Current inversion

The SAR image in Figure 9.11, taken on day 197 of 2016 on the leading front of a TIV, shows obvious refraction of the wavefronts visible in the image. To the left of the front, wave crests stretch from left to right with virtually no tilt, while to the right of the front, the crests tilt down to the right. What causes this refraction of wavefronts?

When waves travel through an area with currents, the currents refract the waves, giving them apparent frequencies that are related to the wave frequencies in the frame of reference moving with the water, also known as the intrinsic frequency, but are modified by background current velocities:

$$\omega_{obs} = \omega + \vec{k} \cdot \vec{u}, \tag{9.9}$$

where ω_{obs} is the observed frequency, ω is the intrinsic wave frequency, $\vec{k}$ is the wavenumber vector, and $\vec{u}$ is the background current velocity.

The wavenumber vector is unaffected by the background velocity field, but the frequency is. These quantities are related by the kinematic conservation equation, also called the conservation of crests equation:

$$\frac{\partial \vec{k}}{\partial t} + \nabla \omega_{obs} = 0. \tag{9.10}$$

Because the wavenumber vector is the gradient of the phase S (i.e., $\vec{k} = \vec{\nabla} S$), we have

$$\vec{\nabla} \times \vec{k} = 0. \tag{9.11}$$

While energy in a wave is not conserved, the energy density E and thus the wave action A are:

$$A = E/\omega \tag{9.12a}$$

$$\frac{\partial A}{\partial t} + \nabla \cdot [(\vec{u} + \vec{c}_g)A] = 0 \tag{9.12b}$$

for wave group velocity $\vec{c}_g$.

Specific cases have been solved analytically [e.g., *Phillips*, 1981], and several studies have looked at the relationship between surface currents and wave fronts observed in SAR images. *Meadows et al.* [1983] used weekly reports of Gulf Stream position and currents along with the location, track, and estimated wind of Hurricane Ella to estimate the surface waves produced by the hurricane and the path of those waves, including the influences of bathymetric refraction and interaction with the Gulf Stream; the estimated waves were compared with wavelengths and directions derived from optical Fourier transforms performed on sections of a SEASAT SAR track. There was general agreement between waves from the two data sources, and disagreement was attributed to the fact that the reports about Gulf Stream conditions were produced only weekly and in a subjective manner, so the conditions were not well known. They also inverted the SAR-derived surface wave data to get a profile of Gulf Stream currents, which positioned the Gulf Steam more shoreward and headed in a more northerly direction than the weekly report. They use a simplified equation used later in our analysis, Equation 9.42.

A second study by *Barnett et al.* [1989] focused on using SIR-B SAR images from Antarctic Circumpolar Current south of Africa to derive surface currents; they used a least-squares method also explored later in this chapter, though with only one wave component. There were regions of their study area that violated assumptions made during the development of the theoretical method, but outside those areas they found “realistic” surface current velocity fields but had no ground truth with which to compare.

One final example of previous wave-current interaction studies with SAR was by *Liu et al.* [1994], who used ray tracing in a SAR image to look at the refraction to surface waves caused by their passage through an eddy in the Gulf of Alaska; they compared the observed paths with modeled rays that passed through a simplified eddy field and found good agreement.

We do not have enough information to determine a unique solution using this method because we lack information about wave heights, which is needed to estimate the energy in the wave action. A simplified method that does not use the full conservation relations starts with assuming stationarity in the conservation of crests equation. If $\vec{k}$ does not depend on time, then the observed frequency is constant, so

$$\omega_{obs} = \omega + \vec{k} \cdot \vec{u} = constant \tag{9.13}$$

across a region. As $\omega = \sqrt{kg}$ where $k = |\vec{k}|$, we can expand this to

$$\omega_{obs} = \sqrt{kg} + ku_k, \tag{9.14}$$

where u_k is the current velocity in the direction of $\vec{k}$. This method will be called the direct inversion method, and it can be solved directly for the velocity using a single estimate of $\vec{k}$. While we have ω_{obs} estimates from the reanalysis, the spatial resolution of those estimates is poor, which causes very large currents. We instead use the mean $\vec{k}$ to calculate a frequency ω_{kmean} to substitute for ω_{obs}; the error in the calculated current velocity caused by this substitution is

$$\Delta u_k = \epsilon / k \tag{9.15}$$

for frequency error $\epsilon = \omega_{obs} - \omega_{kmean}$. Locations with smaller k have larger errors. Estimates of the velocity using wave periods from the reanalysis are in Appendix E.

If we divide the image on day 197 in 2016 into a 4-by-4 grid of tiles, we can get an estimate of the wavelength and direction, and thus $\vec{k}$, for each tile from the visible wave fronts [Figure 9.12a]. The wavenumber vector is larger and in a more counterclockwise direction to the west of the front. Using equation 9.14 with $\omega_{kmean} = 0.384$ rad/s as ω_{obs}, we can get estimates of the velocity at the surface in the direction of $\vec{k}$ [Figure 9.12b]. Surface currents are north-northeast for all tiles to the east of the front, but those to the west of the front are weaker and to the south. There is strong zonal shear of the meridional current across the front. Current magnitudes are unrealistically large, with maximum values of 6 m/s.

However, this method only yields currents in the direction of the wavenumber vector. One way to get an estimate of the two-dimensional currents involves using multiple estimates of the wavenumber vector to form a system of equations based on Equation 9.13. We can expand $\vec{k}$ into azimuthal and range components:

$$\omega_{obs} = \sqrt{kg} + k_a u_a + k_r u_r. \tag{9.16}$$

Examination of the velocity shows:

$$u_a = \bar{u}_a + \delta u_a$$
$$u_r = \bar{u}_r + \delta u_r$$

where

$$\delta u_a = \frac{\partial u_a}{\partial a}\delta A + \frac{\partial u_a}{\partial r}\delta R$$
$$\delta u_r = \frac{\partial u_r}{\partial a}\delta A + \frac{\partial u_r}{\partial r}\delta R$$

Assuming that the shear is constant over δA and δR, we can simplify this to

$$\Delta u_a = l_a \Delta A + l_r \Delta R$$
$$\Delta u_r = m_a \Delta A + m_r \Delta R$$

The velocity is then:

$$u_a = \bar{u}_a + l_a \Delta A + l_r \Delta R \tag{9.20a}$$
$$u_r = \bar{u}_r + m_a \Delta A + m_r \Delta R \tag{9.20b}$$

If we put this into our above equation, we get

$$\sigma_{obs} = \sqrt{kg} + k_a[\bar{u}_a + l_a\Delta A + l_r\Delta R] + k_r[\bar{u}_r + m_a\Delta A + m_r\Delta R]. \tag{9.21}$$

If we divide a SAR image into tiles, we can use four adjacent tiles with their estimates of the wavenumber vector to solve for the four unknown parameters, l_a, l_r, m_a, m_r assuming those unknown parameters are constant over all four tiles:

$$\mathbf{A}\mathbf{x} = \mathbf{b} \tag{9.22a}$$

$$\mathbf{A} = \begin{pmatrix} k_{1a}x\Delta A & k_{1a}y\Delta R & k_{1r}x\Delta A & k_{1r}y\Delta R \\ k_{2a}x\Delta A & k_{2a}y\Delta R & k_{2r}x\Delta A & k_{2r}y\Delta R \\ k_{3a}x\Delta A & k_{3a}y\Delta R & k_{3r}x\Delta A & k_{3r}y\Delta R \\ k_{4a}x\Delta A & k_{4a}y\Delta R & k_{4r}x\Delta A & k_{4r}y\Delta R \end{pmatrix} \tag{9.22b}$$

$$\mathbf{x} = \begin{pmatrix} l_a \\ l_r \\ m_a \\ m_r \end{pmatrix} \tag{9.22c}$$

$$\mathbf{b} = \begin{pmatrix} \omega_{obs} - \sqrt{k_1 g} - k_{1a}\bar{u}_a - k_{1r}\bar{u}_r \\ \omega_{obs} - \sqrt{k_2 g} - k_{2a}\bar{u}_a - k_{2r}\bar{u}_r \\ \omega_{obs} - \sqrt{k_3 g} - k_{3a}\bar{u}_a - k_{3r}\bar{u}_r \\ \omega_{obs} - \sqrt{k_4 g} - k_{4a}\bar{u}_a - k_{4r}\bar{u}_r \end{pmatrix} \tag{9.22d}$$

with x and y being the azimuthal and range indices for the location of the estimate of $\vec{k}$, respectively. To solve this, we need four independent estimates of $\vec{k}$, an estimate of the background current $\bar{u}$, and an estimate of the observed frequency ω_{obs}. We take $\bar{u}$ from modeled currents, with the same current used for all locations in a single image, and we again substitute ω_{kmean} for ω_{obs}. Reported currents from this method are Δu, without the mean current.

Applying this to the image on day 197 of 2016, with $\bar{u} = 0.452$ m/s at 292° relative to north, shows that there is very strong shear at the transition across the front and velocities change sharply there [Figure 9.13]. This is also the situation in a SAR image from day 361 in 2017 [Figure 9.14], which also has obvious refraction and currents in the direction of the wavenumber vector [Figure 9.15]; the $\omega_{kmean} = 0.408$ rad/s here, while $\bar{u} = 0.070$ m/s at 342° relative to north. This image has very different currents across the front when calculating the shear from the system of equations [Figure 9.16]. This system of equations method cannot be used reliably because the small variation in the $\vec{k}$ makes estimates of the currents perpendicular to $\vec{k}$ not well-constrained. The matrix $\mathbf{A}$ in Equation 9.22 is also ill-conditioned with condition numbers at O 10^{17}; this means that small changes in the constants $\mathbf{b}$ results in large changes in the answers $\mathbf{x}$.

While tiles for the SAR image on day 296 in 2017 [Figure 9.17] have the same issue with current estimates perpendicular to the wavenumber vector being unconstrained, there are waves from two directions in this image, which can both be used to make an estimate of the currents $\vec{u}_k$. Both of the $\vec{k}$ can be used in the system of equations method simultaneously, helping to constrain the solutions. Now, Equation 9.22 is:

$$\mathbf{A}\mathbf{x} = \mathbf{b} \tag{9.23a}$$

$$\mathbf{A} = \begin{pmatrix} k^P_{1a}x\Delta A & k^P_{1a}y\Delta R & k^P_{1r}x\Delta A & k^P_{1r}y\Delta R \\ k^P_{2a}x\Delta A & k^P_{2a}y\Delta R & k^P_{2r}x\Delta A & k^P_{2r}y\Delta R \\ k^P_{3a}x\Delta A & k^P_{3a}y\Delta R & k^P_{3r}x\Delta A & k^P_{3r}y\Delta R \\ k^P_{4a}x\Delta A & k^P_{4a}y\Delta R & k^P_{4r}x\Delta A & k^P_{4r}y\Delta R \\ k^S_{1a}x\Delta A & k^S_{1a}y\Delta R & k^S_{1r}x\Delta A & k^S_{1r}y\Delta R \\ k^S_{2a}x\Delta A & k^S_{2a}y\Delta R & k^S_{2r}x\Delta A & k^S_{2r}y\Delta R \\ k^S_{3a}x\Delta A & k^S_{3a}y\Delta R & k^S_{3r}x\Delta A & k^S_{3r}y\Delta R \\ k^S_{4a}x\Delta A & k^S_{4a}y\Delta R & k^S_{4r}x\Delta A & k^S_{4r}y\Delta R \end{pmatrix} \tag{9.23b}$$

$$\mathbf{x} = \begin{pmatrix} l_a \\ l_r \\ m_a \\ m_r \end{pmatrix} \tag{9.23c}$$

$$\mathbf{b} = \begin{pmatrix} \omega_{obs}^P - \sqrt{k_1^P g} - k_{1a}^P \bar{u}_a - k_{1r}^P \bar{u}_r \\ \omega_{obs}^P - \sqrt{k_2^P g} - k_{2a}^P \bar{u}_a - k_{2r}^P \bar{u}_r \\ \omega_{obs}^P - \sqrt{k_3^P g} - k_{3a}^P \bar{u}_a - k_{3r}^P \bar{u}_r \\ \omega_{obs}^P - \sqrt{k_4^P g} - k_{4a}^P \bar{u}_a - k_{4r}^P \bar{u}_r \\ \omega_{obs}^S - \sqrt{k_1^S g} - k_{1a}^S \bar{u}_a - k_{1r}^S \bar{u}_r \\ \omega_{obs}^S - \sqrt{k_2^S g} - k_{2a}^S \bar{u}_a - k_{2r}^S \bar{u}_r \\ \omega_{obs}^S - \sqrt{k_3^S g} - k_{3a}^S \bar{u}_a - k_{3r}^S \bar{u}_r \\ \omega_{obs}^S - \sqrt{k_4^S g} - k_{4a}^S \bar{u}_a - k_{4r}^S \bar{u}_r \end{pmatrix} \tag{9.23d}$$

where k^P and k^S are the k from the primary and secondary swells, respectively; $\omega_{kmean}^P = 0.406$ rad/s and $\omega_{kmean}^S = 0.375$ rad/s are substituted for the ω_{obs}^P and ω_{obs}^S from the primary and secondary swells, respectively; and $\bar{u} = 0.335$ m/s at 292° relative to north. Notably, because the system is now overdetermined, we use least-squares methods to solve this. Currents from the least-squares method [Figure 9.18, bottom row] have unrealistically large values in a few tiles, indicating that those specific tiles have vastly different estimates of $\vec{k}$. This method cannot be used reliably because this image and the tiles may violate the assumption made earlier that the shear is constant over the set of tiles used to get the estimate. The north-most shear estimates contain tiles on both sides of the front, which, presumably, have different current shears.

The least-squares currents can be compared with the direct inversion currents [Figure 9.18, middle row]. The two estimates are not very similar, with the directions of the currents from the direct inversion changing rapidly between adjacent tiles. This results from using rather subjective methods to derive wavenumber estimates: wavefronts that were clear and had at least 3 waves in a train were selected, but that still left significant differences between some of the waves in a single tile. Using directional spectral analysis would be more objective, but each Sentinel SAR image is only large enough to produce one spectrum with good spectral resolution, so such methods cannot be used on the imagettes. It can, however, be used on SIR-C/X-SAR images.

The directional wave spectra for each SIR-C image [Figure 9.19] were computed from non-overlapping tiles of 512 x 512 pixels in azimuth/range coordinates, or 3.2 km x 3.2 km for X-SAR and 6.4 km x 6.4 km for SIR-C/L, using a Hamming window. For each tile, the spectrum is smoothed in wavenumber space with a 9-point mean filter and a Gaussian filter with a standard deviation of 0.72. The vector wavenumber of each spectral peak is defined as the weighted average power spectral density. The spectra were averaged over all tiles for each image.

The directional spectra contain three main domains of variance: swell, appearing as single or multiple narrow peaks at 150-500 m wavelengths; wind seas, appearing as wedges of weaker spectral density with broad angular distribution and 50-150 m wavelengths, most affected by the modulation transfer function; and atmospheric wind rows, appearing as strong power spectral density peaks with >1000 m wavelengths, scaling with the height of the trade-wind inversion layer.

The directional spectra on day 279 for all three radar bands show four main peaks that correspond to: (i) a primary swell with wavelengths of 300-450 m, originating from ~218° (or ~38°), (ii) a secondary swell with wavelengths of 400-550 m originating from ~336° (or ~156°), (iii) wind-seas with wavelengths of 60-300 m with a broad angular distribution from 80° to 210° (or 260° to 30°), and (iv) windrows. Directional spectra for day 280 are similar: (i) a primary swell originating from ~210° (or ~30°), (ii) a secondary swell with wavelengths of 250-350 m originating from 330° (or 150°), (iii) wind seas with an angular distribution from 90° to 180° (or 270° to 360°). On day 282, the swell is split into multiple peaks: two peaks with wavelengths of 160-220 m and 250-325 m, both originating from 210° (or 30°), and a secondary swell with wavelengths of 180-225 m originating from 332° (or 152°). The directional spectrum of a multi-look SAR image has a 180° ambiguity, i.e., the actual direction of propagation of waves cannot be determined without external information. Resolution of the directional ambiguities has been suggested using the wave reanalysis and scatterometer wind archives, the opposite (less likely) solutions being listed in parentheses.

Spectral analysis of SAR images is complicated by the SAR imaging mechanisms, meaning that the SAR image spectrum S_i is not equal to the wave spectrum of the ocean at that location and time, S_w. They are related by the modulation transfer function M and the azimuthal falloff function F:

$$\frac{S_i}{S_w} = |M|^2 k^2 F \tag{9.24}$$

There are three primary mechanisms by which SAR imaging distorts wave spectra with direction, and each of these is represented by a modulation transfer function; the modulation transfer function M is the sum of these three. The tilt of the wave slope relative to the SAR platform causes distortion in the range direction, and this is represented by the tilt MTF:

$$M_t = \frac{4cot\theta}{1 + sin^2\theta} ik_r/k \tag{9.25}$$

where θ is the SAR incidence angle, k is the total wavenumber, k_r is the component of k in the range direction. An example of M_t is Figure 9.20a. The second mechanism is one relating to the hydrodynamic model, which also primarily impacts range-traveling waves, and it is represented as:

$$M_h = 4.5k\omega \frac{\omega - i\mu}{\omega^2 + \mu^2} \tag{9.26}$$

where $\omega = \sqrt{gk}$ is the angular frequency of the waves and μ is a dampening constant of 0.92 s^{-1} for wind speeds over 7 m/s and 0.13 s^{-1} for smaller wind speeds. An example of M_h is in Figure 9.20b. The velocity bunching mechanism primarily impacts azimuthal traveling waves, and it results from the movement of the platform causing incorrect spacing between wave fronts. While this mechanism can and frequently is non-linear, for simplicity a reasonable linear representation of this MTF is:

$$M_v = \frac{\omega R k_a}{vk}[-cos\theta + i(k_a/k)sin\theta] \tag{9.27}$$

where R is the platform slant range, v is the platform velocity, and k_a is the azimuthal component of the wavenumber. An example of M_v is in Figure 9.20c.

The azimuthal cutoff, which is the lowest limit of wavelengths that can be imaged, can be modeled as:

$$\lambda_m = C_0(R/v)H_s^{1/2} \tag{9.28}$$

for constant C_0 approximately 1 $\mathrm{m}^{1/2}$/s, range R, platform velocity v, and significant wave height H_s. For the Sentinel image on day 197 in 2016, $R = 693$ km, $v = 7508$ m/s, and $H_s = 1.6$ m, so $\lambda_m = 117$ m. For SIR-C data, $R = 225$ km, $v = 7255$ m/s, and $H_s = 1.9$ m, so $\lambda_m = 43$ m. The significant wave heights were estimated based on WAVERYS reanalysis for the approximate time and location of each SAR image. Waves with wavelengths longer than this can be imaged by the SAR. This is taken as the limit of the azimuthal falloff function F:

$$F(k) = \begin{cases} 1 & k < 2\pi/\lambda_m \\ 0 & k > 2\pi/\lambda_m \end{cases}$$

There is no example plot of $F(k)$ given because the wavenumbers associated with the λ_m values are outside the visible axis limits on the plots shown. The total MTF, given as $|M|^2 = |M_t + M_h + M_v|^2$, is in Figure 9.20d, displays stronger modulation in the azimuth direction than the range direction, resulting from the strong values of the velocity bunching MTF. If the spectra in Figure 9.19 are divided by the total MTF [Figure 9.21], the primary swell peaks are very close to the amplified line along $k_a = 0$, with some of them being indistinct. The secondary swell peaks are still separate and visible.

The wavelengths and wavenumber vectors show variability between days, bands, and tiles. For day 279 [Figure 9.22], L- and C-band images have longer wavelengths to the northwest for primary swell peak and to the southwest for the secondary swell peak; the X-band image has longer wavelengths right along the front for both swell peaks. For day 280 [Figure 9.23], both L- and C-band images have larger wavelengths to the northwest. For day 282 [Figure 9.24], the primary swell is split into two peaks; for both bands, the shorter wavelengths are concentrated in the east for the primary peak with shortest wavelengths and the secondary peak but are fairly evenly distributed for the other primary peak.

Surface currents derived using the least-squares method with both primary and secondary swell peaks are spatially organized in all days and bands [Figures 9.25, 9.26, 9.27]. Maximum magnitudes are approximately 3 m/s, though magnitudes as large as 2 m/s are fairly common, though unrealistically large. Background velocities $\bar{u}$ from GLORYS reanalysis are 0.196 m/s at 81° relative to north, 0.180 m/s at 26° relative to north, and 0.378 m/s at 80° relative to north for days 279, 280, and 282, respectively. Currents on day 279 from L- and C- bands are similar, with southeastward velocities northeast of the front and along-front currents on the front, which runs through the center of the image from left to right with an upward tilt. The X-band image has stronger currents right along the front that head eastward to the west of the front, crossing it; currents off the front are less coherent. For day 280, currents in the north are northeastward, curling around to the southeast in the more southern parts of the image; currents are stronger in the L-band image. The front is in the upper third of the image, crossing from left to right with a downward tilt; currents cross the front in the northern part of the image but run along it in the southern section. For day 282, currents using the short-wave primary swell peak are very different across the front, with those from the L-band image being very weak to the east of the front and stronger in the west, with westward or northwestward currents; those from the X-band image are very weak to the west of the front, with stronger eastward or southeastward currents to the east of the front. Currents found from the long-wave primary swell share some features with those from the other primary peak: L-band currents are westward to the west of the front, and X-band images are weak to the west of the front but stronger and eastward or southeastward to the east of the front. However, the L-band currents are of equal magnitude to the east of the front in the southern part of the image, and they cross the front to the west; they are weaker on the northern part of the image east of the front, but still stronger than the currents there from the shorter wave primary peak. The X-band currents are stronger using the long-wavelength primary swell peak and remain strong over a slightly larger area extending across the front.

Even though the estimates for $\vec{k}$ are significantly better for SIR-C data than for Sentinel-1 data, the least squares method still has large condition numbers, $O\ 10^{17}$. The singular values and eigenvectors of the matrix $\mathbf{A}$ also indicate problems with the computation: only two singular values are large, and the eigenvectors corresponding to these two large singular values are identical except for the signs of the different terms. The first two terms of each row in **A** are either identical or multiples of one another, and the same is true of the last two terms in each row.

If we compare the least-squares derived currents with those from the direct inversion method, we can see some similarities between the two. Total currents for day 279 are along-front for L- and C- bands and across-front for the X-band, with stronger currents in the latter right at the front. Magnitudes are also slightly larger for C-band currents than L-band currents; magnitudes are slightly larger by the direct inversion method than the least-squares method. The total currents for day 280 are to the northeast in the north but curve down to the southeast in the more southern parts of the image. The currents in the north of the image are more counterclockwise than in the least-squares results, but the area of northeastward currents spreads further to the south in the L-band than the C-band, just as in the least-squares results. The magnitudes in the direct inversion method are again slightly larger. For day 282, the total currents are slightly weaker in magnitude from the direct inversion method, but are otherwise similar. For currents using the short-wave primary swell peak, the L-band currents are exactly opposite those from the least-squares method, with very weak currents to the west of the front and stronger eastward currents to the east of the front. The X-band currents are stronger to the east of the front as in the least-squares method, but they are westward here. For currents using the long-wave primary swell peak, the L-band currents are westward or southwestward, counterclockwise of those in the least-squares method, while the X-band currents are westward or southwestward to the east of the front; the area of stronger currents is larger, crossing the front, just as in the least-squares method.

Because the SIR-C images are large enough that we have multiple tiles on each side of the front in each image, we can look at statistical changes between tilesets. New directional wave spectra were computed from half-overlapping tiles of 512 x 512 pixels in azimuth/range coordinates with points only on one side of the front (missing parts of tiles right along the fronts were zero-padded to be the correct size, and tiles missing more than 1/50 points were skipped). For either region separated by the front, the mean vector wavenumber of each spectral peak is computed over the ensemble of tiles in that region. The differences in mean vector wavenumbers of each spectral peak on opposite sides of the front will be called peak differences. Standard errors on the estimation of the mean wavenumbers are obtained for each ensemble, and statistical procedures for testing the significance of these peak differences are applied.

Because we have two dimensions to each wavenumber vector estimate, a standard Student's t-test or Welch's t-test is not appropriate; instead, Hotelling's t^2 test, which tests multiple variables once, is the correct tool. If there are n_1 estimates of the wavenumber k_1 for the primary swell peak on one side of the front, with each estimate consisting of two components in azimuth and range (k_{1a}, k_{1r}), the mean wavenumber $\bar{k}_1$ can be defined as:

$$\bar{k}_1 = \frac{1}{n_1} \sum_{i=1}^{n_1} k_1^i \tag{9.29}$$

where $k_1^i = (k_{1a}^i, k_{1r}^i)$ is the ith estimate of k_1; the covariance is:

$$\hat{\Sigma}_{\bar{k}_1} = \frac{1}{n_1 - 1} \sum_{i=1}^{n_1} (k_1^i - \bar{k}_1)(k_1^i - \bar{k}_1)^T \tag{9.30}$$

where the exponent T denotes the transpose. To determine if the mean wavenumber is different from the population mean $\mu_1 = (\mu_{1a}, \mu_{1r})$, we can compose a statistic called Hotelling's t^2 statistic as:

$$t^2 = (\bar{k}_1 - \mu_1)^T \hat{\Sigma}_{\bar{k}_1}^{-1} (\bar{k}_1 - \mu_1) \tag{9.31}$$

where the exponent -1 denotes the inverse.

Since there are two sides of the front in our problem, the mean and covariance of the wavenumber on the other side of the front k_2 are also needed:

$$\bar{k}_2 = \frac{1}{n_2} \sum_{i=1}^{n_2} k_2^i \tag{9.32}$$

$$\hat{\Sigma}_{\bar{k}_2} = \frac{1}{n_2 - 1} \sum_{i=1}^{n_2} (k_2^i - \bar{k}_2)(k_2^i - \bar{k}_2)^T \tag{9.33}$$

The two covariances must be combined into a single measure. This can be done through pooling if the number of samples in both variables and their variances are similar, which is not the case here: the area and thus number of tiles on the eastern sides of the front is significantly smaller. The total covariance is then just their sum:

$$\hat{\Sigma} = \hat{\Sigma}_{\bar{k}_1} + \hat{\Sigma}_{\bar{k}_2} \tag{9.34}$$

The two-sample t-squared statistic is:

$$t^2 = \frac{n_1 n_2}{n_1 + n_2} (\bar{k}_1 - \bar{k}_2)^T \hat{\Sigma}^{-1} (\bar{k}_1 - \bar{k}_2) \tag{9.35}$$

The t-squared statistic can be made to follow an F distribution by multiplying by a factor:

$$F(d_1, d_2) \sim \frac{d_2}{d_1(d_1 + d_2 - 1)} T^2(d_1, d_1 + d_2 - 1) \tag{9.36}$$

where d_1 and d_2 are the degrees of freedom in the F distribution. Since the Hotelling's t-squared statistic is related to the t-squared distribution by:

$$t^2 \sim T^2(p, n_1 + n_2 - 2) \tag{9.37}$$

where p is the number of variables, the p-values can be taken from the F distribution where $d_1 = p$ and $d_2 = n_1 + n_2 - p - 1$:

$$F(p, n_1 + n_2 - p - 1) \sim \frac{n_1 + n_2 - p - 1}{p(n_1 + n_2 - 2)} t^2 \tag{9.38}$$

where p is the number of variables in the data. The above procedure can also be done for the secondary swell peaks.

The wavenumber values, their means, and the 1-σ ellipses are plotted in Figures 9.31, 9.32, and 9.33. There are more tiles on the west/southwest side of the fronts, so the 1-σ ellipses are smaller. Generally, estimates of $\vec{k}$ from X-band images are more diffuse than those of other bands.

The p-values show that cross-front differences in $\vec{k}$ are statistically significant at a 90% level for primary peaks on days 279 and 280 for L- and C- bands, day 282 for the short wave primary peak in the L-band, and day 282 for both peaks for the X-band. Only one of the secondary swell peaks is statistically significant, that on day 279 in the X-band. For the statistically-significant changes, primary swell peaks indicate that the direction shifts slightly, sometimes clockwise and other times not, and the wavelength of the waves shrinks slightly moving from west of the front to east. The secondary peak shows counterclockwise rotation and a shortening of the wavelength from west of the front to east of the front.

Differences in $\vec{k}$ across the front that are significant can be related to changes in surface current velocity if we assume that the observed frequency is constant across the image. Then:

$$\sqrt{gk_1} + \vec{k}_1 \cdot \vec{u}_1 = \sqrt{gk_2} + \vec{k}_2 \cdot \vec{u}_2 \tag{9.39}$$

If we define the velocity on one side of the front as $\vec{u}_2 = \vec{u}_1 + \delta\vec{u}$, then we can solve for part of the change in velocity:

$$\sqrt{gk_1} - \sqrt{gk_2} = \vec{k}_2 \cdot (\vec{u}_1 + \delta\vec{u}) - \vec{k}_1 \cdot \vec{u}_1 \tag{9.40}$$

$$\sqrt{gk_1} - \sqrt{gk_2} = (\vec{k}_2 - \vec{k}_1) \cdot \vec{u}_1 + \vec{k}_2 \cdot \delta\vec{u} \tag{9.41}$$

$$\delta u_{k_2} = \frac{\sqrt{gk_1} - \sqrt{gk_2} + (\vec{k}_1 - \vec{k}_2) \cdot \vec{u}_1}{k_2} \tag{9.42}$$

If both primary and secondary swell peak differences are significant, we can get two components to $\delta\vec{u}$. This is not the case for any of the bands or images. Assuming currents east of the front are as in the model ($\vec{u}_1 = \bar{u}$), then changes to the currents west of the front relative to those east of the front derived from the cross-front mean differences are in Figure 9.34. All of the primary swell derived estimates have currents crossing the front, while the one estimate from the secondary peak has currents moving away from the front at an angle.

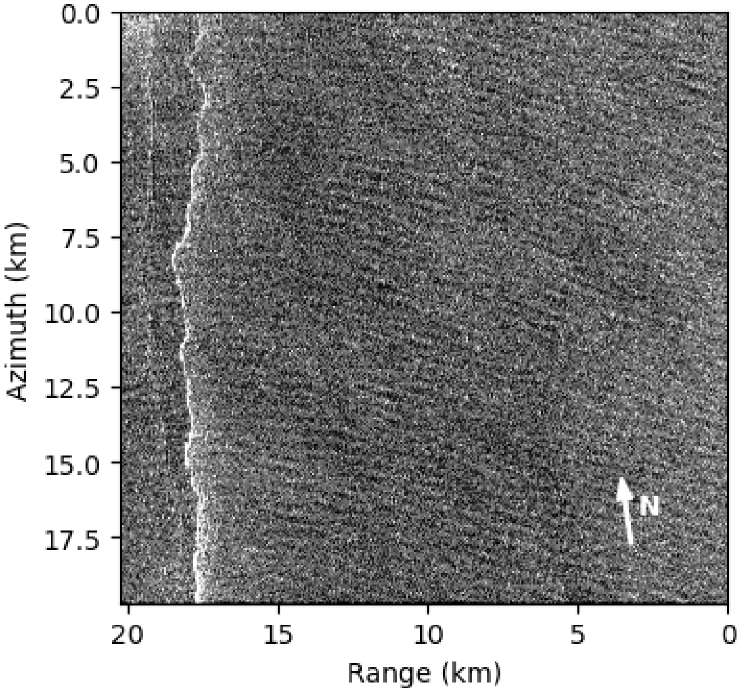

Figure 9.11: Sentinel image from day 197 in 2016 centered on ∼4°N, 119.5°W in the equatorial Pacific.

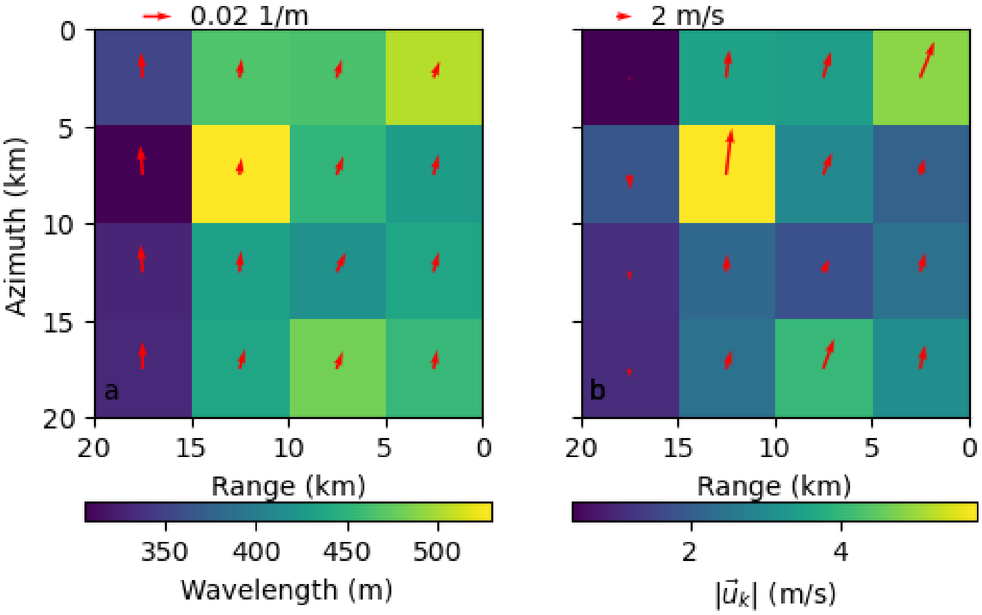

Figure 9.12: (a) Wavelength (color) and $\vec{k}$ (arrows), as well as (b) current magnitude (color) and vector (arrow) for the sentinel image from day 197 in 2016 centered on ∼4°N, 119.5°W. Currents are derived with the direct method using the $\vec{k}$ from (a) and a calculated wave period of 15.3 s.

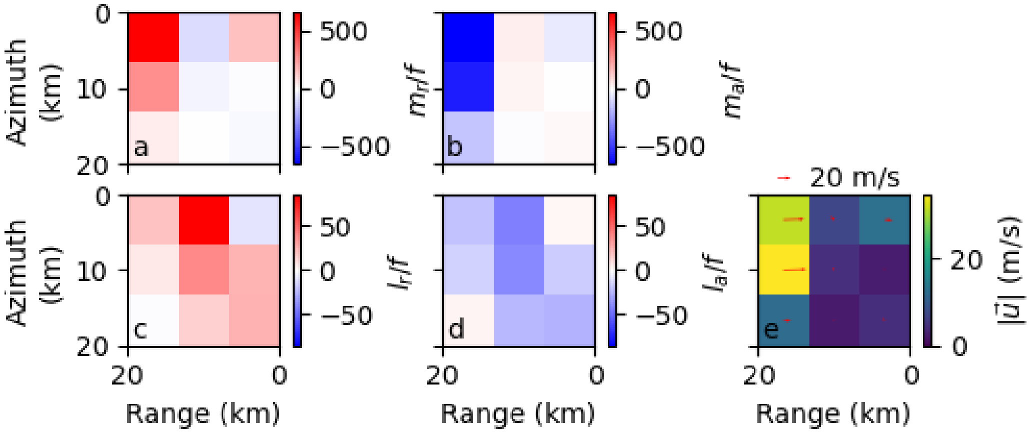

Figure 9.13: Shear scaled by f (color) for (a) range-direction velocity in range direction (m_r), (b) range-direction velocity in azimuthal direction (m_a), (c) azimuthal-direction velocity in range direction (l_r), and (d) azimuthal-direction velocity in azimuthal direction (l_a) for the Sentinel-1 image from day 197 in 2016 centered on ∼4°N, 119.5°W using least-squares methods. Also, (e) the velocity magnitude (color) and vector (arrow) that the shear in (a) through (d) imply.

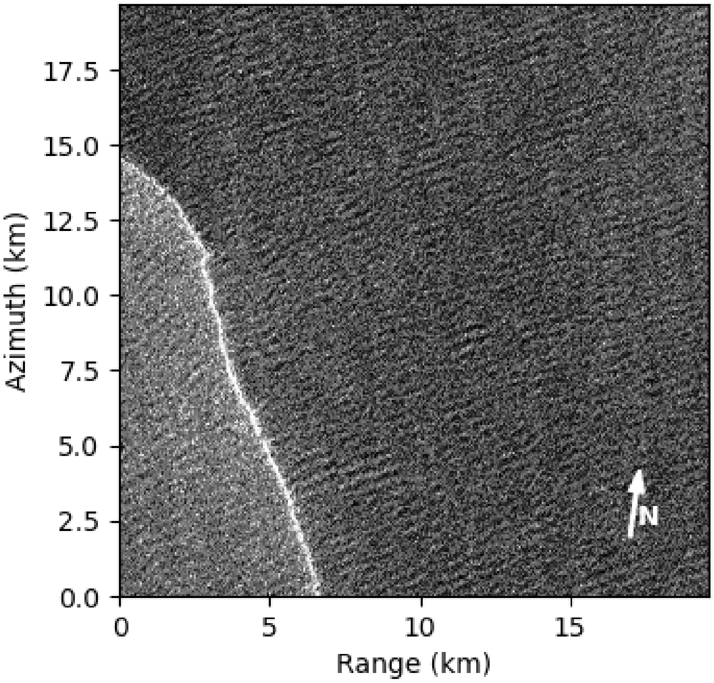

Figure 9.14: Sentinel image from day 361 in 2017 centered on ∼6°N, 128.5°W.

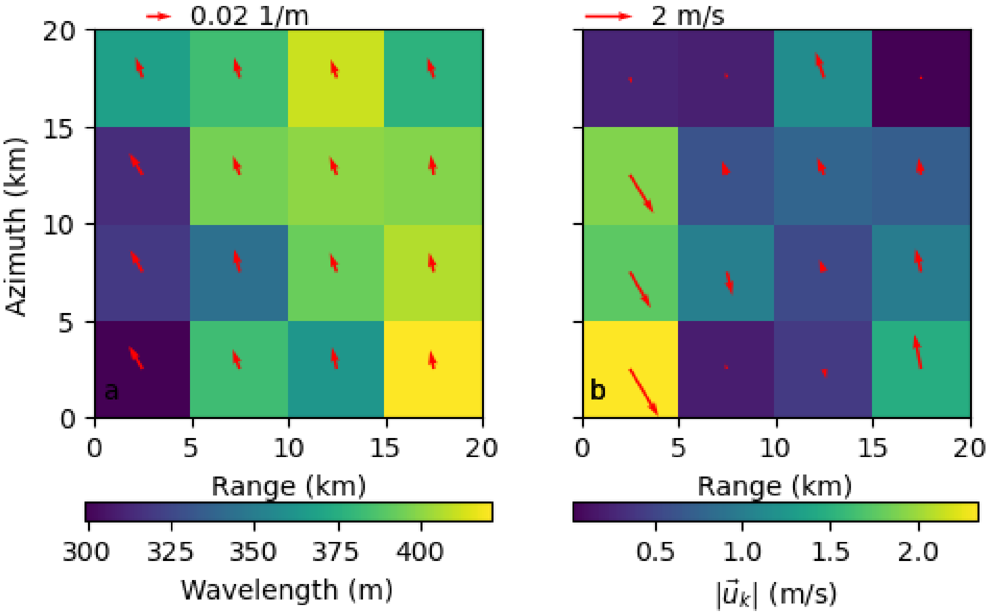

Figure 9.15: (a) Wavelength (color) and $\vec{k}$ (arrows), as well as (b) current magnitude (color) and vector (arrow) for the sentinel image from day 361 in 2017 centered on ∼6°N, 128.5°W. Currents are derived with the direct method using the $\vec{k}$ from (a) and a calculated wave period of 15.3 s.

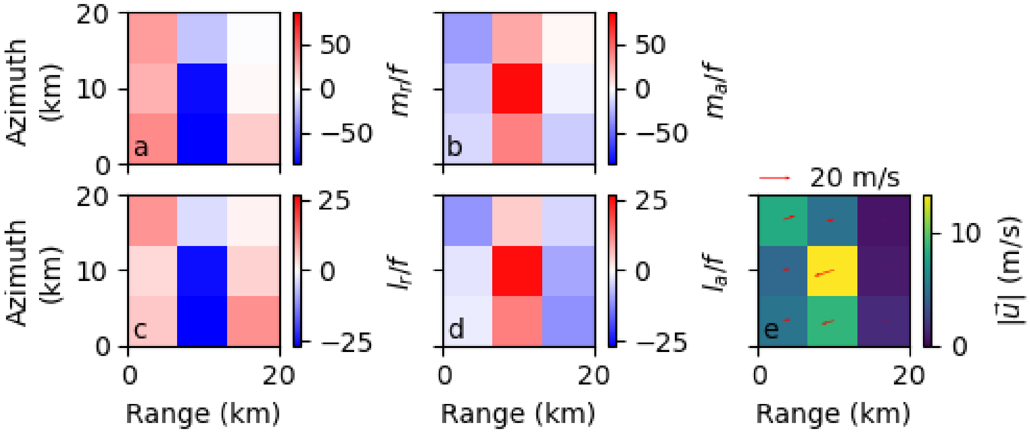

Figure 9.16: Shear scaled by f (color) for (a) range-direction velocity in range direction (m_r), (b) range-direction velocity in azimuthal direction (m_a), (c) azimuthal-direction velocity in range direction (l_r), and (d) azimuthal-direction velocity in azimuthal direction (l_a) for the Sentinel-1 image from day 361 in 2017 centered on ∼6°N, 128.5°W using least-squares methods. Also, (e) the velocity magnitude (color) and vector (arrow) that the shear in (a) through (d) imply.

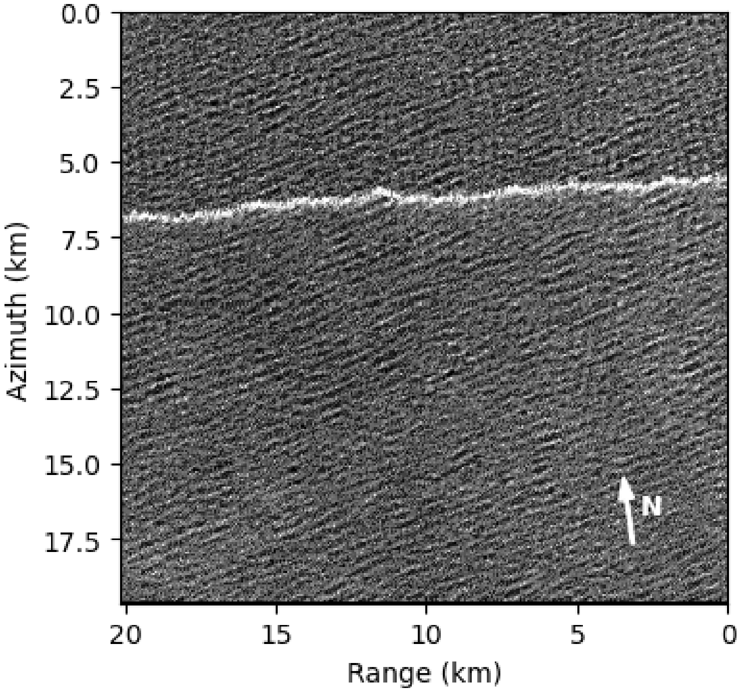

Figure 9.17: Sentinel image from day 296 in 2017 centered on ∼2°N, 126°W.

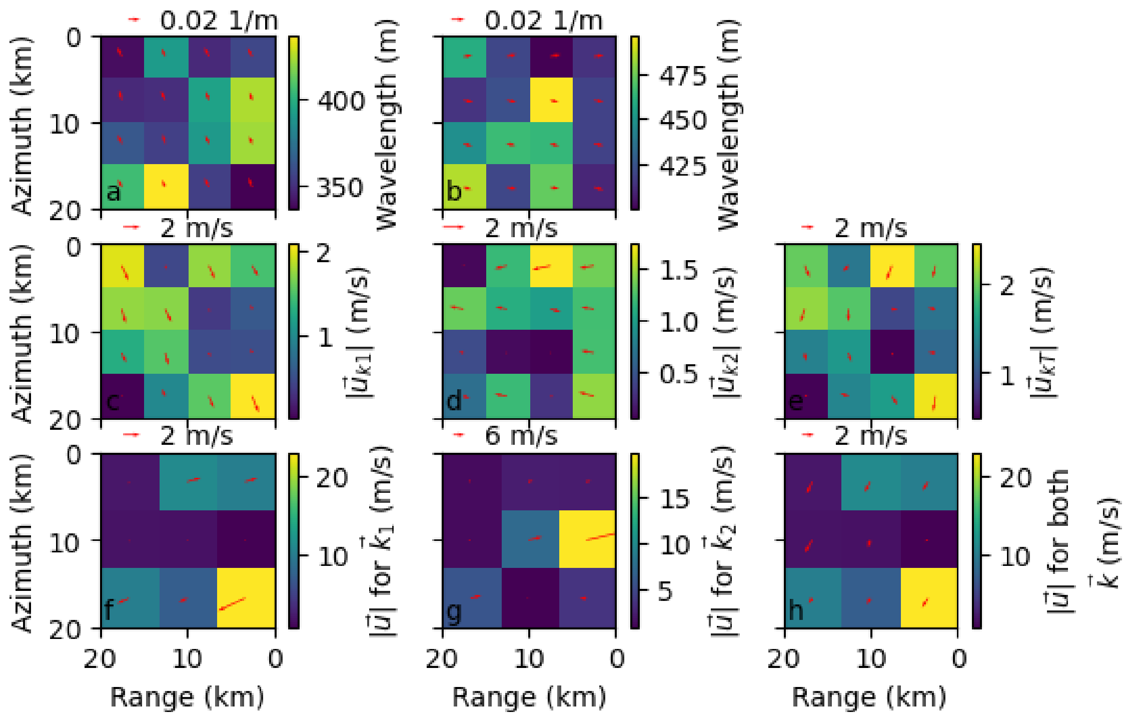

Figure 9.18: (top row) Wavelengths (color) and wavenumber vectors for the (a) primary and (b) secondary swell waves; (middle row) velocity magnitudes (color) and vectors from direct inversion method using the (c) primary and (d) secondary swell, and (e) full vector combination of (c) and (d); and (bottom row) velocity magnitudes (color) and vectors from the least-squares method using the (f) primary and (g) secondary swell, and (h) using both swell wavenumber vectors together, for the Sentinel image from day 296 in 2017 centered on ~2°N, 126°W. Calculated wave frequencies ω_{kmean} were 0.406 rad/s and 0.375 rad/s for primary and secondary swell, respectively.

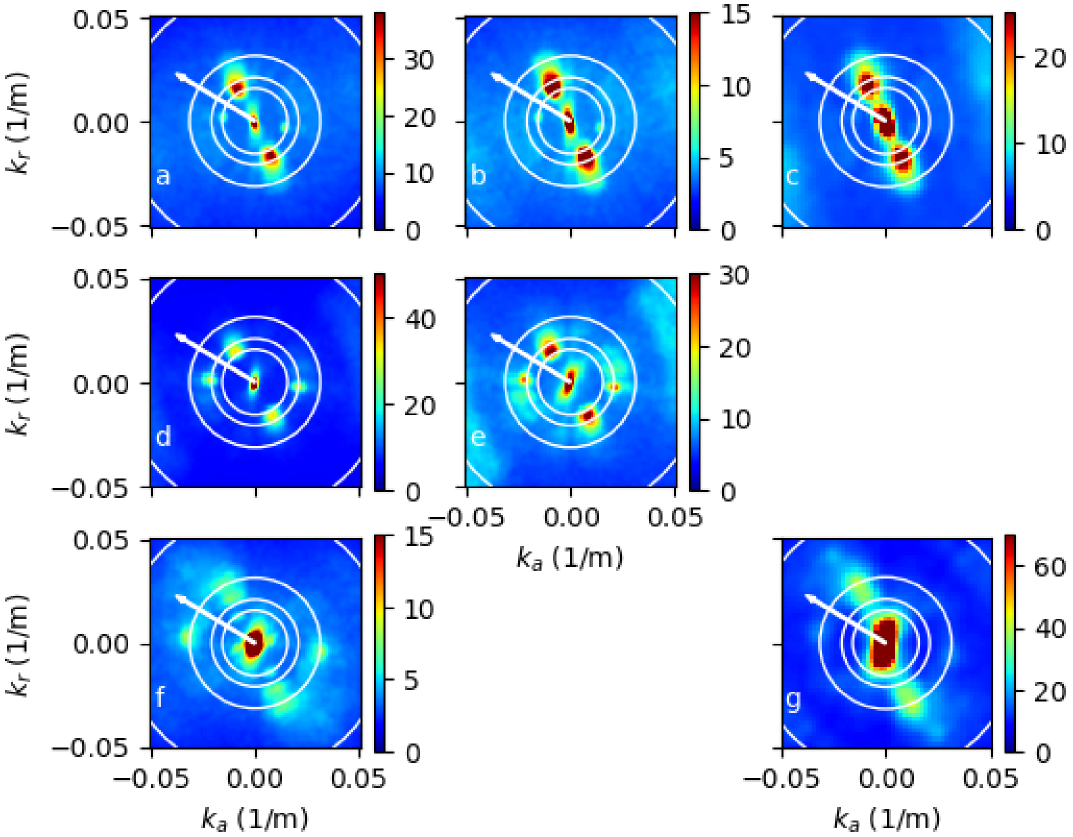

Figure 9.19: Mean spectral amplitude for (top row) day 279, (second row) day 280, (bottom row) day 282, and (left column) L-band, (middle column) C-band, and (right column) X-band, for SIR-C images taken around 5°N, 141°W. White rings are at 100-m wavelength intervals from 100 m to 400 m. The white arrow points northward.

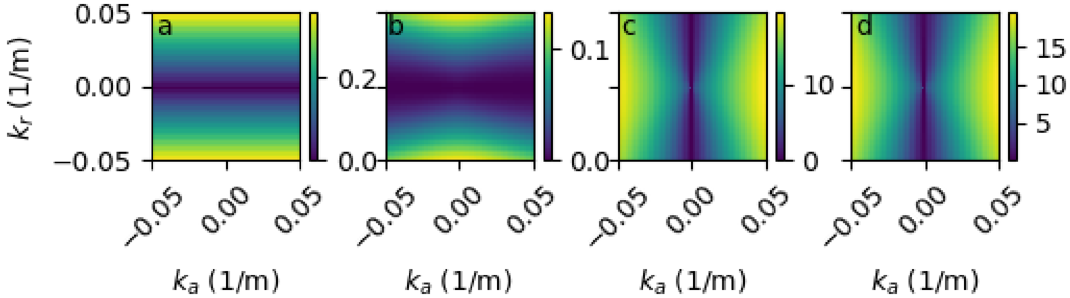

Figure 9.20: X-SAR (a) tilt, (b) hydrodynamic, (c) and velocity bunching MTFs, plus (d) the total MTF function divided by k^2 for yearday 282 in 1994 taken around 5°N, 141°W. The L- and C- band MTFs look similar in shape, but scales of tilt and velocity bunching MTFs are larger for them.

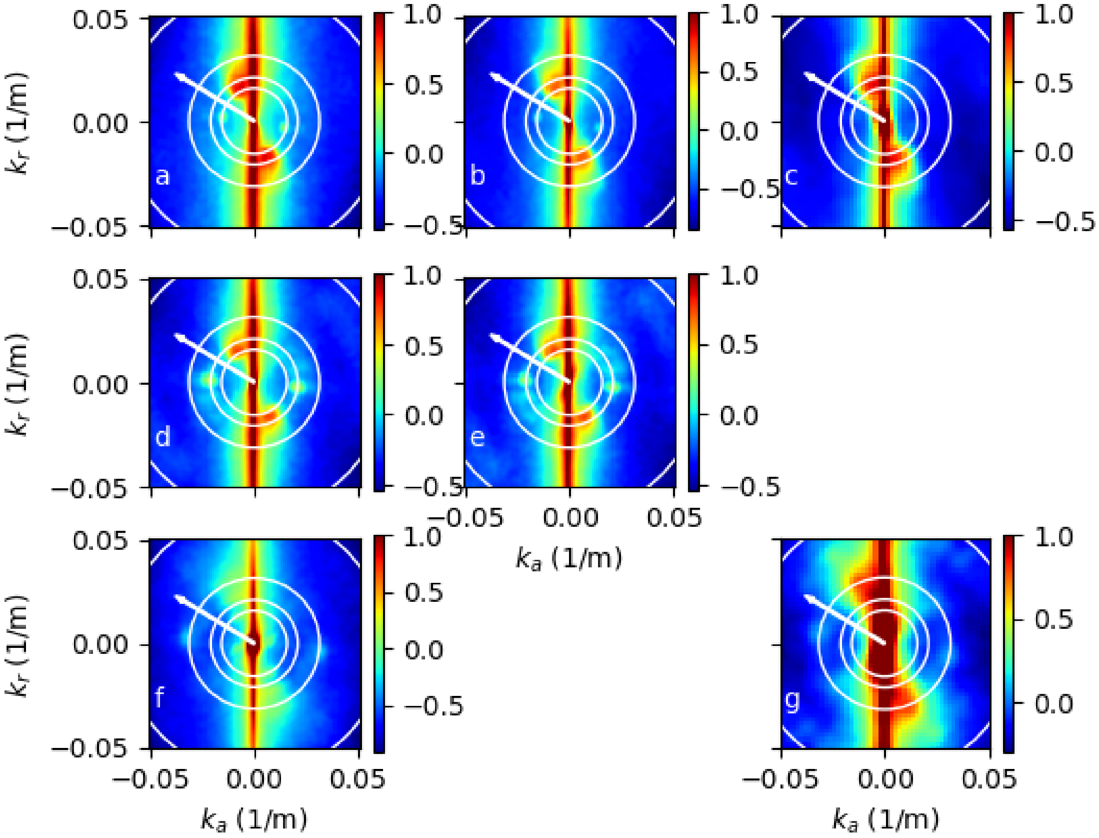

Figure 9.21: Logarithm of mean spectral amplitude over all tiles for (top row) day 279, (second row) day 280, (bottom row) day 282, and (left column) L-band, (middle column) C-band, and (right column) X-band SIR-C images divided by the MTF for SIR-C images taken around 5°N, 141°W. White rings are at 100-m wavelength intervals from 100 m to 400 m. The white arrow points northward.

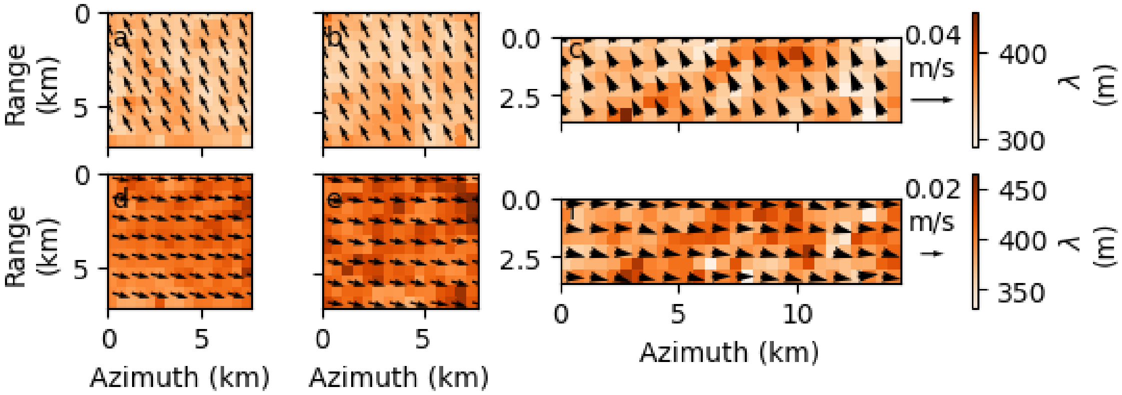

Figure 9.22: Wavelengths (color) and wavenumber vectors (arrows) of (top row) the primary swell and (bottom row) secondary swell for (left) L-band, (middle) C-band, and (right) X-band SIR-C images for day 279 in 1994 taken around 5°N, 141°W.

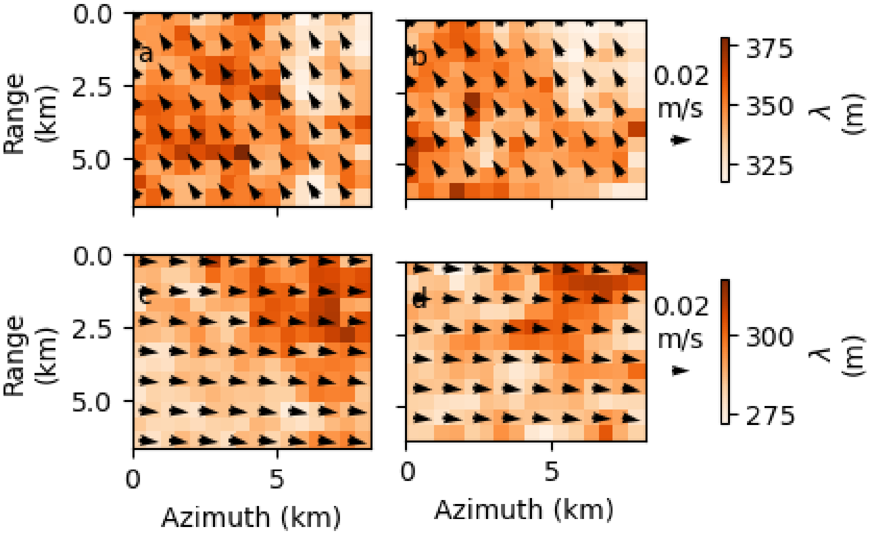

Figure 9.23: Wavelengths (color) and wavenumber vectors (arrows) of (top row) the primary swell and (bottom row) secondary swell for (left) L-band and (right) C-band SIR-C images for day 280 in 1994 taken around 5°N, 141°W.

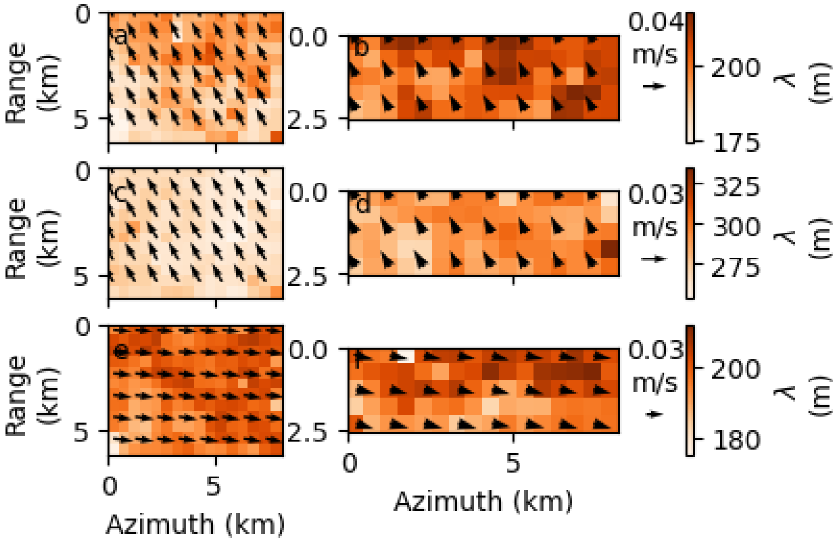

Figure 9.24: Wavelengths (color) and wavenumber vectors (arrows) of (top two rows) the primary swell peak, with the peak with longer wavelengths being in the middle row, and (bottom row) secondary swell for (left) L-band and (right) X-band SIR-C images for day 282 in 1994 taken around 5°N, 141°W.

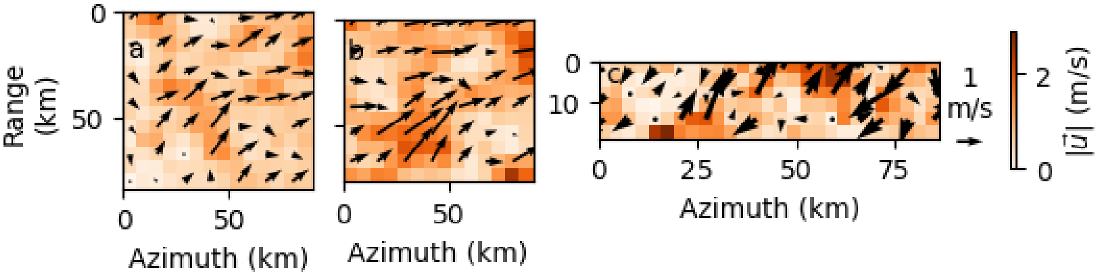

Figure 9.25: Magnitudes (color) and vectors (arrows) for velocities derived using both primary swell and secondary swell peaks with the least-squares method for (left) L-band, (middle) C-band, and (right) X-band SIR-C images taken on day 279 in 1994 centered around 5°N, 141°W.

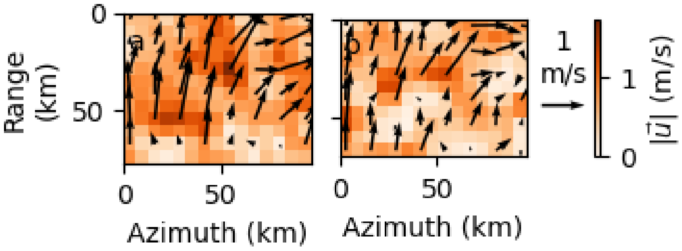

Figure 9.26: Magnitudes (color) and vectors (arrows) for velocities derived using both primary swell and secondary swell peaks with the least-squares method for (left) L-band and (right) C-band SIR-C images for day 280 in 1994 taken around 5°N, 141°W.

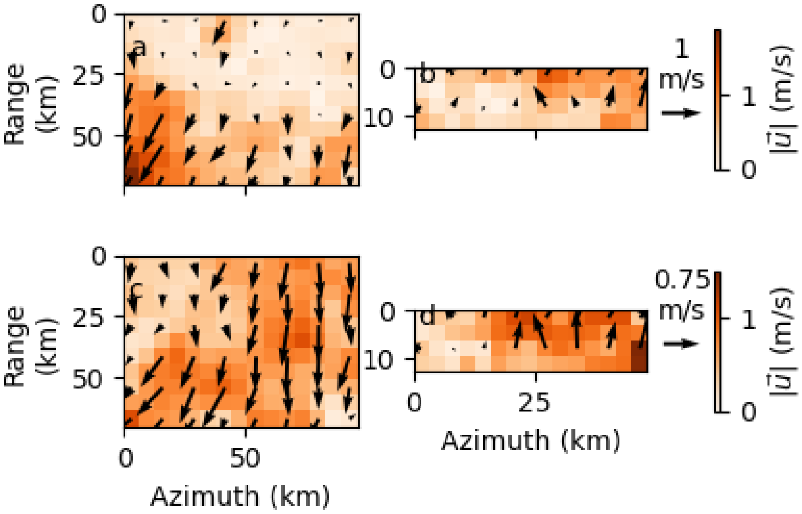

Figure 9.27: Magnitudes (color) and vectors (arrows) for velocities derived using both primary swell and secondary swell peaks with the least-squares method with (top row) the shorter-wavelength primary swell and (bottom row) the longer-wavelength primary swell for (left) L-band and (right) X-band SIR-C images for day 282 in 1994 taken around 5°N, 141°W.

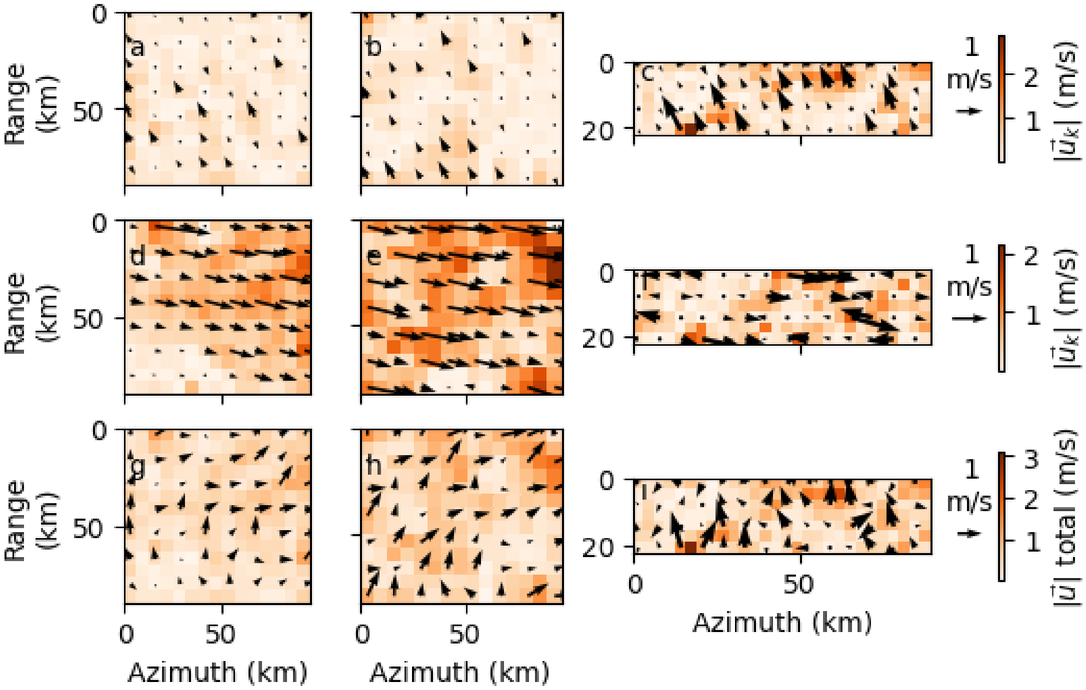

Figure 9.28: Magnitudes (color) and vectors (arrows) for velocities from SIR-C images on day 279 in 1994 taken around 5°N, 141°W derived by direct inversion method for (top) the primary swell, (middle) the secondary swell, and (bottom) the two combined. These are for (left column) L-band, (middle column) C-band, and (right column) X-band.

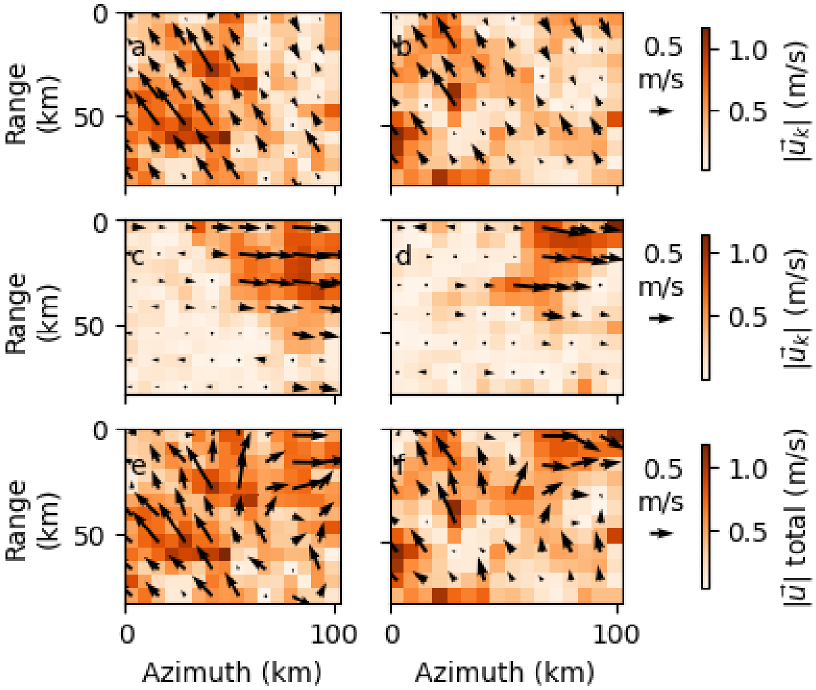

Figure 9.29: Magnitudes (color) and vectors (arrows) for velocities from SIR-C images on day 280 in 1994 taken around 5°N, 141°W derived by direct inversion method for (top) the primary swell, (middle) the secondary swell, and (bottom) the two combined. These are for (left column) L-band and (right column) C-band.

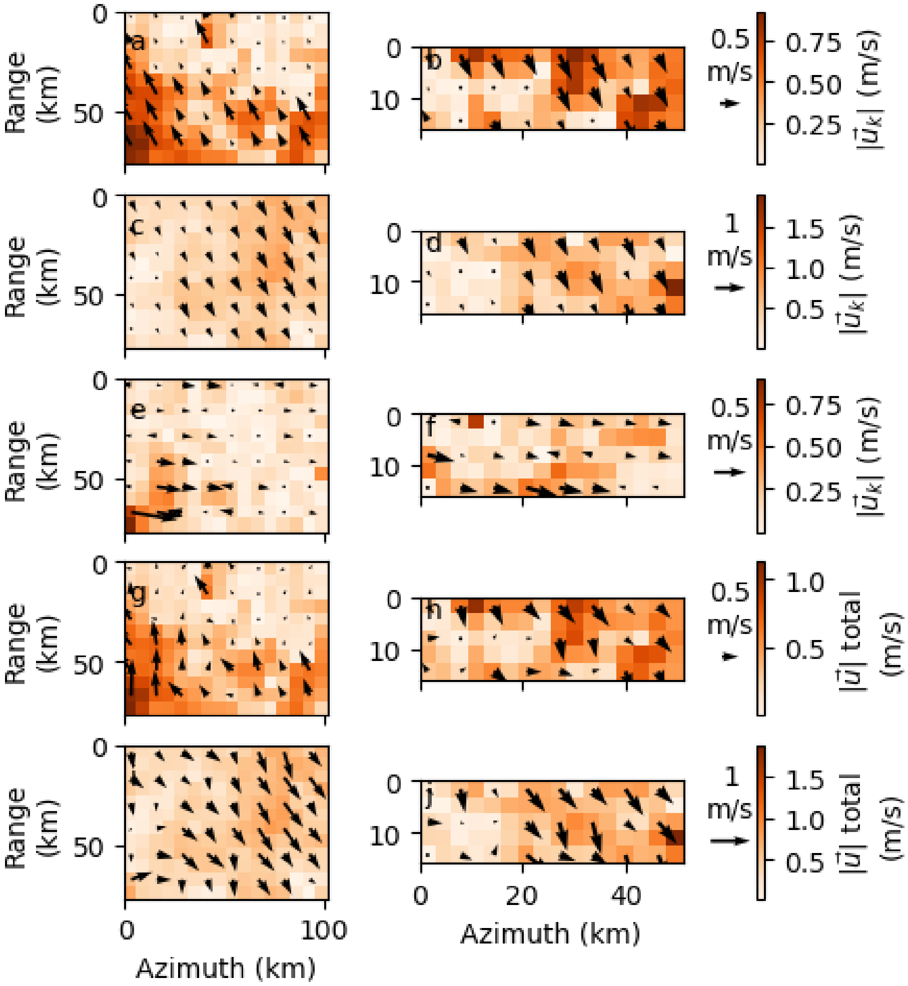

Figure 9.30: Magnitudes (color) and vectors (arrows) for velocities from SIR-C images on day 282 in 1994 taken around 5°N, 141°W derived by direct inversion method for (top two rows) the primary swell peaks, (third row) the secondary swell, and (bottom two rows) the primary and secondary swells combined. These are for (left column) L-band and (right column) X-band.

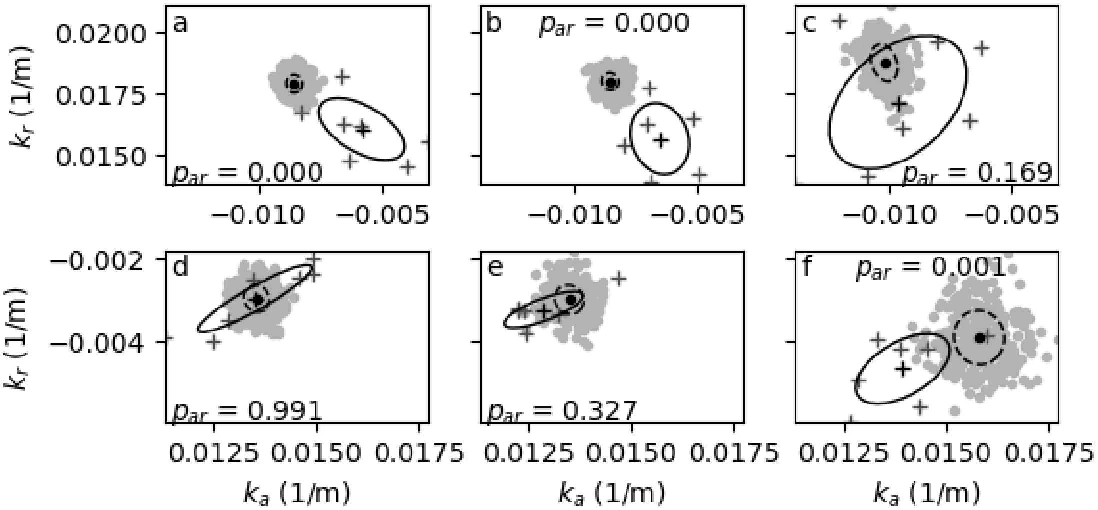

Figure 9.31: Centroid locations, mean centroid location, and 1-σ confidence ellipse for northeast of the front (grey +, black +, and solid ellipses, respectively) and southwest of the front (grey ·, black ·, and dashed ellipses, respectively) from the (left column) L-band, the (middle column) C-band, and the (right column) X-band SIR-C images on day 279 in 1994 taken around 5°N, 141°W. Shown are the primary peak (top) and the secondary peak (bottom). Note that northeast of the front is the top of the SAR image in range-azimuth coordinates. The p-values listed are two-dimensional.

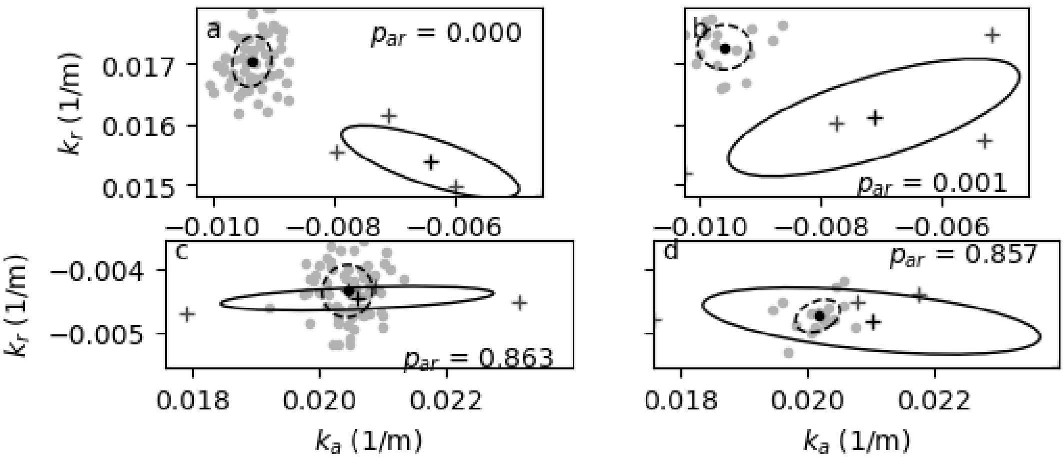

Figure 9.32: Centroid locations, mean centroid location, and 1-σ confidence ellipse for northeast of the front (grey +, black +, and solid ellipses, respectively) and southwest of the front (grey ·, black ·, and dashed ellipses, respectively) from the (left column) L-band and the (right column) C-band SIR-C images on day 280 in 1994 taken around 5°N, 141°W. Shown are the primary peak (top row) and the secondary peak (bottom row). Note that northeast of the front is the top of the SAR image in range-azimuth coordinates. The p-values listed are two-dimensional.

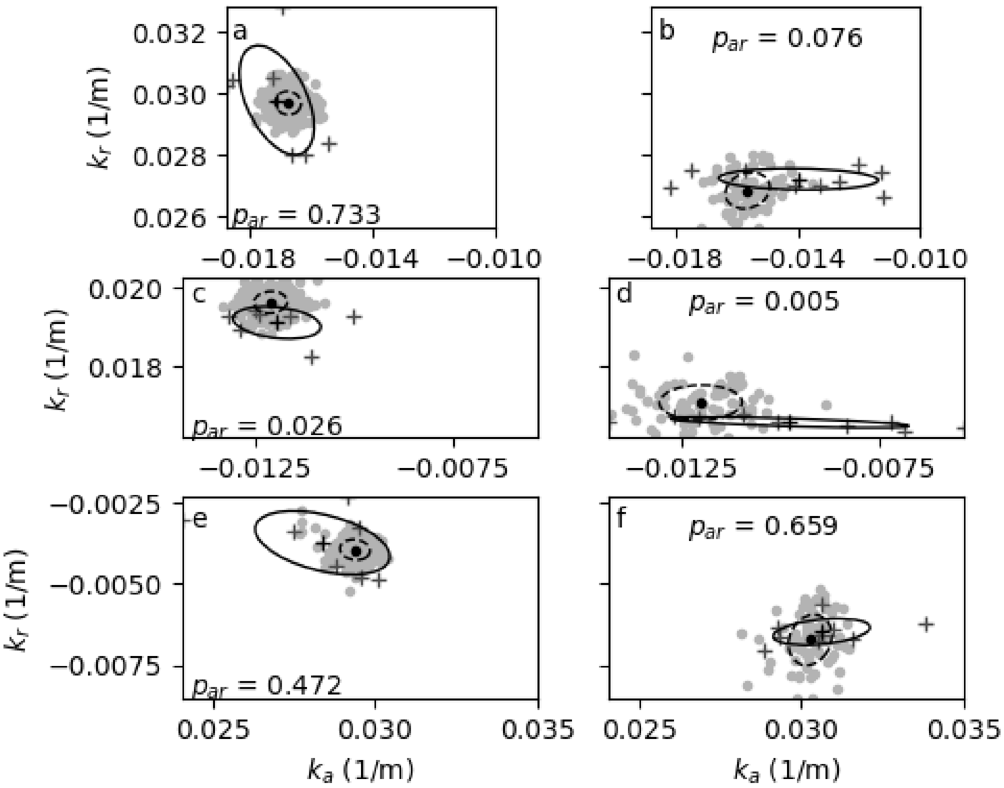

Figure 9.33: Centroid locations, mean centroid location, and 1-σ confidence ellipse for northeast of the front (grey +, black +, and solid ellipses, respectively) and southwest of the front (grey $\cdot$, black $\cdot$, and dashed ellipses, respectively) from the (left column) L-band and the (right column) X-band SIR-C images on day 282 in 1994 taken around 5°N, 141°W. Shown are two primary peak (top two rows) and a secondary peak (bottom row). Note that northeast of the front is at the top of the SAR image in range-azimuth coordinates. The p-values listed are two-dimensional.

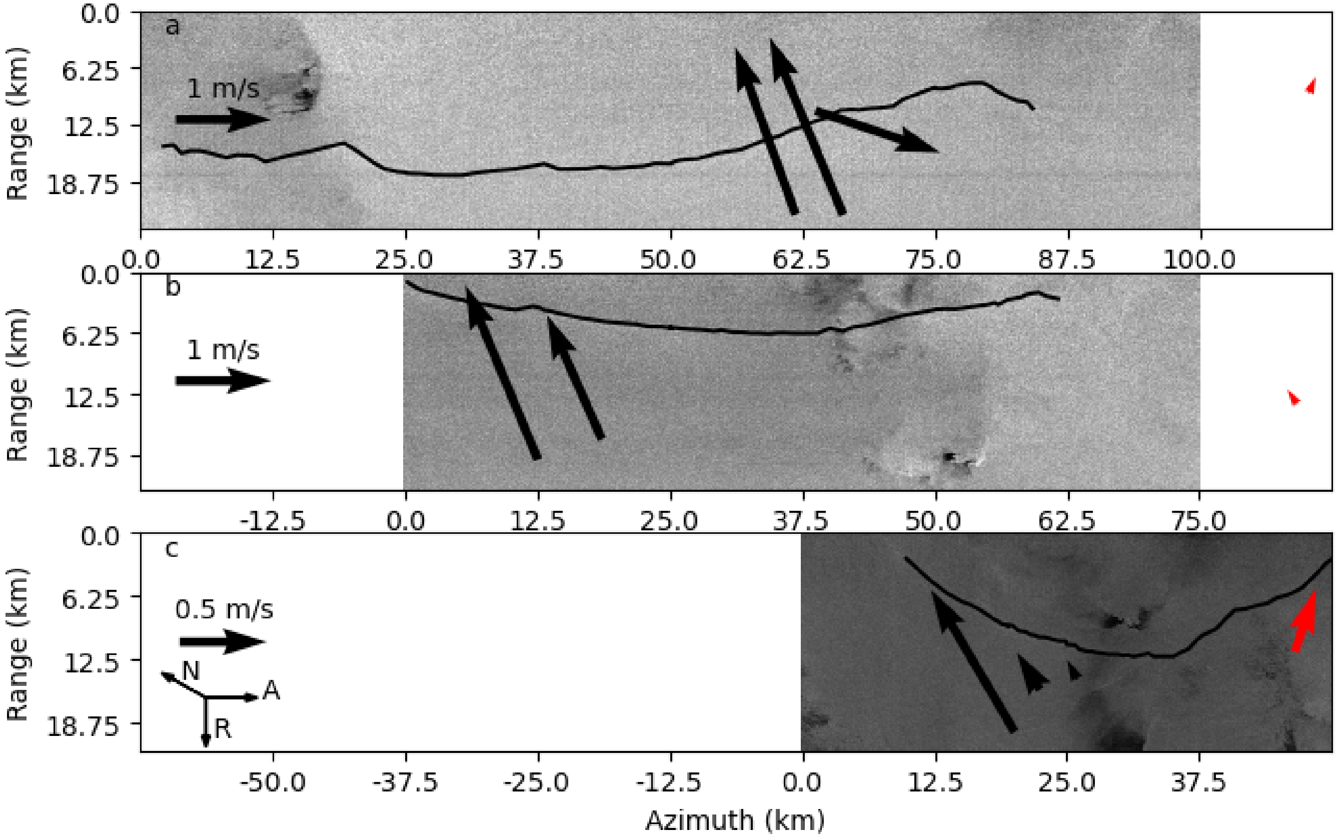

Figure 9.34: Velocity vectors in the k-vector direction inferred from the differences in wavenumber across the front for SIR-C images on days (from top) 279, 280, and 282 in 1994 taken around 5°N, 141°W. Velocities on day 279 are from the primary peaks of the L- and C- bands and the secondary peak of the X-band; on day 280, the vectors are from the primary peaks of the L- and C-band images. On day 282, the vectors are from the longer-wavelength primary peak for both L- and X-bands, and from the shorter wavelength primary peak for the X-band image. Red vectors to the right of each panel are the background velocity determined by reanalysis.

9.5 Conclusions

SAR images can have different levels of background back-scatter across a front, which could be caused by a variety of processes. On the leading front, the cold (eastern) side of the front has lower background back-scatter intensity than the warm (bright) side of the front. Cross-front winds, which blow from southeast to northwest, are weaker over the colder water and stronger over the warmer water; this magnitude difference can explain the back-scatter difference. On the other hand, trailing front images are frequently accompanied by along-front winds, which are still stronger over warmer water, but which then contradict the higher back-scatter observed over colder water. Surface currents, which should be considered as part of the total surface stress, can explain the observed back-scatter difference. Because SAR back-scatter intensity depends not only on the magnitude of the surface stress but also its direction relative to the instrument, variations in current magnitude (∼0.5 m/s) and direction (∼80°) can explain the back-scatter difference.

Surface currents affect SAR imagery not only through the total surface stress, but also through wave-current interactions. They refract surface waves, so the surface wave field in SAR images contains information about currents. Because the effect depends on the angle of the current relative to the wave front and thus wave-number vector k, SAR images with waves from only one direction can only yield information about current magnitudes in that direction. While least-squares methods do technically allow one to seek two-dimensional solutions, a lack of information orthogonal to the single wave-number vector means those solutions are not well-constrained in that direction. Images with waves from two directions can be analyzed using either the direct inversion method or the least-squares method; these two methods produce currents that are qualitatively similar. For smaller images, such as the Sentinel-1 imagettes, determination of $\vec{k}$ is more subjective because there are not enough points to produce the multiple directional spectra with good spectral resolution needed, the values of the wave-number vector obtained are therefore much less certain. Additionally, smaller images frequently lack enough space on both sides of the front to make multiple $\vec{k}$ estimates needed to ensure that one of the method assumptions (namely, that the shear could be constant in the area where estimates are fed into the least-squares algorithm, which naturally precludes lumping estimates from opposite sides of the front together) is not violated. SIR-C/X-SAR images are large enough to use directional spectra on many smaller image sections to get more accurate and consistent $\vec{k}$. The least-squares solutions obtained indicate that there are sections of both along-front flow as well as cross-front flow on the trailing front, and that the currents are different on the two sides of the front.

This last point is supported by a statistical analysis of the $\vec{k}$ estimates on the two sides of the front. Hotelling's t-squared test found that, of nine estimates of $\vec{k}$ from the primary swell peaks and seven from the secondary swell peaks, only seven of the former and one of the latter were significant at a 90% level. All seven of the significant primary peak differences indicated relative currents on the west of the front flowing in a cross-front direction, while the single secondary swell peak estimate was for southeastward currents on the west side of the front.

However, even the properly-derived currents are still unrealistically large in some cases, with magnitudes frequently up to 2 m/s. There is no in-situ data available to compare these estimates with to determine whether the spatial variability of the currents is similar to observations, even if the magnitudes are inaccurate.

Chapter 10

Part 2 conclusions

When tropical instability vortices (TIVs) swirl cold equatorial waters northward and warm ITCZ-origin waters southward while translating westward, they rotate and deform fronts separating waters of differing temperatures, salinities, densities, chlorophyll-a concentrations, surface current magnitudes, and current directions. Recent studies of TIVs on sub-mesoscales skew heavily to modeling; some have focused on core water origin and potential vorticity (PV) dynamics [*Holmes et al.*, 2014] or spectral kinetic energy budgets [*Marchesiello et al.*, 2011]. The observations here focus on TIV fronts, frontal instabilities, and cross-frontal differences; we utilize some of the model results to fill-in for missing *in-situ* observations of PV. The orientation of TIV fronts, which changes as they are advected by swirling large-scale currents, means that winds generally support frontogenesis on the trailing front, but either oppose frontogenesis or have little impact on leading fronts. Simultaneously, the fronts may develop waves, cusps, and breaks due to shear current instabilities that develop right at the interface between equatorial and tropical waters. The difference in sea surface temperature (SST) across the front alters the marine atmospheric boundary layer (MABL) stability, leading to changes in wind stress through changes in wind speed and drag coefficients; in some instances on the trailing front, variations in surface current magnitude and/or direction across the front are sufficient to overpower this MABL stability influence such that regions that would have lower wind stress actually have higher total surface stress. Currents around TIV fronts can be complex and are subject to change during the lifetime of a vortex; in the particular TIV studied here, they evolve over the course of four days from along-front to cross-front in orientation and from relatively uniform in magnitude to being divergent at the front.

What are the implications of these results on energy budgets? Frontogenesis and frontal instabilities transfer energy away from mesoscale flows to smaller scales, which effects energy by both increasing vertical restratification and enhancing dissipation [*Capet et al.*, 2008a]. The energy from frontal instabilities could easily impact larger-scale studies of TIV energy that do not take the energy fluxes from sub-mesoscale frontal instabilities. This is also true of heat budgets, as sub-mesoscale fronts have been modeled to significantly alter local surface winds [*Redelsperger et al.*, 2019; *Wenegrat and Arthur*, 2018], which play an important role in regulating the magnitude of air-sea exchanges. Additionally, observations show an increase in heat fluxes at sub-mesoscale fronts over 1.5 times the bulk calculated values [*Shao et al.*, 2019]. More information, likely from modeling these fronts within the larger vortex structure, is needed to understand exactly what shear current instability or instabilities is responsible, exactly how much energy is involved, and how heat and momentum fluxes change. This will not be a simple prospect as there is significant variability within a TIV in its lifetime and between different TIVs, so the answer may vary based on conditions. On even larger scales and outside of TIVs, sub-mesoscale instabilities need to be accounted for as well, and these results indicate that such instabilities may be quite common even outside previously noted regions, such as coastal upwelling areas [e.g., *Capet et al.*, 2008b].

What are the implications of these results on the use of current inversions with synthetic aperture radar (SAR)? Surface studies could be eased by determining convergence and divergence from satellite data. Presently, costly (in terms of time and money) field work is necessary for observing surface divergence, though modeling can provide information as well. Using SAR to derive surface divergence would allow both more widespread and more frequent analysis. However, further refraction studies must be done to address the many questions left by this work. First, because of this project's focus on TIVs, the SAR images available were severely limited to the SIR-C/X-SAR images that had unknown preprocessing applied; while Sentinel-1 satellites are operational, only the imagettes are available in the equatorial Pacific, which are too small to effectively apply the technique. Thus none of the images used could be considered even close to ideal for this application and the limited utility caused by that is apparent in this work. Testing with better images would give a more useful idea of the utility of current inversions from SAR. Second, there were no *in-situ* sub-mesoscale observations of the surface currents within the studied TIV to allow validation or ground-truthing of the results. Future work should address both of these points and would not necessarily be limited to the equatorial Pacific as a coastal study where larger SAR images and *in-situ* current data are available would be sufficient.

What are the implications of these results on the use of SAR-derived winds? While the typical wind response to sea surface temperature (SST) fronts on sub-mesoscales has higher wind speeds over warmer water, surface currents have now been shown to have a significant influence on backscatter in SAR imagery and may, under certain circumstances, cause wind-inversions to fail in predicting winds. Winds are frequently derived from SAR imagery, but since currents have a large influence, they must be taken into account. Application of wind inversions on SAR should consider local currents, much like in scatterometry; the assumptions about what currents are present should be carefully made, and, given the high resolution of the images, the fact that currents can change appreciably within a single image should not be forgotten.

Finally, these results have shown that SAR can act as a tool to observe sub-mesoscale frontal instabilities as it can provide important information about where and when sub-mesoscale frontal instabilities occur. Numerical data are vital to understanding ocean processes as analysis tools like calculating diagnostic numbers and plotting relationships between variables can shed light on the kinematic and dynamical features and processes occurring; in contrast, SAR lets you see at a glance what the front is doing: the spatial scales (and time scales, if multiple images are available), the exact location and orientation, and the physical form of the perturbations.

Appendices

Appendix A

Data sources and credit

Pathfinder data were provided by GHRSST and the NOAA National Centers for Environmental Information (NCEI). This project was supported in part by a grant from the NOAA Climate Data Record (CDR) Program for satellites.

This study has been conducted using E.U. Copernicus Marine Service Information:

- https://doi.org/10.48670/moi-00021
- https://doi.org/10.48670/moi-00022
- https://doi.org/10.48670/moi-00050
- https://doi.org/10.48670/moi-00182

Generated using Copernicus Climate Change Service information [2020]:

- https://doi.org/10.24381/cds.adbb2d47

Appendix B

EOF Calculation and Scaling

This appendix is from *Benjamin et al.* [2016].

Empirical orthogonal function (EOF) analysis rotates a set of time series in hyperspace such that the new EOF time series are uncorrelated. This is done by first finding an orthonormal basis that can describe the data in physical space the most efficiently (i.e., using the fewest vectors), and then transforming the data into the new basis to find the uncorrelated time series [*Lorenz*, 1956; *Richman*, 1986].

EOFs were computed over subset areas of interest, such as Penguin Bank or near-shore Oahu. The data is $\mathbf{D}$, an $n \times t$ matrix with n as the number of grid positions and t as the number of time steps, and its covariance is $\mathbf{C}$, an $n \times n$ matrix defined as

$$\mathbf{C} = \frac{1}{t-1}\mathbf{D}\mathbf{D}^T \tag{B.1}$$

The factor of $\frac{1}{t-1}$ is required for an unbiased estimate of both variance and the covariance matrix.

Using the covariance method, the eigenvalue problem is posed as

$$\mathbf{C}\mathbf{V} = \mathbf{V}\boldsymbol{\Lambda} \tag{B.2}$$

in which $\boldsymbol{\Lambda}$ is the diagonal eigenvalue matrix and $\mathbf{V}$ is the $n \times n$ orthonormal eigenvector matrix, i.e., $\mathbf{V}^T\mathbf{V} = \mathbf{I}$. Rearranging (B.2) for just one $n \times 1$ eigenvector E_i and one eigenvalue λ_i,

$$\mathbf{C}E_i = \lambda_i E_i \tag{B.3}$$

$$(\mathbf{C} - \lambda_i \mathbf{I})E_i = \vec{0} \tag{B.4}$$

The existence of a nontrivial solution to this problem requires that

$$det(\mathbf{C} - \lambda_i \mathbf{I}) = 0 \tag{B.5}$$

After solving for the eigenvalues, the eigenvectors are found from (B.4). Then, the $n \times t$ matrix $\mathbf{F}$ of the timeseries of the eigenvectors is

$$\mathbf{F} = \mathbf{V}^T\mathbf{D} \tag{B.6}$$

The correlation matrix can then be rewritten as

$$\mathbf{C} = \frac{1}{t-1}\mathbf{D}\mathbf{D}^T = \frac{1}{t-1}\mathbf{V}\mathbf{F}\mathbf{F}^T\mathbf{V}^T \tag{B.7}$$

therefore

$$\mathbf{\Lambda} = \frac{1}{t-1}\mathbf{F}\mathbf{F}^T \tag{B.8}$$

(unbiased variance eigenvalues contain the $\frac{1}{t-1}$ factor as well, consistent with (B.2) and (B.8)). Eigenvalues and eigenvectors were computed using the singular value decomposition algorithm, or SVD.

The subset areas and times used to calculate the EOFs influence the resulting modes. Selecting the area over Penguin Bank, and the first 12 hours of the tsunami, isolates this specific process. Increasing or decreasing the period over which the EOF is calculated reduces or increases the amount of variance in each mode, but their spatial structure does not significantly change.

Appendix C

EOF method sensitivity

How sensitive is this decomposition method to the specifics of the modes used? Several tests were run by altering the 2011 Tōhoku modes, computing the new mode indices and their spectra, and comparing those with the originals during the 2011 Tōhoku tsunami. The alterations involved increasing either the positive or negative parts of the modes, shifting the modes inwards or outwards in range, shifting the modes eastward or westward in azimuth, or expanding or collapsing the modes in range (i.e., moving the antinodes towards or away from one another) [Figure C.1].

Changing the amplitude of the negative parts of the modes did not impact the M1 index or spectrum [Figure C.2], but it did increase the M2 index, particularly the 42-min oscillations that were not prominent in that mode with the original basis. Increasing the positive parts of the modes increased both M1 and M2 indices and their spectral amplitudes, though this was particularly strong at 42-min in M2. Note that because EOFs are symmetric with respect to sign (i.e., multiplying a spatial mode and associated timeseries by -1 does not actually change anything), the terms "positive" and "negative" are relative.

Shifting the modes outward in range decreases the M1 index and spectral amplitudes at all periods, but for M2 it increases the spectral amplitude at 16 and 42 min while decreasing elsewhere [Figure C.3]. Shifting the modes inwards in range also decreases the M1 index and spectral amplitudes at all periods, while the M2 index and spectral changes depend on the strength of the shift: for small shifts, the index shifts such that the spectral amplitude decreases at 16 min, increases at 42 min, and remains fairly steady for other periods. For large shifts, the spectral amplitude decreases at all periods except 42 min, which has a small increase in amplitude.

Shifting modes in azimuth causes small decreases in mode index and spectral amplitude [Figure C.4]; these decreases are slightly larger for westward shifts than for eastward ones, and also slightly larger for larger shifts. The spectral peaks remain at the same periods.

Collapsing and expanding modes by a small amount [Figure C.5] causes little change in the M1 index or spectrum, but they cause an increase in the 42-min oscillation of M2 and a decrease at 22 and 26 min. Collapsing a mode causes a stronger change in M2. Expanding or collapsing a mode more causes a stronger response. Overall, the sensitivity tests show that the modes are fairly stable for small amplitude and location shifts, though M2 does have a tendency to show larger 42-min spectral peaks in several types of alterations.

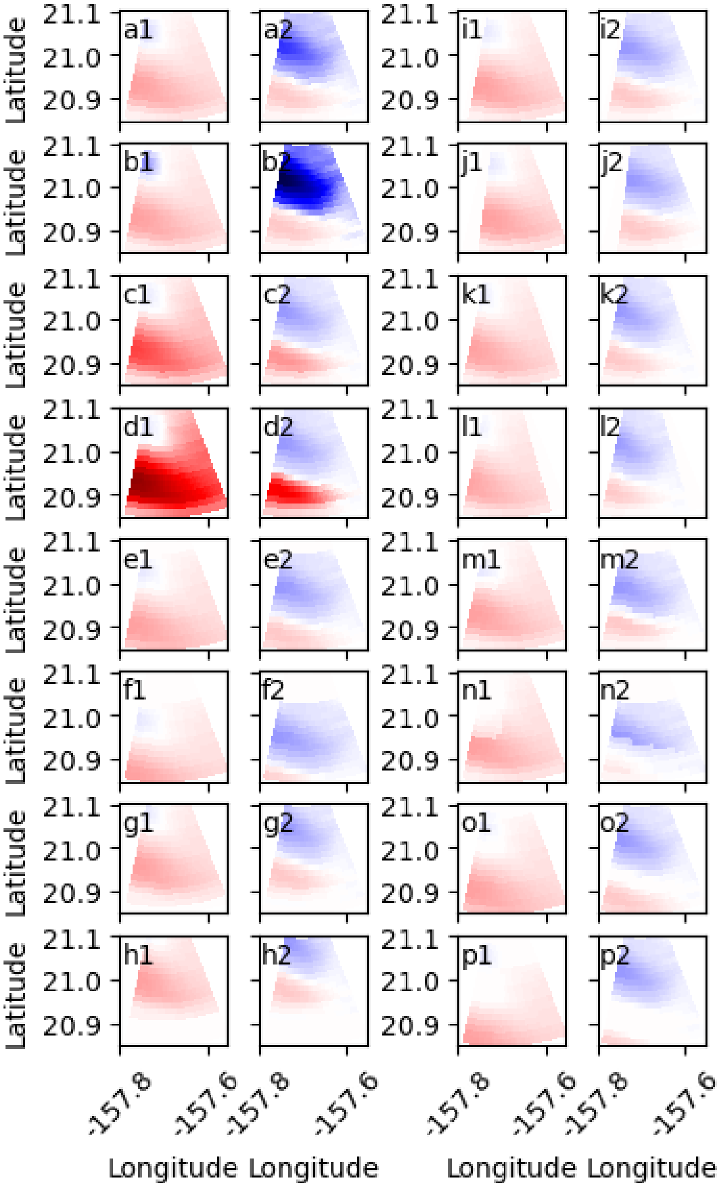

Figure C.1: Modified modes 1 and 2 (numbered) for the 16 different sensitivity tests (lettered).

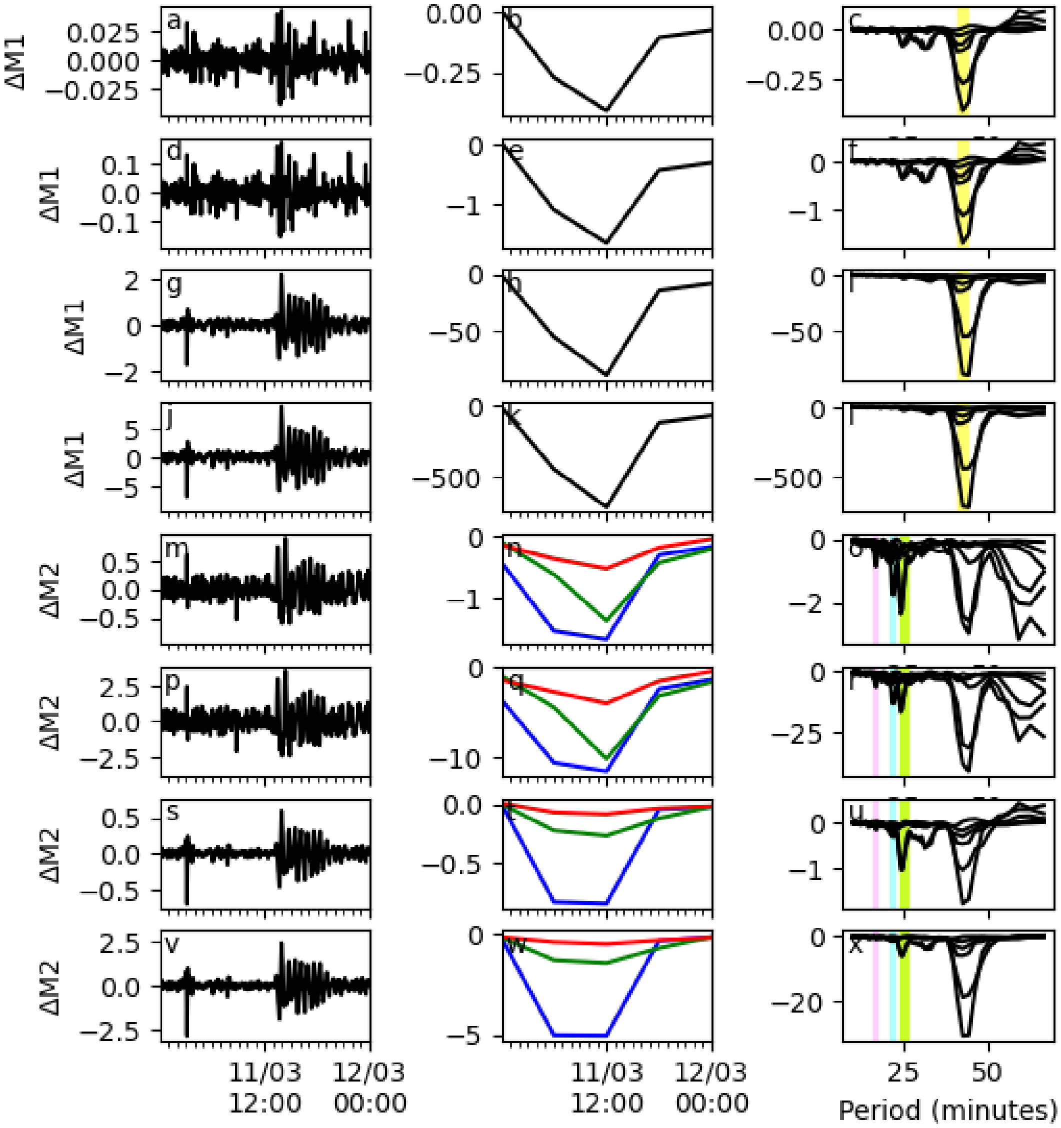

Figure C.2: Difference between 2011 Tōhoku tsunami using original modes (solid lines) and using modified modes: top four rows are M1, and bottom four are M2. At left are mode indices, in middle are band spectral amplitudes, and at right are line spectrograms. Modified modes have the negative parts doubled (rows a/b/c and m/n/o), negative parts quintupled (rows d/e/f and p/q/r), positive parts doubled (rows g/h/i and s/t/u), and positive parts quintupled (rows j/k/l and v/w/x). These correspond to tests a through d in Figure C.1.

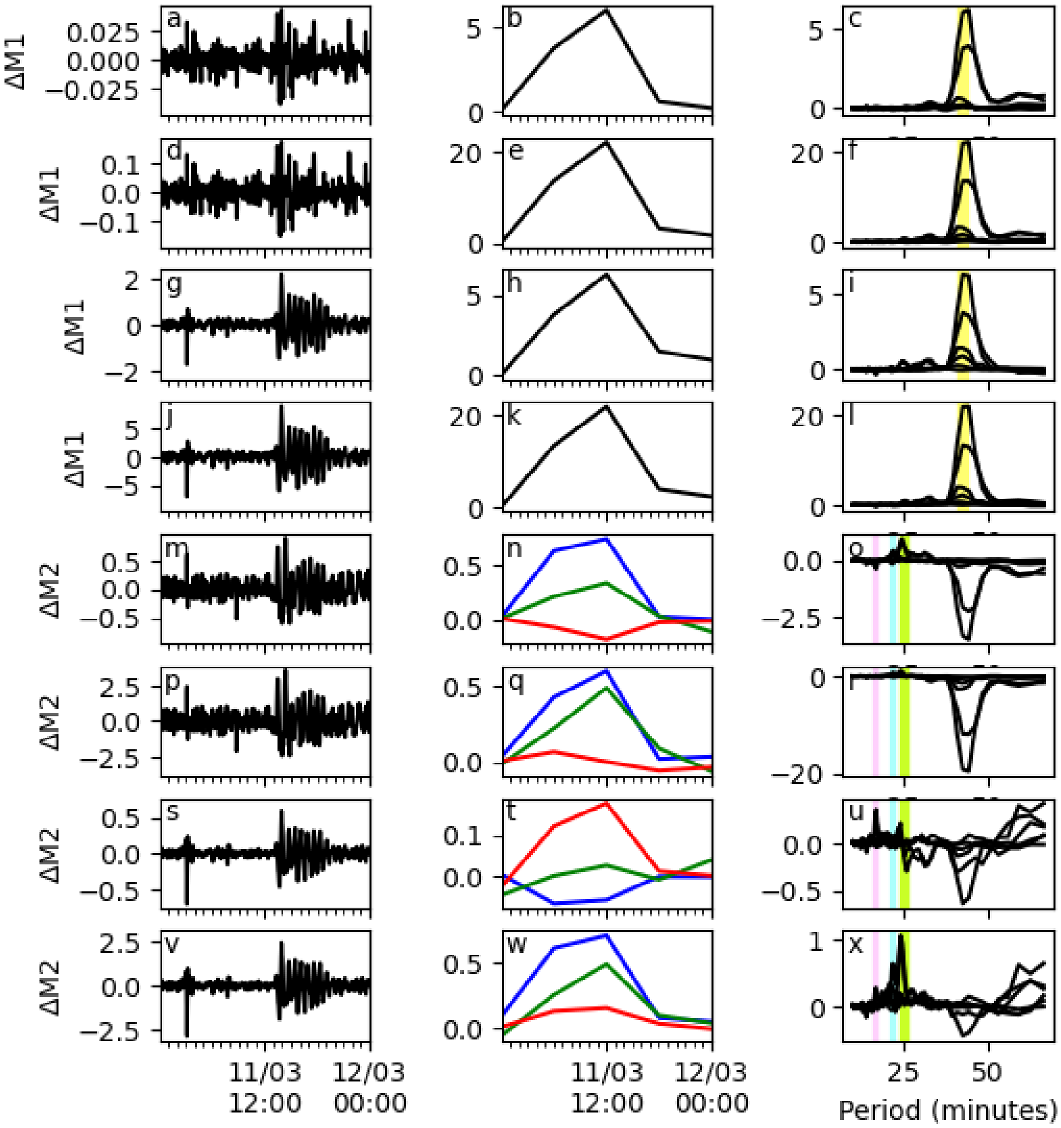

Figure C.3: Same as Figure C.2, but modified modes have been moved away from HFDR by two range cells (rows a/b/c and m/n/o), away from HFDR by five range cells (rows d/e/f and p/q/r), toward the HFDR by two range cells (rows g/h/i and s/t/u), and toward the HFDR by five range cells (rows j/k/l and v/w/x). These are tests e through h in Figure C.1.

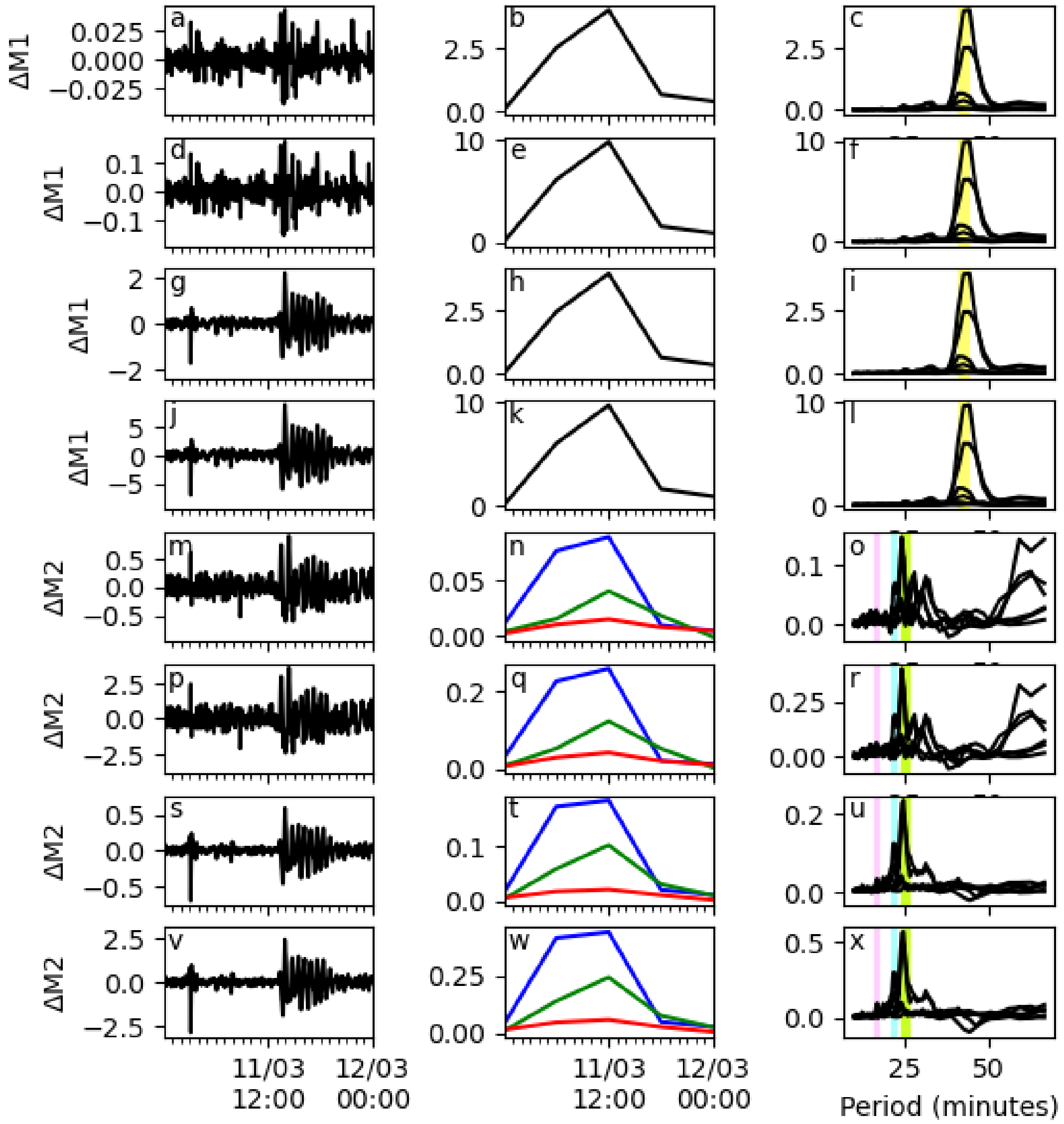

Figure C.4: Same as Figure C.2, but modified modes have been moved eastward by two azimuth cells (rows a/b/c and m/n/o), eastward by five azimuth cells (rows d/e/f and p/q/r), westward by two azimuth cells (rows g/h/i and s/t/u), and westward by five azimuth cells (rows j/k/l and v/w/x). These are tests i through l in Figure C.1.

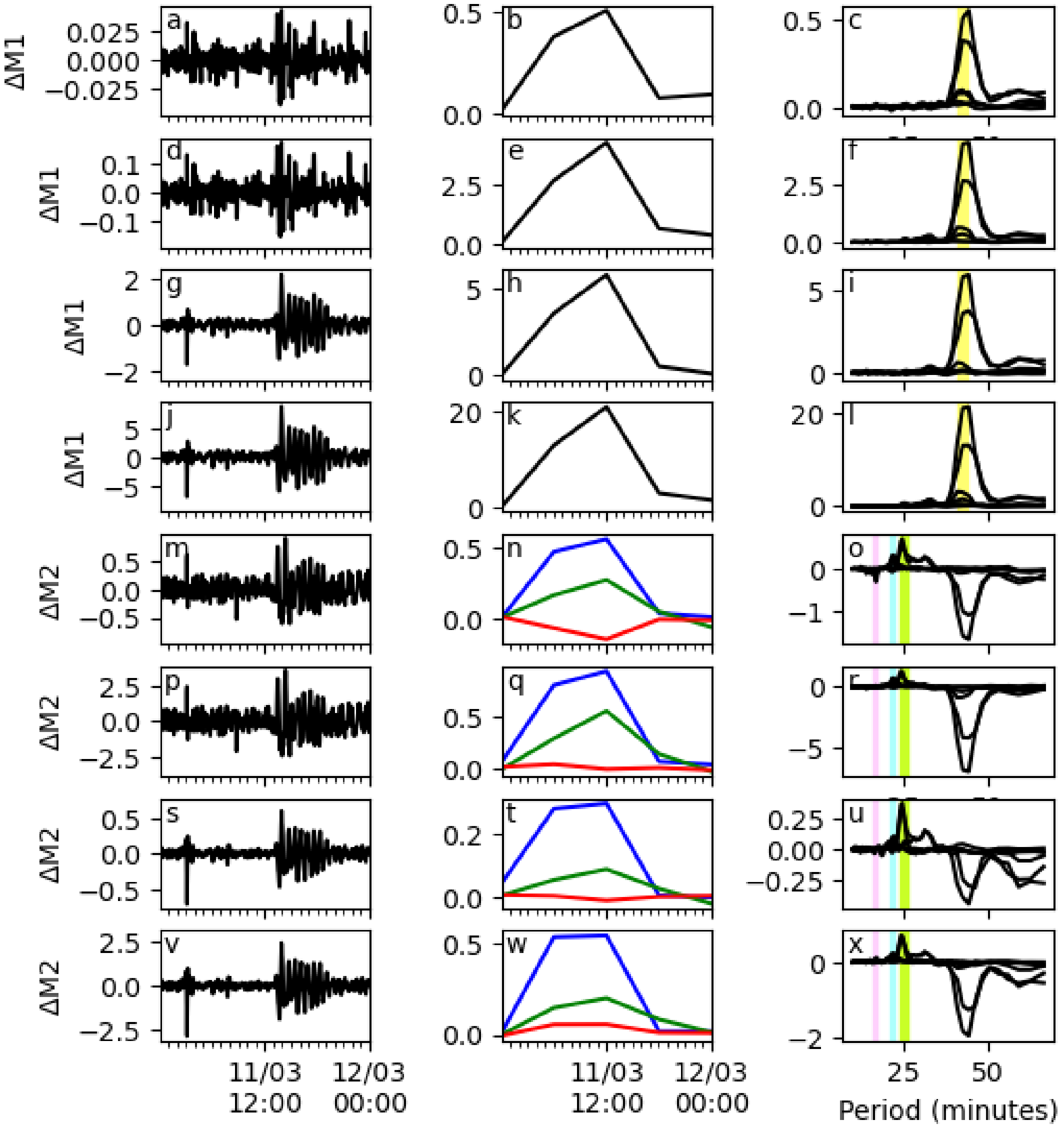

Figure C.5: Same as Figure C.2, but modified modes had their positive and negative poles moved closer together by two range cells (rows a/b/c and m/n/o), moved closer together by five range cells (rows d/e/f and p/q/r), moved further apart by two range cells (rows g/h/i and s/t/u), and moved further apart by five range cells. These correspond to tests m through p in Figure C.1.

Appendix D

Other Hawaii results

Event 10 started at ∼1400 UTC on day 270 of 2009 and ended around 1200 UTC on day 280 of 2009 [Figure D.1]. M1 amplitudes increased from 1400 UTC to 1800 UTC and stayed strong until ∼0600 UTC on day 280; the peak in the spectrum at 41 min to 45 min indicates strong activity from 1400 UTC on day 270 to 0900 UTC the next day. The M2 amplitude increase starts later at ∼2100 UTC and lasts past the end of the event; peaks at periods of interest indicate strong activity from 1400 UTC on day 279 to 2100 UTC on day 280. The line spectrogram shows peaks at the 3 periods of interest for M2, but the peak for M1 is shifted slightly to shorter periods. Radial velocity timeseries in range and azimuth show evidence of a packet of oscillations arriving at ∼1600 UTC on day 279 at the southeast part of the bank that spreads northward and westward, reaching maximum northward extend at ∼0000 UTC on day 280, while maximum westward extent is reached twice, once at 2000 UTC and once at 0200 UTC. The oscillations retreat back southeastward, reaching a minimum extent at 1000 UTC on day 280. The EOF 1 map has a single antinode at the southeast side of the bank; its timeseries has a double-packet structure seen in the azimuth-time velocity plot. The 42 min peak in the EOF spectrum is notably absent here with no peaks at frequencies of interest except 26 min. The maps of EOF 2 and EOF 3 have two and three antinodes, respectively, and less clear packets in their timeseries. Spectral peaks at periods of interest are found for EOF 2 at 16 min and 42 min and for EOF 3 at 18 min, 24 min, and 35-44 min. While event 10 does have the correct EOF spatial structure, packets of oscillations, and spectral peaks at all four periods bands of interest, the period bands are not linked to the proper EOF structures that would indicate tsunami mode excitation, nor are the oscillations sufficiently regular enough.

Event 36 starts at ∼0000 UTC on day 209 of 2010 and ends at ∼1300 UTC [Figure D.2]. The M1 band spectral amplitude does not get large enough for this to be considered an event for that mode, but the M2 band spectral amplitude peaks for 21 min to 22 min and 24 min to 26 min periods at the beginning of the event. The line spectrogram show peaks at the M2 periods of interest, with the larger two periods having larger peaks. The radial velocity timeseries shows stronger currents on the south half of the bank between 0100 UTC and 0700 UTC and on the whole bank from 0900 UTC to 1200 UTC. These strong currents are confined to the eastern edge of the bank. The EOF 1 map has an antinode on the southeast part of the bank and a timeseries that shows the two sections of strong currents. The periods of interest that have peaks in the EOF 1 spectrum are 16 min to 17 min and 22 min. The EOF 2 map has two antinodes on the eastern side of the bank that produce oscillations in the north-south direction. The packet of oscillations is less well-defined in the EOF 2 timeseries, but there is a very strong spectral peak at 25 min. The EOF 3 map has three antinodes, and the associated timeseries has a less defined packet of waves; the spectrum has no peaks at any periods of interest. This event does not include tsunami M1 at all, which is the stronger of the two tsunami resonance modes. It also splits some of the periods of interest into two EOF modes that ideally belong in one.

Event 39 starts at about 0000 UTC on day 256 of 2010 and ends at about 1600 [Figure D.3]. M1 index increases in magnitude after 0600 UTC and drops after 1600 UTC, while the M2 index is large between 0800 UTC and 1200 UTC. Peaks in the M1 and M2 band spectral amplitudes at periods of interest occur at 0900 UTC and 0300 UTC, respectively. The line spectrograms indicates that there are strong peaks at 38 min for M1 and 35 min for M2 in addition to peaks at the expected periods. The radial velocity timeseries shows strong currents on the northern half of the bank between 0500 UTC and 0900 UTC and strong currents on the north and south parts separately from 1000 UTC to 1400 UTC. The currents for the latter are confined to the eastern edge of the bank. The EOF 1 map has one antinode on the northeast part of the bank, and the timeseries has a packet of oscillations with periods of 17 min, 25 min, and 45 min arriving at 0500 UTC and lasting until 1400 UTC. The EOF 2 map has two antinodes on the northeast and southeast parts of the bank; the timeseries has less packet-like structure but many peaks in the spectrum, including at 22 min, 24 min, and 39 min to 42 min. This event, like those described above, does not seem to be an excitation of the tsunami modes found in the 2011 Tōhoku tsunami because it lacks the alignment of EOF modes and spectral periods.

While the five S1-T1-E1 events share many characteristics with the 2011 Tōhoku tsunami, none of them are convincingly a meteotsunami. In general, while all of the elements are there, they are not put together in a way that indicates resonance of the seismic tsunami modes and thus a possible meteotsunami. What about events that share only two of the classifications with the tsunami?

There are three types of partial match events: those that match in spectra and timeseries (S1-T1), those that match in spectra and EOF (S1-E1), and those that match in timeseries and EOF (T1-E1). There were five of the first case, two of the second case, and four of the third case.

Events 14, 18, 33, 41, and 73 were S1-T1 events. They had the mode spectral peak at the correct frequencies and had packets of oscillations in their timeseries. However, they all had spectral peaks at other frequencies as well, and, in many cases, the magnitudes of other peaks were stronger than those at the expected frequencies. The EOFs had different forms, as these were not E1 events, but even then the packets of oscillations in the EOF timeseries did not have the appropriate frequencies.

Events 27 and 70 were S1-E1 events. They had the mode spectral peak at the correct frequencies and had the correct spatial patterns in their EOFs. However, like the S1-T1 events described above, they all had spectral peaks (in many cases very strong ones) at other frequencies. The EOFs did have the correct spatial pattern, but the associated timeseries shows spikes rather than true oscillations, and the spectra of those EOF timeseries did not have peaks at the correct frequencies.

Events 11, 20, 21, 30, and 43 were T1-E1 events. They had packets of oscillations in their timeseries and had the correct spatial patterns in their EOFs. The EOF spatial maps had the correct pattern type, and the associated timeseries were usually packets, though some represented spikes. The EOF timeseries spectra did not have strong peaks at the expected frequencies or indeed at any one frequency at all, but rather they had fairly equal peaks at several frequencies.

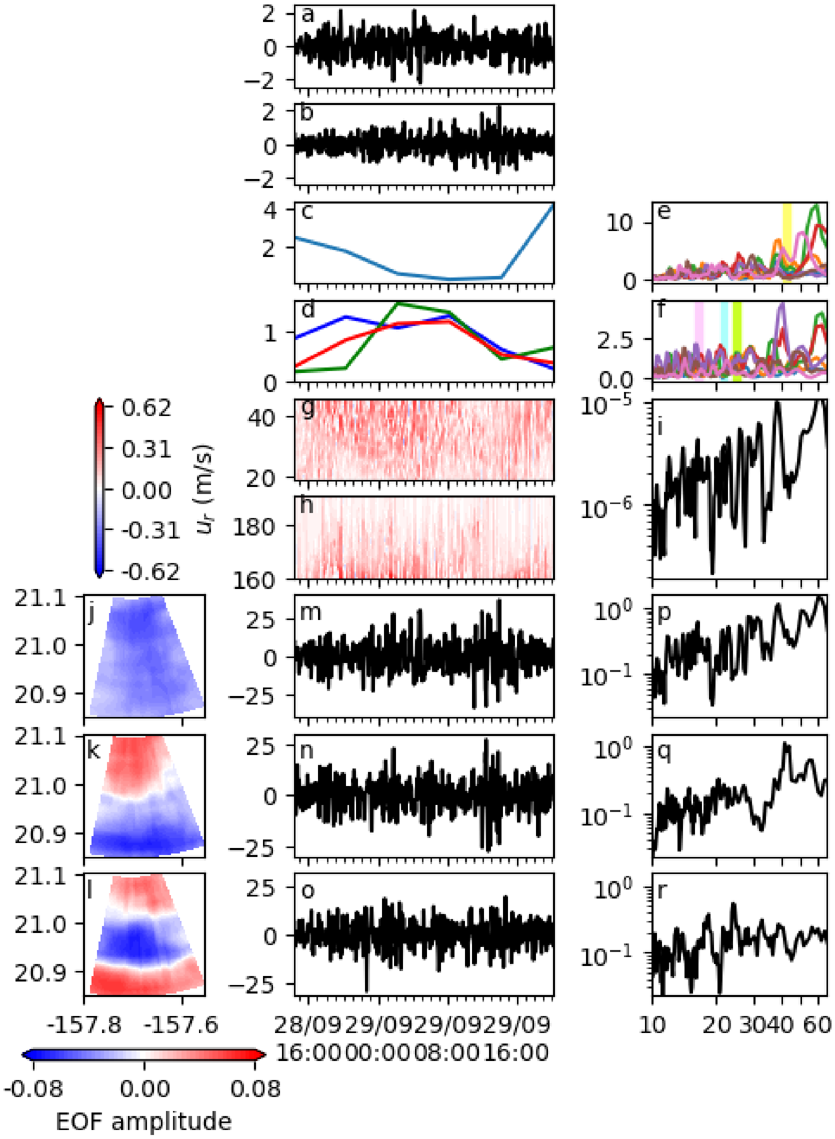

Figure D.1: Event 10: (a and b) the M1 and M2 indices; (c and d) band spectral amplitudes for M1 and M2;, (e and f) line spectrograms for M1 and M2; (g and h) radial velocity timeseries in range and azimuth; (i) spectrum of radial velocity averaged over Penguin Bank; (j, k, and l) EOF 1, EOF 2, and EOF 3 maps; (m, n, and o) EOF 1, EOF 2, and EOF 3 timeseries; and (p, q, and r) EOF 1, EOF 2, and EOF 3 spectra.

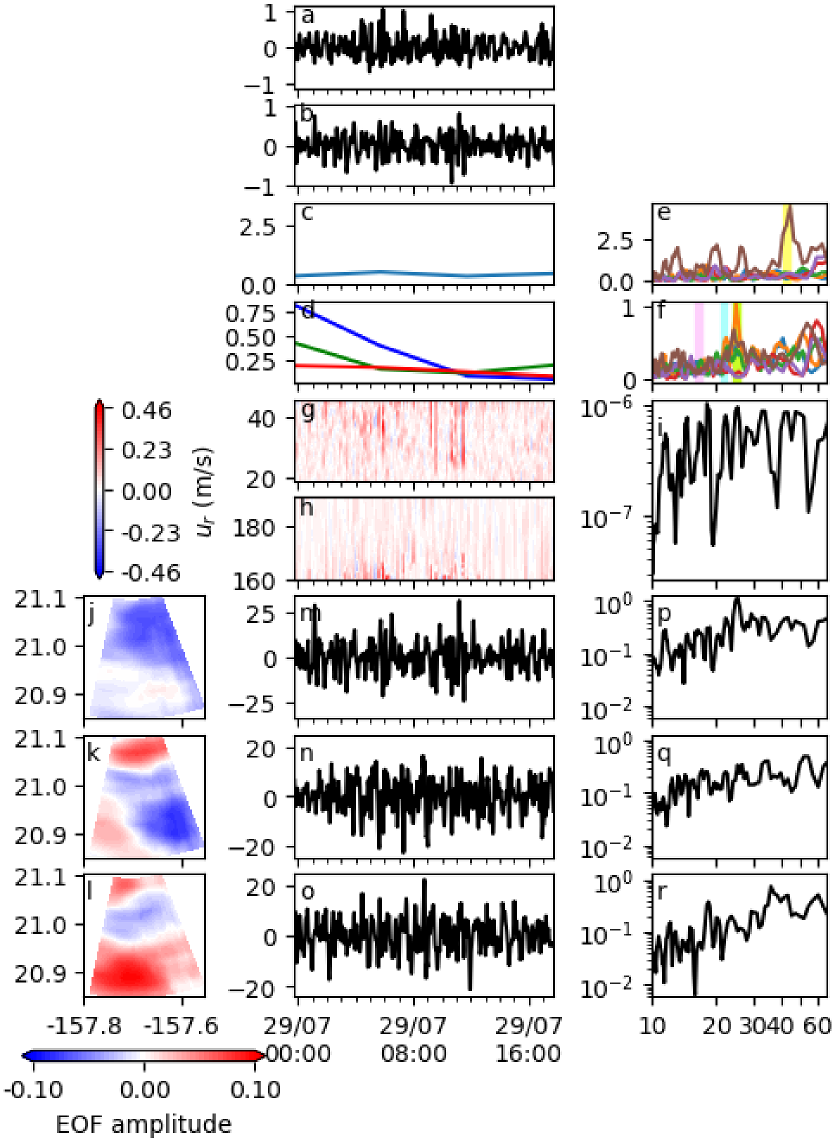

Figure D.2: Event 36: (a and b) the M1 and M2 indices; (c and d) band spectral amplitudes for M1 and M2;, (e and f) line spectrograms for M1 and M2; (g and h) radial velocity timeseries in range and azimuth; (i) spectrum of radial velocity averaged over Penguin Bank; (j, k, and l) EOF 1, EOF 2, and EOF 3 maps; (m, n, and o) EOF 1, EOF 2, and EOF 3 timeseries; and (p, q, and r) EOF 1, EOF 2, and EOF 3 spectra.

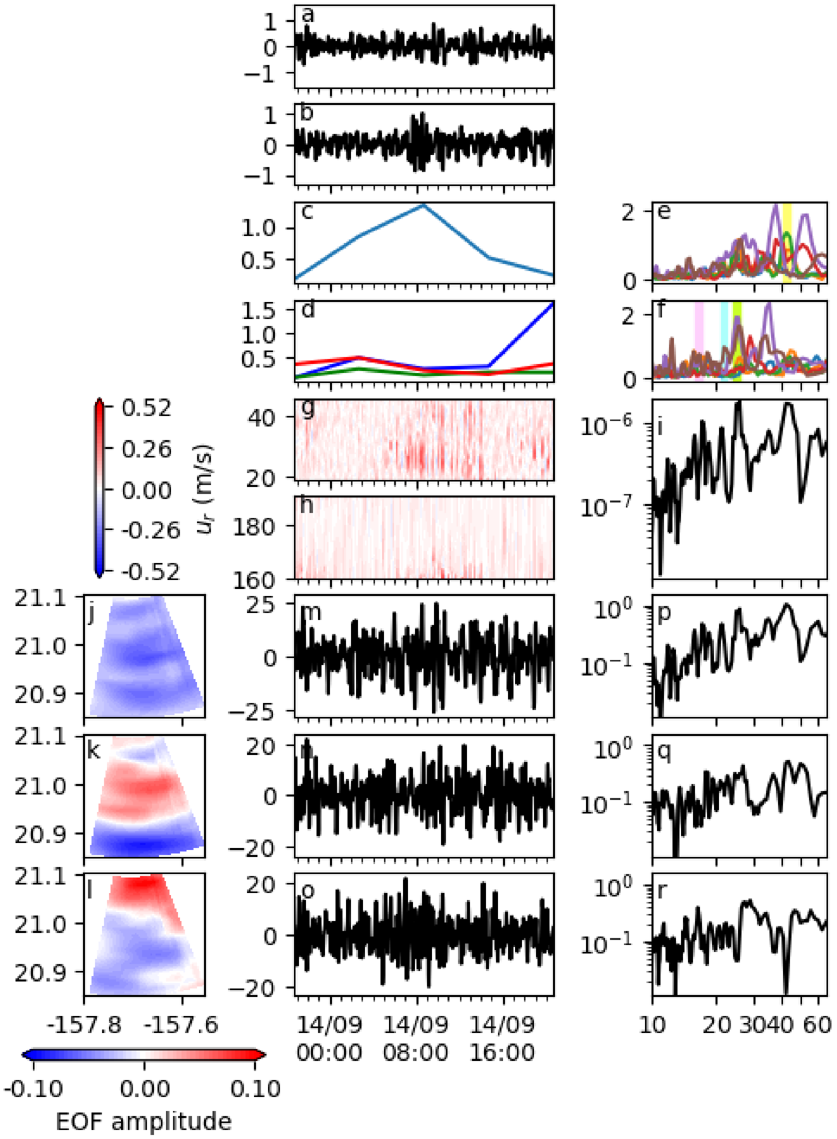

Figure D.3: Event 39: (a and b) the M1 and M2 indices; (c and d) band spectral amplitudes for M1 and M2;, (e and f) line spectrograms for M1 and M2; (g and h) radial velocity timeseries in range and azimuth; (i) spectrum of radial velocity averaged over Penguin Bank; (j, k, and l) EOF 1, EOF 2, and EOF 3 maps; (m, n, and o) EOF 1, EOF 2, and EOF 3 timeseries; and (p, q, and r) EOF 1, EOF 2, and EOF 3 spectra.

Table D.1: Classification of possible resonance mode excitation events with date, modes detected by (M), the spectral type (S), the velocity type (V), and the EOF type (E).

Event	Date	M	S	V	E	Event	Date	M	S	V	E
0	2009-07-13	B	S4	T2	E6	38	2010-09-11	2	S2	T1	E3
1	2009-07-15	1	S3	T2	E5	39	2010-09-13	1	S1	T1	E1
2	2009-07-23	1	S3	T2	E6	40	2010-09-13	2	S1	T1	E1
3	2009-07-25	2	S3	T1	E6	41	2010-09-15	1	S1	T1	E3
4	2009-07-27	2	S3	T1	E5	42	2010-10-04	2	S2	T3	E1
5	2009-07-30	2	S1	T1	E6	43	2010-10-26	B	S2	T1	E1
6	2009-08-02	B	S4	T2	E5	44	2010-11-22	1	S2	T3	E3
7	2009-08-03	2	S1	T1	E6	45	2010-11-23	B	S2	T2	E3
8	2009-08-11	B	S2	T1	E2	46	2010-12-11	B	S2	T2	E1
9	2009-08-19	2	S3	T1	E2	47	2010-12-12	B	S3	T1	E4
10	2009-09-27	B	S1	T1	E1	48	2011-01-12	1	S2	T2	E6
11	2009-09-28	B	S2	T1	E1	49	2011-01-13	B	S2	T2	E6
12	2009-10-02	1	S2	T1	E3	50	2011-01-14	B	S4	T2	E6
13	2009-10-03	B	S3	T1	E2	51	2011-02-09	B	S4	T2	E6
14	2009-10-13	B	S1	T1	E3	52	2011-03-11	B	S1	T1	E1
15	2009-10-17	1	S3	T1	E5	53	2011-03-22	2	S2	T1	E3
16	2009-10-18	B	S2	T1	E2	54	2011-06-19	B	S4	T1	E6
17	2009-10-19	1	S2	T1	E2	55	2011-06-20	B	S4	T2	E6
18	2009-10-20	1	S1	T1	E3	56	2011-06-22	1	S4	T2	E6
19	2009-10-29	3	S4	T2	E6	57	2011-06-24	B	S3	T2	E6
20	2009-12-01	1	S2	T1	E1	58	2011-06-25	B	S3	T1	E6
21	2009-12-02	B	S2	T1	E1	59	2011-07-06	1	S3	T1	E6
22	2010-01-02	B	S4	T2	E2	60	2011-07-07	1	S3	T2	E5
23	2010-01-07	B	S2	T2	E2	61	2011-07-12	B	S4	T2	E6
24	2010-01-12	2	S2	T3	E1	62	2011-07-18	1	S4	T2	E6
25	2010-01-30	B	S4	T2	E6	63	2011-07-28	B	S3	T2	E5
26	2010-02-16	2	S1	T2	E6	64	2011-08-04	B	S4	T2	E6
27	2010-02-28	B	S1	T2	E1	65	2011-08-05	1	S2	T2	E5
28	2010-04-01	B	S2	T1	E3	66	2011-08-09	B	S2	T2	E6
29	2010-05-11	2	S2	T3	E1	67	2011-08-15	B	S2	T2	E5
30	2010-05-25	2	S2	T1	E1	68	2011-08-21	2	S4	T2	E6
31	2010-06-01	2	S2	T1	E4	69	2011-09-01	B	S2	T2	E6
32	2010-06-02	2	S2	T2	E4	70	2011-10-12	B	S1	T2	E1
33	2010-06-03	1	S1	T1	E4	71	2011-11-26	1	S3	T2	E6
34	2010-06-04	B	S1	T1	E1	72	2011-11-27	1	S3	T2	E6
35	2010-07-24	2	S3	T1	E4	73	2011-12-04	2	S1	T1	E2
36	2010-07-28	2	S1	T1	E1	74	2011-12-05	B	S2	T1	E4
37	2010-07-28	1	S2	T1	E4	75	2011-12-09	B	S4	T1	E2

Appendix E

Least-squares method for velocity shear

The observed wave frequency ω_{obs} has been taken from the wave reanalysis.

The velocities derived by least-squares methods from the primary swell peaks [all rows but the bottom of Figures E.1, E.2, E.3] vary greatly from 0 to 1000 m/s. A majority of tiles for all days and bands have magnitudes <20 m/s, but that is still unrealistically large. Additionally, many of the tiles with very large magnitudes are adjacent to tiles with small magnitudes, meaning current strength appears to jump rapidly and at random. Shifting focus to current directions shows that, while currents are primarily northwest or southeast in orientation, the current can rapidly reverse direction such as on day 279 in all bands or may appear to be pointing in a different direction for every tile, such as in the L-band image on day 282. Currents derived from the secondary swell peaks are just as bad if not worse.

Condition numbers for using only 1 k are frequently as large as O 10^{35}.

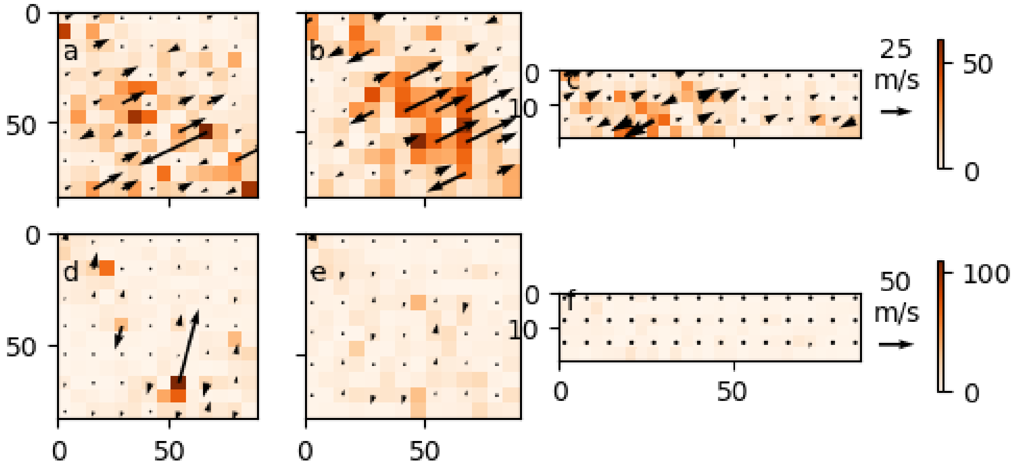

Figure E.1: Currents derived using least-squares method with only (top) the primary swell peaks and (bottom) the secondary swell peaks for (left) L-band, (middle) C-band, and (right) X-band images on day 279.

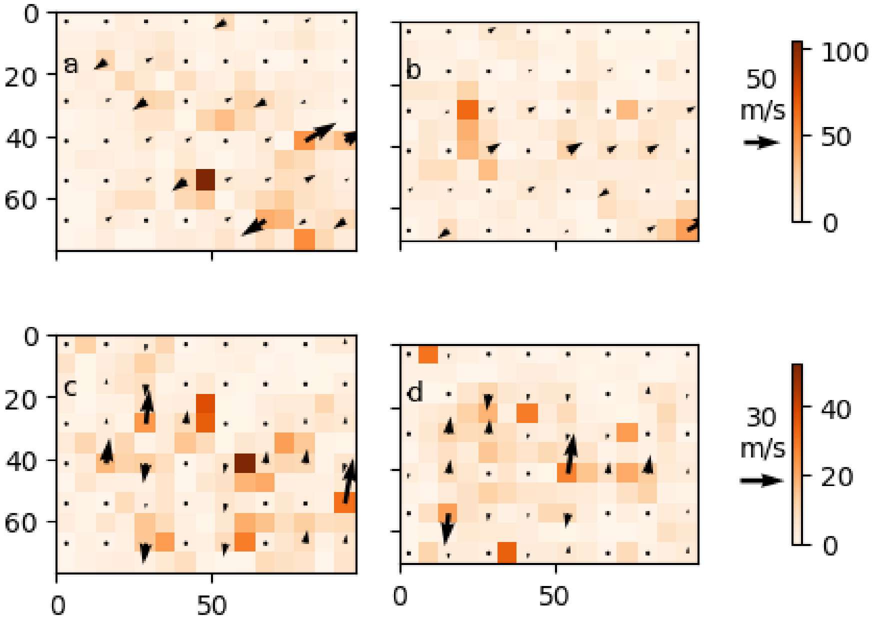

Figure E.2: Currents derived using least-squares method with only (top) the primary swell peaks and (bottom) the secondary swell peaks for (left) L-band and (right) C-band images on day 280.

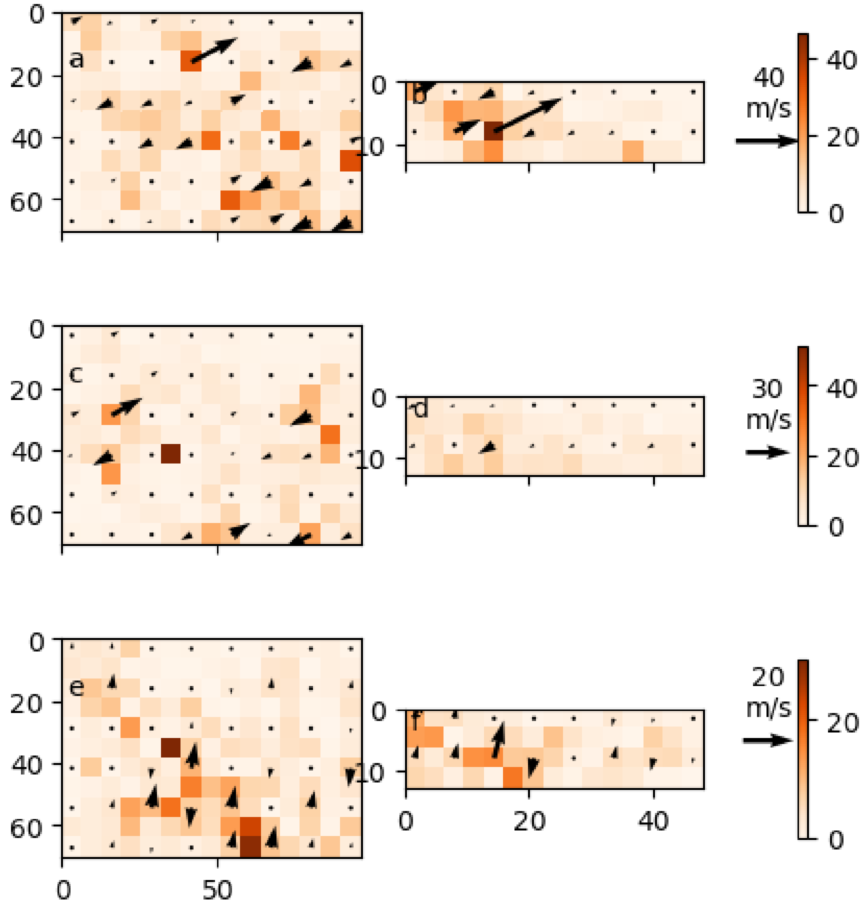

Figure E.3: The currents derived using least-squares method with only (top) the short-wave primary swell peak, (middle row) the long-wave primary swell peaks, and (bottom) the secondary swell peaks for (left) L-band and (right) X-band images on day 282.

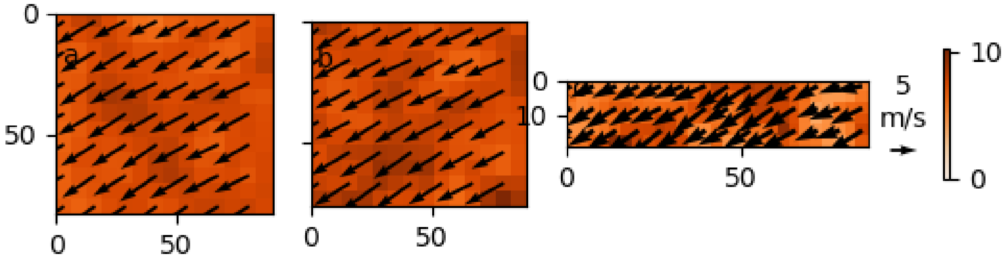

Figure E.4: Magnitudes (color) and vectors (arrows) for velocities derived using primary swell and secondary swell peaks by the least-squares method but with the ω_{obs} from the reanalysis for (left) L-band, (middle) C-band, and (right) X-band images for day 279. The estimate of ω_{obs} is not very fitting, which adds a large-magnitude background current to the velocity changes found in the main text that makes the details impossible to discern. Compare with Figure 9.25.

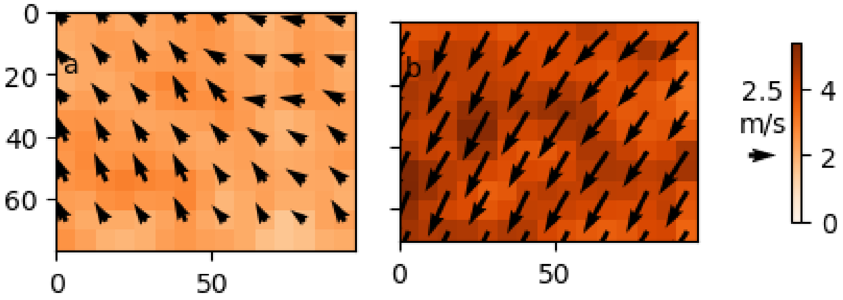

Figure E.5: The currents derived using least-squares method with only (top) primary swell peaks and (bottom) secondary swell peaks but using the ω_{obs} from the reanalysis for (left) L-band and (right) C-band images on day 280. Compare with Figure 9.26, which uses the mean k of each peak to derive an ω_{obs}.

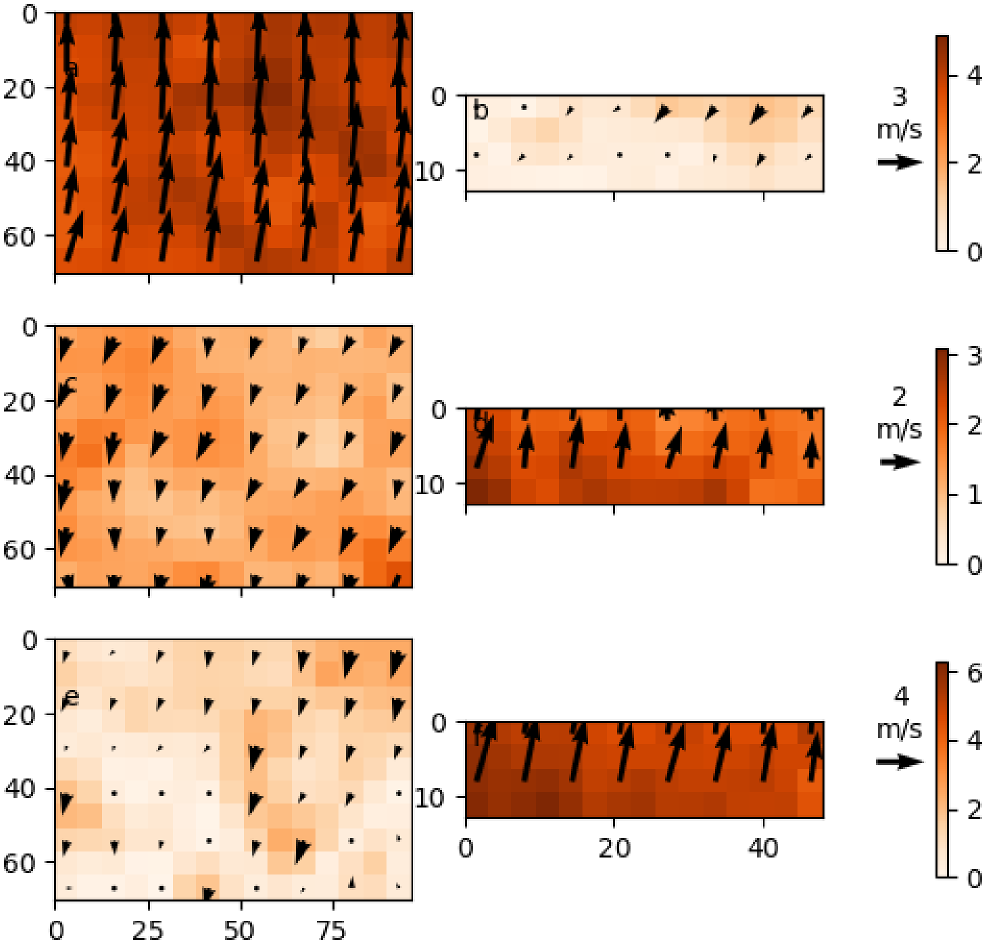

Figure E.6: The currents derived using least-squares method with only (top) the short-wave primary swell peak, (middle row) the long-wave primary swell peaks, and (bottom) the secondary swell peaks but using the ω_{obs} from the reanalysis for (left) L-band and (right) X-band images on day 282. Compare with Figure 9.27, which uses the mean k of each peak to derive an ω_{obs}.

References

References

Allan, J. C., P. D. Komar, P. Ruggiero, and R. Witter (2012), The March 2011 Tohoku tsunami and its impacts along the U.S. West Coast, *J. Coastal Res.*, *28*(5), 1142–1153, doi:10.2112/JCOASTRES-D-11-00115.1.

Bai, Y., Y. Yamazaki, and K. F. Cheung (2015), Interconnection of multi-scale standing waves across the Pacific Basin from the 2011 Tohoku Tsunami, *Ocean model.*, *92*, 183–197, doi:10.1016/j.ocemod.2015.06.007.

Barnett, T., F. Kelley, and B. Holt (1989), Estimation of the two-dimensional ocean current shear field with a synthetic aperture radar, *J. Geophys. Res.*, *94*(C11), 16,087–16,095.

Barrick, D. E. (1979), A coastal radar system for tsunami warning, *Remote Sens. Environ.*, *8*, 353–358.

Barth, J. A. (1994), Short-wavelength instabilities on coastal jets and fronts, *J. Geophys. Res.*, *99*(C8), 16,095–16,115, doi:10.1029/94JC01270.

Beal, R. C., V. N. Kudryavtsev, D. R. Thompson, S. A. Grodsky, D. G. Tilley, V. A. Dulov, and H. C. Graber (1997), The influence of the marine atmospheric boundary layer on ERS 1 synthetic aperture radar imagery of the Gulf Stream, *J. Geophys. Res.*, *102*(C3), 5799–5814.

Bechle, A. J., C. H. Wu, D. A. R. Kristovich, E. J. Anderson, D. J. Schwab, and A. B. Rabinovich (2016), Meteotsunamis in the Laurentian Great Lakes, *Sci. Rep.*, *6*, 37832, doi:10.1038/srep37832.

Beckley, B. D., N. Zelensky, S. Holmes, F. Lemoine, R. Ray, G. Mitchum, S. Desai, and S. Brown (2017), Integrated Multi-Mission Ocean Altimeter Data for Climate Research complete time series Version 4.2., PO.DAAC, dOI: https://doi.org/10.5067/ALTTS-TJ142. Dataset accessed 20181010.

Benjamin, L. R., P. Flament, K. F. Cheung, and D. S. Luther (2016), The 2011 Tohoku tsunami south of Oahu: High-frequency Doppler radio observations and model simulations of currents, *J. Geophys. Res.*, *121*, 1133–1144, doi:10.1002/2015JC011207.

Bentamy, A., Q. Yves, and P. Flament (2002), Scatterometer wind fields: A new release over the decade 1991-2001, *Can. J. Remote Sens.*, *28*, 431–449, doi:10.5589/m02-041.

Bertin, X., A. de Bakker, A. van Dongeren, G. Coco, G. André, F. Ardhuin, P. Bonneton, F. Bouchette, B. Castelle, W. C. Crawford, M. Davidson, M. Deen, G. Dodet, T. Guérin, K. Inch, F. Leckler, R. McCall, H. Muller, M. Olabarrieta, D. Roelvink, G. Ruessink, D. Sous, Éléonore Stutzmann, and M. Tissier (2018), Infragravity waves: From driving mechanisms to impacts, *Earth-Sci. Rev.*, *177*, 774–799, doi:10.1016/j.earscirev.2018.01.002.

Boccaletti, G., R. Ferrari, and B. Fox-Kemper (2007), Mixed layer instabilities and restratification, *J. Phys. Oceanogr.*, *37*(9), 2228–2250, doi:10.1175/JPO3101.1.

Borrero, J. C., R. Bell, C. Csato, W. DeLange, D. Goring, S. D. Greer, V. Pickett, and W. Power (2013), Observations, effects, and real time assessment of the March 11, 2011 Tohoku-oki tsunami in New Zealand, *Pure Appl. Geophys.*, *170*, 1229–1248, doi:10.1007/s00024-012-0492-6.

Brandt, P., A. Rubino, W. Alpers, and J. O. Backhaus (1997), Internal waves in the Strait of Messina studied by a numerical model and synthetic aperture radar images from the ERS 1/2 satellites, *J. Phys. Oceanogr.*, *27*, 648–663.

Bricker, J. D., S. Munger, C. Pequignet, J. R. Wells, G. Pawlak, and K. F. Cheung (2007), ADCP observations of edge waves off Oahu in the wake of the November 2006 Kuril Islands tsunami, *Geophys. Res. Lett.*, *34*, L23617, doi:10.1029/2007GL032015.

Buckingham, C. E., Z. Khaleel, A. Lazar, A. P. Martin, J. T. Allen, A. C. Naveira Garabato, A. F. Thompson, and C. Vic (2017), Testing Munk's hypothesis for submesoscale eddy generation using observations in the North Atlantic, *J. Geophys. Res.*, *112*, 6725–6745, doi: 10.1002/2017JC012910.

Callies, J., and R. Ferrari (2018), Baroclinic instability in the presence of convection, *J. Phys. Oceanogr.*, *48*, 45–60, doi:10.1175/JPO-D-17-0028.1.

Candela, J., S. Mazzola, C. Sammari, R. Limeburner, C. J. Lozano, B. Patti, and A. Bonanno (1999), The "mad sea" phenomenon in the Strait of Sicily, *J. Phys. Oceanogr.*, *29*, 2210–2231.

Capet, X., J. C. McWilliams, M. J. Molemaker, and A. F. Shchepetkin (2008a), Mesoscale to submesoscale transition in the California Current system: Part III: Energy balance and flux, *J. Phys. Oceanogr.*, *38*, 2256–2269, doi:10.1175/2008JPO3810.1.

Capet, X., J. C. McWilliams, M. J. Molemaker, and A. F. Shchepetkin (2008b), Mesoscale to submesoscale transition in the California Current system: Part I: Flow structure, eddy flux, and observational tests, *J. Phys. Oceanogr.*, *38*, 29–43, doi:10.1175/2007JPO3671.1.

Castelão, G. P., and W. E. Johns (2011), Sea surface structure of North Brazil Current rings derived from shipboard and moored acoustic doppler current profiler observations, *J. Geophys. Res.*, *116*, C01010, doi:10.1029/2010JC006575.

Chavanne, C., P. Flament, and K.-W. Gurgel (2010), Interactions between a submesoscale anticyclonic vortex and a front, *J. Phys. Oceanogr.*, *40*, 1802–1818, doi:10.1175/2010JPO4055.1.

Cheung, K. F., Y. Bai, and Y. Yamazaki (2013), Surges around the Hawaiian Islands from the 2011 Tohoku tsunami, *J. Geophys. Res.*, *118*, 5703–5719, doi:10.1002/jgrc.20413.

Contreras, R. F. (2002), Long-term observations of tropical instability waves, *J. Phys. Oceanogr.*, *32*, 2715–2722.

Copernicus; European Space Agency (2011), Sentinel 1A: C-band Synthetic Aperture Radar (SAR) data, Copernicus Open Access Hub, https://scihub.copernicus.eu. Dataset accessed 20200401.

D'Asaro, R. A. (1988), Generation of submesoscale vortices: a new mechanism, *J. Geophys. Res.*, *93*(C6), 6685–6693.

de Bakker, A. T. M., . F. S. Tissier, and B. G. Ruessink (2016), Beach steepness effects on nonlinear infragravity-wave interactions: a numerical study, *J. Geophys. Res.*, *121*, 554–570, doi: 10.1002/2015JC011268.

Duhat, T. H. A., and D. N. Straub (2006), Wind stress dependence on ocean surface velocity: implications for mechanical energy input to ocean circulation, *J. Phys. Oceanogr.*, *36*, 202–211.

Dunbar, P., H. McCullough, G. Mungov, J. Varner, and K. Stroker (2011), 2011 Tohoku earthquake and tsunami data available from the National Oceanic and Atmospheric Administration/National Geophysical Data Center, *Geomat. Nat. Haz. Risk*, *2*(4), 305–323, doi:10.1080/19475705.632443.

Dutrieux, P., C. E. Menkes, J. Vialard, P. Flament, and B. Blanke (2008), Lagrangian study of tropical instability vortices in the Atlantic, *J. Phys. Oceanogr.*, *38*, 400–417, doi:10.1175/2007JPO3763.1.

Dzvonkovskaya, A., D. Figueroa, K.-W. Gurgel, H. Rohling, and T. Schlick (2011), HF radar obsevation of a tsunami near Chile after the recent great earthquake in Japan, in *International Radar Symposium, IRS 2011: Leipzig, Germany, September 7 - 9, 2011 - Proceedings*, edited by H. Rohling, pp. 125–130, DCM Druck Center Meckenheim GmbH, Meckenheim, Germany.

E.U. Copernicus Marine Service Information (2021a), Global Ocean Waves Reanalysis WAVERYS set, Copernicus Monitoring Environment Marine Service (CMEMS), https://doi.org/10.48670/moi-00022. Dataset accessed 20200601.

E.U. Copernicus Marine Service Information (2021b), Global Ocean Daily Gridded Sea Surface Winds from Scatterometer set, Copernicus Monitoring Environment Marine Service (CMEMS), https://doi.org/10.48670/moi-00182. Dataset accessed 20200601.

E.U. Copernicus Marine Service Information (2021c), Global Total Surface and 15m Current (COPERNICUS-GLOBCURRENT) from Altimetric Geostrophic Current and Modeled Ekman Current Reprocessing set, Copernicus Monitoring Environment Marine Service (CMEMS), https://doi.org/10.48670/moi-00050. Dataset accessed 20200601.

E.U. Copernicus Marine Service Information (2021d), Global Surface Currents (GLORYS12V1) Global Ocean Physics Reanalysis set, Copernicus Monitoring Environment Marine Service (CMEMS), https://doi.org/10.48670/moi-00021. Dataset accessed 20200601.

Evans, D. L., C. Elachi, E. R. Stofan, B. Holt, J. B. Way, M. Kobrick, M. Vogt, S. Wall, J. van Zyl, M. Schier, H. Öttl, and P. Pampaloni (1993), The shuttle imaging radar-C and X-SAR mission, *Eos*, *74*(13), 145–158.

Fiedler, J. W., M. A. McManus, M. S. Tomlinson, E. H. D. Carlo, G. R. Pawlak, G. F. Steward, O. D. Nigro, R. E. Timmerman, P. S. Drupp, and C. E. Ostrander (2014), Real-time observations of the February 2010 Chile and March 2011 Japan tsunamis recorded in Honolulu by the Pacific Islands Ocean Observing System, *Oceanography*, *27*(2), 186–200, doi: 10.5670/oceanog.2014.36.

Firing, J., P. Flament, E. Firing, and R. Knox (1994), Ship-board acoustic Doppler current profiler data from the Moana Wave cruises MW-9010 and MW-9012, *SOEST-93-05*.

Flament, P. (1995), SIR-C/X-SAR observations of convergent fronts in the Central Equatorial Pacific, in *International Geoscience and Remote Sensing Symposium 1995*, edited by T. L. Stein, pp. 1323–1324, I.E.E.E.

Flament, P., R. Lumpkin, J. Tournadre, and L. Armi (2001), Vortex pairing in an unstable anticyclonic shear flow: discrete subharmonics of one pendulum day, *J. of Fluid Mech.*, *440*, 401–409.

Flament, P. J., S. C. Kennan, R. A. Knox, P. P. Niiler, and R. L. Bernstein (1996), The three-dimensional structure of an upper ocean vortex in the tropical Pacific Ocean, *Nature*, *383*(6601), 610–613.

Goring, D. G. (2009), Meteotsunami resulting from the propagation of synoptic-scale weather systems, *Phys. Chem. Earth*, *34*, 1009–1015, doi:10.1016/j.pce.2009.10.004.

Grilli, S. T., S. Grosdidier, and C.-A. Guérin (2015), Modeling of tsunami detection by high frequency radar based on simulated tsunami case studies in the Mediterranean Sea, in *ISOPE 2015 International Conference*, Kona, Hawaii.

Gurgel, K.-W., H.-H. Essen, and S. P. Kingsley (1999a), High-frequency radars: Physical limitations and recent developments, *Coast. Eng.*, *37*, 201–218.

Gurgel, K.-W., G. Antonischki, H.-H. Essen, and T. Schlick (1999b), Wellen radar (WERA): A new groundwave HF radar for ocean remote sensing, *Coast. Eng.*, *37*, 219–234.

Gurgel, K.-W., A. Dzvonkovskaya, T. Pohlmann, T. Schlick, and E. Gill (2011), Simulation and detection of tsunami signatures in ocean surface currents measured by HF radar, *Ocean Dynam.*, *61*(10), 1495–1507, doi:10.1007/s10236-011-0420-9.

Haine, T. W. N., and J. Marshall (1998), Gravitational, symmetric, and baroclinic instability of the ocean mixed layer, *J. Phys. Oceanogr.*, *28*, 634–658.

Halpern, D., R. A. Knox, and D. S. Luther (1988), Observations of 10-day period meridional current oscillations in the upper ocean along the Pacific equator, *J. Phys. Oceanogr.*, *18*, 1514–1534.

Hamlington, B. D., R. R. Leben, O. A. Godin, E. Gica, V. V. Titov, B. J. Haines, and S. D. Desai (2012), Could satellite altimetry have improved early detection and warning of the 2011 Tohoku tsunami?, *Geophys. Res. Lett.*, *39*, L15605, doi:10.1029/2012GL052386.

Hansen, D. V., and C. A. Paul (1984), Genesis and effects of long waves in the Equatorial Pacific, *J. Geophys. Res.*, *89*(C6), 10,431–10,440.

Hersbach, H. (2010), Comparison of C-band scatterometer CMOD5.N equivalent neutral winds with ECMWF, *J. Atmos. Ocean. Technol.*, *27*(4), 721–736.

Hersbach, H., B. Bell, P. Berrisford, G. Biavati, A. Horányi, J. Muños Sabater, J. Nicolas, V. Peuby, R. Radu, I. Rozum, D. Schepers, A. Simmons, C. Soci, D. Dee, and J.-N. Thépaut (2018), ERA5 hourly data on pressure levels from 1979 to present, Copernicus Climate Change

Service (C3S) Climate Data Store (CDS), https://doi.org/10.24381/cds.bd0915c6. Dataset accessed 20200601.

Hinata, H., S. Fujii, K. Furukawa, T. Kataoka, M. Miyata, T. Kobayashi, M. Mizutani, T. Kokai, and N. Kanatsu (2011), Propagating tsunami wave and subsequent resonant response signals detected by HF radar in the Kii Channel, Japan, *Estuar. Coast. Shelf S.*, *95*, 268–273, doi:10.1016/j.ecss.2011.08.009.

Holmes, R. M., L. N. Thomas, L. Thompson, and D. Darr (2014), Potential vorticity dynamics of tropical instability vortices, *J. Phys. Oceanogr.*, *44*, 995–1011, doi:10.1175/JPO-D-13-0157.1.

IFREMER/CERSAT (2007), GHRSST Level 4 ODYSSEA Global Foundation Sea Surface Temperature Analysis. Ver. 1.0., PO.DAAC, https://doi.org/10.5067/GHGOY-4FE01. Dataset accessed 20200131.

Johannessen, J. A., R. A. Shuchman, O. M. Johannessen, K. L. Davidson, and D. R. Lyzenga (1991), Synthetic aperture radar imaging of upper ocean circulation features and wind fronts, *J. Geophys. Res.*, *96*(C6), 10,411–10,422.

Johannessen, J. A., P. W. Vachon, and O. M. Johannessen (1997), ERS-1 SAR imaging of marine boundary layer process, *Earth Obs. and Remot. Sens.*, *14*, 449–461.

Johannessen, J. A., V. Kudryavtsev, D. Akimov, T. Eldevik, N. Winther, and B. Chapron (2005), On radar imaging of current features: 2. mesoscale eddy and current front detection, *J. Geophys. Res.*, *110*, C07017, doi:10.1029/2004JC002802.

Kaistrenko, V., N. Razjigaeva, A. Kharlamov, and A. Shishkin (2013), Manifestation of the 2011 Great Tohoku Tsunami on the coast of the Kuril Islands: A tsunami with ice, *Pure Appl. Geophys.*, *170*, 1103–1114, doi:10.1007/s00024-012-0546-9.

Kennan, S. C. (1997), Observations of a tropical instability vortex, Ph.D. thesis, SOEST, University of Hawaiʻi at Mānoa, 190 p.

Kennan, S. C., and P. J. Flament (2000), Observations of a tropical instability vortex, *J. Phys. Oceanogr.*, *30*, 2277–2301.

Killworth, P. D. (1980), Barotropic and baroclinic instability in rotating stratified fluids, *Dynam. Atmos. Oceans*, *4*, 143–184.

Kilpatrick, T., N. Schneider, and B. Qiu (2016), Atmospheric response to a midlatitude sst front: Alongfront winds, *J. Atmos. Sci.*, *73*, 3489–3509, doi:10.1175/JAS-D-15-0312.1.

Kloosterziel, R. C., G. F. Carnevale, and P. Orlandi (2000), Inertial instability in rotating and stratified fluids: barotropic vortices, *J. Fluid Mech.*, *583*, 379–412, doi:10.1017/S0022112007006325.

Knox, J. A. (2003), Inertial instability, in *Encyclopedia of the Atmospheric Sciences*, edited by J. R. Holton, J. Pyle, and J. A. Curry, pp. 1000–1013, Elsevier, New York.

Kuang, H.-L., W. Perrie, T. Xie, B. Zhang, and W. Chen (2012), Retrievals of sea surface temperature fronts from SAR imagery, *Geophys. Res. Lett.*, *34*, L10607, doi:10.1029/2012GL051288.

Kudryavtsev, V., D. Akimov, J. Johannessen, and B. Chapron (2005), On radar imaging of current features: 1. Model and comparison with observations, *J. Geophys. Res.*, *110*, C07016, doi:10.1029/2004JC002505.

Kudryavtsev, V., A. Myasoedov, B. Chapron, J. A. Johannessen, and F. Collard (2012), Imaging mesoscale upper ocean dynamics using synthetic aperture radar and optical data, *J. Geophys. Res.*, *117*, C04029, doi:10.1029/2011JC007492.

Legeckis, R. (1977), Long waves in the eastern equatorial Pacific Ocean: a view from a geostationary satellite, *Science*, *197*(4309), 1179–1181.

Linares, Á., A. J. Bechle, and C. H. Wu (2016), Characterization and assessment of the meteotsunami hazard in northern Lake Michigan, *J. Geophys. Res.*, *121*, 7141–7158, doi:10.1002/2016JC011979.

Lipa, B., D. Barrick, S.-I. Saitoh, Y. Ishikawa, T. Awaji, J. Largier, and N. Garfield (2011), Japan tsunami current flows observed by HF radars on two continents, *Remote Sens.*, *3*, 1663–1679, doi:10.3390/rs3081663.

Lipa, B., D. Barrick, S. Diposaptono, J. Isaacson, B. K. Jena, B. Nyden, K. Rajesh, and T. S. Kumar (2012), High frequency (HF) radar detection of the weak 2012 Indonesian tsunamis, *Remote Sens.*, *4*, 2944–2956, doi:10.3390/rs4102944.

Lipa, B., H. Parikh, D. Barrick, H. Roarty, and S. Glenn (2013), High-frequency radar observations of the June 2013 US East Coast meteotsunami, *Nat. Hazards*, *74* (1), 109–122, doi:10.1007/s11069-013-0992-4.

Lipa, B. J., D. E. Barrick, J. Bourg, and B. B. Nyden (2006), HF radar detection of tsunamis, *J. Oceanogr.*, *62*, 705–716.

Liu, A. K., C. Y. Peng, and J. D. Schumacher (1994), Wave-current interaction study in the Gulf of Alaska for detection of eddies by synthetic aperture radar, *J. Geophys. Res.*, *99* (C5), 10,075–10,085.

Lorenz, E. N. (1956), Empirical orthogonal functions and statistical weather prediction, *Scientific report 1*, Department of Meteorology, MIT, Cambridge, Massachusetts.

Luther, D. S., and E. S. Johnson (1990), Eddy energetics in the upper Equatorial Pacific during the Hawaii-to-Tahiti Shuttle Experiment, *J. Phys. Oceanogr.*, *20*, 913–944.

Lynett, P., R. Weiss, W. Renteria, G. D. L. T. Morales, S. Son, M. E. M. Arcos, and B. T. MacInnes (2013), Coastal impacts of the March 11th Tohoku, Japan tsunami in the Galapagos Islands, *Pure Appl. Geophys.*, *170*, 1189–1206, doi:10.1007/s00024-012-0568-3.

Mahadevan, A., A. Tandon, and R. Ferrari (2010), Rapid changes in mixed layer stratification driven by submesoscale instabilities and winds, *J. Geophys. Res.*, *115*, C03017, doi:10.1029/2008JC005203.

Marchesiello, P., X. Capet, C. Menkes, and S. C. Kennan (2011), Submesoscale dynamics in tropical instability waves, *Ocean Model.*, *39*, 31–46, doi:10.1016/j.ocemod.2011.04.011.

McWilliams, J. C. (2016), Submesoscale currents in the ocean, *P. Roy. Soc. A-Math. Phy.*, *472*, 20160117, doi:10.1098/rspa.2016.0117.

Meadows, G. A., R. A. Shuchman, Y. C. Tseng, and E. S. Kasischke (1983), Seasat synthetic aperture radar observations of wave-current and wave-topographic interactions, *J. Geophys. Res.*, *88*(1C7), 4393–4406.

Menkes, C. E., S. C. Kennan, P. J. Flament, Y. Fandonneau, S. Masson, B. Biessy, E. Marchal, E. Eldin, J. Grelet, Y. Montel, A. Morlière, A. Lebourges-Dhaussy, C. Moulin, G. Champalbert, and A. Herbland (2002), A whirling ecosystem in the equatorial Atlantic, *Geophys. Res. Lett.*, *29*(11), 1553.

Mercer, D., J. Sheng, R. J. Greatbatch, and J. Bobanović (2002), Barotropic waves generated by storms moving rapidly over shallow water, *J. Geophys. Res.*, *107*(C10), 3152, doi: 10.1029/2001JC001140.

Mied, R. P., C. Y. Shen, G. J. Lindemann, and T. E. Evans (1999), Symmetric baroclinic instability during frontogenesis with horizontal density gradients and ageostrophic vertical shears, *J. Geophys. Res.*, *104*(C5), 10,903–10,915, doi:10.1029/1998JC900111.

Mimura, N., K. Yasuhara, S. Kawagoe, H. Yokoki, and S. Kazama (2011), Damage from the Great East Japan Earthquake and Tsunami— A quick report, *Mitig. Adapt. Strat. Gl.*, *16*, 803–818, doi:10.1007/s11027-011-9297-7.

Monserrat, S., I. Vilibić, and A. B. Rabinovich (2008), Meteotsunamis: atmospherically induced destructive ocean waves in the tsunami frequency band, *Nat. Hazard. Earth Sys.*, *6*(6), 1035–1051.

Moreira, A., P. Prats-Iraola, M. Younis, G. Krieger, I. Hajnsek, and K. P. Papathanassiou (2013), A tutorial on synthetic aperture radar, *IEEE Geosci. Remote S.*, *1*(1), 6 – 43, doi: 10.1109/MGRS.2013.2248301.

Mori, N., T. Takahashi, T. Yasuda, and H. Yanagisawa (2008), Survey of the 2011 Tohoku earthquake tsunami inundation and run-up, *Geophys. Res. Lett.*, *38*, L00G14, doi:10.1029/2011GL049210.

Munger, S., and K. F. Cheung (2008), Resonance in Hawaii waters from the 2006 Kuril Islands tsunami, *Geophys. Res. Lett.*, *35*, L07605, doi:10.1029/2007GL032843.

NASA Goddard SFC, OEL OBPG (2018a), MODIS-Aqua Ocean Color Data, NASA Goddard Space Flight Center, Ocean Ecology Laboratory, Ocean Biology Processing Group, http://doi.org/10.5067/AQUA/MODIS/L3M/CHL/2018. Dataset accessed 20201010.

NASA Goddard SFC, OEL OBPG (2018b), MODIS-Terra Ocean Color Data, NASA Goddard Space Flight Center, Ocean Ecology Laboratory, Ocean Biology Processing Group, http://doi.org/10.5067/AQUA/TERRA/L3M/CHL/2018. Dataset accessed 20201010.

NASA Goddard SFC, OEL OBPG (2020a), MODIS-Aqua Global Level 3 Mapped SST, Physical Oceanography Distributed Active Archive Center, https://doi.org/10.5067/MODSA-1D4D9. Dataset accessed 20201010.

NASA Goddard SFC, OEL OBPG (2020b), MODIS-Terra Global Level 3 Mapped SST, Physical Oceanography Distributed Active Archive Center, https://doi.org/10.5067/MODST-1D4D9. Dataset accessed 20201010.

National Police Agency of Japan (2011), Damage Situation and Police Countermeasures Associated With 2011 Tohoku District—Off Pacific Ocean Earthquake, *Tech. rep.*, Emergency Disaster Countermeasures Headquarters, Tokyo, Japan.

Okihiro, M., R. T. Guza, and R. J. Seymour (1993), Excitation of seiche observed in a small harbor, *J. Geophys. Res.*, *98*, 18,201–18,211.

Ortiz-Huerta, L. G., and M. Ortiz (2022), On the Hunga Tonga complex tsunami as observed along the Pacific coast of Mexico on January 15, 2022, *Pure Appl. Geophys.*, *179*, 1139–1145, doi:10.1007/s00024-022-03027-7.

Pattiaratchi, C. B., and E. M. S. Wijeratne (2015), Are meteotsunamis an underrated hazard?, *Philos. T. R. Soc. A*, *373*, 20140377, doi:10.1098/rsta.2014.0377.

Peng, J.-P., P. Holtermann, and L. Umlauf (2020), Frontal instability and energy dissipation in a submesoscale upwelling front, *J. Phys. Oceanogr.*, *50*, 2017–2035, doi:10.1175/JPO-D-19-0270.1.

Philander, S. G. H. (1976), A whirling ecosystem in the equatorial Atlantic, *Geophys. Res. Lett.*, *81*(21), 3725–3735.

Philander, S. G. H. (1978), Instabilities of zonal equatorial currents, *Geophys. Res. Lett.*, *83*(C7), 3679–3682.

Phillips, O. M. (1981), The structure of short gravity waves on the ocean surface, in *Spaceborne synthetic aperture radar for oceanography*, edited by R. C. Beal, P. S. DeLeonibus, and I. Katz, pp. 24–31, Johns Hopkins Press, Baltimore.

Pingree, R. D., and B. L. Cann (1992), Anticyclonic eddy X91 in the southern Bay of Biscay, May 1991 to February 1992, *J. Geophys. Res.*, *97*(C9), 14,353–14,367.

Qiao, L., and R. H. Weisberg (1995), Tropical instability wave kinematics: observations from the Tropical Instability Wave Experiment, *J. Geophys. Res.*, *100*(C5), 8677–8693.

Qiao, L., and R. H. Weisberg (1998), Tropical instability wave energetics: observations from the Tropical Instability Wave Experiment, *J. Phys. Oceanogr.*, *28*, 345–360.

Quilfen, Y., B. Chapron, T. Elfouhaily, K. Katsaros, and J. Tournadre (1998), Observations of tropical cyclones by high-resolution scatterometry, *J. Geophys. Res.*, *103*(C4), 7767–7786.

Ramírez-Herrera, M. T., O. Coca, and V. Vargar-Espinosa (2022), Tsunami effects on the coast of Mexico by the Hunga Tonga-Hunga Ha‘apai volcano eruption, Tonga, *Pure Appl. Geophys.*, *179*, 1117–1137, doi:10.1007/s00024-022-03017-9.

Redelsperger, J.-L., M.-N. Bouin, J. Pianezze, V. Garnier, and L. Marié (2019), Impact of a sharp, small-scale SST front on the marine atmospheric boundary layer on the Iroise Sea: analysis from a hectometric simulation, *Q. J. Roy. Meteor. Soc.*, *145*, 3692–3714, doi:10.1002/qj.3650.

Richman, M. B. (1986), Rotation of principal components, *J. Climatol.*, *6*, 293–335, doi:10.1002/joc.3370060305.

Roeber, V., Y. Yamazaki, and K. F. Cheung (2010), Resonance and impact of the 2009 Samoa tsunami around Tutuila, American Samoa, *Geophys. Res. Lett.*, *37*, L21604, doi:10.1029/2010GL044419.

Romeiser, R., and W. Alpers (1997), An improved composite surface model for the radar backscattering cross section of the ocean surface 2. model response to surface roughness variations and the radar imaging of underwater bottom topography, *J. Geophys. Res.*, *102*(C11), 25,251–25,267.

Saha, K., X. Zhao, H. min Zhang, K. S. Casey, D. Zhang, S. Baker-Yeboah, K. A. Kilpatrick, R. H. Evans, T. Ryan, and J. M. Relph (2018), AVHRR Pathfinder version 5.3 level 3 collated (L3C) global 4km sea surface temperature for 1981-Present., NOAA National Centers for Environmental Information, https://doi.org/10.7289/v52j68xx. Dataset accessed 20190101.

Sallenger, A. H., J. H. List, G. Gelfenbaum, R. P. Stumpf, and M. Hansen (1995), Large wave at Daytona Beach, Florida, explained as a squall-line surge, *J. Coastal Res.*, *11*(4), 1383–1388.

Sangrà, P., J. L. Pelegrí, A. Hernández-Guerra, I. Arregui, J. M. Martín, A. Marrero-Díaz, A. Martínez, A. W. Ratsimandressy, and A. Rodríguez-Santana (2005), Life history of an anticyclonic eddy, *J. Geophys. Res.*, *110*, C03021, doi:10.1029/2004JC002526.

Sangrà, P., M. Auladell, A. Marrero-Díaz, J. L. Pelegrí, E. Fraile-Nuez, A. Rodríguez-Santana, J. M. Martín, E. Mason, and A. Hernández-Guerra (2007), On the nature of oceanic eddies shed by the Island of Gran Canaria, *Deep-Sea Res. Pt. I*, *54*, 687–709, doi:10.1016/j.dsr.2007.02.004.

Sawyer, M., P. Flament, and R. Knox (1995), Hydrographic SeaSoar data from the R/V Moana Wave cruises mw9010 and mw9012, *Tech. Rep. 94-04*, SOEST, University of Hawai'i at Mānoa, 101 pp.

Šepić, J., I. Vilibić, and N. Strelec Mahović (2012), Northern Adriatic meteorological tsunamis: Observations, link to the atmosphere, and predictability, *J. Geophys. Res.*, *117*, C02002, doi:10.1029/2011JC007608.

Šepić, J., I. Međugorac, I. Janeković, N. Dunić, and I. Vilibić (2016), Multi-meteotsunami event in the Adriatic Sea generated by atmospheric disturbances of 25-26 June 2014, *Pure Appl. Geophys.*, *173*(12), 4117–4138, doi:10.1007/s00024-016-1249-4.

Shao, M., D. G. Ortiz-Suslow, B. K. Haus, B. Lund, N. J. Williams, T. M. Ozgokmen, N. J. M. Laxague, J. Horstmann, and J. M. Klymak (2019), The variability of winds and fluxes observed near submesoscale fronts, *J. Geophys. Res.*, *124*, 7756–7780, doi:10.1029/2019JC015236.

Sheremet, A., U. Gravois, and V. Shrira (2016), Observations of meteotsunami on the Louisiana shelf: a lone soliton with a soliton pack, *Nat. Hazard.*, *84*, S471–S491, doi:10.1007/s11069-016-2446-2.

Skyllingstad, E. D., and R. M. Samelson (2020), Instability processes in simulated finite-width ocean fronts, *J. Phys. Oceanogr.*, *50*, 2781–2796, doi:10.1175/JPO-D-20-0030.1.

Smith, S. D. (1988), Coefficients for sea surface wind stress, heat flux, and wind profiles as a function of wind speed and temperature, *J. Geophys. Res.*, *93*(C12), 15,467–15,472.

Stamper, M. A., and J. R. Taylor (2017), The transition from symmetric to baroclinic instability in the Eady model, *Ocean Dynam.*, *67*, 65–80, doi:10.1007/s10236-016-1011-6.

Stanton, K. (2011), First look at King Kamehameha hotel damage, Hawaii 24/7, https://hawaii247.com/2011/03/11/first-look-at-king-kamehameha-hotel-damage/. Article accessed 20220531.

Tanaka, K. (2010), Atmospheric pressure-wave bands around a cold front resulted in a meteotsunami in the East China Sea in February 2009, *Nat. Hazard. Earth Sys.*, *10*, 2599–2610, doi:10.5194/nhess-10-2599-2010.

Tchilibou, M., L. Gourdeau, R. Morrow, G. Serazin, B. Djath, and F. Lyard (2018), Spectral signatures of the tropical Pacific dynamics from model and altimetry: a focus on the meso-/submesoscale range, *Ocean Sci.*, *14*, 1283—-1301, doi:10.5194/os-14-1283-2018.

The Open University (2001), *Ocean Circulation*, Volumes on Oceanography, 2nd ed., Butterworth-Heinemann, Linacre House, Jordan Hill, Oxford OX2 8DP.

Thomas, L. N., J. R. Taylor, R. Ferrari, and T. M. Joyce (2013), Symmetric instability in the Gulf Stream, *Deep Sea Res. Pt. II*, *91*, 96–110, doi:10.1016/j.dsr2.2013.02.025.

Thorpe, S. A. (2004), Langmuir circulation, *Annu. Rev. Fluid Mech.*, *36*, 55–79, doi:10.1146/annurev.fluid.36.052203.071431.

Tintoré, J., D. Gomis, S. Alonso, and D.-P. Wang (1988), A theoretical study of large sea level oscillations in the western Mediterranean, *J. Geophys. Res.*, *93*(C9), 10,797–10,803.

Tsai, V. C., J.-P. Ampuero, H. Kanamori, and D. J. Stevenson (2013), Estimating the effect of Earth elasticity and variable water density on tsunami speeds, *Geophys. Res. Lett.*, *40*, 492–496, doi:10.1002/grl.50147.

Ubelmann, C., and L.-L. Fu (2011a), Cyclonic eddies formed at the pacific tropical instability wave fronts, *J. Geophys. Res.*, *116*, C12021, doi:10.1029/2011JC007204.

Ubelmann, C., and L.-L. Fu (2011b), Vorticity structures in the tropical pacific from a numerical simulation, *J. Phys. Oceanogr.*, *41*, 1455–1464, doi:10.1175/2011JPO4507.1.

Vallis, G. K. (2006), *Atmospheric and Oceanic Fluid Dynamics*, 745 pp., Cambridge University Press, Cambridge, U.K.

Watada, S. (2013), Tsunami speed variations in density-stratified compressible global oceans, *Geophys. Res. Lett.*, *40*, 4001–4006, doi:10.1002/grl.50785.

Weisberg, R. H. (1984), Instability waves observed on the equator in the Atlantic Ocean during 1983, *Geophys. Res. Lett.*, *11*(8), 753–756.

Wenegrat, J. O., and R. S. Arthur (2018), Response of the atmospheric boundary layer to submesoscale sea surface temperature fronts, *Geophys. Res. Lett.*, *45*, 13,505–13,512, doi:10.10029/2018GL081034.

Yamazaki, Y., and K. F. Cheung (2011), Shelf resonance and impact of near-field tsunami generated by the 2010 Chile earthquake, *Geophys. Res. Lett.*, *38*, L12605, doi:10.1029/2011GL047508.

Yamazaki, Y., Z. Kowalik, and K. F. Cheung (2009), Depth-integrated, non-hydrostatic model for wave breaking and run-up, *Int. J. Numer. Method. F.*, *61*(5), 473–497, doi:10.1002/fld.1952.

Yamazaki, Y., T. Lay, K. F. Cheung, Y. Hue, and H. Kanamori (2011a), Modeling near-field tsunami observations to improve finite-fault slip models for the 11 March 2011 Tohoku earthquake, *Geophys. Res. Lett.*, *38*, L00G15, doi:10.1029/2011GL049130.

Yamazaki, Y., K. F. Cheung, and Z. Kowalik (2011b), Depth-integrated, non-hydrostatic model with grid nesting for tsunami generation, propagation, and run-up, *Int. J. Numer. Method. F.*, *67*(12), 2081–2107, doi:10.1002/fld.2485.

Yamazaki, Y., K. F. Cheung, G. Pawlak, and T. Lay (2012), Surges along the Honolulu coast from the 2011 Tohoku tsunami, *Geophys. Res. Lett.*, *39*, L09604, doi:10.1029/2012GL051624.

Yamazaki, Y., K. F. Cheung, and T. Lay (2013), Modeling of the 2011 tohoku near-field tsunami from finite-fault inversion of seismic waves, *B. Seismol. Soc. Am.*, *103*(2B), 1444–1455, doi:10.1785/0120120103.

Yoder, J. A., S. G. Ackelson, R. T. Barber, P. Flament, and W. Bach (1994), A line in the sea, *Nature*, *371*, 689–692.

Zhou, H., Y. Wei, L. Wright, and V. V. Titob (2014), Waves and currents in Hawaiian waters induced by the dispersive 2011 Tohoku tsunami, *Pure Appl. Geophys.*, *171*(12), 3365–3384, doi:10.1007/s00024-014-0781-3.